Investigation and Control of Spin Waves in Ferromagnetic Thin Films, Interface and Nanostructures

Thesis submitted for the degree of

Doctor of Philosophy (Science)

in

Physics (Experimental)

by

Avinash Kumar Chaurasiya

Department of Physics

Jadavpur University

2020

CERTIFICATE FROM THE SUPERVISOR

This is to certify that the thesis entitled "**Investigation and Control of Spin Waves in Ferromagnetic Thin Films, Interface and Nanostructures**" submitted by **Shri Avinash Kumar Chaurasiya** who got his name registered on 26th April 2016 for the award of Ph.D. (Science) degree of Jadavpur University, is absolutely based upon his own work under the supervision of **Prof. Anjan Barman** and that neither this thesis nor any part of it has been submitted for either any degree / diploma or any other academic award anywhere before.

09/11/2020

(Signature of the Supervisor (s) with date and official seal)

Dr. Anjan Barman, Ph.D.
Senior Professor & Associate Dean (Faculty)
Dept. of Condensed Matter Physics and Material Sciences
S. N. Bose National Centre for Basic Sciences
Block-JD, Sector-III, Salt Lake, Kolkata-700106, India

i

To My Loving Family........

Abstract

The primary requirements for the development of spintronics are its potential for miniaturization, speed of operation, thermal stability, low power consumption and cost. It is possible to tailor and fabricate thin film heterostructures with added functionalities for the improved interface induced phenomena such as interfacial Dzyaloshinskii Moriya interaction (iDMI, an essential parameter required for the stabilization of chiral spin texture known as skyrmions), reconfigurable spin-wave (SW) nonreciprocity, spin pumping, spin Hall effect, etc. The framework of this thesis is based on the experimental and theoretical investigation of SW in ferromagnetic (FM)/nonmagnetic (NM) thin film heterostructures and nanostructures. Primarily, wave vector resolved Brillouin light scattering technique (conventional-BLS) and microfocused BLS have been employed to probe the characteristic behaviour of SW in various combination of thin film heterostructures, 1D magnonic crystal and 2D artificial spin ice systems. The tunability in the magnetic properties have been achieved via varying thickness of thin films, choosing an appropriate combination of materials, nanostructuring, electric field, etc. Specifically, the studied systems are classified as follows:

i) Investigation of asymmetric spin wave dispersion in thin film heterostructures: A detailed investigation of pure iDMI in technologically relevant heavy metal (HM)/ ferromagnet (FM) thin film heterostructures, namely $W/CoFeB/SiO_2$, $Ta/CoFeB/TaO_x$, and $TaN/CoFeB/MgO$ have been carried out by measuring the asymmetric SW dispersion using BLS technique. Further, the presence of iDMI in 2D Material/FM interface namely graphene/$Ni_{80}Fe_{20}$ have been investigated and occurrence of sizable iDMI have been revealed, despite the fact that carbon is a low-Z material. The observed iDMI in graphene/$Ni_{80}Fe_{20}$ is found to originate primarily from the defect induced extrinsic spin-orbit coupling of the monolayer graphene. A linear correlation between spin-mixing conductance and surface DMI constant with respect to the defect density in graphene has been established. Next, we examine the SW nonreciprocity induced by dipolar interactions in a coupled bilayer consisting of two FM layers separated by a NM spacer (NiFe/Ir/CoFeB). The study is carried out by means of BLS spectroscopy that is complemented by analytical calculations. It is revealed that relative magnetic orientation can be controlled through a bias magnetic field, and the ensuing magnon nonreciprocity

can be turned on and off, which lends an important functionality to the coupled FM bilayers paving a way for reconfigurable SW frequency nonreciprocity.

ii) Magnonic crystals in the form of artificial spin ice and voltage-controlled 1D magnonic crystal: A comprehensive study of the spin wave dynamics of connected and disconnected kagome artificial spin ice nanostructures made of $Ni_{80}Fe_{20}$ nanobars using BLS technique complemented by micromagnetic simulations have been performed. The controllability of the various SW modes with the magnitude as well as direction of the applied field has been demonstrated. The propagating SWs in $Ni_{80}Fe_{20}$ and CoFeB waveguide have been studied using custom-built microfocused BLS technique. In the case of NiFe, imaging of the propagating SWs yields essential parameters of the SWs such as decay length, group velocity etc. Further, the tunability in the magnonic band gap by an electric field across the CoFeB/MgO interface applied through patterned 1D array of stripe-like electrodes pave the way to new generation reprogrammable magnonic devices with minimum Ohmic dissipation.

List of Publications

I. Included in the Thesis

[1] "Improved Magnetic Damping in CoFeB/MgO with an N-doped Ta Underlayer Investigated using Brillouin Light Scattering Technique"

J. Sinha, C. Banerjee, **A. K. Chaurasiya,** M. Hayashi and A. Barman, RSC Adv. **5**, 57815 (2015).

[2] "Direct Observation of Interfacial Dzyaloshinskii Moriya Interaction from Asymmetric Spin wave Propagation in W/CoFeB/SiO$_2$ Heterostructures Down to Subnanometer CoFeB Thickness"

A. K. Chaurasiya, C. Banerjee, S. Pan, S. Sahoo, S. Choudhury, J. Sinha and A. Barman, Sci. Rep. **6**, 32592 (2016).

[3] "Dependence of Interfacial Dzyaloshinskii Moriya Interaction on Layer Thicknesses in Ta/CoFeB/TaO$_x$ Heterostructures from Brillouin Light Scattering Technique"

A. K. Chaurasiya, S. Choudhury, J. Sinha, and A. Barman, Phys. Rev. Appl. **9,** 014008 (2018).

[4] "Direct Observation of Unusual Interfacial Dzyaloshinskii Moriya Interaction in Graphene/NiFe/Ta Heterostructures"

A.K. Chaurasiya, A. Kumar, R. Gupta, S. Chaudhary, P. K. Muduli, and A. Barman, Phys. Rev. B **99**, 035402 (2019).

[5] "Reconfigurable Spin-wave Nonreciprocity Induced by Dipolar Interaction in a Coupled Ferromagnetic Bilayer"

R. A. Gallarado, T. Schneider, **A. K. Chaurasiya,** A. Oelschlägel, S. S. P. K. Arekapudi, A. Roldán-Molina, R. Hübner, K. Lenz, A. Barman, J. Fassbender, J. Lindner, O. Hellwig, and P. Landeros, Phys. Rev. Appl. **12**, 034012 (2019).

[6] "Magnetic Field Controlled Transition in Spin-Wave Dynamics in Kagome Artificial Spin Ice Structure"

A. K. Chaurasiya *et al*. (Manuscript to be submitted)

[7] "Propagating Spin Waves in Magnonic Waveguides Studied using Microfocused Brillouin Light Scattering"

A. K. Chaurasiya *et al*. (Manuscript to be submitted)

II. Not Included in the Thesis

[8] "Tunable Spin Wave Properties in [Co/NiFe]r Multilayer with the Number of Bilayer Repetition"

C. Banerjee, **A. K. Chaurasiya**, S. Saha, J. Sinha and A. Barman; J. Phys. D: Appl. Phys. **39**, 395001 (2015).

[9] "Investigation of Magnetization Dynamics in Two dimensional $Ni_{80}Fe_{20}$ Diatomic Nanodot Arrays"

A. De, S. Mondal, C. Banerjee, **A. K. Chaurasiya**, R. Mandal, Y. Otani, R. K. Mitra, and A. Barman, J. Phys. D: Appl. Phys. **50**, 385002 (2017).

[10] "Observation of Skyrmions at room temperature in Co_2FeAl Heusler Alloy Ultrathin Film Heterostructures"

S. Hussain, N. Sisodia, **A.K. Chaurasiya**, A. Kumar, J. P. Singh, B. S. Yadav, S. Akansel. K. W. Chae, A. Barman, P. K. Muduli, P. Svedlindh, and S. Chaudhary, Sci. Rep. **9**, 1085 (2019).

[11] "Anisotropic Spin-wave Dispersion in Two Dimensional $Ni_{80}Fe_{20}$ Diatomic Dot Array" A. De, C. Banerjee, **A. K. Chaurasiya**, R. Mandal, Y. Otani, R. K. Mitra and A. Barman, J. Magn. Magn. Mater. **491**, 165557 (2019).

[12] "Spin Texture Driven Reconfigurable Magnonics in Chains of Connected $Ni_{80}Fe_{20}$ Submicron Dots"

A. K. Mondal, C. Banerjee, A. Adhikari, **A. K. Chaurasiya,** S. Choudhury, J. Sinha, S. Barman, and A. Barman, Phys. Rev. B **101**, 224426 (2020).

[13] "Direct measurement of interfacial Dzyaloshinskii–Moriya interaction at the $MoS_2/Ni_{80}Fe_{20}$ interface"

A. Kumar*, **A. K. Chaurasiya***, N. Chowdhury, A. K. Mondal, R. Bansal, A. Barvat, S. P. Khanna, P. Pal, S. Chaudhary, A. Barman, and P. K. Muduli, *Appl. Phys. Lett.* **116**, 232405 (2020) (*Joint first authors)

[14] "Voltage Controlled On-Demand Magnonic Nanochannels"

S. Choudhury. **A. K. Chaurasiya**, A. K. Mondal, B. Rana, K. Miura, H. Takahashi, Y. Otani, and A. Barman, Sci. Adv. **6**, eaba5457 (2020)

[15] "Anisotropic Spin-wave Propagation in Asymmetric Width Modulated $Ni_{80}Fe_{20}$ Nanostripes"

A. Adhikari, C. Banerjee, A. K. Mondal, **A. K. Chaurasiya,** S. Choudhury, J. Sinha, S. Barman, and A. Barman, (Manuscript communicated).

Acknowledgements

In 2013, I joined the S. N. Bose National Centre for Basic Sciences (SNBNCBS), Kolkata as an integrated PhD student. During my B.Sc. days in Banaras Hindu University, Varanasi, I got a little bit of motivation to do research but the real exposure was realized after joining SNBNCBS. Hailing from a small town of Kushinagar (the place where Lord Gautam Buddha attained Parinirvana after his death) in Uttar Pradesh, getting a chance in a reputed research institute like SNBNCBS for higher studies was indeed a remarkable achievement for me. There has been a lot of ups and downs during my PhD, handling those hurdles successfully has been an inspiring journey that I will remember forever. Firstly, I would like to express my sincere gratitude and deepest respect to my supervisor Prof. Anjan Barman for his countless efforts and constant support throughout my PhD journey. I am forever indebted to him for making me learn the basic research methodology to carry out the research and to present the research works as clearly as possible. It was a great privilege and honour to work under his excellent guidance. I also thank him for providing me an opportunity and showing his faith in me for my M.Sc. projects. I remember how difficult was to get that chance to join his research team and do research in his world class laboratory. His dynamism, vision, seriousness, discipline and dedication towards research has deeply motivated me to pursue research. I gratefully acknowledge his efforts to improve my presentation skills and allowing me to communicate my research to the global communities through various national and international conferences. He has always been supportive and caring in all circumstances.

I am also very grateful to Dr. Jaivardhan Sinha for his enrich understanding and research experience which helped me quite a lot. He is such a humble person that everyone appreciates him. Coincidently, he was also new in Prof. Barman's lab when I joined for my M.Sc. project. The stimulating discussion with him specially in starting years of my Ph.D. dissertation has helped me to grow as a researcher. I thank him for making me learn the various sample characterization tools, helping me to interpret the results and writing the manuscript in a scientific manner.

I specially thank Dr. Chandrima Banerjee for her guidance and care during my initial days in lab. She is the one who first introduced me BLS spectroscopy and taught me to handle and perform BLS measurement. She trained me to align the tandem Fabry-Pérot interferometer and other sophisticated optical alignment. Few times, I also got scolded by her for my mistakes in the lab but in some sense, it helped me a lot to grow myself and

List of Abbreviations

AFM   : Atomic force microscopy

(A)FM   : (Anti) Ferromagnet

ASI   : Artificial spin ice

AHE   : Anomalous Hall effect

Å   : Angstrom

BLS   : Brillouin light scattering

BZ   : Brillouin zone

BG   : Bandgap

CMOS   : Complementary -metal-oxide semiconductor

CVD   : Chemical vapor deposition

CW   : Continuous wave

DC (dc)   : Direct current

DE   : Damon–Eshbach

(i)DMI   : Interfacial Dzyaloshinskii-Moriya interaction

DOS   : Density of state

DPSS   : Diode pumped solid state laser

DW   : Domain wall

EBL   : Electron beam lithography

EBE   : Electron beam evaporation

EM   : Electromagnetic

EMF   : Electromotive force

EY   : Elliott-Yafet

ECMA   : Electric field controlled magnetic anisotropy

EDXS   : Energy dispersive x-ray spectroscopy

EFCMWG   : Electric field controlled magnonic waveguide

e.g.   : For example

FDM   : Finite difference method

FE   : Ferroelectric

FFT   : Fast Fourier transform

(FE)SEM   : (Field emission) scanning electron microscopy

FEM   : Finite element method

FMR	: Ferromagnetic resonance
(T)FPI	: (Tandem) Fabry-Pérot interferometer
FSR	: Free spectral range
fs	: Femtosecond
FWHM	: Full width at half maximum
GMR	: Giant magnetoresistance
GSG	: Ground-signal-ground
HAMR	: Heat assisted magnetic recording
HM	: Heavy metal
HWHM	: Half width at half maximum
HWP	: Half wave plate
Hz	: Hertz
i.e.	: That is
IP	: In plane
IPA	: Iso-propyl alcohol
(I)SHE	: (Inverse) spin Hall effect
LBO	: Lithium triborate
LLG	: Landau-Lifshitz-Gilbert
LED	: Light emitting diode
MAMR	: Microwave assisted magnetic recording
MSBVM	: Magnetostatic backward volume wave
MC	: Magnonic crystal
ME	: Magneto-elastic
MSFVM	: Magnetostatic forward volume wave
MFM	: Magnetic force microscopy
MHz	: Megahertz
MIBK	: Methyl isobutyl ketone
mm	: Millimeter
MO	: Microscope objective
(TR)MOKE	: (Time resolved) Magneto-optical Kerr effect
MPMS	: Magnetic properties measurement system
MRAM	: Magneto-resistive random-access memory
ms	: Millisecond

MSSW   : Magnetostatic surface spin wave

MTJ   : Magnetic tunnel junction

mW   : Milliwatt

MWG   : Magnonic Waveguide

µm   : Micrometer or micron

N. A.   : Numerical aperture

nm   : Nanometer

NM   : Nonmagnetic

ns   : Nanosecond

OBD   : Optical bridge detector

OOP   : Out of plane

OOMMF   : Object oriented micromagnetic framework

(i)PMA   : (Interfacial) Perpendicular magnetic anisotropy

(P)BS   : (Polarized) beam splitter

PSSW   : Perpendicular standing spin wave

PVD   : Physical vapor deposition

Py   : Permalloy

(P)MMA   : (Poly)methyl methacrylate

RF (rf)   : Radio frequency

RKKY   : Ruderman–Kittel–Kasuya–Yosida

RT   : Room temperature

SAF   : Synthetic antiferromagnet

SIA   : Structure Inversion Asymmetry

SHA   : Spin Hall angle

SOT   : Spin-orbit torque

SOC   : Spin-orbit coupling

SOI   : Spin-orbit interaction

STNO   : Spin torque nano oscillator

STT   : Spin transfer torque

SW   : Spin wave

SQUID   : Superconducting quantum interference device

TD   : Topological defect

(HR)TEM   : (High resolution) Transmission electron microscopy

THz	: Terahertz
TMR	: Tunnelling magnetoresistance
TOM	: Torsion oscillating magnetometry
VCMA	: Voltage controlled magnetic anisotropy
viz.	: In other words
vs.	: versus
VSM	: Vibrating sample magnetometry
XRD	: X-ray diffraction
YIG	: Yttrium iron garnet

List of Figures

of Δf vs k for both values of H. Symbols represent the experimental data points and solid lines are the fit using Eq. (8.4).

Table of Contents

Chapter 1

1. Introduction

Human life in the modern day has changed substantially because of the ever-increasing technological growth complemented by fundamental science. A lot of progress in the field of electronics and data communication has been made by science and technology which promises better lifestyle of the human in terms of health, knowledge and security. In the previous century, an immense development in the physics of charge current was made which has become an essential backbone of the modern electronics. As we know that an electron having a negative electric charge reign over various properties in condensed matter system. Apart from the charge degree of freedom, electron also has internal angular momentum, which is analogous to the rotation of a classical particle, named spin. Although the spin of an electron was known long ago, the spin-related exotic properties have been unravelled during last few decades only. This has revolutionized the material research field in terms of technological and fundamental science viewpoints. The development and implementation of this research field is growing tremendously by the hard work and the dedication which are being put together by the researchers globally. According to the international technology roadmap for semiconductors (ITRS), both the miniaturization as well as the operating speed of semiconductor devices will be reaching their extreme limits in the next few years [1]. In addition, the translational motion of electrons in semiconductor devices generate a huge amount of heat waste (due to Joule heating) leading towards high power consumption. It is the need of the hour to overcome these challenges to make a positive impact on the society. Initial attempts were made by introducing photonic (phononic) crystals [2-9] which are optical (acoustic) analogues of the atomic crystal where manipulation of frequency band is done using light (sound) waves by periodically modulated dielectric constants (elastic constant) and by varying the geometrical parameters of these artificial structures [10-15]. Thus, photonic crystals offer a high spectral selectivity which forms the basis for its potential application in optical nanodevices such as photonic waveguides [16-23] and integrated circuits [24-28]. On the other hand, a plethora of research activities have gained momentum in the field of nanomagnetism where novel and intriguing phenomena are observed at nanoscale. In the late 1980s, a considerable interest in the study of magnetic properties of the materials

had illuminated and as a result, a new term spintronics which is analogous to electronics came into the existence [29]. The spintronics (spin + electronics) mainly deals with the study of the role plays by electron spin in solid state physics and possible device applications that exploits the spin degree of freedom of electron. The achievement of the minimal power consumption, high speed information processing, nonvolatility and giant storage capacity in magnetic memory based on thin film heterostructures [30-36]. The successful spintronic device already being utilized in the industry as a read head and memory storage cell consists of giant magneto resistive (GMR) structure having alternating ferromagnetic (FM) and nonmagnetic (NM) metal layers [37-40]. The resistance of GMR device (commonly known as magnetoresistance) changes from large (antiparallel magnetization) to small (parallel magnetization) depending upon the relative orientation of the magnetization in the magnetic layers. The technological realization of the GMR is evident in non-volatile magnetic memories such as magnetoresistive random-access memory (MRAM) and magnetic hard disk drive (HDD) [30]. Recent progress in GMR technology also includes the magnetic tunnel junction [41-43] where tunnelling current depends upon the relative spin orientation of the electrodes. Therefore, the discovery of GMR can be thought of nothing less than a revolution in the field of data communication and hence to recognize this work, Peter Grunberg and Albert Fert were awarded Nobel prize in 2007. A number of intriguing and technologically important phenomena are also observed in thin film heterostructures, namely perpendicular magnetic anisotropy (PMA) [44], exchange spring effect [45]. (Inverse) Spin Hall effect ((I) SHE) [44-49], Rashba-Edelstein effect [49], spin pumping [50-52], interfacial Dzyaloshinskii-Moriya interaction (iDMI) [53-54], voltage controlled magnetic anisotropy (VCMA) [55-58], spin transfer torque (STT) [59-60], spin-Seebeck effect (SSE) [61-62] and spin Nernst effect [63-68]. In recent years, scientific community has explored plenty of sub-branches under magnetism research such as spintronics [69-71], magnonics [72-76], topological magnonics [77,78], spin-orbitronics [79-81], antiferromagnetic spintronics [82], magnon-spintronics [83], magneto-electronics [84,85], magneto-photonics [86,87], magneto-phononics [88-90], spin mechatronics [91], skyrmionics [92] etc.

To harness the spin degree of freedom over the charge, spin waves (SWs) have a potential to make an impact for energy efficient data transfer and processing. SWs and their quanta, magnons (with spin 1 obeying Bose-Einstein statistics) are the low-lying energy states of

spin systems coupled by exchange interaction [93-94]. In 1929, SWs were first predicted by F. Bloch [95-98]. SWs can be visualized as propagating phase of precession of microscopic magnetization vector in a magnetic medium. Interestingly, the frequency of the SW lies in the GHz regime which makes it suitable for on-chip data communications at nanoscale. On the other hand, they present a broad variety of linear and non-linear properties which offers an ample room for fundamental research. Because of the intriguing properties shown by SWs propagating through a periodically modulated magnetic media, the name *magnon crystal* was coined by Nikitov [99]. The main advantage of the magnonics lies in the fact that the transport and processing of information by SWs occurs without the movement of any real particle which makes it lucrative from the technological point of view. SW in periodically patterned ferromagnets, the magnonic crystal (MC), is analogues to the electromagnetic (EM) waves in photonic crystals (where periodic structures moulds the flow of plasmon, elastic or acoustic waves). The MC belongs to an unusual class of artificial crystals as it offers tunability in the magnon band structures not only due to the periodic nature of the crystal but also due to the spatial arrangement of the magnetization vectors within it [100-103]. The SW dispersion characteristics can be controlled by the geometrical parameters of the lattices such as element shape, element size, lattice constant and lattice symmetry combined with the magnitude and angle of the applied magnetic field, electric field by modulating VCMA. This feature offers a remarkable flexibility for tailoring the SW properties in unconventional artificial structures, such as skyrmion lattice [104-107], artificial spin ice [108-114], fractal structures [115,116] and quasicrystals [117]. In the case of dipole dominated SWs, SW dispersion is anisotropic and can be classified on the basis of the relative orientation of magnetic field and the SW wave vector, namely the Damon-Eshbach (DE) [118], backward volume (BV) [119,120] and forward volume characteristics [121]. Further, perpendicular standing SWs (PSSW) with different nodal planes across the thickness of FM thin film can be found. The comprehensive control over the fundamental properties of SWs like frequency dispersion [122-123], amplitude [124], phase [125], group velocity [126], anisotropy [127], nonreciprocity [128] is undoubtedly necessary to pave the way for the next generation SW-based multifunctional devices. It is also worth mentioning here that hybridization of magnonics and spintronics with various other research fields is also growing steadily. For example, the interplay of the intriguing properties of magnonic, photonic and phononic crystals gives rise to newer emerging

3

artificial crystals called as magneto-photonics or mag-phonic crystals [129]. Furthermore, the spin orbit coupling induced interface related phenomena such as (inverse) SHE, iDMI, Rashba effect, spin pumping has grown tremendously in the recent years. The investigation and precise control of these effects are necessary for the technological relevance.

In the following, an overview of the potential systems related to the spintronic and magnonic based research will be presented in order to set a motivation of this thesis. Finally, the layout of the thesis will be given.

1.1. Thin Films for Information Storage

The development in the growth facilities of high-quality thin film heterostructures and nanostructure fabrication has led to the exploratory realization of many new physics in the recent years. The discovery of the GMR led to the revolution in the magnetic recording industry and the scope for demonstrating high density magnetic storage along with the controlled and fast magnetization switching has caught significant attention of the scientific community. Initially, the magnetic drum, tape, bubble memory and disk were being used to store the data in the form of magnetic domains where the orientation of magnetization in each grain/domain were used as the single bit of information. The read and write of the data was done using GMR or tunnelling magnetoresistance (TMR) based read head [130-135]. After this, longitudinal recording media [136,137] came into the picture where grain of a granular film was thought of as individual domain with in-plane magnetization. The shortcomings of these media were their thermal instability predominantly due to superparamagnetic effect and inadequacy for the higher storage capacity [138]. This repercussion happened due to the combined effect of the reduced size of the grains and the increased possibilities of the cross talk between the magnetic bits. The possible way out of this problem was observed in magnetic alloys (such as CoPt, CoCrPt) and multilayers (such as Co/Pt, Co/Pd, Fe/Pt, Co/Ni) with high PMA [139-141]. A higher areal density of about 340 GB/inch^2 [142] was achieved in PMA media which are thermally and magnetically more stable at room temperature (RT). Therefore, a great effort is needed to search for material for tailoring PMA by introducing defect adatoms and tuning thickness of the FM layer. Also, the doping of highly electronegative elements (like nitrogen) affects the strength of PMA leading towards the different characteristic behaviour of the thin film heterostructures [143].

4

On the other hand, despite of having the improved thermal stability in PMA systems, they still require a very high magnetic field to switch the magnetization. To solve this issue, heat assisted magnetic recording (HAMR) has been proposed by tuning the magnetic anisotropy locally by applying heat preferably using focused laser source [144]. Consequently, the search for the thin film heterostructures exhibiting favourable properties like tunable magnetic anisotropy, nonreciprocity due to Ruderman–Kittel–Kasuya–Yosida (RKKY) mediated interlayer interaction, chiral spin texture, topologically protected and stabilized skyrmions due to iDMI had begun. To this end, we have studied the SW properties of various class of FM thin film heterostructures as described below:

1.1.1. Systems with Structure Inversion Asymmetry

As mentioned above, thin film heterostructures of FM with a heavy metal (HM) having large spin-orbit coupling (SOC) gives rise to the fascinating phenomena such as PMA, SHE, spin pumping, Rashba-Edelstein (RE) effect and iDMI. Specifically, the effect of structure inversion asymmetry (SIA) in low dimensional systems of the type HM/FM/Oxide leads to DMI which is a type of indirect exchange interaction as predicted by Levy and Fert in 1980 [145]. However, because of the massive potential to explore new physics such as chiral domain walls and skyrmions (topologically protected magnetic solitons) experimentally, it has attracted huge attention recently. In the following, a brief description of the ongoing research based on these systems will be presented:

1.1.1.1. Heavy metal/Ferromagnet Interface

From the very beginning, HM/FM thin film heterostructures have shown tremendous opportunities for the advancement of the magnetic recording industry. In general, the pivotal role played by HM possessing large SOC leads to the occurrence of various phenomena as mentioned above. Interestingly, these spin-based phenomena are robust to defects, disorders and room temperature fluctuations making them appealing for room temperature spin-based device application. HM/FM-based heterostructures have emerged as a powerful entity to generate chiral magnetic structures, spin-charge interconversion under electric current and control over the magnetization dynamics. The switching of the magnetization has been possible via current induced spin orbit torque (SOT) by transferring the spin angular momentum from lattice to spin. As mentioned earlier, the broken inversion symmetry at HM (with large SOC)/FM interface leads to iDMI. The resulting spin textures due to large iDMI were first observed in ultrathin

epitaxial film structure Mn/W (110) [146] and skyrmions were observed in Fe and Fe/Pd on Ir layer [147-148]. More recently, the demonstration of skyrmions induced by iDMI has been possible at room temperature in magnetic multilayers grown by technologically relevant sputtering technique [149, 150]. These iDMI stabilized skyrmions are potential candidates for next generation information storage and logic devices. Different experimental tools like current induced domain wall motion [151], spin polarized scanning tunnelling microscopy [152], high resolution spin-polarized electron energy loss spectroscopy [153], scanning nitrogen vacancy magnetometer [154], synchrotron-based x-ray scattering [155], asymmetric hysteresis loop-based measurement [156] have been used to characterize the strength of DMI. It is worth to mention here that magnetic field and current driven domain wall measurements were definitely linked to the PMA. Hence, at present, an independent measurement by employing Brillouin light scattering (BLS) is widely being used to accurately explore iDMI in these SIA systems [157-167]. In most of the studies, Pt/FM heterostructures have been used. Since the Pt is an expensive material and also induces interface anisotropy, so the search of other alternative HM/FM such as W, Ta, Ir, TaN [160,161] systems with significant and pure iDMI is of high demand. Also, both W and Ta can show a thickness dependent structural phase transition from β to α phase and may affects the strength of iDMI. Therefore, it would be interesting to investigate how iDMI is affected by this phase transition. Furthermore, the investigation of iDMI in N-doped-Ta/CoFeB/MgO thin film heterostructures is important because it offers a unique opportunity to tune the magnetic properties as a function of nitrogen doping. Another important parameter is the magnetic damping, which is greatly influenced by the extrinsic contributions such as two-magnon scattering, spin flip scattering, spin pumping, etc, and it is important to explore the effect of Gilbert damping of an FM layer on the doping concentration of its adjacent HM layer and the ensuing magnetic inhomogeneity [168]. Hence, the manipulation and control of DMI, which plays a vital role in the context of chiral domain walls and skyrmions, offers a novel route to design spintronics devices for data storage and non-volatile logic.

1.1.1.2. 2D-Material/FM Interface

Two-dimensional (2D) materials are generally crystalline materials in nature formed by single layer of atoms. These materials are either 2D allotropes of various elements or compounds. The widely known 2D material made up of a single layer of graphitic carbon

is the graphene. The observation of spin transport with unprecedented spin diffusion lengths of the order of several micrometers at room temperature make the graphene a very favourable spin channel material [169]. The tunability of the carrier concentration and high electron mobility in graphene by application of gate voltage has also attracted significant interest recently [170,171]. There has been significant development in the field of graphene spintronics that includes defect induced magnetism in graphene [172], efficient spin injection [173,174], intrinsic and extrinsic SOC [175], enhancement of SOC in the graphene achieved via hydrogenation [176], fluorination [177], the presence of adatoms [178] etc. The presence of SOC in graphene leads to many other intriguing phenomena such as SHE [176], topological quantum SHE [179], quantum anomalous HE [180], Rashba effect [181], spin dependent Klein tunnelling [182], weak anti-localization [183] and modification of plasmon spectrum at large scale [184]. Hence, the tunability and controllability of SOC in graphene by gating and functionalization offers a very versatile route in pursuit of spintronics application. A major part of the graphene research is also being carried out to underpin the rich physics involved in graphene/FM interface making them useful candidate for magnetic memory devices. For example, recent observation of sizable iDMI at graphene/FM interface originating from Rashba effect when investigated using first principles calculation [185] and spin polarized electron microscopy [186] have not only ignited the research to explore the impact of it on the chiral spin texture but also to tune the strength of iDMI with thickness, localized defects etc. It also motivates to employ the direct measurement tools to asses iDMI in more industrial friendly graphene/FM systems [187]. Despite of the fact that graphene has very low intrinsic SOC, graphene induced iDMI should be adequate to stabilize skyrmions in graphene/FM-based heterostructures.

On the other hand, owing to the presence of larger intrinsic SOC in transition metal dichalcogenides (TMDs, e.g. MoS_2) than graphene, the possibility to enhance the DMI in the 2D-TMDs/FM-based heterostructures is more promising. Most importantly, the absence of the inversion centres in TMDs [188] bestows considerable advantage for generating unconventional SOT in TMDs/FM heterostructures [189-191].

1.1.1.3. Synthetic Antiferromagnet

Synthetic antiferromagnets (SAFs), which are artificial antiferromagnets consisting of two or more thin FM layers separated by NM spacers, are potentially important for applications in spintronics. The FM layers in SAF are coupled by thin NM spacer via

interlayer exchange coupling widely known as RKKY coupling [192-194]. In addition, by tuning the thickness of the NM spacer between two FM layers leads to the FM (parallel alignment) to antiferromagnet (AFM; antiparallel alignment). However, the quantitative comparison of the interlayer exchange coupling reveals that synthetic antiferromagnets possess a rather weak interlayer exchange coupling as opposed to the super exchange coupling in antiferromagnetic crystals. Nonreciprocal properties of SWs can be introduced into FM materials by the intrinsic dipolar interactions. Recently, SOT induced magnetization switching has also been demonstrated in devices consists of SAFs [195,196]. Moreover, the dipolarly coupled arrays of magnetic nanopillars [197], FM nanotubes [198], 1D FM periodic structure [199],and trilayers based of antiferromagnets [200] exhibit SW nonreciprocity which make SAFs desirable for applications in magnetic field sensing, MRAM and nanoscale nonreciprocal magnonic devices [201-203]. A detailed study regarding the reconfigurability of SW frequency nonreciprocities investigated using BLS has been carried out recently [204].

1.1.2. Magnonic Crystals

As mentioned earlier, there have been extensive research on the photonic crystals while its magnonic counterpart have not been very thoroughly studied from all possible angles. Owing to the controllability of the magnon frequency, band structure and band gap by internal structure and external stimuli and the presence of inherent anisotropy fields in magnetic systems, MCs derive more advantage over photonic or sonic crystals. Thanks to the combination of advanced nanofabrication facilities and advanced experimental tools to probe the dynamics of SW, a massive upsurge in the research activities based on the MCs has been seen over the last few years. Because of its very low damping, yttrium iron garnet (YIG, an insulating ferrimagnet) [205] has been heavily used to study the SW propagation. However, YIG suffers from the difficulty of nanopatterning and very low magnetic moment, and to overcome these problems several metallic FMs and their alloys, e.g. Ni [206], Fe [207], Ni_xFe_{1-x} (low magnetic moment and negligible magneto-crystalline anisotropy) [208] have proved to be efficient. On the other hand, Co [126], CoFe and CoFeB (having relatively higher magnetic moment) have been used in the spin valves and magnetic tunnel junctions (MTJs) to obtain high GMR or TMR values [208]. Magnetic multilayers with high PMA are also prospective for fabrication of MCs. Categorically, one can classify the types of MCs depending upon how the parameters like saturation

magnetization and magnetic anisotropy [210] or external stimuli such as magnetic field [211], electric current [212], stress [213], electric field [214], etc. vary. Array of nanostripes, nanowires, chains of nanoparticles, etc. are classified as 1D MCs while 2D arrays of nanodots [215], antidots [216,217], artificial spin ice structures [112], magnetic solitons [218] and skyrmions lattices [219,220] can be classified as 2D MCs. Extension of MC in the 3rd dimensions can offer huge flexibility functionality. Conventionally, investigation of spin dynamics of 2D lattices of nanoelements by varying the element shape and size as well as the lattice parameters have been conducted by using time-resolved magneto-optical Kerr effect (TRMOKE) magnetometry, ferromagnetic resonance (FMR) technique and BLS spectroscopy [221-228] and a plethora of knowledge base on the spin-wave propagation, confinement, localization, hybridization, mode splitting, line broadening, mode hopping, crossover, dephasing, etc. have been found. In order to further improve the ultra-high-density data storage and memory devices, several new research avenues are being explored in the third dimension of magnetic system and a new sub area of research known as 3D nanomagnetism and 3D magnonics have emerged [229, 230].

1.1.2.1. Artificial Spin Ice

Artificial spin ice (ASI) is a kind of artificial magnetic structure designed by strongly interacting single domain nano islands in a geometrically frustrated array [231]. Frustration in a physical system emerges from inability of simultaneously minimizing all interactions [232]. In 2006, Wang *et al.* carried out pioneering experiments on lithographically defined arrays of interacting nanomagnets and explored physics analogous to spin ice materials (Pyrochlores, $Dy_2Ti_2O_7$ etc.) [112]. Following this work, immense research interests have emerged in the study of ASI because of the fundamental physics involved as well as considerable application potential such as reprogrammable memory, logic and more recently reconfigurable magnonics [114,233-235]. The quasiparticle monopole – anti monopole pair in these systems are often manifested as topological defects (TDs) and are separated by Dirac string [236,237]. In addition, a lot of attention is being paid by the scientific community to address the emergence of tunability in the high frequency dynamics due to TDs in these ASI [238]. These high frequency responses are somewhat closely related to the microstate which leads to further functional design of these ASIs for the tunability in their magnonic response [239]. To further enhance the knowledge base regarding the TDs, novel mechanisms are being

proposed. Recently, the ground state in the kagome ASI has been realized via topological magnetic writing [240]. In the context of experimental probing of the spin dynamics, FMR technique has been mostly employed which is based on the global excitation of a large area ASI subject to an external swept field [235]. The optical technique such as Brillouin light scattering (BLS), which is a powerful tool for probing spin dynamics, has been recently employed for the investigation of kagome ASI [241]. Subsequently, the chiral control of magnetic charge can provide an interesting tool leading to a new architecture for parallel computation, reprogrammable magnonics in both 2D and 3D systems.

1.1.2.2. **Magnonic Waveguide**

The vital concept to guide and manipulate SW propagation and miniaturization of SW conduits toward submicron dimensions has triggered a huge interest among the researchers. The direct imaging of the propagating SW with improved spatial resolution is imperative for emerging magnonic devices [242-245]. In this context, the micro-BLS technique has been proved to be a well-established technique to investigate the propagating SWs in various microstructure elements such as stripes [246], spin torque nano oscillators (STNOs) [247-248], rhomboid shaped nanoelements [249], curved ring waveguide [250] etc. However, the advanced nanofabrication techniques to make integrated antenna along with nanostructures enable us to think beyond the conventional structure and propose to utilize electric field-controlled SW propagation adding an extra control parameter for guiding the SW. Hence, the search for new MCs with provision of an energy efficient stimuli such as strain, electric field etc. may hold a key promise in the development of magnonic circuits with minimal power utilization.

1.2. Objective of the Thesis

The framework of this thesis is based on the experimental and theoretical investigation of SW in FM thin film, FM/NM heterostructures and nanostructure. Primarily, wave vector resolved Brillouin light scattering technique (conventional) and microfocused BLS have been employed to probe the characteristic behaviour of SW in various combination of thin film heterostructures, 1D magnonic crystal and 2D artificial spin ice systems. The tunability in the magnetic properties have been achieved via varying thickness of thin films, choosing an appropriate combination of materials, nanostructuring, electric field, etc. Specifically, the studies systems are classified as follows:

I. Investigation of Asymmetric Spin Wave Dispersion

(A) Heavy Metal/Ferromagnet/Oxide Heterostructures: A detailed investigation of pure iDMI in technologically relevant HM/FM thin film heterostructures, namely W/CoFeB/SiO_2, Ta/CoFeB/TaO_x, and TaN/CoFeB/MgO have been carried out by measuring the asymmetric SW dispersion using BLS technique.

(B) Graphene/Ferromagnet System: The presence of iDMI in 2D Material/FM interface namely graphene/$Ni_{80}Fe_{20}$ have been investigated and occurrence of sizable iDMI have been revealed, despite the fact that carbon is a low-Z material. The observed iDMI in graphene/$Ni_{80}Fe_{20}$ is found to originate primarily from the defect induced extrinsic spin-orbit coupling of the monolayer graphene. Furthermore, a linear correlation between spin-mixing conductance and surface DMI constant with respect to the defect density in graphene has been established.

(C) Synthetic Antiferromagnetic System: The experimental investigation of SW nonreciprocity induced by dipolar interactions in a coupled bilayer involving two FM layers separated by a thin NM spacer layer (permalloy/Ir/CoFeB) is carried out by means of BLS spectroscopy complemented by analytical calculations.

II. Magnonic Crystals in the Form of Artificial Spin Ice and Voltage Controlled 1D Magnonic Crystal

(A) Artificial Spin Ice System: A comprehensive study of the SW dynamics of connected and disconnected kagome artificial spin ice nanostructures made of $Ni_{80}Fe_{20}$ nanobars using Brillouin light scattering technique complemented by micromagnetic simulations have been performed. The controllability of the various SW modes with the magnitude as well as direction of the applied field is demonstrated.

(B) Voltage Controlled 1D Magnonic Crystal: The propagating SWs in $Ni_{80}Fe_{20}$ and CoFeB microwires are imaged using microfocused BLS technique. In the case of NiFe, imaging of the propagating yields essential parameters of the SWs such as decay length, group velocity etc. The role of the electric field applied across the CoFeB/MgO for tuning the magnonic band gap has been revealed.

References

[1] Semiconductor Industry and Association., "International Techn"logy Roadmap for Semiconductors," http://www.itrs.ne"/Links/2011ITRS/2011Chapters/2011ERD.pdf., (2011).

[2] S. S. Oh, C. S. Kee, J.-E. Kim, *et al.*, Appl. Phys. Lett. **76**, 2301 (2000).

[3] A. D'Orazio, M. D. Sario, V. Petruzzelli, *et al.*, Opt. Express **11**, 230 (2003).

[4] M. Loncar, T. Doll, J. Vuckovic, *et al.*, J. Lightwave Technol. **18**, 10 (2000).

[5] M. Loncar, T. Doll, J. Vuckovic, *et al.*, J. Lightwave Technol. **18**, 1402 (2000).

[6] E. Yablonovitch, J. Mod. Opt. **41,** 173 (1994).

[7] M.-H. Lu, L. Feng, and Y.-F. Chen, Mater. Today **12,** 34 (2009).

[8] M. S. Kushwaha, P. Halevi, L. Dobrzynski, and B. D. Rouhani, Phys. Rev. Lett. **71,** 2022 (1993).

[9] M. Jacoby, Chem. Eng. News **76,** 38 (1998).

[10] M. N. Armenise, C. E. Campanella, C. Ciminelli, F. Dell'Olio, and V. M. N. Passaro, Phys. Procedia **3,** 357 (2010).

[11] E. Yablonovitch, J. Opt. Soc. Am. B **10**, 283 (1993).

[12] M. E. Zoorob, M. D. B. Charlton, G. J. Parker, *et al.,* Nature **404,** 740 (2000).

[13] A. L. Chen, Y.-S. Wang, Y.-F. Guo, and Z.-D. Wang, Solid State Commun. **145,** 103 (2008).

[14] M. Florescu, S. Torquato, and P. J. Steinhardt, Phys. Rev. B **80,** 155112 (2009).

[15] I. E. Psarobas, N. Stefanou, and A. Modinos, Phys. Rev. B **62,** 5536 (2000).

[16] J. Li, and K. S. Chiang, J. Opt. Soc. Am. B **24,** 1942 (2007).

[17] A. Yu. Petrov, and M. Eich, IEEE J. Sel. Areas Commun. **23,** 1396 (2005).

[18] J. Li, T. P. White, L. O'Faolain, A. Gomez-Iglesias, and T. F. Krauss, Opt. Express **16,** 6227 (2008).

[19] J. C. Knight, Nature **424**, 847 (2003).

[20] J. Li, and K. S. Chiang, Opt. Commun. **281**, 5797 (2008).

[21] N. T. Otterstrom, R. O. Behunin, E. A. Kittlaus, Z. Wang, and P. T. Rakich, Science **360** 1113 (2018).

[22] A. Khelif, B. Djafari-Rouhani, J. O. Vasseur, and P. A. Deymier, Phys. Rev. B **68** 024302 (2003).

[23] M. Kurosu, D. Hatanaka, K. Onomitsu, and H. Yamaguchi, Nat. Commun. **9,** 1331 (2018).

[24] S. J. McNab, N. Moll, and Y. A. Vlasov, Opt. Express **11**, 2927 (2003).

[25] F. V. Laere, T. Stomeo, C. Cambournac, *et al.*, J. Lightwave Technol. **27**, 417 (2009).

[26] F. V. Laere, G. Roelkens, M. Ayre, *et al.*, J. Lightwave Technol. **25**, 151 (2007).

[27] Y.-F. Wang, T.-T. Wang, Y.-S. Wang, V. Laude, Phys. Rev. Appl. **8,** 014006 (2017).

[28] S.-Y. Yu, C. He, Z. Wang, *et al.,* Nat. Commun. **9,** 3072 (2018).

[29] S. A. Wolf, D. D. Awschalom, R. A. Buhrman, *et al.*, Science **294**, 1488 (2001).

[30] S. Tehrani, E. Chen, M. Durlam, *et al.*, J. Appl. Phys. **85**, 5822 (1999).

[31] A. Imre, G. Csaba, L. Ji, *et al.*, Science **311**, 205 (2006).

[32] D. A. Allwood, G. Xiong, C. C. Faulkner, *et al.*, Science, **309**, 1688 (2005).

[33] K.-S. Lee, D.-S. Han, and S.-K. Kim, Phys. Rev. Lett. **102**, 127202 (2009).

[34] Y. L. Etko and A. B. Ustinov, Tech. Phys. Lett. **37**, 1015 (2011).

[35] S. S. P. Parkin, M. Hayashi, and L. Thomas, Science **320**, 190 (2008).

[36] T. Thomson, G. Hu, and B. D. Terris, Phys. Rev. Lett. **96**, 257204 (2006).

[37] P. Grünberg, R. Schreiber, Y. Pang, M. B. Brodsky, and H. Sowers, Phys. Rev. Lett. **57**, 2442 (1986).

[38] M. N. Baibich, J. M. Broto, A. Fert, *et al.*, Phys. Rev. Lett. **61** 2472 (1988).

[39] G. Binasch, P. Griinberg, F. Saurenbach, *et al.*, Phys. Rev. B **39**, 4828 (1989).

[40] S. S. P. Parkin, Z. G. Li, and D. J. Smith, Appl. Phys. Lett. **58,** 2710 (1991).

[41] M. Bowen, V. Cros, F. Petroff, and A. Fert, Appl. Phys. Lett. **79,** 1655 (2001).

[42] S. Yuasa, T. Nagahama, A. Fukushima, Y. Suzuki, and K. Ando, Nat. Mater. **3,** 868 (2004).

[43] J. M. Teixeira, J. D. Costa, J. Ventura, *et al.*, Appl. Phys. Lett. **102,** 212413 (2013).

[44] B. M. Lairson, M. R. Visokay, R. Sinclair, and B. M. Clemens, Appl. Phys. Lett. **62**, 639 (1993).

[45] R. Coehoorn, D. B. de Mooij, and C. de Waard, J. Mag. Magn. Mater. **80**, 101 (1989).

[46] J. E. Hirsch, Phys. Rev. Lett. **83,** 1834 (1999).

[47] Y. K. Kato, R. C. Myers, A. C. Gossard, and D. D. Awschalom, Science **306,** 1910 (2004).

[48] E. H. Hall, Am. J. Math. **2** 287 (1879).

[49] V. M. Edelstein, Solid State Commun. **73**, 233 (1990).

[50] A. Brataas, Y. Tserkovnyak, G. E. W. Bauer, B. I. Halperin, Phys. Rev. B **66,** 060404 (2002).

[51] Y. Tserkovnyak, A. Brataas, and G. E. W. Bauer, Phys. Rev. Lett. **88,** 117601 (2002).

[52] A. Brataas, A. D. Kent, and H. Ohno, Nat. Mater. **11,** 372 (2012).

[53] I. Dzyaloshinsky, J. Phys. Chem. Solids **4**, 241 (1958).

[54] T. Moriya, Phys. Rev. **120,** 91 (1960).

[55] M. Todorovic, S. Schultz, J. Wong, and A. Scherer, Appl. Phys. Lett. **74,** 2516 (1999).

[56] K. Kobayashi, G. Ishida, J. Appl. Phys. **52,** 2453 (1981).

[57] D. Makarov, E. Bermúdez-Ureña, O. G. Schmidt, *et al.*, Appl. Phys. Lett. **93,** 153112 (2008).

[58] Q. Leng, M. Mao, C. Hiner, *et al.,* IEEE Trans. Magn. **35,** 2553 (1999).

[59] L. Berger, Phys. Rev. B **54**, 9353 (1996).

[60] J. Slonczewski, J. Magn. Magn. Mater. **159**, L1 (1996).

[61] K. Uchida, S. Takahashi, K. Harii, *et al.*, Nature **455**, 778 (2008).

[62] K. Uchida, J. Xiao, H. Adachi, *et al.,* Nat. Mater. **9,** 894 (2010).

[63] S.-G. Cheng, Y. Xing, Q.-F. Sun, and X. C. Xie, Phys. Rev. B **78,** 045302 (2008).

[64] X. Liu, X. C. Xie, Solid State Commun. **150**, 471 (2010).

[65] S. Meyer, Y. T. Chen, S. Wimmer, *et al.*, Nat. Mater. **16,** 977 (2017).

[66] P. Sheng, Y. Sakuraba, Y.-C. Lau, S. Takahashi, S. Mitani, and M. Hayashi, Sci. Adv. **3**, e1701503 (2017).

[67] A. V. Ettingshausen, and W. Nernst, Ann. Phys. **265**, 343 (1886).

[68] M. T. Dau, C. Vergnaud, A. Marty, *et al.,* Nat. Commun. **10**, 5796 (2019).

[69] S. A. Wolf, D. D. Awschalom, R. A. Buhrman, *et al.*, Science **294,** 1488 (2001).

[70] A. Fert, Rev. Mod. Phys. **80,** 1517 (2008).

[71] G. Beach, Nat. Mater. **9,** 959 (2010).

[72] V. V. Kruglyak and R. J. Hicken, J. Magn. Magn. Mater. **306,** 191 (2006).

[73] S. Neusser and D. Grundler, Adv. Mater. **21,** 2927 (2009).

[74] V. V. Kruglyak, S. O. Demokritov, and D. Grundler, J. Phys. D: Appl. Phys. **43,** 264001 (2010).

[75] B. Lenk, H. Ulrichs, F. Garbs, and M. Münzenberg, Phys. Rep. **507,** 107 (2011).

[76] A. A. Serga, A. V. Chumak, and B. Hillebrands, J. Phys. D: Appl. Phys. **43,** 264002 (2010).

[77] X. S. Wang, H. W. Zhang, and X. R. Wang, Phys, Rev. Appl. **9**, 024029 (2018).

[78] X S Wang and X R Wang, *J. Phys. D: Appl. Phys.* **51,** 194001 (2018).

[79] A. Manchon, H. C. Koo, J. Nitta, S. M. Frolov, and R. A. Duine, Nat. Mater. **14,** 871 (2015).

[80] T. Kuschel and G. Reiss, Nat. Nanotechnol. **10,** 22 (2014).

[81] V. Dugaev, I. Tralle, A. Wal, and J. Barna, Spin Orbitronics and Topological Properties of Nanostructures (World Scientific, 2017).

[82] V. Baltz, A. Manchon, M. Tsoi, T. Moriyama, T. Ono, and Y. Tserkovnyak, Rev. Mod. Phys. **90**, 015005 (2018).

[83] A. V. Chumak, V. I. Vasyuchka, A. A. Serga, and B. Hillebrands, Nat. Phys. **11,** 453 (2015).

[84] G. A. Prinz, Science **282,** 1660 (1998).

[85] C. Chappert, A. Fert, and F. N. Van Dau, Nat. Mater. **6** 813 (2007).

[86] J. Wang, C. Zhang, H. Liu, *et al.*, Nat. Commun. **10,** 129 (2019).

[87] G. Ctistis, E. Papaioannou, P. Patoka, *et al.*, Nano Lett. **9,** 1 (2009).

[88] V. L. Zhang, F. S. Ma, H. H. Pan, *et al.*, Appl. Phys. Lett. **100,** 163118 (2012).

[89] H. H. Pan, V. L. Zhang, K. Di, *et al.*, Nanoscale Res. Lett. **8,** 115 (2013).

[90] P. Graczyk and M. Krawczyk, Phys. Rev. B **96,** 024407 (2017).

[91] M. Matsuo, E. Saitoh, and S. Maekawa, J. Phys. Soc. Jpn. 86 (2016) 011011.

[92] C. Back, V. Cros, H. Ebert *et al.*, J. Phys. D: Appl. Phys. 122829.R1 (2020)

[93] A. I. Akhiezer, V. G. Bar'yakhtar, and S. V. Peletminskii, "Spin Waves," Amsterdam, North-Holland, (1968).

[94] A. G. Gurevich and G. A. Melkov, "Magnetization Oscillations and Waves," New York, Chemical Rubber Corp., (1996).

[95] F. Bloch, "Zur theorie des ferromagnetismus," Z. Phys. **61**, 206 (1930)

[96] T. Holstein and H. Primakoff. Phys. Rev., **58,** 1098 (1940).

[97] Conyers Herring and Charles Kittel, Phys. Rev. **81**, 869 (1951).

[98] F. J. Dyson. Phys. Rev., **102**, 1217 (1956).

[99] S. A. Nikitova, P. Tailhadesa, and C. S. Tsai, J. Magn. Magn. Mater. **236**, 320 (2001)

[100] J. Jorzick, S. O. Demokritov, B. Hillebrands *et al.*, Phys. Rev. Lett. **88**, 4 (2002).

[101] G. Gubbiotti, L. Albini, G. Carlotti*, et al.*, J. Appl. Phys. **87**, 5633 (2000)

[102] B. Hillebrands, C. Mathieu, C. Hartmann*, et al.*, J. Magn. Magn. Mater. **175**, 10 (1997).

[103] M. Grimsditch, Y. Jaccard, and I. K. Schuller, Phys. Rev. B **58**, 11539 (1998).

[104] L. Sun, R. X. Cao, B. F. Miao, *et al.*, Phys. Rev. Lett. **110**, 167201 (2013).

[105] F. S. Ma, Y. Zhou, H. B. Braun, and W. S. Lew, Nano Lett. **15**, 4029 (2015).

[106] A. Fert, N. Reyren, and V. Cros, Nat. Rev. Mater. **2,** 17031 (2017).

[107] Y. Fujishiro, N. Kanazawa, T. Nakajima, *et al.*, Nat. Commun. **10**, 1059 (2019).

[108] Y. Qi, T. Brintlinger, and J. Cumings, Phys. Rev. B **77**, 094418 (2008).

[109] W. R. Branford, S. Ladak, D. E. Read, K. Zeissler, and L. F. Cohen, Science **335,** 1597 (2012).

[110] A. P. Ramirez, A. Hayashi, R. J. Cava, R. Siddharthan, and B. S. Shastry, Nature **399**, 333 (1999).

[111] Y.-L. Wang, Z.-L. Xiao, A. Snezhko, *et al.*, Science **352**, 962 (2016).

[112] R. F. Wang, C. Nisoli, R. S. Freitas, *et al.*, Nature **439**, 303 (2006).

[113] C. Castelnovo, R. Moessner, and S. L. Sondhi, Nature **451,** 42 (2008).

[114] Z. Budrikis, P. Politi, and R. L. Stamps, New J. Phys. **14**, 045008 (2012).

[115] E. L. Albuquerque and M. G. Cottam, Phys. Rep. **376**, 225 (2003).

[116] M. Wu, B. A. Kalinikos, L. D. Carr, and C. E. Patton, Phys. Rev. Lett. **96,** 187202 (2006).

[117] D. Levine and P. J. Steinhardt, Phys. Rev. Lett. **53**, 26 (1984).

[118] R. W. Damon and J. R. Eshbach, J. Phys. Chem. Solids **19,** 308 (1961).

[119] A. N. Slavin, S. O. Demokritov, and B. Hillebrands, *Spin Dynamics in Confined Magnetic Structures I*, edited by B. Hillebrands, and K. Ounadjela (Springer Berlin Heidelberg, Berlin, Heidelberg, 2002), p. 35.

[120] M. Chen, M. A. Tsankov, J. M. Nash, and C. E. Patton, Phys. Rev. B **49,** 12773 (1994).

[121] R. Carter, C. Smith, and J. Owens, IEEE Trans. Magn. **16** 1159 (1980).

[122] V. L. Zhang, H. S. Lim, C. S. Lin, *et al.*, Appl. Phys. Lett. **99,** 143118 (2011).

[123] J. O. Vasseur, L. Dobrzynski, B. Djafari-Rouhani, and H. Puszkarski, Phys. Rev. B **54**, 1043 (1996).

[124] P. S. Keatley, P. Gangmei, M. Dvornik, *et al.*, Appl. Phys. Lett. **98,** 082506 (2011).

[125] V. E. Demidov, S. Urazhdin, and S. O. Demokritov, Appl. Phys. Lett. **95,** 262509 (2009).

[126] T. Schwarze and D. Grundler, Appl. Phys. Lett. **102,** 222412 (2013).

[127] B. Rana, D. Kumar, S. Barman, *et al.*, J. Appl. Phys. **111,** 07D503 (2012).

[128] M. Mruczkiewicz, M. Krawczyk, G. Gubbiotti, *et al.*, New J. Phys. **15,** 113023 (2013).

[129] H. H. Pan, V. L. Zhang, K. Di, *et al.*, Nanoscale Res. Lett. **8,** 115 (2013)

[130] M. Julliere, Phys. Lett. A **54,** 225 (1975).

[132] J. S. Moodera, L. R. Kinder, T. M. Wong, and R. Meservey, Phys. Rev.Lett. **74**, 3273 (1995).

[133] T. Miyazaki and N. Tezuka, J. Magn. Magn. Mater. **139,** L231 (1995).

[134] S. S. P. Parkin, C. Kaiser, A. Panchula, *et al.*, Nat. Mater. **3,** 862 (2004).

[135] S. Ikeda, J. Hayakawa, Y. Ashizawa, *et al.*, Appl. Phys. Lett. **93,** 082508 (2008).

[136] A. Moser and D. Weller, IEEE Trans. Magn. **35**, 2808 (1999).

[137] H. N. Bertram, H. Zhou, and R. Gustafson, IEEE Trans. Magn. **34**, 1845 (1998).

[138] S. H. Charap, L. Pu-Ling, and H. Yanjun, IEEE Trans. Magn. 33 (1997) 978.

[139] D. Weller and A. Moser, IEEE Trans. Magn. 35, 4423 (1999).

[140] S.-I. Iwasaki, J. Magn. Magn. Mater. **235,** 227 (2001).

[141] J. Moritz, S. Landis, J. C. Toussaint, *et al.*, IEEE Trans. Magn. **38**, 1731 (2002).

[142] Y. Hsu, V. Nikitin, D. Hsiao, *et al.*, IEEE Trans. Magn. **43**, 605 (2007).

[143] J. Sinha, M. Hayashi, A. J. Kellock, *et al.*, Appl. Phys. Lett. **102,** 242405 (2013).

[144] W. Peng, Y.-T. Hsia, K. Sendur, and T. McDaniel, Tribol. Int. **38**, 588 (2005).

[145] A. Fert and P. M. Levy, Phys. Rev. Lett. **44**, 1538 (1980).

[146] M. Bode, M. Heide, K. von Bergmann, *et al.*, *Nature*, **447**, 190 (2007).

[147] S. Heinze, K. von Bergmann, M. Menzel, *et al.*, Nat. Phys. **7**, 713 (2011).

[148] N. Romming, C. Hanneken, M. Menzel, *et al.*, Science **341**, 636 (2013).

[149] S. Woo, K. Litzius, B. Krüger, *et al.,* Nat. Mater. **15,** 501 (2016).

[150] S. Hussain, N. Sisodia, A. K. Chaurasiya, *et al.*, Sci. Rep. **9**, 1085 (2019).

[151] V.E. Dmitrienko, E.N. Ovchinnikova, S.P. Collins, *et al.*, Nat. Phys. **10**, 202 (2014).

[152] M. Bode, M. Heide, K. von Bergmann, *et al.,* Nature **447**, 190 (2007).

[153] K. Zakeri, Y. Zhang, J. Prokop, *et al.*, Phys. Rev. Lett. **104**, 137203 (2010).

[154] I. Gross, L.J. Martínez, J.P. Tetienne, *et al.*, Phys. Rev. B **94**, 064413 (2016).

[155] V. E. V. Dmitrienko, E. Ovchinnikova, S. Collins, *et al.,* Nat. Phys. **10**, 202 (2014).

[156] D. S. Han, N.-H. Kim, J. S. Y. Kim, *et al.,* Nano Lett. **16,** 4438 (2016).

[157] K. Di, V.L. Zhang, H.S. Lim, *et al.,* Phys. Rev. Lett. **114**, 047201 (2015).

[158] K. Di, V.L. Zhang, H.S. Lim, *et al.*, Appl. Phys. Lett. **106**, 052403 (2015).

[159] J. Cho, N.-H. Kim, S. Lee, *et al.*, Nat. Commun. **6**, 7635 (2015).

[160] A.K. Chaurasiya, C. Banerjee, S. Pan, *et al*, Sci. Rep. **6**, 32592 (2016).

[161] A.K. Chaurasiya, S. Choudhury, J. Sinha, and A. Barman, Phys. Rev. Appl. **9**, 014008 (2018).

[162] R. Soucaille, M. Belmeguenai, J. Torrejon, *et al.*, Phys. Rev. B **94**, 104431 (2016).

[163] S. Tacchi, R. E. Troncoso, M. Ahlberg, *et al.*, Phys. Rev. Lett. **118**, 147201 (2017).

[164] X. Ma, G. Yu, C. Tang, *et al.,* Phys. Rev. Lett. **120**, 157204 (2018).

[165] A.A. Stashkevich, M. Belmeguenai, Y. Roussigné, *et al.*, Phys. Rev. B **91**, 214409 (2015).

[166] J. Cho, N.-H. Kim, S. Lee, *et al.,* Nat. Commun. **6**, 7635 (2015).

[167] H.T. Nembach, J.M. Shaw, M. Weiler, E. Jué, and T.J. Silva, Nat. Phys. **11**, 825 (2015).

[168] J. Sinha, C. Banerjee, A. Chaurasiya, M. Hayashi and A. Barman, RSC Adv. **5**, 57815 (2015).

[169] N. Tombros, C. Jozsa, M. Popinciuc, *et al*., Nature **448,** 571 (2007).

[170] A. H. Castro Neto, F. Guinea, N. M. R. Peres, K. S. Novoselov, and A. K. Geim, Rev. Mod. Phys. **81**, 109 (2009).

[171] S. D. Sarma,S. Adam, E. H. Hwang, and E. Rossi, Rev. Mod. Phys. **83,** 407 (2011).

[172] O. V. Yazyev and L. Helm, Phys. Rev. B **75,** 125108 (2007).

[173] M. Johnson and R. H. Silsbee, Phys. Rev. Lett. **55,** 1790 (1985).

[174] W. Han, K. Pi, K. M. McCreary, *et al,* Phys. Rev. Lett. **105**, 167202 (2010).

[175] S. Konschuh, M. Gmitra, and J. Fabian, Phys. Rev. B **82**, 245412 (2010).

[176] J. Balakrishnan, G. K. W. Koon, M. Jaiswal, A. H. Castro Neto, and B. Özyilmaz, Nat. Phys. **9**, 284 (2013).

[177] D. Marchenko, A. Varykhalov, M. R. Scholz, *et al*., Nat. Commun. **3**, 1232 (2012).

[178] A. K. Patra, S. Singh, B. Barin, *et al*., Appl. Phys. Lett. **101**, 162407 (2012).

[179] C. L. Kane and E. J. Mele, Phys. Rev. Lett. **95,** 226801 (2005).

[180]W.-K. Tse, Z. Qiao, and Y. Yao, *et al*., Phys. Rev. B **83,** 155447 (2011).

[181] X. Wang and A. Manchon, Phys. Rev. Lett. **108**, 117201 (2012).

[182] M.-H. Liu, J. Bundesmann, and K. Richter, Phys. Rev. B **85,** 085406 (2012).

[183] E. McCann and V. I. Fal'ko, Phys. Rev. Lett. **108,** 166606 (2012).

[184] A. Scholz, A. López, and J. Schliemann, Phys. Rev. B **88,** 045118 (2013).

[185] F. Ajejas, A. Gud´ın, R. Guerrero, *et al*., Nano Lett. **18**, 5364 (2018).

[186] H. Yang, G. Chen, A. A. C. Cotta, *et al.*, Nat. Mater. **17**, 605 (2018).

[187] A. K. Chaurasiya, A. Kumar, R. Gupta, *et al*., Phys. Rev. B **99**, 035402 (2019).

[188] D. Xiao, G.-B. Liu, W. Feng, *et al*., Phys. Rev. Lett. **108**, 196802 (2012).

[189] D. MacNeill, G. M. Stiehl, M. H. D. Guimaraes, *et al*., Nat. Phys. **13**, 300 (2017).

[190] Q. Shao, G. Yu, Y.-W. Lan, *et al*., Nano lett. **16**, 7514 (2016).

[191] M. H. Guimaraes, G. M. Stiehl, D. MacNeill, *et al*., Nano Lett. **18**, 1311 (2018).

[192]. P. Gruünberg, R. Schreiber, Y. Pang, *et al*., Phys. Rev. Lett. **57**, 2442 (1986).

[193] C. F. Majkrzak, J. W. Cable, J. Kwo, *et al*., Phys. Rev. Lett. **56,** 2700 (1986).

[194]. M. B. Salamon, S. Sinha, J. J. Rhyne, *et al*. Phys. Rev. Lett. **56**, 259 (1986).

[195] Y.-C. Lau, D. Betto, K. Rode, J. M. D. Coey, and P. Stamenov, Nat. Nanotech. **11**, 758 (2016).

[196] C. Bi, H. Almasi, K. Price, *et al.,* Phys. Rev. B **95**, 104434 (2017).

[197] R. Verba, V. Tiberkevich, E. Bankowski, *et al*., Appl. Phys. Lett. **103**, 082407 (2013)

[198] J. A. Otálora, M. Yan, H. Schultheiss, R. Hertel, and A. Kákay, Phys. Rev. Lett. **117**, 227203 (2016).

[199] K. Di, S. X. Feng, S. N. Piramanayagam, *et al,* Sci. Rep. **5**, 10153 (2015).

[200] V. Sluka, T. Schneider, R. A. Gallardo, *et al*., Nat. Nanotech. **14**, 328 (2019).

[201] S. S. P. Parkin, X. Jiang, C. Kaiser, *et al.,* Proc. IEEE **91**, 661 (2003).

[202] *S. Bandiera*, R. C. Sousa, Y. Dahmane*, et al.,* IEEE Magn. Lett. **1**, 3000204 (2010).

[203]. N. Smith, S. Maat, M. J. Carey, and J. R. Childress, Phys. Rev. Lett. **101**, 247205 (2008).

[204] R. A. Gallardo, T. Schneider, A. K. Chaurasiya, *et al*., Phys. Rev. Appl. **12**, 034012 (2019).

[205] A. A. Serga, A. V. Chumak, B. Hillebrands, J. Phys. D: Appl. Phys. **43,** 264002 (2010).

[206] M. Rollinger, P. Thielen, E. Melander, *et al*., Nano Lett. **16,** 2432 (2016).

[207] E. T. Papaioannou, V. Kapaklis, P. Patoka, *et al,* Phys. Rev. B **81** 054424 (2010).

[208] B. Rana, D. Kumar, S. Barman, *et al*., ACS Nano **5,** 9559 (2011).

[209] H. Ulrichs, B. Lenk, and M. Münzenberg, Appl. Phys. Lett. **97,** 092506 (2010).

[210] N. I. Polushkin, S. A. Michalski, L. Yue, and R. D. Kirby, Phys. Rev. Lett. **97**, 256401 (2006).

[211] L. Bai, M. Kohda, and J. Nitta, Appl. Phys. Lett. **98,** 172508 (2011).

[212] K. Roy, S. Bandyopadhyay, and J. Atulasimha, Phys. Rev. B **83,** 224412 (2011).

[213] A. V. Chumak, T. Neumann, A. A. Serga, B. Hillebrands, and M. P. Kostylev, J. Phys. D: Appl. Phys. **42**, 205005 (2009).

[214] Q. Wang, A. V. Chumak, L. Jin, *et al*., Phys. Rev. B **95**, 134433 (2017).

[215] S. Jung, B. Watkins, L. DeLong, J. B. Ketterson, and V. Chandrasekhar, Phys. Rev. B **66**, 132401 (2002).

[216] S. Neusser, B. Botters, and D. Grundler, Phys. Rev. B **78**, 054406 (2008).

[217] S. Neusser, B. Botters, M. Becherer, D. Schmitt-Landsiedel, and D. Grundler, Appl. Phys. Lett. **93**, 122501 (2008).

[218] A. Fernández-Pacheco, D. Petit, R. Mansell, R. Lavrijsen, J. H. Lee, and R. P. Cowburn, Phys. Rev. B **86**, 104422 (2012).

[219] D. A. Gilbert, B. B. Maranville, A. L. Balk, *et al.*, Nat. Commun. **6**, 8462 (2015).

[220] S. Heinze, K. von Bergmann, M. Menzel, *et al.*, Nat. Phys. **7**, 713 (2011).

[221] S. Choudhury, S. Barman, Y. Otani, and A. Barman, ACS Nano **11**, 8814 (2017).

[222] A. De, S. Mondal, C. Banerjee, *et al.*, J. Phys. D: Appl. Phys. **50**, 385002 (2017).

[223]. B. K. Mahato, B. Rana, D. Kumar, *et al.*, Appl. Phys. Lett. **105**, 012406 (2014).

[224] K. Adhikari, S. Barman, R. Mandal, Y. Otani, and A. Barman, Phys. Rev. Appl. **10**, 044010 (2018).

[225]. B. Rana, S. Pal, S. Barman, *et al.*, Appl. Phys. Exp. **4**, 113003 (2011).

[226] S. Mondal, S. Choudhury, S. Barman, Y. Otani, and A. Barman, RSC Adv. **6**, 110393 (2016).

[227] S. Mondal, S. Barman, S. Choudhury, Y. Otani, and A. Barman, J. Magn. Magn. Mater. **458**, 95 (2018).

[228] S. Tacchi, M. Madami, G. Gubbiotti, *et al.*, Phys. Rev. B **82**, 024401 (2010).

[229] S. Sahoo, S. Mondal, G. Williams, *et al.*, Nanoscale **10**, 9981 (2018).

[230] A. Fernández-Pacheco, R. Streubel, O. Fruchart, *et al.*, Nat. Commun. **8**, 15756 (2017).

[231] L. J. Heyderman and R. L. Stamps, J. Phys.: Condens. Matter **25,** 363201 (2013).

[232] E. Mengotti, L. J. Heyderman, A. F. Rodríguez, *et al.*, Nat. Phys. **7**, 68 (2011).

[233] C. Nisoli, R. Wang, J. Li, *et al.*, Phys. Rev. Lett. **98**, 217203 (2007).

[234] L. D. Jaubert and P. C. Holdsworth, Nat. Phys. **5**, 258 (2009).

[235] S. Gliga, A. Kákay, R. Hertel, and O. G. Heinonen, Phys. Rev. Lett. **110**, 117205 (2013).

[236] W. R. Branford, S. Ladak, D. E. Read, K. Zeissler, and L. F. Cohen, Science **335**, 1597 (2012).

[237] S. Ladak, D. Read, T. Tyliszczak, W. R. Branford, and L. F. Cohen, New J. Phys. **13**, 023023 (2011).

[238] V. S. Bhat, F. Heimbach, I. Stasinopoulos, and D. Grundler, Phys. Rev. B **93**, 140401© (2016).

[239] M. B. Jungfleisch, W. Zhang, E. Iacocca, *et al.*, Phys. Rev. B **93**, 100401© (2016).

[240] J. C. Gartside, D. M. Arroo, D. M. Burn, *et al.*, Nat. Nanotechnol. **13,** 53 (2018).

[241] Y Li, G. Gubbiotti, F Casoli, *et al.*, J. Phys. D: Appl. Phys. **50,** 015003 (2017).

[242] T. Sebastian, K. Schultheiss, B. Obry, B. Hillebrands, and H. Schultheiss, Frontiers in Phys. **3**, 35 (2015).

[243] T. Schneider, A. A. Serga, B. Leven, and B. Hillebrands, Appl. Phys. Lett. **92**, 022505 (2008).

[244] W. Yu, J. Lan, and J. Xiao, Phys. Rev. Appl. **13**, 024055 (2020).

[245] K. Vogt, F. Fradin, J. Pearson, *et al.,* Nature Commun. **5**, 3727 (2014).

[246] V. E. Demidov, S. O. Demokritov, K. Rott, *et al.,* Phys. Rev. B **77**, 064406 (2008).

[247] V. E. Demidov, S. Urazhdin, and S. O. Demokritov, Nat. Mater. **9**, 984 (2010).

[248] M. Zahedinejad, A. A. Awad, S. Muralidhar, *et al.,* Nat. Nanotechnol. **15,** 47 (2020).

[249] A. Haldar, D. Kumar, and A. Adeyeye, Nat. Nanotech **11,** 437 (2016).

[250] H. Schultheiss, S. Schäfer, P. Candeloro, *et al*., Phys. Rev. Lett. **100**, 047204 (2008).

Chapter 2

2. Theoretical Aspects

2.1. Introduction

The molecular and electronic structure of a material are the major deciding factors for exhibiting magnetic properties. The interaction between spin and orbital angular momenta determines the magnetic behaviour both in microscopic and macroscopic level. On the basis of their interactions, the materials can be broadly categorized into diamagnet [1], paramagnet [2], ferromagnet [3-6], antiferromagnet [7] and ferrimagnet [8]. Ferromagnetic (FM) materials possess spontaneous magnetization [9]. The transition metals (e.g. iron, cobalt and nickel) are characterized by partially filled internal electron shell corresponding to the $3d$ levels. Owing to the high density of states (DOS) and narrow 3d band, ferromagnetic materials possess magnetic ordering as a result of exchange interaction. According to the Weiss theory [10,11], first introduced in 1907, the exchange interaction has to compete with the dipolar interaction caused by the free magnetic poles on the surface (i.e. demagnetizing field), which results in the FM material to break up into small domains for the minimization of the free energy. This chapter addresses magnetic interactions, starting with a brief introduction to the origin of ferromagnetism through a discussion of the exchange interaction arising between electron spins. A particular emphasis will be given to the FM and antiferromagnetic (AFM) systems. Following that, the spin-orbit interaction will be introduced and the antisymmetric exchange, namely Dzyaloshinskii-Moriya interaction will be discussed which forms a major part of this thesis. Further, an overview of different aspects of spin waves will be presented.

The individual moments of an FM material collectively contribute to a volume magnetization M, which is maximum when the moments are fully aligned under a large enough external magnetic field. In presence of the magnetic field, the coupled moments precess about the field direction, which is called the ferromagnetic resonance in case of uniform precession (the moments have same frequency and phase) [12]. When the precession is not uniform, each individual dipole precesses slightly out of phase with its nearest neighbour. This produces a propagating wave, known as SW [13] with its energy and momentum related by characteristic dispersion relations. The parameter that

describes the rate of energy loss of precessing magnetization, is called magnetic damping, which can be intrinsic (e.g. due to SOC) or extrinsic (e.g. due to two-magnon scattering) depending upon its origin. Another exotic property observed in FM materials is the magnetic anisotropy, i.e. the dependence of magnetic energy on the direction of the spins w.r.t. the crystal lattice, or, in patterned structures, w.r.t. the geometrical axes.

2.2. Magnetic Energies

The static and dynamic behaviours of magnetic materials are strongly dependent on the relative contribution of different energy terms, e.g. Zeeman energy, magnetostatic self-energy (demagnetizing energy), exchange energy, and magnetic anisotropy energy [14]. Different energy contributions in a magnetic system can be given as follows:

2.2.1. Zeeman Energy

The interaction between the magnetization ($\boldsymbol{M}$) and the externally applied magnetic field ($\boldsymbol{H}$) can be given as [15]:

$$E_{\text{Zeeman}} = -\mu_0 \int_0^V \boldsymbol{M}.\boldsymbol{H} \, dV \tag{2.1}$$

where V is the total volume of the magnetic specimen, dV is the volume element and μ_0 refers to the vacuum permeability. In order to keep the energy to minimum, $\boldsymbol{M}$ tends to align in the direction of $\boldsymbol{H}$.

2.2.2. Exchange Energy

Exchange energy is quantum-mechanical in nature which gives rise to the short-range magnetic ordering in magnetic materials through exchange interaction [16,17]. This interaction has a strong influence not only in ferromagnets but also in ferrimagnets and antiferromagnets, where the exchange interaction between the neighbouring magnetic ions tend to force the moments for parallel or antiparallel alignment to each other. Its origin can be explained from the coulombic interaction energy and Pauli exclusion principle. The Heisenberg exchange Hamiltonian can be phenomenologically written as:

$$\widehat{H}_{Ex} = -\sum_{i \neq j} J_{ij} \, \boldsymbol{S}_i \cdot \boldsymbol{S}_j \tag{2.2}$$

where, $\boldsymbol{S}_i$ and $\boldsymbol{S}_j$ are the spin operators of the ith and jth atoms, respectively, and J_{ij} is the exchange integral between them [29]. Here, depending upon the polarity (sign) of J_{ij} the material can be classified as ferromagnet or antiferromagnet. In the continuum model, the above equation can be written as:

$$E_{ex} = A \int_0^V (\nabla \boldsymbol{m})^2 \, dV \tag{2.3}$$

where the magnetic moment (m) is a continuously varying vector quantity and A is called the exchange stiffness constant given by:

$$A = \frac{2JS^2}{a} \qquad (2.4)$$

Here a is the lattice constant and J is considered to be isotropic in the FM medium. The aforementioned exchange interaction is known as direct exchange interaction where the electrons of magnetic atoms interact with its nearest neighbours. However, such exchange interaction can also take place in indirect ways [30,31], which couples magnetic moments over relatively larger distances. Some indirect exchange interactions are listed below.

2.2.2.1. RKKY Exchange

This is a type of indirect exchange which couples magnetic moments over large distances. It acts through itinerary electrons in metals and was first proposed by Ruderman and Kittel [18,19] and later extended by Kasuya and Yosida to make the theory known as RKKY interaction [20]. Mostly in rare earth materials, whose magnetic electrons in 4f shells are shielded by 5s and 5p electrons, direct exchange is rather weak and the magnetic order arises mainly due to the indirect exchange via the conduction electrons.

2.2.2.2. Superexchange

Direct exchange, arises due to the localized d-orbitals of transition metals, can't explain the antiferromagnetism of most transition metal compounds. Because of the localization of d-orbitals, hopping can only occur between orbitals of different atoms that are very close to each other. But most of the antiferromagnetic insulators are transition metal oxides so that the transition metal cations are separated by large oxygen anions. In these cases, the concept of direct exchange can be extended by taking into account the hopping via intermediate p-orbital of oxygen. This mechanism is called superexchange [21].

2.2.2.3. Antisymmetric Exchange

It is a kind of three site indirect exchange interaction originated mostly due to the interplay of SOC and superexchange interaction leading towards the canting of spins by a small angle.

2.2.2.3.1. Dzyaloshinskii Moriya Interaction

Dzyaloshinskii Moriya Interaction (DMI) is an antisymmetric exchange interaction which favours the canted neighbouring spins. DMI can arise from inversion symmetry breaking

at the surfaces or interfaces between a ferromagnetic layer and nonmagnetic one having strong SOC due to three-site indirect exchange mechanism [22-23]. Recently, DMI has attracted much interest due to their fundamental role in various novel phenomena like magnon Hall effect, molecular magnetism and multiferroicity. DMI is responsible for stabilizing chiral spin textures such as magnetic skyrmions which show tremendous application potential in spintronics and high speed, ultra-high-density storage technology due to their unique properties like SW propagation under ultra-low current densities and rewritability under spin polarized currents. The Hamiltonian for DMI can be written as $H_{DM} = -D_{ij} \cdot (S_i \times S_j)$. The schematic of occurrence of interfacial DMI is presented in Fig. 2.1.
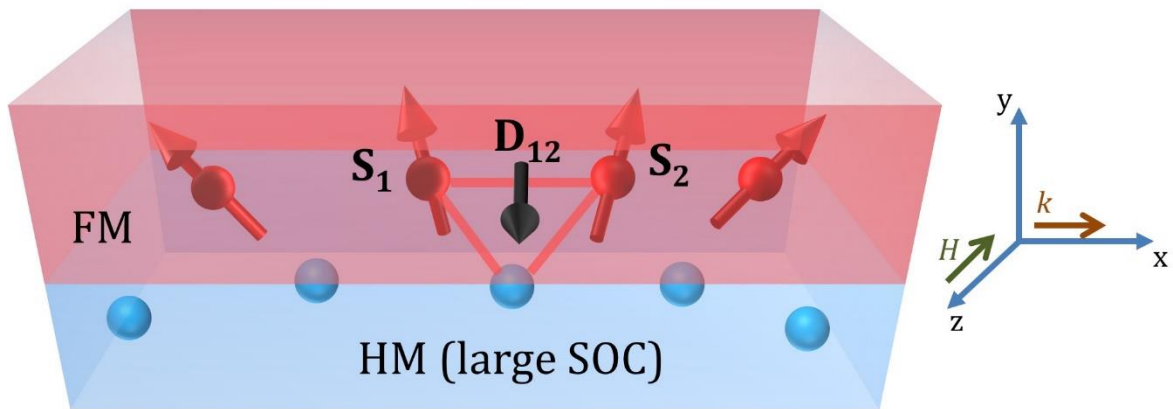
Figure 2.1: Schematic of Dzyaloshinskii-Moriya interaction at HM/FM interface.

Phenomenologically, the DMI energy density is given by [24-26]

$$E_{DM} = \frac{D}{M_S^2}\left(M_y \frac{\partial M_x}{\partial x} - M_x \frac{\partial M_y}{\partial x} + M_y \frac{\partial M_z}{\partial y} - M_z \frac{\partial M_y}{\partial z}\right) \tag{2.5}$$

Where D is the DMI constant and M_i the ith component of the magnetization. The magnetization of linear SW can be expressed as $M(x,t) = M_S m(x,t)$. The unit vector along the magnetization direction can be expressed as

$$m(x,t) = m_x \hat{e}_x + m_y \hat{e}_y - m_z \hat{e}_z \tag{2.6}$$

$$m(x,t) = m_{x0}e^{i(\omega t - kx)}\hat{e}_x + m_{y0}e^{i(\omega t - ky)}\hat{e}_y - \hat{e}_z \tag{2.7}$$

Where m_{x0}, m_{y0} are much less than 1, $\hat{e}_x$, $\hat{e}_y$ and $\hat{e}_z$ are the unit vectors co-directional with the coordinate axis. For SW travelling in the x direction, the expression of the field due to DMI is given by [27]:

$$H_{DM} = -\frac{1}{\mu_0}\frac{\delta E_{DM}}{\delta M} = \frac{2D}{\mu_0 M_S}\left(\frac{\partial m_y}{\partial x}\hat{e}_x - \frac{\partial m_x}{\partial x}\hat{e}_y\right) \qquad (2.8)$$

The total effective field is given by:

$$H_{eff} = -H\hat{e}_z + J\nabla^2 M + H_{dip} + H_{ani} + H_{DM} \qquad (2.9)$$

where $J = 2A/(\mu_0 M_s)$, and the dipolar field in the film is given as $H_{dip} = -M_s\xi(kL)m_x\hat{e}_x - M_s[1 - \xi(kL)]m_y\hat{e}_y$, where L is the magnetic film thickness, $\xi(x) = 1 - \left(1 - e^{-|x|}/|x|\right)$, the perpendicular magnetic anisotropy field $H_{ani} = \frac{2K}{\mu_0 M_s}m_y\hat{e}_y$ and K is the anisotropy constant. Inserting equation in the famous LLG equation:

$$\frac{dm}{dt} = -\mu_0\gamma m \times H_{eff} + \alpha m \times \frac{dm}{dt} \qquad (2.10)$$

we end up with the following SW dispersion relation:

$$\omega = \omega_0 + \omega_{DM} = \mu_0\gamma\sqrt{([H + Jk^2 + \xi(kL)M_S][H - H_U + Jk^2 + M_S - \xi(kL)M_S])} - \frac{2\gamma}{M_S}Dk$$

$$(2.11)$$

The DMI induced frequency difference of counter propagating SW is given by:

$$\Delta f = [\omega(-k) - \omega(k)]/2\pi = \frac{2\gamma}{\pi M_S}Dk \qquad (2.12)$$

It is obvious from the above equation that frequency difference is linear in SW vector and DMI constant but independent of the applied in-plane (IP) magnetic field.

In order to get a quantitative expression of the magnon line width, the linearized LLG equation may be solved after including the Gilbert damping term and neglecting the high order terms like o(α^2). The imaginary part of the angular frequency is given by:

$$Im[\omega] = \alpha\gamma\mu_0(H + Jk^2 - H_U/2 + M_S/2)\left[1 + \frac{\omega_{DM}(k)}{\omega_0(k)}\right] \qquad (2.13)$$

with the real part Re[ω] given by equation (2.11) –

The Brillouin intensity is given by:

$$I(\omega') \propto |m(\omega',k)|^2 \propto \frac{1}{\left(\omega' - Re[\omega]\right)^2 + Im[\omega]^2} \qquad (2.14)$$

where $m(\omega', k)$ is the Fourier transform of $m(x, t)$ and the linewidth of the SW peak is given by $2Im[\omega]$. Equation (2.13) reveals that in the presence of DMI, magnon linewidth is modified by the term ω_{DM}/ω_0, which is antisymmetric in the wave vector.

2.2.3. Magnetic Dipolar Interaction

The interaction between two magnetic dipoles and the associated energy can be defined as follows [28]:

$$E_d = \frac{\mu_0}{4\Pi r^3}\left[\boldsymbol{m_1} \cdot \boldsymbol{m_2} - \frac{3}{r^2}(\boldsymbol{m_1} \cdot \boldsymbol{r})(\boldsymbol{m_2} \cdot \boldsymbol{r})\right] \tag{2.15}$$

where, μ_0 is the permeability in free space, $\boldsymbol{m_1}$ and $\boldsymbol{m_2}$ are the moments of the two magnetic dipoles and $\boldsymbol{r}$ is the vector connecting the two dipoles which experience the magnetic field generated by each other. The above equation (2.15) explains that the energy reduces with the third order of their separation, r. In case of ferromagnets, although this interaction does not contribute to magnetic ordering, it plays a pivotal role in a number of phenomena such as domain formation, demagnetizing field distributions, confined SW modes and anisotropy of SW dispersion in the long wavelength regime.

2.3. Magnetic Anisotropy

Magnetic anisotropy is the direction dependence of the magnetic properties of materials [29-30]. The tailoring and tunability of magnetic anisotropy have been possible due to the presence of symmetry breaking interfaces, surfaces, selectivity of materials and choosing appropriate thickness of the individual layers. There are mainly two primary sources of magnetic anisotropy, namely SOC and long-range dipolar interaction. In the case of dipolar interaction, the shape of the specimen plays a crucial role whereas the coupling of spin with orbital angular momenta lead to the SOC related effect. Some of the prominent magnetic anisotropies are described below:

2.3.1. Magneto-crystalline anisotropy

The origin of the magneto-crystalline anisotropy is an intrinsic property of the FM materials caused by SOC. The crystallographic structure is greatly affected by the spatial atomic arrangement [31]. Consequently, the interaction of spins with crystallographic structure leads to the preferential alignment along the crystallographic axes. Further, the foldedness of the magnetic anisotropy is determined by the detailed symmetry of the lattice. For example, in cubic systems, the energy density is given by:

$$E_{ani} = K_0 + K_1(\alpha_x^2\alpha_y^2 + \alpha_y^2\alpha_z^2 + \alpha_z^2\alpha_x^2) + K_2\alpha_x^2\alpha_y^2\alpha_z^2 \tag{2.16}$$

where α_i's are the direction cosines of the normalized magnetization $\boldsymbol{m}$ with respect to the cartesian axes of the lattice. K_i's are the magneto-crystalline anisotropy constants, K_0, K_1, and K_2 are the crystalline anisotropy constants of zero, first and second order, respectively. On the other hand, for crystals having uniaxial anisotropy, the energy density is given by

$$E_{ani} = K_U\alpha_x^2 \tag{2.17}$$

Where K_U is the uniaxial anisotropy constant.

2.3.2. Shape anisotropy and Demagnetizing Energy

Anisotropic shape of the magnetic specimen gives rise to the shape anisotropy which originates due to the anisotropic dipolar interaction of free magnetic poles (stray and demagnetizing fields) coming into the picture when the geometry of micrometer and submicrometer sized magnetic elements is not symmetric [32].

The energy corresponding to the stray field is given by:

$$E_{demag} = -\frac{1}{2}\int_0^V \mu_0\, \boldsymbol{M}.\boldsymbol{H}_{demag}dV \tag{2.18}$$

For an arbitrarily shaped element, $\boldsymbol{H}_{demag}$ is strongly dependent on the shape and geometry of the element and forms a complex function of position. Finally, the preferred orientation of magnetization lies along which E_{demag} becomes minimum.

2.3.3. Volume, Surface and Interface Anisotropy

The broken symmetry at surfaces and interfaces of magnetic thin films and multilayers often induces some anisotropy in the system. This results in the effective anisotropy (K_{eff}) constant to be divided into two parts as given below:

$$K_{eff} = K_V + \frac{2K_S}{t} \tag{2.19}$$

Here, K_V denotes the volume dependent magneto-crystalline anisotropy constant while K_S is the contribution from the surface anisotropy. The latter generally possesses an inverse dependence on the thickness (t) of the system and prefers an out of plane magnetization of the sample. The competition between volume and surface anisotropy gives rise to a dependence of the magnetization on the film thickness.

2.3.4. Strain Induced Anisotropy

Because of the change in the magnetoelastic energy, a magnetic system subjected to strain can acquire some anisotropy. A number of factors are responsible for inducing strain in the thin films, e.g. intrinsic strain brought about by the nature of the deposition

process, strain because of non-matching lattice parameters of adjacent layers and thermal strain associated with differences in thermal expansion coefficients. It is also evident that under strain the symmetry of the material will be lowered. Consequently, new energy terms in the total anisotropy energy can be included which is forbidden in the unstrained state. On the other hand, as the magneto-elastic energy [33] is linear with respect to strain so the system tries to minimize its energy by acquiring an anisotropic non-zero strain, and this phenomenon is known as magnetostriction. The modulation of magneto-crystalline anisotropy is also possible by strain in FM which may alter the direction of the magnetization. This effect can be interpreted as the inverse of magnetostriction which can be defined as the change in the sample dimensions when the direction of the magnetization (M) is altered [34].

For an elastically isotropic medium with isotropic magnetostriction, the energy per unit volume associated with this effect can be expressed as:

$$E_{ME} = -K_{ME}cos^2\theta \tag{2.20}$$

$$K_{ME} = -\frac{3}{2}\lambda\sigma = -\frac{3}{2}\lambda M_E\varepsilon \tag{2.21}$$

Here, σ is the stress tensor which is related to the strain tensor (ε) via the elastic modulus ME by:

$$\sigma = \varepsilon M_E \tag{2.22}$$

The magnetostriction constant λ can be positive or negative depending upon the orientation. The angle θ denotes the direction of the magnetization (M) relative to the direction of uniform stress. As the strain being present throughout the sample, this strain induced anisotropy contribution can be interpreted as a volume contribution to the total magnetic anisotropy.

2.3.5. Perpendicular Magnetic Anisotropy

The preferred magnetization orientation in ultrathin magnetic films and multilayer can deviate substantially in contrast to their bulk counterpart. The change of the magnetization (M) direction from in-plane (IP) to out-of-plane (OOP) orientation (perpendicular to sample plane) occurs due to the perpendicular magnetic anisotropy (PMA) [35]. The PMA in magnetic material is very crucial in order to enhance the thermal stability in nanomagnets at room temperature which makes it desirable for information storage. Microscopically, PMA is observed if the electronic orbitals in an FM material are

deformed in the direction perpendicular to the film interface. When M of the specimen is maintained along the OOP direction, the effective magnetic field (H_{eff}) of the system is substantially increased due to SOI (orbital deformation occurs in OOP direction). However, there is no effect of SOI when M lies IP (as the orbital is not deformed along the IP direction). Consequently, there is a stark difference in the absolute value of the magnetic energy (i.e. $|$-$(M \cdot H_{eff})|$) between the IP and OOP orientation of M, and as a result, the direction of the easy axis of magnetization lies perpendicular to the sample plane. However, the origin of PMA has become a debated issue where few possible interpretations are: i) reduced coordination symmetry, ii) altered electronic structure, iii) localized epitaxial strain at the interface, iv) electronic band structure interactions etc. Generally, strong PMA is observed at the interfaces between $3d$ transition metal FMs (e.g. Co) and nonmagnetic (NM) heavy metal (HM) (e.g. W, Au, Pt, Pd) [36]. Since the spins of electrons from localized d or f orbitals primarily contribute to the magnetization of an FM material, the PMA is mainly determined by the deformation and symmetry of these orbitals via interfacial hybridization. On the other hand, PMA can also be observed at the interfaces between $3d$ transition FMs (e.g. Co, Fe and their alloys like CoFeB) and MO$_x$ (M = Mg, Al, Ta, Ru). However, the heterostructures made from CoFeB and MgO have drawn particular attention among the aforementioned materials due to lower damping constant of CoFeB and high tunnelling magnetoresistance (TMR) ratio at room temperature. At CoFeB/MgO interface, the OOP $3d_{z^2}$ orbitals of Fe strongly bond with OOP $2p_z$ orbitals of O which results in a significant charge transfer from $3d_{z^2}$ to $2p_z$ orbitals. Thus, the number of electrons in OOP orbitals is decreased as compared to that in IP orbitals which introduces a moderate PMA via SOC [37].

2.3.6. Exchange Anisotropy

Exchange bias or exchange anisotropy [38,39] is found at the interface of FM/antiferromagnet (AFM) heterostructure when it is cooled in the presence of a static magnetic field through the Néel temperature (T_N) of the AFM (the Curie temperature (T_C) of the FM should be larger than T_N). This is a unidirectional anisotropy, e.g. the hysteresis loop of the such system, when it is field cooled (i.e. in the presence of the magnetic field, H) at temperature $T < T_N$, has an increased coercivity and the loop shifts along the applied field axis (this is generally termed as the exchange bias). Both these effects disappear at $T \approx T_N$ which confirms that the presence of the antiferromagnet is crucial to achieve the exchange anisotropy. The exchange bias properties disappear if the FM/AFM interface is

cooled at zero field from demagnetized state although, the properties are retained if it is cooled at zero field from a remanent state. Magnetic anisotropy can be measured from either static or dynamic response of the magnetic system. The static response can be investigated by torque magnetometry, torsion oscillating magnetometry (TOM), the magneto-optical Kerr effect (MOKE: static MOKE) [40] and other methods which can measure the magnetic moment e.g. vibrating sample magnetometry (VSM), fluxgate magnetometry, superconducting quantum interference device (SQUID) magnetometry, pendulum magnetometry, alternating gradient magnetometry (AGM), Faraday balance etc. However, the magnetic anisotropy is most frequently measured from magnetization measurements (by SQUID or VSM) along the two orthogonal directions of the magnetic field relative to the sample. On the other hand, the dynamic response of the magnetic systems can be investigated by Brillouin light scattering (BLS), ferromagnetic resonance (FMR) and MOKE (e.g. time-resolved MOKE: TRMOKE) [41] etc.

2.4. Voltage (or Electric Field) Controlled Magnetic Anisotropy (VCMA or ECMA)

The voltage (i.e. electric field) controlled magnetic anisotropy (VCMA) is generally observed at the interface between ultrathin $3d$ transition FM materials (e.g. Co, Fe and their alloys such as CoFeB) and nonmagnetic insulators (e.g. MgO, Al_2O_3) [42]. The VCMA is believed to be observed because of the relative changes of electronic occupation state in $3d$ orbitals of FM under the application of electric field [43,44]. VCMA is primarily studied at the interfaces between FM and oxide heterostructures. When an electric field is applied at FM/oxide interface, the number of electrons in OOP d orbitals of FM is changed with respect to IP orbitals as explained from the first principles calculations [45]. This affects the bonding strength between d and p orbitals leading to a substantial change of interfacial PMA (iPMA). Although electric field control of electronic occupation state is believed to be the main mechanism behind VCMA, several alternative theories are also found in the literature. One of the alternative approaches claims that the inhomogeneous electric field at the FM metal/oxide interface couples to the quadrupole of electronic orbital in FM. This electric quadrupole again couples to the magnetic dipoles and controls the iPMA. Also, iPMA can be generated due to the presence of Rashba SOC at FM/oxide interface while, the applied electric field at the interface modifies Rashba SOC which further modulates iPMA [46]. First principles calculation reveals that the change in the number of electrons in d orbitals of FM material is linearly proportional to the applied

electric field at the FM/oxide interface [47]. Thus, the modulation in the magnetic moment and iPMA should also be linearly proportional to the electric field, i.e.

$$\Delta K_s = \beta E \tag{2.23}$$

Here, ΔK_s denotes the change in iPMA while, β is known as magneto-electric or VCMA coefficient.

2.5. Magnetization Dynamics

Under the application of applied bias magnetic field and a time varying field or other sources of excitation, the magnetic moments of a magnetic material experience a torque which induces a precessional motion of the magnetization. Due to the presence of various sources of damping, the moments try to align themselves along the effective field. Consequently, they carry out a damped spiral motion about the effective field direction. The phenomenological interpretation of the dynamic behaviour of the magnetization is well described by the Landau-Lifshitz-Gilbert (LLG) equation of motion. The LLG equation is a torque equation which was first introduced by Lev Landau and Evgeny Lifshitz in 1935 as Landau-Lifshitz (LL) equation [48]. Later, Gilbert modified it by inserting a Gilbert damping term [49]. The formulation is given as follows:
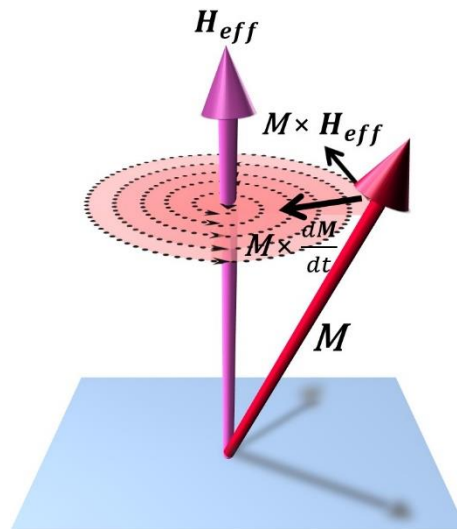
Figure 2.2: The schematic representation of magnetization precession around the effective magnetic field direction.

When a magnetic moment is placed under the application of effective magnetic field $\boldsymbol{H}_{eff}$, the experienced torque can be written as:

$$\boldsymbol{\tau} = \boldsymbol{\mu}_m \times \boldsymbol{H}_{eff} \qquad (2.24)$$

In a semiclassical approach, the magnetic moment ($\boldsymbol{\mu_m}$) can be related to the angular momentum $\boldsymbol{L}$ of electrons as follows:

$$\boldsymbol{\mu_m} = -\gamma \boldsymbol{L} \qquad (2.25)$$

where, $$\gamma = \frac{g\mu_B}{\hbar}$$

is the gyromagnetic ratio, g is the Lande' g-factor ($g \approx 2$), μ_B ($=\frac{e\hbar}{2m_e}$, e and m_e being the charge and mass of the electron) is the Bohr magneton and $\hbar$ ($=\frac{h}{2\pi}$, h being the Planck's constant) is the reduced Planck's constant. By applying the momentum theorem, the equation (2.24) can be represented as the rate of change of angular momentum $\boldsymbol{L}$:

$$\frac{d\boldsymbol{L}}{dt} = \boldsymbol{\mu}_m \times \boldsymbol{H}_{eff} \qquad (2.27)$$

This can be simplified as:

$$\frac{d\boldsymbol{\mu}}{dt} = -\gamma \boldsymbol{\mu} \times \boldsymbol{H}_{eff} \qquad (2.28)$$

Here the effective magnetic field, $H_{eff,}$ is a sum of all external and internal magnetic fields which can be expressed as:

$$\boldsymbol{H}_{eff} = \boldsymbol{H}_{ext} + \boldsymbol{H}_{ex} + \boldsymbol{H}_{demag} + \boldsymbol{H}_{ani} + \boldsymbol{h}(t) \qquad (2.29)$$

Here, $\boldsymbol{H}_{ext}$ is the applied bias magnetic field, $\boldsymbol{H}_{ex}$ is the exchange field and $\boldsymbol{H}_{demag}$ represents the demagnetization field created by the dipolar interaction of magnetic surface and volume charges. The field, $\boldsymbol{H}_{ani}$ includes all kinds of anisotropic fields described above while, $\boldsymbol{h}(t)$ is the time varying field.

Replacing atomic moment by macroscopic magnetization $\boldsymbol{M}$ after taking continuum limit into consideration, the equation of motion (LL) reads:

$$\frac{d\boldsymbol{M}}{dt} = -\gamma \boldsymbol{M} \times \boldsymbol{H}_{eff} \qquad (2.30)$$

The above equation features a continuum precession resulting into a non-dissipative system. To avoid this impractical situation, Landau and Lifshitz proposed the damping term to be $(-\lambda \boldsymbol{m} \times (\boldsymbol{m} \times \boldsymbol{H}_{eff}))$

Later, Gilbert introduced another damping term [177,182] into the LL equation resulting in the modified Landau-Lifshitz-Gilbert (LLG) equation as:

$$\frac{d\boldsymbol{M}}{dt} = -\gamma(\boldsymbol{M} \times \boldsymbol{H}_{eff}) + \frac{\alpha}{M_S}\left(\boldsymbol{M} \times \frac{d\boldsymbol{M}}{dt}\right) \qquad (2.31)$$

Here α is the dimensionless Gilbert damping parameter, while Ms is the saturation magnetization of the magnetic material.

Figure 2.2 schematically represents the interplay between different torques acting on the magnetization vector ($\boldsymbol{M}$). The precessional torque (the first term on the right-hand side of Equation 2.31) acts tangentially to the circle traced by the tip of the magnetization vector, while the damping torque (second term) acts radially to align the magnetization along the effective magnetic field. The effective damping can arise due to the intrinsic and extrinsic factors. The intrinsic mechanism [50] of damping primarily originates from the SOI by which the spin is coupled to the lattice making the damping parameter (α) a material parameter [51] or due to the interfacial effects such as interfacial *d-d* hybridization, spin pumping etc. occurring across the interface in case of FM/NM heterostructures [52,53]. However, apart from SOI, different external stimuli, such as magnon-electron scattering, eddy currents, spin pumping, multimagnon scattering etc. can also contribute to the relaxation of magnetization precession amplitude.

2.5.1. Magnetic Damping

The control and tunability of damping in a magnetic system offers one to speed up the relaxation process and accelerate the approach of magnetization to equilibrium in reversal processes making its importance in magnetic recording technology. Memory pixels in MRAM must have a high damping. The fastest magnetization reversal is achieved by tuning the critical damping where the required time is about one period of precession whereas low damping materials are desirable candidates for SW propagation-based devices and to reduce write current in MRAM devices.

There are two types of magnetic damping: intrinsic damping and extrinsic damping [54]. Intrinsic damping in a magnetic material with perfect crystal structure mainly originates from the itinerant electrons and SOC. The well-known models for the description of intrinsic damping in magnetic system includes: s-d exchange interaction model, breathing Fermi surface model etc. Extrinsic damping of the system can be caused due to the introduction of multiple energy dissipation channels during the spin precession. Phonon drag [55], eddy current [56], doping or capping [57] with another material, injection of spin current [58], magnon-magnon scattering [59] and controlling the temperature of the system [60] are few processes which can externally modulate the damping. Inversion symmetry breaking at the interface can lead to modification of Gilbert damping [61]. Presence of magnetic inhomogeneity can cause generation of large number

of local resonance fields which, in turn, gives rise to other nonuniform modes causing decoherence of the uniform one. Spin current generated spin torque can modulate the damping in heterostructures with HM/FM interface. Spin pumping is another mechanism where angular momentum transferred from the FM to HM (the strength is characterized by spin mixing conductance and spin transparency) causes enhancement of damping. Moreover, in FMR measurements, global excitation takes into account the effect of superposition of local resonance in case of long wavelength (small k) variation in magnetic properties. This arises mainly due to defects in large area averaging. Magnetostatic contribution plays an important role in affecting the magnon-energy dispersion.

2.6. Spin Waves

The idea of spin wave (SW) was first introduced in 1930 by Bloch [13] in order to describe the reduction of spontaneous magnetization in ferromagnetic medium. At absolute zero temperature, all the atomic magnetic moments of a ferromagnet tend to align in the same direction (as shown in Fig. 2.3(a)), which is the ground state of the system. As the temperature rises, the thermal agitation perturbs the spontaneous magnetization causing a deviation of the spins from the aligned direction. This phase of the disturbance propagates through the system in the form of a wave as depicted in Fig. 2.3(b) and 2.3(c). In the case of uniform precession under the influence of a magnetic field, the magnetic spins precess in phase about the magnetic field direction. After solving the LLG equation (Eq. 2.31) under small angle approximation the frequency of uniform precession, which is also known as the FMR frequency, can be achieved by setting $d\mathbf{M}/dt$ equal to zero. The solution for a thin film as calculated by Kittel is given as:

$$\omega^2 = \gamma[H + (Ny - N_x)4\pi M_s][H + (N_z - N_x)4\pi M_s] \tag{2.32}$$

Here N_x, N_y and N_z are the demagnetizing factors in the x, y and z directions respectively, and the magnetic field is applied along the z axis.

In the case of non-uniform precession, it is the propagation of the phase shift across the spin system and the interaction between magnetic moments play a pivotal role in characterizing the wavelength, frequency and associated SW dispersion. In the long wavelength regime, the phase difference between consecutive spins is rather small, the SW energy is primarily dominated by dipolar energy and hence the SW is manifested as dipolar dominated or magnetostatic SWs (first reported by Damon and Eshbach in 1961

[62]) as opposed to the short wavelengths SWs which are governed by exchange interaction and hence are called exchange SWs.
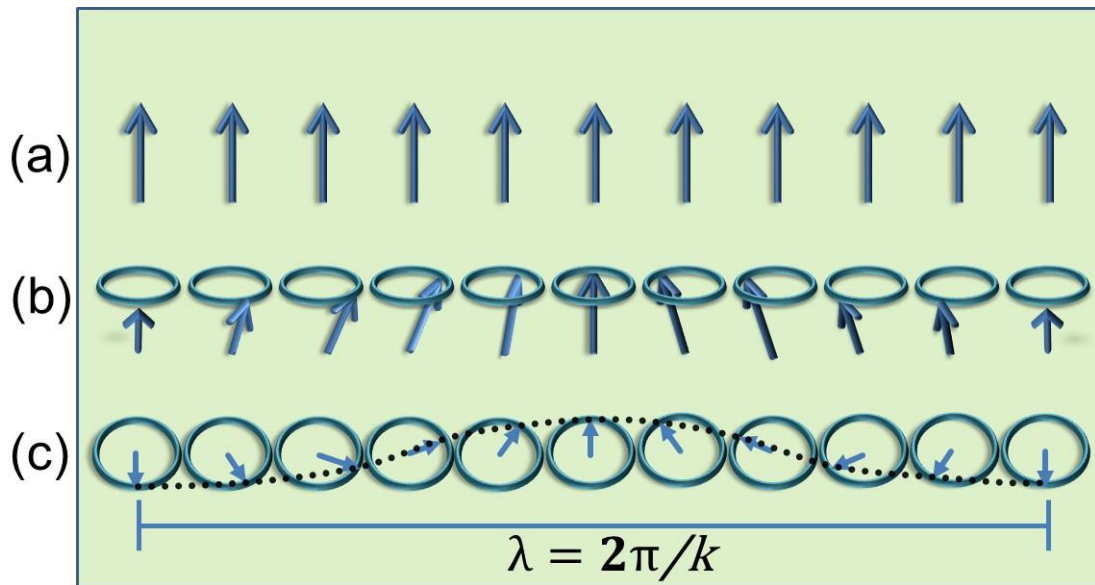
Figure 2.3: Semiclassical representation of SWs in a ferromagnet: (a) the ground state, (b) SW of precessing magnetic moment, (c) SW (top view) showing a complete wavelength.

The dipolar interaction being anisotropic, the frequency, amplitude and propagation properties of magnetostatic modes strongly depend on the geometry of their propagation direction *w.r.t.* the applied field and the film plane. When both the applied field and the SW wave vector lie in the film plane and are perpendicular (parallel) to each other, a magnetostatic surface SW (MSSW) mode (magnetostatic backward volume mode (MSBVM)) appears. If the magnetic field is applied out of the film plane and SW propagates parallel to the surface, it is known as magnetostatic forward volume mode (MSFV) mode. The frequency vs. wave vector dispersion characteristics of these modes are presented in Fig. 2.4(b).
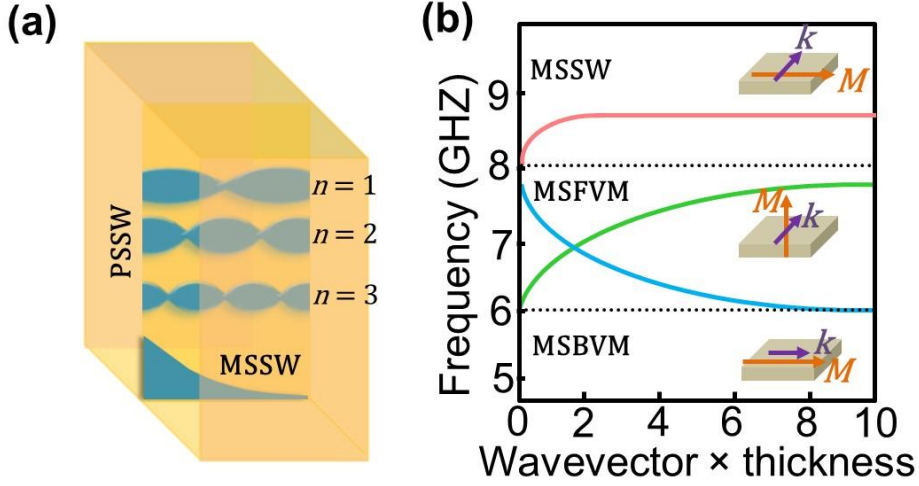
Figure 2.4: (a) Schematics of PSSW mode confined along the thickness of a FM thin film and MSSW mode. (b) The dispersion relation for different types of magnetostatic SW modes.

The MSSW, also known as Damon and Eshbach (DE) mode, shows a positive dispersion starting from the Kittel mode at zero wave vector. This mode is further characterized by the localization of SW amplitude in the vicinity of the top and bottom surfaces along with its nonreciprocal behaviour, i.e. the propagation is possible for either positive or negative direction of the wave vector for each surface. The simplified expression for the dispersion relation of the DE mode in absence of any exchange interaction and magnetic anisotropy is given by [63]:

$$f_{DE} = \frac{\gamma}{2\pi} [H(H + M_S) + (2\pi M_S)^2 (1 - e^{-2k_\parallel d})]^{1/2} \tag{2.33}$$

Where $k_\parallel$ is the in-plane component of the of the wave vector and d is the thickness of the magnetic film.

In case of MSBVM, the SW amplitude prevails throughout the thickness of the sample and the dispersion features a negative slope (group and phase velocities are in opposite directions). The corresponding dispersion relation is given by [64]:

$$f_{MSBVM} = \frac{\gamma}{2\pi} [H(H + 4\pi M_S \frac{1 - e^{-k_\parallel d}}{k_\parallel d})]^{1/2} \tag{2.34}$$

2.6.1. Exchange Spin Waves

The exchange interaction comes into play when the wave vector of SW is increased (decreased wavelength). The exchange length can be written as:

$$l_{ex}(r) = \sqrt{\frac{2A}{\mu_0 M_S^2}} \qquad (2.35)$$

where A is the exchange stiffness constant. It is worth mentioning that exchange SWs are isotropic, i.e. independent of the relative orientation of the wave vector and magnetic field. The characteristic dispersion relation by taking dipole-exchange interaction into account is given by [65]:

$$f = \frac{\gamma}{2\pi}\left[\left(H + 2\pi M_S k_\parallel d \, sin^2\phi_{k_\parallel} + \frac{2A}{M_S}k_\parallel^2\right)\left(H + 4\pi M_S - 2\pi M_S k_\parallel d + \frac{2A}{M_S}k_\parallel^2\right)\right]^{1/2} \qquad (2.36)$$

Where $\phi_{k_\parallel}$ is the angle between the applied field H and $k_\parallel$.

Further, it is also possible to excite SWs which propagate perpendicular to the film plane to form perpendicular standing spin wave (PSSW) (Fig. 2.4(a)). For a given thickness of d, the wavevector for PSSW reads:

$$k_\perp = \frac{n\pi}{d} \qquad (2.37)$$

Their dynamic magnetization profile is sinusoidal and depends on their quantization number n:

$$m_n(z) = a_n \cos\left[k_{\perp,n}\left(z + \frac{d}{2}\right)\right], \quad -\frac{d}{2} < z < \frac{d}{2} \qquad (2.38)$$

where z denotes the coordinate along the film thickness. The above equation actually describes a standing wave mode consisting of two counter propagating waves with quantized wave vectors. Without considering the contribution of in-plane wave vector, the frequency for the PSSW mode is given by:

$$f = \frac{\gamma}{2\pi}\left[\left(H_{eff} + \frac{2A}{M_S}k_\perp^2\right)\left(H_{eff} + 4\pi M_{eff} + \frac{2A}{M_S}k_\perp^2\right)\right]^{1/2} \qquad (2.39)$$

2.6.2. Confined Spin Wave Modes in Magnetic Nanostructures

After getting the flavour of the properties of SWs in infinite thin films, a brief overview of the confined structure also needs to be addressed. The boundary conditions imposed by the lateral dimensions modifies the spectrum of SW [66]. In particular, the SW finds a propagation channel [67] or form standing waves [68] in the distribution of 'potential wells' defined by the geometry of the structure. As a result, the formation of standing wave occurs leading towards localized mode or quantized mode (with multiple quantization numbers) when the feature dimensions are of the order of the wavelength of the SW. Overall, the number of SW modes increases whose properties are strongly dependent on the system geometry as well as on the orientation of the magnetic field. The

structural confinement also affects the dispersion relation, resulting in a number of allowed and forbidden magnonic bands in case of periodic patterning (Magnonic crystal or MC) [69]. The band structure of MC consisting of several Brillouin Zones (BZs) offers a novel route for the flexibility to mould the SW properties by changing the external structuring parameters.

2.7. Magneto Optical Kerr Effect

The phenomenon of magneto-optical effect was first discovered by Michael Faraday in 1845. He observed that the plane of polarization of a linearly polarized light is rotated when the light is transmitted through a magnetized material. Later on, John Kerr observed a similar rotation of polarization in reflected light as well [70]. A plane polarized light is converted into elliptically polarized light after getting reflected from a magnetized sample. This phenomenon is known as magneto-optical Kerr effect (MOKE) and the corresponding rotation of the plane of polarization (i.e. the major axis of the ellipse) is called the Kerr rotation. MOKE has been proved to be an important tool to study quasistatic and dynamic properties of magnetic system.
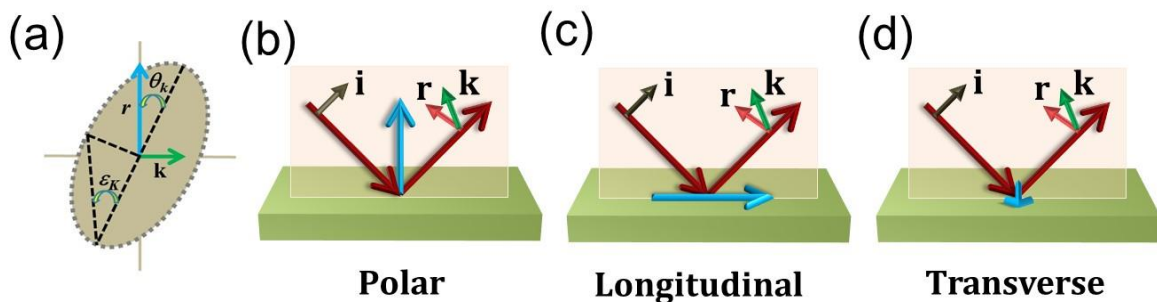
Figure 2.5: (a) Geometry of the Kerr rotation (θ_k) and Kerr ellipticity (ε_k). Schematics of various MOKE geometries: (a) polar (b) longitudinal and (c) transverse.

Figure 2.5(a) schematically depicts the Kerr rotation (θ_k) and ellipticity (ε_k), which are proportional to the magnetization of the sample. If r and k denote the parallel and perpendicular electric vector components of the reflected light with respect to that of the incident light, then one can write the following expression:

$$\theta_k + i\epsilon_k = \frac{k}{r} \; ; where \; k \ll r \tag{2.40}$$

2.7.1. Origin of MOKE

When light traverses through a medium, the generated electric field sets electrons into motion [71,72]. The left(right) circularly polarized (LCP(RCP)) light drives left(right)-circular motion of the electrons. The radii of these two circular motions become equal in the absence of magnetic field resulting into nil difference in the dielectric constants. However, under the influence of a magnetic field, an additional Lorentz force will be experienced by electrons, thereby affecting the radii of the right and left circular path. This will lead to a finite difference in the dielectric constants of both the polarized modes. The amplitude and phase of each component is altered upon reflection and it becomes elliptically polarized. Microscopically, Kerr effect is mainly originated from the motion of electrons which couples electron spin via SOI according to the quantum mechanical description. The movement of the electrons in presence of the electric field vector of light creates an effective magnetic field vector potential, which develops complex interaction between the spin and incident light. This potential can be expressed as $\boldsymbol{s} \times \nabla \boldsymbol{V}$, where $\boldsymbol{s}$ and $\nabla \boldsymbol{V}$ are the electron spin and electric field respectively. For ferromagnetic materials, the effect is prominent because of the unbalanced population of electron spins. However, the effect is present in all materials except in nonmagnets, because of the presence of equal amount of up and down spins cancelling the effect.

2.7.2. MOKE Geometries

On the basis of the relative orientation of magnetization vector *w.r.t.* the surface of the specimen and light's plane of incidence, MOKE can be categorized as follows (see Fig. 2.5): when the magnetization lies perpendicular to the sample surface but parallel to the plane of incidence of light, then the effect is known to happen in polar geometry. If the magnetization lies in sample plane and also parallel to the plane of incidence of light, then the geometry is called longitudinal geometry. These two geometries occur both for p- and s-polarized light. On the other hand, if magnetization lies in the plane of sample but perpendicular to the plane of incidence then it is called transverse MOKE geometry and it occurs only for p-polarized light. In transverse geometry, the reflectivity changes only when the magnetization reverses [73]. The schematics for various geometries are presented in Fig. 2.5(b).

References

[1] L. Landau, Z. Phys. **64,** 629 (1930).

[2] A. Abragam and B. Bleaney, *Electron Paramagnetic Resonance of Transition Ions* (OUP Oxford, 2012).

[3] R. M. Bozorth, *Ferromagnetism* 1978.

[4] B. D. Cullity and C. D. Graham, in *Introduction to Magnetic Materials* (IEEE, 2009), p. 1.

[5] A. Aharoni, *Introduction to the Theory of Ferromagnetism* 2000).

[6] S. Chikazumi, *Physics of Ferromagnetism* (OUP Oxford, 2009).

[7] M. L. Néel, Ann. Phys. **12,** 137 (1948).

[8] P. W. Anderson, Phys. Rev. **79,** 350 (1950).

[9] C. N. Yang, Phys. Rev. **85,** 808 (1952).

[10]. P. Weiss and J. Phys. Theor. Appl. **6,** 661 (1907).

[11] N. W. Ashcroft and N. D. Mermin, *Solid State Physics* (Holt, Rinehart and Winston, 1976).

[12] C. Kittel, Phys. Rev. **73,** 155 (1948).

[13] F. Bloch, Z. Physik **61,** 206 (1930).

[14] J. M. D. Coey, *Magnetism and Magnetic Materials* (Cambridge University Press, 2010).

[15] D. J. Griffiths, *Introduction to Quantum Mechanics* (Pearson Prentice Hall, 2005).

[16] W. Heisenberg, Z. Physik **38,** 411 (1926).

[17] P. A. M. Dirac, Philos. Trans. Royal Soc. A **112,** 661 (1926).

[18] M. A. Ruderman, C. Kittel, Phys. Rev. **96,** 99 (1954).

[19] J. H. Van Vleck, Rev. Mod. Phys. **34**, 681 (1962).

[20] T. Kasuya, Prog. Theor. Exp. Phys. **16,** 45 (1956).

[21] M. A. Gilleo, J. Phys. Chem. Solids **13**, 33 (1960).

[22] E. Dzyaloshinskii, Sov. Phys. Jetp, **5,** 1259 (1957).

[23] T. Moriya, Phys. Rev. **120,** 91(1960).

[24] A. N. Bogdanov and U. K. Rößler, Phys. Rev. Lett. **87**, 037203 (2001).

[25] A. N. Bogdanov and D. A. Yablonskii, Sov. Phys. JETP **68**, 101 (1989).

[26] S. Rohart and A. Thiaville, Phys. Rev. B **88**, 184422 (2013)

[27] J.-H. Moon, S.-M. Seo, K.-J. Lee, *et al*., Phys. Rev. B **88**, 184404 (2013).

[28] A. H. Morrish, *The Physical Principles of Magnetism* (R. E. Krieger Publishing Company, 1980).

[29] P. Bruno and J. P. Renard, Appl. Phys. A **49,** 499 (1989).

[30] P. Bruno and J. Seiden, J. Phys. Colloques **49,** C8 (1988).

[31] W. Palmer, Phys. Rev. **131,** 1057 (1963).

[32] D.-X. Chen, J. A. Brug, and R. B. Goldfarb, IEEE Trans. Magn. **27**, 360 (1991).

[33] S. W. Sun and R. C. O'Handley, Phys. Rev. Lett. **66,** 2798 (1991).

[34] V. Novosad, Y. Otani, A. Ohsawa, *et al.*, J. Appl. Phys. **87**, 6400 (2000).

[35] P. F. Carcia, A. D. Meinhaldt, and A. Suna, Appl. Phys. Lett. **47,** 178 (1985).

[36] S. Pal, B. Rana, O. Hellwig, T. Thomson, and A. Barman, Appl. Phys. Lett. **98,** 082501 (2011)

[37] C. Duan, J. P. Velev, R. F. Sabirianov, *et al.*, Phys. Rev. Lett. **101,** 137201 (2008).

[38] W. H. Meiklejohn and C. P. Bean, Phys. Rev. **105,** 904 (1957).

[39] A. E. Berkowitz and K. Takano, J. Magn. Magn. Mater. **200**, 552 (1999).

[40] E. Ohmichi and T. Osada, Rev. Sci. Instrum. **73**, 3022 (2002).

[41] V. P. Denysenkov and A. M. Grishin, Rev. Sci. Instrum. **74**, 3400 (2003).

[42] B. Dieny and M. Chshiev, Rev. Mod. Phys. **89,** 025008 (2017).

[43] C.-G. Duan, J. P. Velev, R. F. Sabirianov, *et al.*, Phys. Rev. Lett. **101,** 137201 (2008).

[44] M. Tsujikawa and T. Oda, Phys. Rev. Lett. **102,** 247203 (2009).

[45] T. Kawabe, K. Yoshikawa, M. Tsujikawa, *et al.*, Phys. Rev. B **96** 220412I (2017).

[46] S. E. Barnes, J. I. Ieda, and S. Maekawa, Sci. Rep. **4,** 4105 (2014).

[47] M. Tsujikawa and T. Oda, Phys. Rev. Lett. **102,** 247203 (2009).

[48] L. Landau and E. Lifshits, Phys. Z. Sowjet. **8**, 153 (1935).

[49] T. Gilbert, IEEE. Trans. Magn. **40**, 3443 (2004).

[50] M. C. Hickey and J. S. Moodera, Phys. Rev. Lett. **102,** 137601 (2009).

[51] H. Suhl, IEEE Trans. Magn. **34,** 1834 (1998).

[52] Y. Tserkovnyak, A. Brataas, and G. E. W. Bauer, Phys. Rev. Lett. **88,** 117601 (2002).

[53] E. Barati, M. Cinal, D. M. Edwards, and A. Umerski, Phys. Rev. B **90,** 014420 (2014).

[54] A. Barman and J. Sinha, *Spin Dynamics and Damping in Ferromagnetic Thin Films and Nanostructures* (Springer Publishing AG, Switzerland, 2017).

[55] B. Heinrich, J. F. Cochran, and K. Myrtle, J. Appl. Phys. **53**, 2092 (1982).

[56] P. Krivosik, N. Mo, S. Kalarickal, and C. E. Patton, J. Appl. Phys. **101**, 083901 (2007).

[57] Y. Tserkovnyak, A. Brataas, and G. E. W. Bauer, Phys. Rev. B **66**, 224403 (2002).

[58] A. Ganguly, R. M. Rowan-Robinson, A. Haldar, *et al.*, Appl. Phys. Lett. **105**, 112409 (2014).

[59] K. Lenz, H. Wende, W. Kuch, K. Baberschke, *et al.*, Phys. Rev. B **73**, 144424 (2006).

[60] Y. Zhao, Q. Song, S.-H. Yang, *et al.*, Sci. Rep. **6**, 22890 (2016).

[61] E. Jué, C. K. Safeer, M. Drouard, *et al.*, Nat. Mater. **15**, 272 (2015).

[62] R. W. Damon and J. R. Eshbach, J. Phys. Chem. Solids. **19**, 308 (1961).

[63] S. O. Demokritov, B. Hillebrands, and A. N. Slavin, Phys. Rep. **348**, 441 (2001).

[64] B. A. Kalinikos and A. N. Slavin, J. Phys. C **19**, 7013 (1986).

[65] R. Arias and D. L. Mills, Phys. Rev. B. **60**, 7395 (1999).

[66] K. Y. Guslienko and A. N. Slavin, Phys. Rev. B **72**, 014463 (2005).

[67] R. Mandal, S. Saha, D. Kumar, *et al.*, ACS Nano. **6**, 3397 (2012).

[68] C. Yu, M. J. Pechan, W. A. Burgei, *et al.*, J. Appl. Phys. **95**, 6648 (2004).

[69] Z. K. Wang, V. L. Zhang, H. S. Lim, *et al.*, ACS Nano. **4**, 643 (2010).

[70] J. Kerr, Philos. Mag. Series 5. **3**, 321 (1877).

[71] Z. Q. Qiu and S. D. Bader, J. Magn. Magn. Mater. **200**, 664 (1999).

[72]. M. Freiser, IEEE Trans. Magn. **4**, 152 (1968).

[73]. A. Barman and A. Haldar, in *Solid State Physics*, edited by R. E. Camley, and R. L. Stamps (Academic Press, 2014).

Chapter 3

3. Experimental Tools

3.1. Introduction

This chapter includes a description regarding various fabrication, characterization and measurement tools that have been implemented to study different systems in this thesis. The continuous evolution of growth and fabrication facilities is undoubtedly necessary to produce high quality thin films, heterostructures and confined structures with minimal unwanted defects. It has always been a challenging task to develop these structures at nanoscale with great perfection as well as in a cost-effective manner. The research works presented in this thesis mainly rely on the thin film heterostructures grown by rf-dc magnetron sputtering, e-beam evaporation and the artificially patterned nanostructures using electron-beam lithography. In order to perform preliminary characterization of the fabricated samples, X-ray diffraction, scanning electron microscopy, surface profiler, atomic force microscopy, magnetic force microscopy, energy dispersive X-ray spectroscopy, magneto-optical Kerr effect, vibrating sample magnetometry and Raman effect have been used. On the other hand, we have also employed the conventional Brillouin light scattering, space resolved microfocused BLS and ferromagnetic resonance technique to investigate the SW dynamics.

In the following, a brief overview regarding the working principles of the aforementioned characterization tools will be presented:

3.2. Fabrication Technique

3.2.1. RF-DC Magnetron Sputtering

Sputtering is basically a widely used physical vapour deposition (PVD) technique to deposit high quality thin film heterostructures and multilayers [1]. The main principle relies on the particle to particle collisions involving an elastic transfer of momentum which leads to the migration of the target material to the substrate. In fact, the positive ions in a gaseous plasma of inert gas is accelerated and made to bombard on a negatively charged target material to dislodge and eject a neutral atom and subsequently deposit it on a substrate. Here, Ar gas is generally used into a pre pumped vacuum chamber. Next,

the creation of gaseous plasma occurs inside the chamber with the help of a high energy source (few hundred to a few thousand eV). The cathode or target consists of the desired material or alloy to be deposited and the substrate serves as the anode. In case of a conductive (non-conductive) target material, a direct current (radio-frequency) power supply is used. Plasma is well known as a fourth state of matter where neutral gas atoms, ions, electrons and photons coexist simultaneously. The free electrons in the plasma immediately accelerate away from the negatively charged cathode under the influence of a high voltage applied through a power supply. The accelerated electrons away from the target undergo multiple collisions with the neutral atoms to produce more secondary electrons and ions (Ar^+) in the diffused plasma. Subsequently, the positively charged ions are accelerated into the target, thereby ejecting neutral atoms and electrons. Then the migration of these ejected atoms happens in a typical line-of-sight cosine path and, as a result, they get deposited on the substrate.

This conventional sputtering technique described above suffers from two major challenges, such as slow deposition rate and overheating of the target (due to extensive electron bombardment). One possibility to address these issues is to use magnetron sputtering. In this case, magnets are used behind the cathode to trap the free electrons in a cyclic path just above the cathode as shown in Figure 3.1.
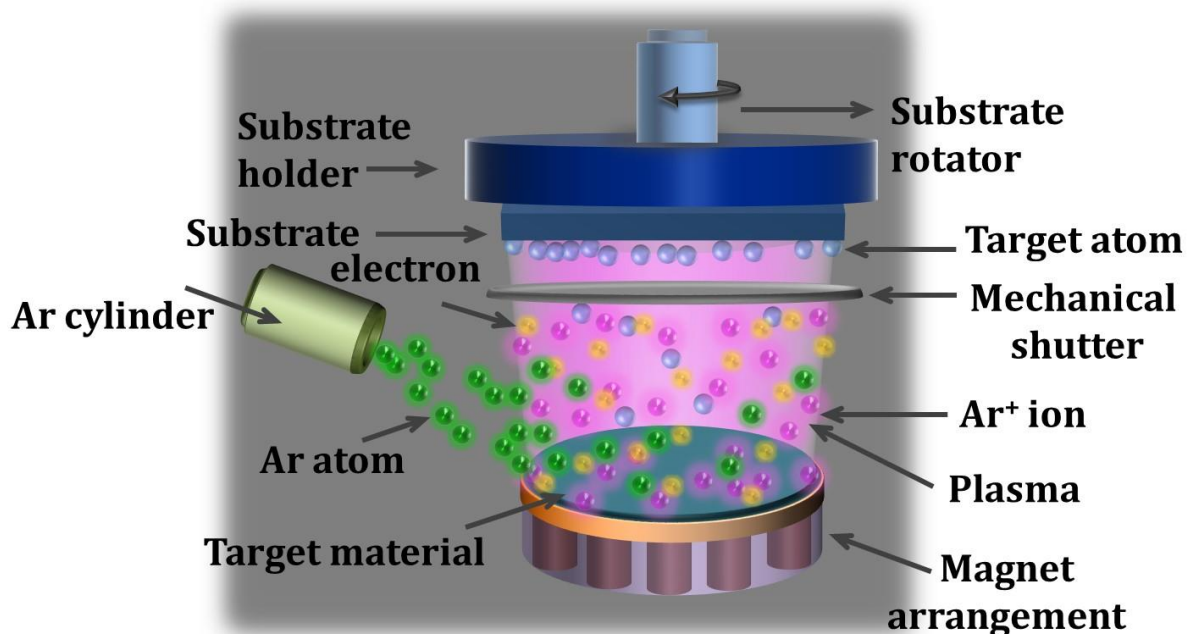
Figure 3.1. Schematic of RF-DC Sputtering.

In this method, Both the increased probability of ionizing neutral gas molecules and decreased velocity of electrons help to achieve enhanced deposition rate. In addition, it is also feasible to deposit layered structures in lesser time and with lower substrate temperature.

3.2.2. Electron Beam Evaporation

This is also a PVD technique, where an intense beam of electrons is generated from a filament via thermionic emission and is steered by the electric and magnetic fields towards the source material [2]. Because of the intense collision with electron beams, heating process of the source material occurs. As a result, it vaporizes after reaching the boiling point within a vacuum environment. The atoms at the surface having sufficient energy traverse the vacuum chamber and gets deposited to a substrate placed above the evaporating material. The sample holder is mounted on a rotation motor, which rotates during the deposition, thereby ensuring uniformity all over the substrate.
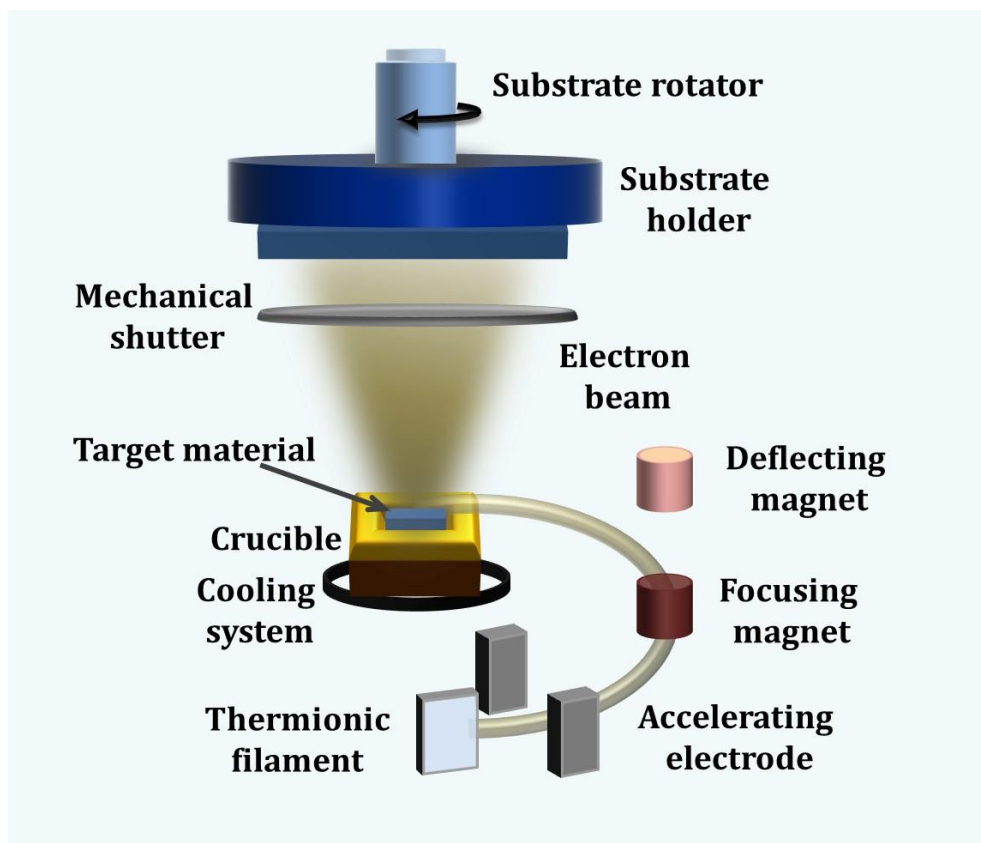
Figure 3.2: Schematic of E-beam evaporation.

This is extremely important while depositing the film on the arrays of patterned micro or nanostructures as it reduces the undesired side-wall coating during the deposition.

Owing to the low thermal energy, the pressure in the chamber is maintained in such a way that the mean free path remains lesser than the distance between the electron beam source and the substrate. The "line of sight" arrival of material is required when masking is employed to generate a pattern in the substrate. The schematic of the setup is given in Fig. 3.2.

3.2.3. Electron Beam Lithography

Lithography techniques offer an elegant way to fabricate samples at nanoscale. Here, different kinds of radiation sources such as optical, electron beam, X-ray and ion-beam are exposed to a chemically active medium known as resist to draw the pattern of ordered arrays of nanostructures [3]. Thanks to the shorter wavelength of high energy electron beam, the resolution is achieved as high as tens of nanometers. In the electron beam lithography (EBL), the beam is directed along a path defined using computer aided design (CAD) software which describes the desired structures in either positive or negative tone. Writing is performed in a layer of electron-sensitive positive or negative tone resist applied either on blank substrate (bottom to top approach) or continuous thin film (top to bottom approach). Polymethyl methacrylate (PMMA) is a model positive tone resist having some important properties such as stability for long periods of time, ease of handling and application, and providing high resolution down to 10-20 nm. It is the most widely used positive tone EBL resist and has also been used for the nanofabrication presented in this thesis. Generally, spin coating is performed using a short chain of perspex suspended in anisole solvent, PMMA (950K: denotes the molecular weight of the resist) on Si substrates and then baked for 5-10 minutes at 180°C to evaporate off the solvent and promote polymer crosslinking, leaving a hardened layer of resist. An electron beam of the order of 200-450 $\mu C/cm^2$ was locally applied to cause de-crosslinking of polymer chains, allowing the exposed regions to be removed through development process with a 3:1 mixture of isopropanol (IPA) and methyl isobutyl ketone (MIBK). After this, the target material was deposited on top of the resist. Sometimes additional capping layer can also be deposited with the material. To remove the unexposed resist, lift-off was done in acetone using ultrasonic agitation. The schematic of the EBL is shown in Fig. 3.3.
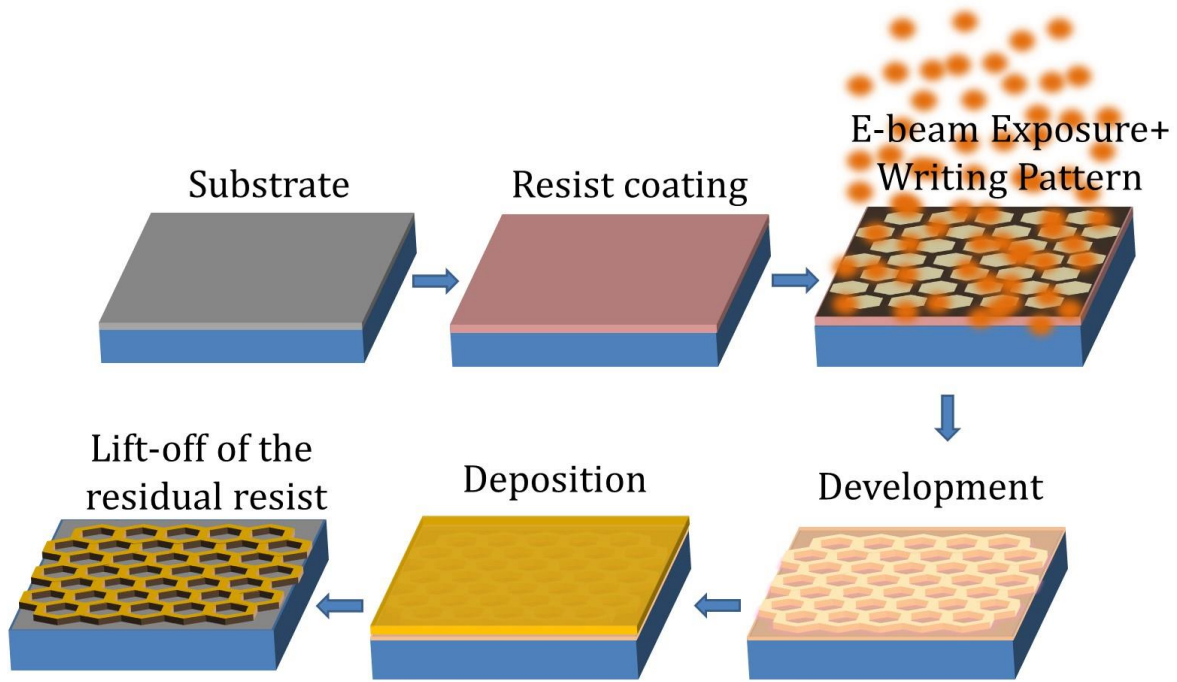
Figure 3.3: Schematic of the E-beam lithography (EBL) process.

3.2.4. Chemical Vapour Deposition (CVD)

In recent years, a considerable development of CVD technique has been made which makes it a versatile tool for novel manufacturing in many industrial sectors such as semiconductor, ceramic, microelectronics industries [4]. Further, an intensive research and development work being pursued by the academic researcher as well as industrial users. In the simplest words, CVD can be defined as a complex process where the deposition of solid materials is done at a high temperature with the aid of chemical reaction. As a result, an ordered crystal is formed from the vapour. The distinction of CVD lies in the fact that it's a kind of reactive processes as opposed to PVD such as sputtering, thermal evaporation etc. The main advantage of using CVD to deposit material onto a substrate is its high quality, fine grain size, high purity and increased hardness. It is important to mention that during the CVD process, the toxic byproducts are removed from the reaction chamber by gas flow for proper disposal. In this thesis, single layer CVD grown graphene from Graphenea [5] has been used. Basically, the creation of CVD grown graphene involves two steps, the precursor pyrolysis of a material to form carbon followed by the formation of carbon structure of graphene using the dissociated carbon atom which requires a very high temperature. The schematic of CVD process is shown in Fig. 3.4.
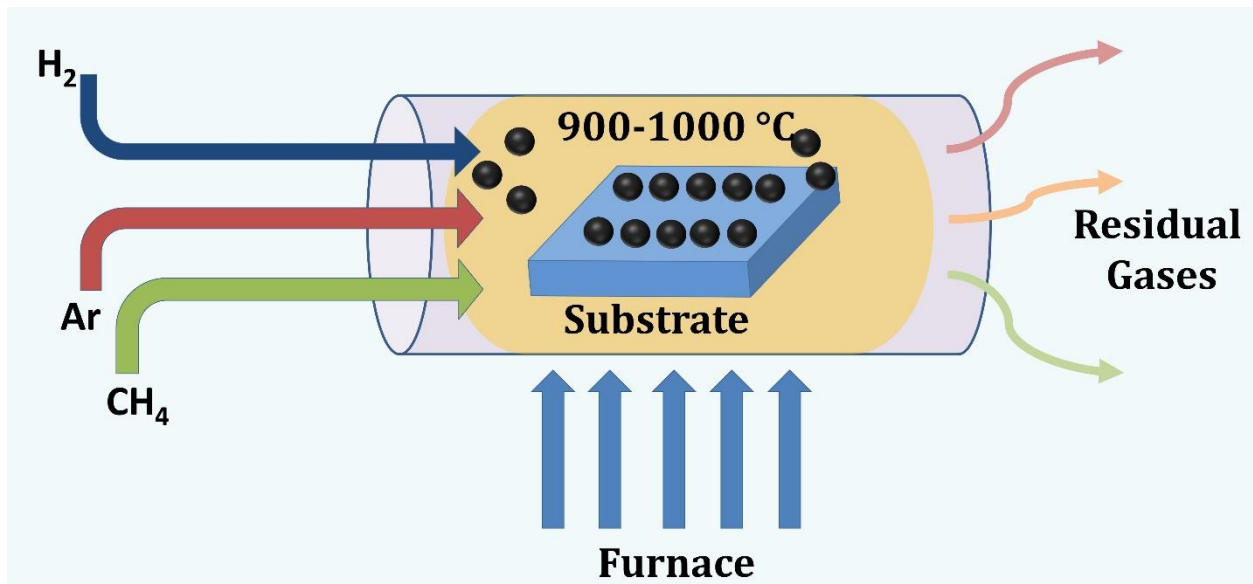
Figure 3.4: Schematic diagram of chemical vapour deposition (CVD) process.

3.3. Characterization Techniques

Here, a brief description and the underlying working principles of the various tools that have been used to perform preliminary characterization of the studied samples, such as thin films, heterostructures and nanostructures, will be presented.

3.3.1. Scanning Electron Microscopy

To characterize the surface topography and morphology of the sample, a widely used sub-optical imaging technique is the scanning electron microscopy (SEM) [6]. The SEM works in a similar fashion to the optical microscopy, replacing photons with electrons and glass lenses with precisely shaped magnetic lenses. However, the SEM is very special due to its high spatial resolution ($\approx$1nm) owing to the much shorter de Broglie wavelength of electrons. The interaction between the electrons and sample leads to the various signals that carries the information about the surface texture and composition. In a typical SEM (see Fig. 3.5), with the aid of thermionic or electric field emission, accelerated electrons are generated and then focused by one or two electromagnetic condenser lenses. Subsequently, this passage of electron beams undergo deflection in a two-dimensional rectangular region of the sample through a pair of scanning coils or deflector plates enabling the raster scanning. The incident electrons are subjected to a range of interactions leading to distinct types of entities leaving the surface such as secondary

electrons (due to inelastic collision), backscattered electrons (due to elastic scattering), transmitted electrons, photons, visible light and heat.
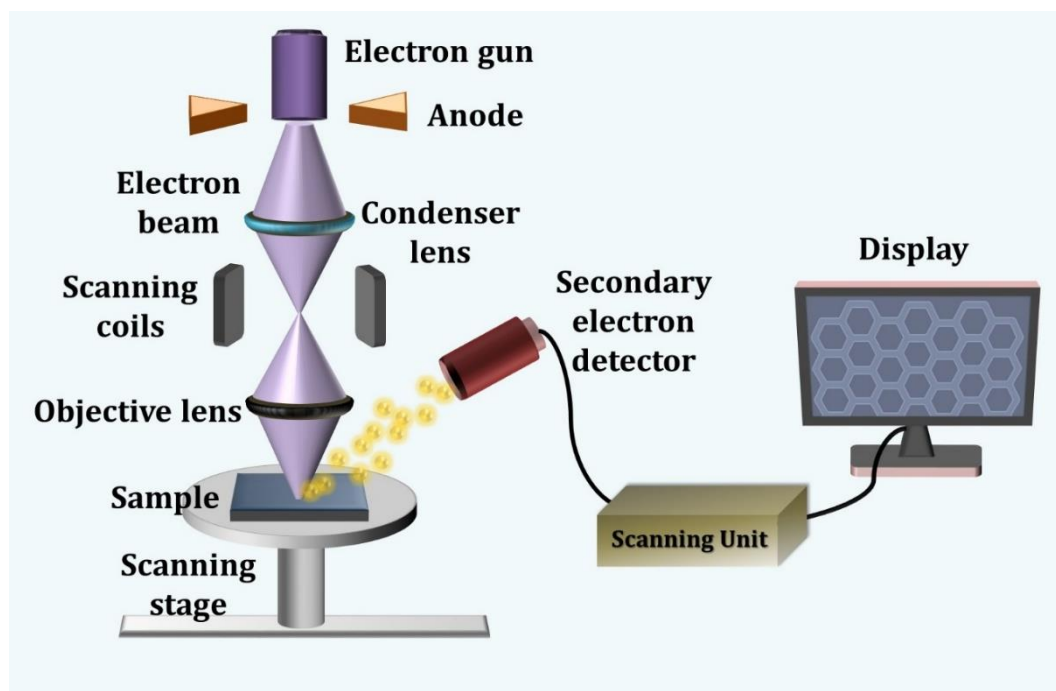
Figure 3.5: Schematic diagram of scanning electron microscope.

The flux of secondary electrons at the detector is sensitive to the sample-detector separation and the electronic structure of the sample which allow the detected intensity to build an image of the sample topography and material composition. It is to be noted that the material sensitivity is not exceptionally high in comparison with other electron microscopy techniques such as Auger electron spectroscopy or transmission electron microscopy, but metallic structures show significantly different contrast to an insulating substrate. We have used model no: FEI QUANTA 200 SEM (at SNBNCBS) & Raith E-line system (at Imperial College London) to characterize the studied samples.

3.3.2. Energy Dispersive X-Ray Spectroscopy

In order to perform the elemental and chemical analysis of the samples, energy dispersive X-ray (EDX) spectroscopy is proved to be an appropriate tool [7]. The basic principle of operation is based on the phenomenon that each element possesses a unique atomic structure as well as emission spectrum, which can be utilized to recognize the elements present in the specimen. Basically, in ground state, an atom consisting of a number of electrons moving around the nucleus, reside in discrete characteristic shells. As a high

energy beam of charged particles (like electrons, protons or x-ray) hits the sample, it excites and ejects out electrons from an inner shell and creates electron-hole pair. The electrons from outer, higher energy shells then jump to the inner shell to fill the hole where the difference in the two energy shells is emitted in the form of an X-ray. A silicon or lithium detector is used as an energy dispersive spectrometer to measure the energy and number of the emitted X-rays. The peak energy values of the X-rays and the relative heights of the peaks provide the identification and atomic percentage of elements present in the sample respectively.

3.3.3. X-Ray Diffraction

The X-ray diffraction (XRD) technique [8] is used to investigate the crystalline material structure, including atomic arrangement, crystallite size and imperfections. Here a beam of X-rays (wavelength ~1.5418 Å) is incident on the sample and is diffracted by the crystalline atoms. By measuring the angles and intensities of these diffracted beams, one can determine the atomic arrangement, its disorder and various other information.

Figure 3.6 presents a schematic of the XRD technique. A crystal can be considered as a regular array of atoms, which can elastically scatter electromagnetic waves like X-rays. The scattered beams form secondary waves which can interfere constructively at certain directions according to the Bragg's condition:

$$2d \sin \theta = n\lambda \qquad (3.1)$$

Here d being the distance between the atomic planes, θ the incident angle, n any integer and λ the wavelength of the X-ray.
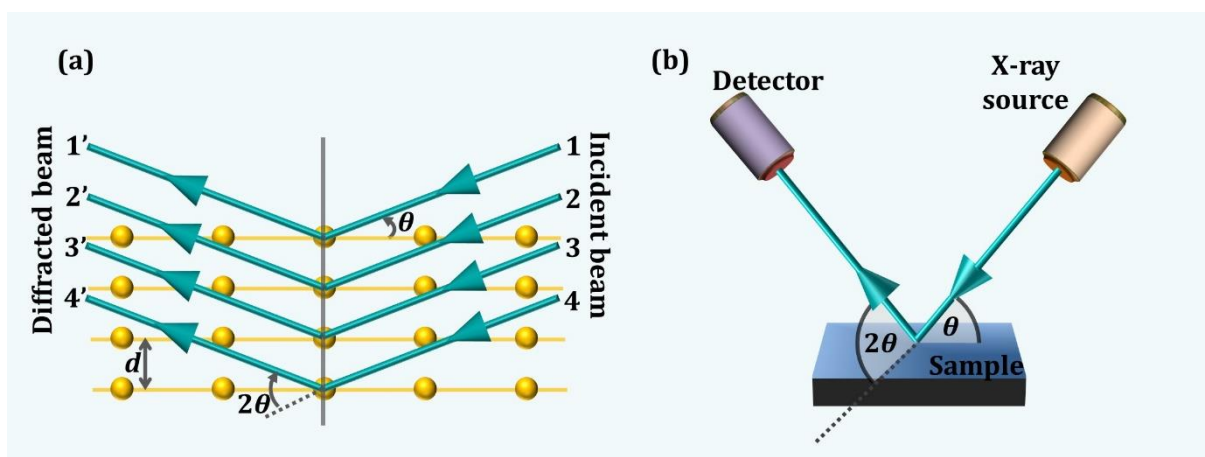
Figure 3.6: (a) Mechanism of X-ray diffraction and (b) schematic diagram of XRD.

Therefore, for a certain lattice structure (that corresponds to *d*), the diffraction spots appear only at certain angles of incidence. In the measurement, the incident angle of X-ray is varied between a range of angles in small steps and the corresponding reflected intensities are measured as a function of the angle of the reflected beam with respect to the direction of the incident beam (2θ). Subsequently, the diffraction peaks are converted to *d*-spacings to identify the elements present in the sample. Typically, this is accomplished by matching the data with standard reference patterns (i.e. Inorganic Crystal Structure Database (ICSD) or International Centre for Diffraction Data (ICDD)).

3.3.4. Atomic Force Microscopy

Atomic force microscopy (AFM), developed at IBM in 1986, is one of the most widely used scanning probe microscopes employed to investigate the surface topography and morphology of the sample [9]. The novelty of this technique is the attainment of high spatial resolution (lateral resolution ~20 nm, vertical resolution ~0.1 nm) under ambient condition. The information is acquired by measuring the force between a probe and the sample. Piezoelectric actuators enabling small and accurate movements of the sample at nanoscale facilitates very precise scanning with a resolution thousand times better than that of the optical diffraction limit. The AFM probe consists of one cantilever (generally coated with Co-Cr, Pt-Ir etc.) having a sharp tip (coated with Co-Cr, Pt-Ir or doped diamond etc.) at its end (see Fig. 3.7). The interaction starts to occur when the tip is brought closer to the sample surface. As a result, the tip experiences vertical and lateral deflections due to forces such as van der Waals force, force due to chemical bonding, capillary force, electrostatic force as well as magnetic force. The mapping of this deflection is done by a laser spot reflected from the top surface of the cantilever. After this, the reflected laser beam hits a space sensitive four segments photodetector. The differences between the signals of different segments of photodetector gives an estimation of the angular deflections of the cantilever. A 2D profile of the local parameters can then be acquired by performing a raster-scan over a small area (generally few tens of μm^2) of the sample. Based on the sample surface and the acting force between the tip and sample, one can categorized three different modes in which AFM imaging can be performed.

3.3.4.1. Contact Mode

In this mode, the tip scans the sample in close contact with its surface while a constant repulsive force between the tip and the surface is applied during the scan. A feedback

amplifier helps to maintain this criterion during scanning by applying a feedback voltage to the piezoelectric actuator. As such measurement of static signal can affect the cantilever as well as sample surface and hence, cantilevers with low stiffness are incorporated to achieve a large enough deflection signal (the amplitude ranges from few tens to few hundreds of nm) while keeping the interaction force feasible.

3.3.4.2. Non-Contact Mode

The act of physically dragging a tip over a rather rough sample surface while in contact can be detrimental to both tip and sample leading to the unwanted damage. In order to avoid that the tip hovers few tens of Å above the specimen and attractive force like van der Waals force is probed to construct the topographical image of its surface in the non-contact mode. However, such force is somewhat weaker than the forces in contact mode so that a small oscillation is applied (the amplitude of oscillation typically ranges from few nm) to the tip. The modulation in amplitude, frequency or phase of the cantilever which results from the small forces acting between the tip and the sample is measured.

3.3.4.3. Tapping Mode

It is based on the cantilever which oscillates at or near its resonant frequency using a piezoelectric actuator. The tip is then brought close to the sample until it begins to lightly touch or tap the surface. The fragmentary contact of the tip with the surface affects the cantilever oscillation causing an energy loss. The resulting change in the oscillation amplitude is employed to identify and interpret the surface features.
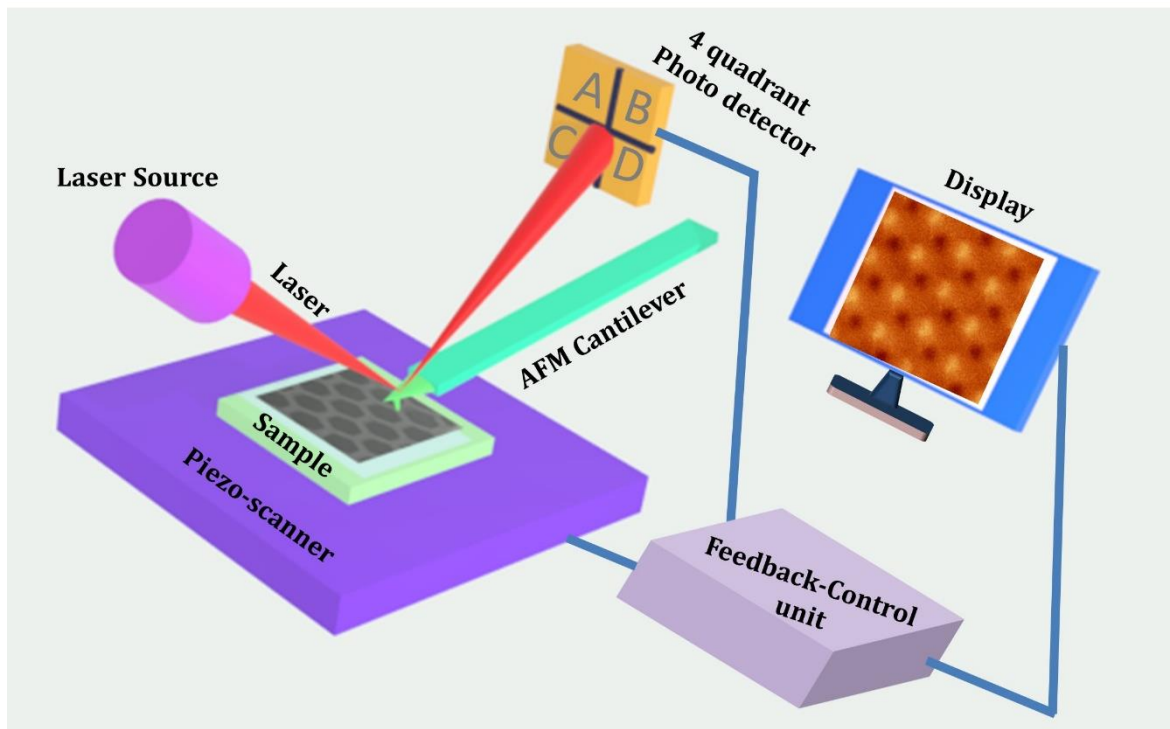
Figure 3.7: Schematic diagram of atomic (magnetic) force microscopy.

3.3.5. Magnetic Force Microscopy

Magnetic force microscopy (MFM) requires a little modification of the basic AFM system to obtain a surface map of the magnetic configuration of the sample [10]. In MFM, magnetization state of a magnetic sample can be obtained by studying the magnetic interactions between the tip and the sample. Necessarily the tip is coated with a thin magnetic layer having high coercivity (i.e. Co or CoCr) for the sustainability of its own magnetization after several scanning. The tip can sense the magnetic forces along with the atomic and electrostatic forces near the surface due to the interaction between the components of stray fields. During the measurements to get a better MFM image it is recommended to take AFM image also. Once the surface topography is recorded the tip is then lifted up and scanned again over the sample surface at that particular height to sense the out-of-plane stray fields. In this process, the magnetic signal is obtained in terms of voltage which is extracted and processed by the requisite software to provide information about magnetic texture. MFM may be operated either in constant height or constant tip-sample separation mode. It is believed that the constant height is easy to perform as the sample stage is kept fixed in the z- direction. However, it may suffer from

an artefact that a region of magnetization at low tip height will appear stronger than another identical region of magnetization at a higher tip height. This problem is avoided in constant tip-sample separation by performing a preliminary AFM scan of the surface which helps to adjust dynamically the z-position of the sample stage during the MFM scan. The spatial resolution of MFM is roughly comparable to the tip-sample separation down to a minimum of around 20 nm that allows to perform MFM scans in smaller separations. At lower separations the tip experiences well-defined stray fields above the sample's poles magnetic charges which then smear out and overlap at larger tip-sample separations, decreasing image resolution. The constant separation mode also has a drawback that bringing the MFM tip close enough to the sample leads to the alteration of the sample's magnetization state.

3.3.6. Vibrating Sample Magnetometer

The magnetic properties of the sample is measured using vibrating sample magnetometry (VSM) technique as a function of applied magnetic field and temperature [11]. The basic principle of functioning of VSM is based on the Faraday's law of induction which states that varying magnetic flux through a coil will generate electromotive force (EMF) induced in the coil in the form of a voltage. The expression can be written as follows:

$$E_{in} = -NA\frac{dB}{dt} \tag{3.2}$$

Here, E_{in} is the induced electric field, A is the area of the coil with N number of turns. Using $B = \mu_0(H + M)$, with the constant magnetic field, Eq. (3.2) reads:

$$E_{in} = -NA\frac{dM}{dt} \tag{3.3}$$

Since the magnetization M depends on the total magnetic moment m and other factors, so the above equation can be modified as:

$$E_{in} = -mwzy_0NN_cG\cos(\omega t) \tag{3.4}$$

where w and z are the frequency and amplitude respectively, the y_0 is defined as the distance between the two pickup coils, N_c is the number of pickup coils and G is the geometric factor of the sample. During the measurement, the measurement protocol is such that the sample is first placed under the influence of constant magnetic field thereby creating stray fields by magnetic dipole moment of the samples. Since the sample is attached to a piezoelectric transducer, sinusoidal electric signal is transformed into a sinusoidal vertical vibration of the sample rod resulting into an overall sinusoidal

oscillation of the sample. Therefore, a voltage in the pickup coil is induced mainly due to the oscillating magnetic dipoles of the sample, which is independent of the applied magnetic field. Basically, the conversion of the dipolar field of the sample in the form of an ac electric signal is further amplified and measured by using a lock in amplifier. The output of the piezoelectric signal acts as the reference signal. Any change in the external parameter such as applied magnetic field and temperature leads to a modification in the magnetization of the sample which can be traced to investigate the *M-H* (for hysteresis loop) or *M-T* (for the estimation of Curie temperature) curves. For magnetic characterization of the samples studied in this thesis, a Lake Shore (model: 7407) VSM system [11] has been extensively used. The schematic of the VSM setup is shown in Fig. 3.8.
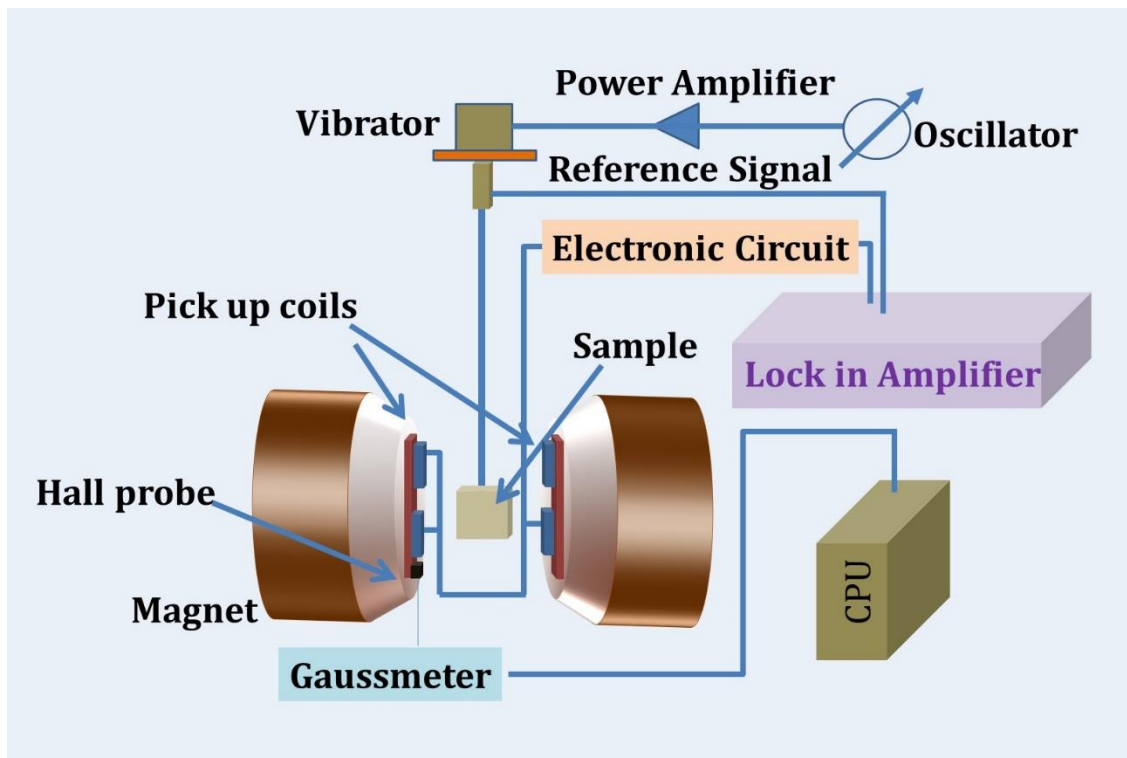
Figure 3.8: Schematic diagram of a vibrating sample magnetometer.

3.3.7. Static Magneto-Optical Kerr Effect Magnetometer

The static magneto-optical Kerr effect (static MOKE) technique relies on the MOKE and is used for the measurement of magnetic hysteresis loops in continuous thin films and patterned nanostructures [13-14]. The striking difference between static-MOKE and VSM is the probing region of the magnetic sample. Static MOKE is a non-invasive, surface

sensitive and local measurement technique, whereas VSM is a global technique. The schematic of the setup is presented in Fig. 3.9.

A continuous wave laser (He-Ne) of wavelength 632.8 nm is used to probe the magnetization of the sample which is placed under the influence of an applied magnetic field. When the laser beam passes through a Glan Thompson (GT) polarizer, the light becomes fully polarized. After chopping the beam at 2 kHz frequency by using an optical chopper, it is steered by a set of mirrors and made to pass through a couple of lenses (L1 & L2) which are used for collimation and expansion of the laser beam. The in-plane magnetic field is supplied via an electromagnet. An optical bridge detector (OBD), which can sense and distinguish the change of polarization and intensity of the laser, is used to detect the signal. The OBD consists of a polarized beam splitter (PBS), which splits any light into two orthogonal components. A couple of photodiodes (A, B) pick those components and convert those into electrical signals. In absence of any magnetic field, the balanced condition (A = B) of OBD is obtained by rotating the axis of the PBS slightly around 45°. The calibration factor is also measured by rotating the PBS by 1° (or as per convenience) on either side of the balanced position in the rotational scale and the dc output of the detector is used to extract the calibration factor. Under the application of a magnetic field, the magnetization in the sample is manipulated and the polarization of the light changes. Thus, the detector moves away from the balanced condition (A ≠ B). The difference signal (A – B) is measured in a phase sensitive manner by using a lock-in amplifier. The frequency of the chopper is fed to the lock-in amplifier in order to set a reference. The output signal is converted to Kerr rotation by multiplying with the calibration factor. To obtain magnetic hysteresis loop, the IP field is varied from positive to negative direction (monitored in terms of current or voltage of the power supply) and measurement protocol is established using a home-built LabVIEW software to capture the change in magnetization as a function of the IP magnetic field.
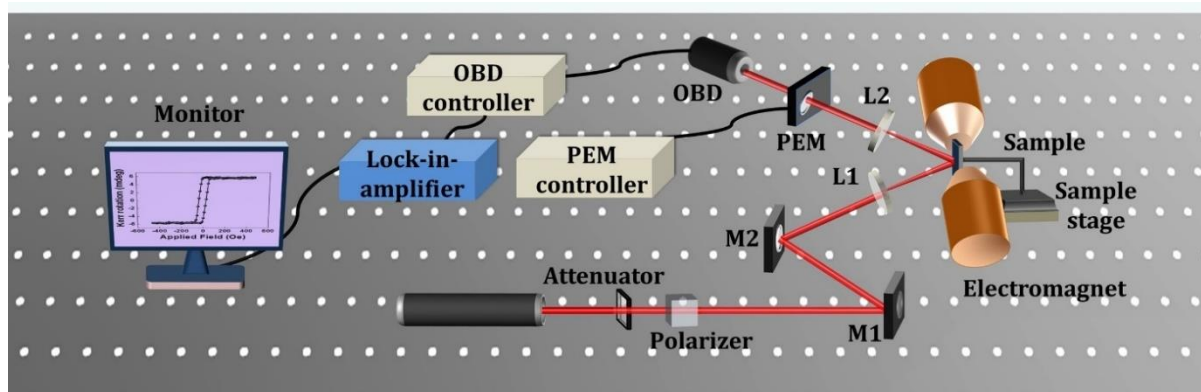
Figure 3.9: Schematic diagram of static MOKE.

3.3.8. Raman Spectroscopy

Raman spectroscopy is one of the molecular spectroscopic techniques where interaction of light with matter gives the insight of the material characteristics [15]. Raman scattering relies on the inelastic light scattering process where energy of the scattered photons are modified with respect to that of the incident photons after interacting with the material, leading to a shift known as the Raman shift. The Raman effect was first discovered by C. V. Raman in 1930 for which he was awarded the Nobel prize in physics. There are two types of scattering event occurs namely, Stokes and anti-Stokes. The former originates due to the less energy of the scattered photon as compared to that of incident photon. When the change in energy of the scattered photon is less than the incident photon, the scattering is called Stokes event. In the later case, Some molecules pre resides in a vibrationally excited state and when they are promoted to a rather higher energy level, they may relax to a final energy state having lower energy than that of the initial excited state. Typically, the wavelength used for the Raman spectroscopy are 488 nm, 514 nm, 532 nm, 785 nm, 830 nm and 1064 nm from different types of laser. The optics cables made of fibre is used to transmit laser energy which is acquired from the sample. A CCD detector collects the light and displays the Raman spectrum.
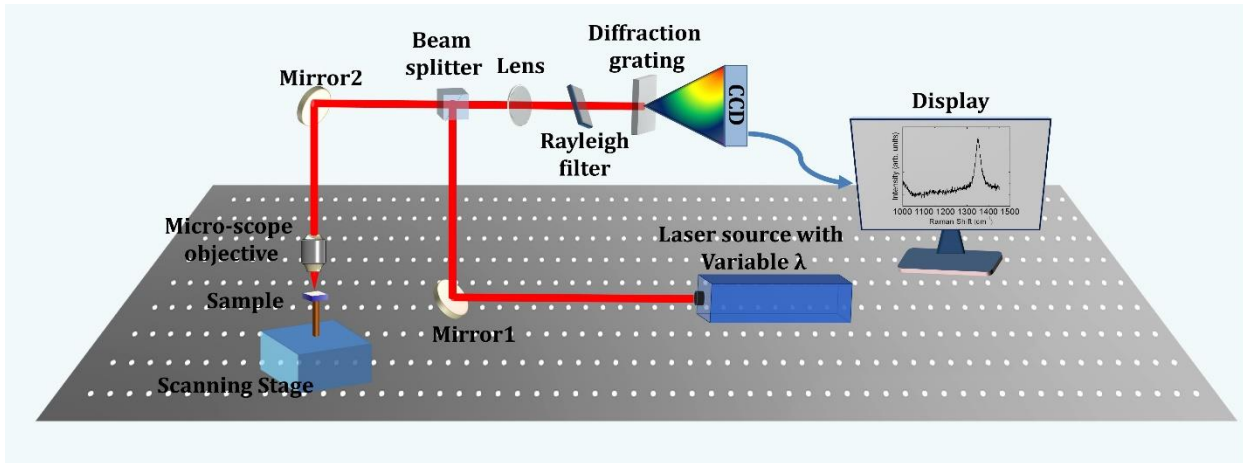
Figure 3.10: Schematic diagram of Raman spectrometer.

Because of the weak signal yielded by Raman scattering, it is highly recommended that high quality, optically well-matched components should be used in the Raman spectrometer. The schematic of Raman spectrometer is given in Fig. 3.10.

3.4. Measurement Techniques of Spin Dynamics

The various measurement tools to investigate the spin dynamics will be presented below:

3.4.1. Brillouin Light Scattering

Light scattering-based experiments are the backbone of the extensive study of various physical phenomena observed in solid, gas and liquid systems. In the Brillouin light scattering (BLS) experiments, the scattered light from a sample carries the information about important physical properties. In BLS, it relies on the inelastic light scattering process where incident photon interacts with various quasiparticles (i.e. phonon, magnon, polariton, plasmon etc.) present in the sample. In fact, BLS being a powerful tool, has been successfully employed to measure the elastic properties of water [16-17], solids [18], as well as bio-organic materials (i.e. eyes lens [19]). Nevertheless, in this thesis our main focus would be on the implementation of BLS to measure SW excitations in ferromagnetic structures, such as thin films heterostructures comprised of HM/FM/oxide, 2D-Material/FM, SAFs and magnonic crystal based on ASI and 1D-MWGs. The theoretical prediction of light scattering from acoustic waves was given independently by in 1922 [20] and Mandelstam in 1926 [21]. Subsequently after few years in 1930, Gross experimentally confirmed the observation of scattering of light in liquids [22]. Thanks to the invention of laser in the 1960s which revolutionized this area of research. The investigation of acoustic waves and SWs in optically opaque material

became possible only after 1971 when John Sandercock developed a highly sophisticated spectrometer known as Fabry-Pérot interferometer (FPI) [23]. The key feature of an FPI is the dramatic increase of its sensitivity if the scattered light passes multiple times through it [24]. Both surface and bulk SWs were detected in polycrystalline films of Fe and Ni by Sandercock and Wettling using tandem operation of two interferometers [25-26]. In recent years, BLS has proved to be versatile tool for the advanced magnetism-based research with particular emphasis on the degree of flexibility in samples, resolution in frequency, phase, time and space. The other key points are mentioned as follows:

1) Probing thermal magnons at ambient condition (at room temperature).
2) Investigation of SW response over a broad frequency range up to 500 GHz with 30 MHz digital resolution.
3) Investigation of SW dispersions with various absolute values and orientations of the corresponding wavevectors.

The information about the properties of magnetic layers, e.g. magnetic damping, magnetic anisotropy, saturation magnetization, DMI strength as well as coupling parameter between different magnetic layers can be extracted.

3.4.1.1. Underlying Principles

In BLS spectroscopy, a monochromatic laser beam is incident on the surface of a sample. A major fraction of incident light undergoes absorption or reflection, and only a small fraction of it scatters from the thermally excited SWs in the sample. The scattered beam consists of two contributions originating from elastic and inelastic scattering process. In case of elastic scattering (like Rayleigh scattering), the frequency or energy of the photons remain unchanged while in the inelastic scattering, the frequency or energy of the scattered beam gets changed. This change in the frequency is attributed to the frequency of the SWs present in the sample. The scattered light is collected via the same lens which is used to focus incident beam on the sample surface, within a solid angle in the direction 180° from the incident light. This geometry, also known as 180° backscattered geometry, has an advantage that it maximizes the magnitude of SW wave vector involved in the scattering process. The scattered light is frequency analysed using a high resolution multi pass tandem FPI to extract the characteristics of surface and bulk magnons.
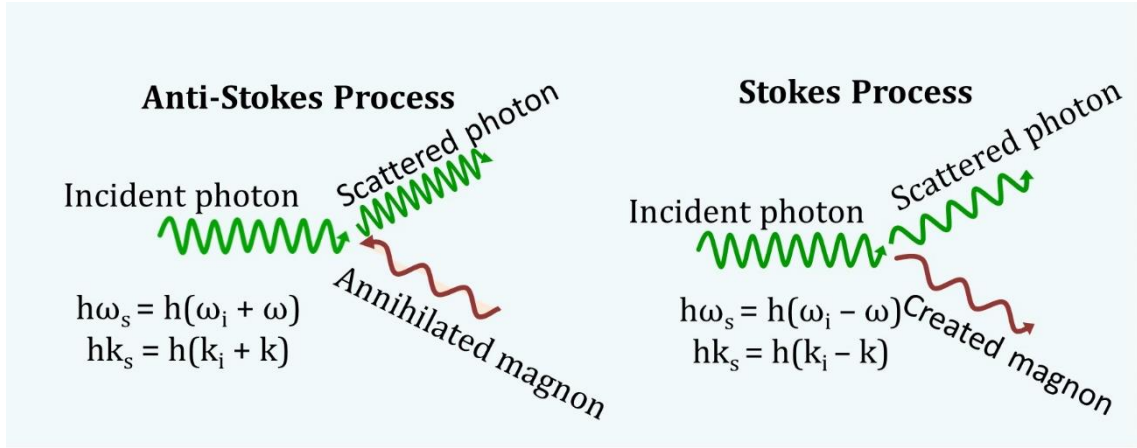
Figure 3.11: Schematic of the Stokes and anti-Stokes processes.

From quantum mechanical point of view, the inelastic light scattering mechanism can be well described as photon-magnon collision. The schematic of the scattering process is shown in the Fig. 3.11.

From the conservation of energy and momentum between the magnon and the incident photon and scattered photon, we can write the following expressions:

$$\hbar\omega_s = \hbar\omega_i \pm \hbar\omega \tag{3.5}$$

$$\hbar k_s = \hbar k_i \pm \hbar k \tag{3.6}$$

where + (-) sign refers to the anti-Stokes (Stokes) frequency shift and $\omega_s, k_s, \omega_i, k_i$ are the respective angular frequencies and wave vectors of incident and scattered photons. It is noteworthy that the perpendicular component of the wave vector is not conserved due to the breaking of translational symmetry. Hence, the above expressions are valid only for k parallel to the thin film. The energy of the magnon ($\approx 10^{-4}$ eV) is very low as compared to that of incident photon ($\approx$ few eV). Consequently, the magnitude of the scattered photon (k_s) is very much close to the wave vector of the incident photon (k_i). The schematic representation of the underlying mechanism related to scattering profile of a photon by a bulk as well as surface magnon is given in the Fig. 3.12. Here, the participated SW in the scattering process has a component perpendicular to surface. The scattered photon wave vector k_s must lie on the shaded green circle, whose radius is equal to the magnitude of incident photon wave vector (k_i). Here, the cone represents the collection angle of the scattered beam in the BLS experiment, whose central axis aligns with the incident photon wave vector. Therefore, it is assumed that k_i and k_s are collinear ($k_i = -k_s$). It means that in

the backscattered geometry, the wave vector magnitude of the emitted or absorbed bulk magnon $|k|$ is always equal to $2|k_i|$.
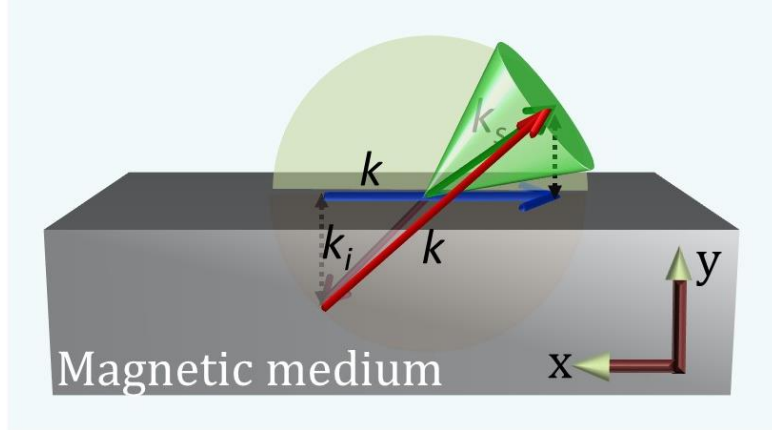
Figure 3.12: Schematic of the scattering of incident laser beam by surface and bulk magnons.

Furthermore, in case of the scattering of a photon by a surface magnon, the direction of k lies in the horizontal plane which results into the conservation of momentum only in the plane along the sample surface. Therefore, the magnon wave vector probed in the experiment is written as:

$$|k| = |k_i \sin\theta - k_s \sin\theta| = 2|k_i| \sin\theta = 2\left(\frac{2\pi}{\lambda}\right)\sin\theta \qquad (3.7)$$

Hence, by varying the angle of incidence, no new information regarding the bulk magnons can be obtained, whereas the surface magnons offer the important f vs k dispersion relation. The above equation is widely known as Bragg's condition used in various light scattering experiments. The magnitude of k can be varied by changing either θ or λ. The k-dependent study presented in this thesis has been done by changing θ.

3.4.1.2. Estimation of the Uncertainty in the SW Wave Vector

Finite aperture angle of the objective lens used for focussing and collecting light from the sample introduces an uncertainty in the SW wave vector. For finite value of θ, the spread in k can be written as:

$$\Delta k = 2k_i \cos\theta \sin\left(\frac{\phi}{2}\right) = 2\frac{2\pi}{\lambda}\cos\theta \; NA \qquad (3.8)$$

where ϕ is the collecting angle of lens and NA is the numerical aperture defined by

$$NA = \sin\left(\frac{\phi}{2}\right) \qquad (3.9)$$

So, for normal incidence (i.e. $\theta = 0°$), this uncertainty becomes maximum. Also, because of the focusing of the incident beam, a possible uncertainty can be present in θ. However, a very narrow beam (width ≈ 500 μm) is used to reduce this during the practical experiment which in turn enhances the focused spot size.

3.4.1.3. Polarization of the Scattered Beam

In order to interpret the scattering of light from SW, magneto-optic interaction mechanism is best suited. In general, the oscillating electric dipoles experience a Lorentz force due to precessing magnetization or SW which gives rise to a spatially periodic fluctuation in polarizability of the medium. It leads to a scattered electromagnetic (EM) wave whose direction of electric field vector is perpendicular to the incident wave. The schematic of this process is shown in Fig. 3.13 for a *p*-polarized incident light in the DE geometry. When the laser beam impinges on the magnetic sample, its electric dipoles start to oscillate mainly due to its oscillatory electric field given as

$$\boldsymbol{E} = E_x \boldsymbol{e_x} + E_y \boldsymbol{e_y} \tag{3.10}$$

Considering the dynamic component of M

$$\boldsymbol{M} = \boldsymbol{M_0} + \boldsymbol{m} \tag{3.11}$$

$$\boldsymbol{m} = m_x \boldsymbol{e_x} + m_y \boldsymbol{e_y} \tag{3.12}$$
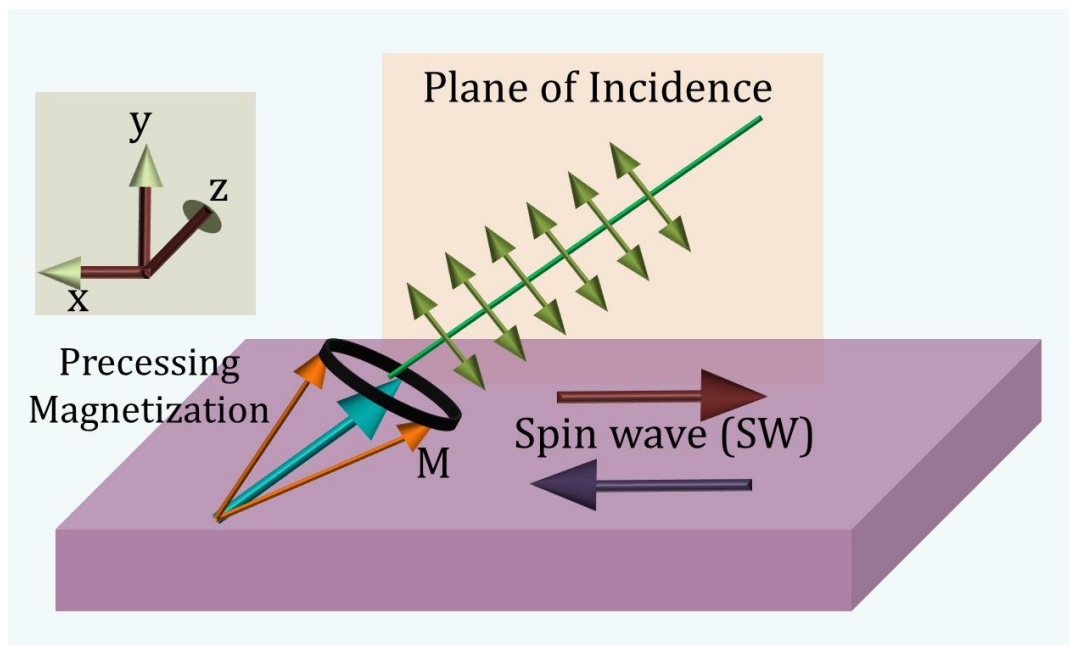
Figure 3.13: Schematic illustration of the interaction between p-polarized incident beam and precessing magnetization.

The oscillating component of **M** exerts a Lorentz force (proportional to **E** × **m**) on the electric dipoles which in this case causes polarization pointing along the *z*-direction. Consequently, the electric field of the radiated light wave is pointed along the *z* direction (i.e. *s*-polarized). A similar argument is applied with the light with *s*-polarization. Hence, the polarization of the incident light is perpendicular to that of light scattered by a magnon. This is different from the circumstance when light is scattered by acoustic phonons as here the polarizations of the incident and scattered lights lie along the same direction. Therefore, the scattered light by magnons can be separated from that scattered by phonons by choosing an appropriate orientation of the analyzing polarizer in the experiment. The schematic of the DE scattering geometry showing the incident light, scattered light, angle of incidence and the direction of spin wave vector is presented in Fig. 3.14.
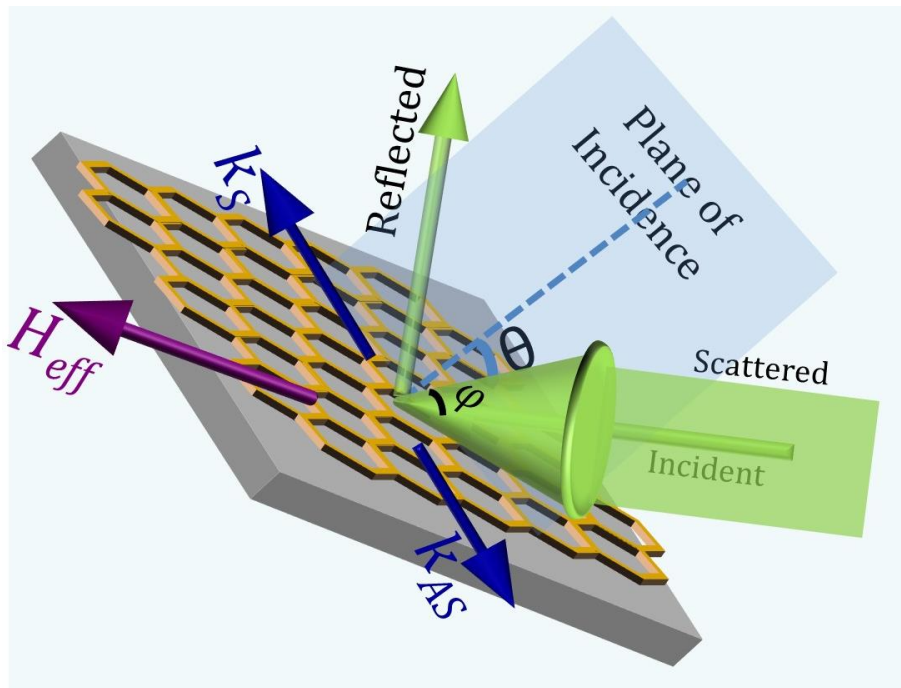
Figure 3.14: The typical DE scattering geometry showing the incident, reflected and scattered beams, the direction of magnon wave vectors for Stokes and anti-Stokes processes in BLS experiment.

3.4.2. Experimental Setup

BLS measurement is generally performed in two different geometries: (i) forward scattering geometry, where the scattered light is collected after transmission of the

probing beam through a transparent sample, and (ii) back scattering geometry, where the beam that is backscattered from the surface of opaque sample is analyzed. Further extension of the backscattered geometry is utilized to perform BLS microscopy (micro-BLS), where the profile of SW can be mapped in a space-, time-and phase-resolved manner. Below, the discussion of the conventional and micro-BLS will be elaborated:

The schematic of the BLS set-up is shown in Fig. 3.15. The experimental assembly of BLS consists of many important components such as continuous single mode solid state laser, beam splitter (BS), half wave plate (HWP), polarizing beam splitter (PBS), mirrors (M), achromatic doublet (Ach), polarizer (P), focusing lens (L), pin hole (Ph), light diffuser, shutter (S), tandem Fabry-Pérot interferometer (TFPI) together with single photon detector (D), a computer equipped with multi-channel analyzer software (GHOST or TFPDAS4.2) and electromagnet.

A laser beam of power 235 mW and wavelength 532 nm emitted from a diode pumped solid state laser is used. After that, the laser beam is split into two parts (1:9) using a beam splitter (BS). The smaller part (10%; act as a reference beam) goes towards the TFPI using mirrors. The reference beam serves the following purpose: it helps (i) to stabilize the mirror spacing of the FP etalons; (ii) to form the central elastic peak in a BLS spectrum in order to measure the frequency shift of the scattered beam w.r.t incident one; and (iii) to estimate the transmission order of the (FP) etalon which is required to deduce the frequencies of SW present in scattered beam. The other part (90%) of the beam is first sent through HWP and PBS, in order to eliminate the small in-plane polarized component from the partially polarized beam of the laser. The beam perpendicularly polarized to the optical table is then guided by the mirrors M3, M4, M5, M6 and Pr towards the sample which is lying between the poles of the electromagnet. The mirror Pr is taken as a tiny prism mirror in order to minimize the blocking of the backscattered beam by itself. Finally, the beam is focused onto the sample using an achromatic doublet (Ach) lens.
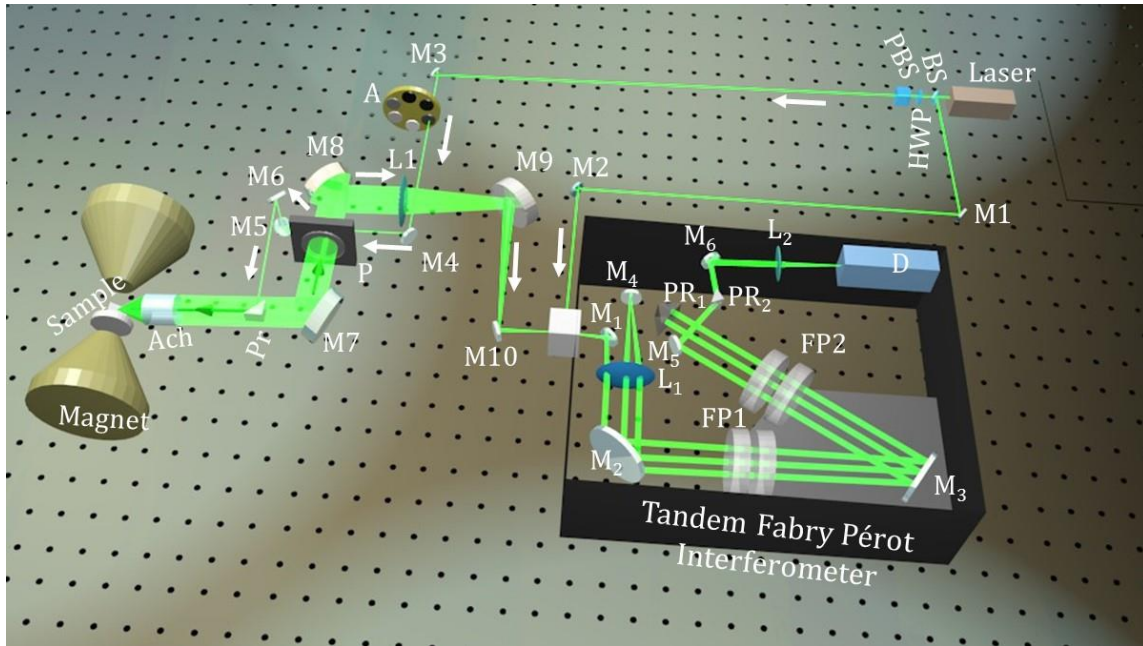
Figure 3.15: Schematic of conventional Brillouin light scattering (BLS) spectrometer.

The sample is mounted on a rotation stage which can be rotated in the vertical plane for the changes in the angle of incidence, thereby addressing different transferred SW wave vector according to Eq. (3.7). A magnetic field is applied perpendicular to the transferred wave vector direction, i.e. in the DE geometry. The measurements are performed for various magnetic field values at different wave vectors of transferred SW. Subsequently, the scattered beam is collected by the same lens and progresses towards the entrance pinhole of a JRS Scientific Instrument (3+3)-pass tandem FPI for frequency analysis using the focusing lens L1. In order to select the light scattered from SWs, a crossed polarizer P is inserted in the path of the scattered light which suppresses the elastically scattered beam as well as the beam containing the signal from phonons. Inside the TFPI, the beam hits mirror M_1 and then reaches FP1 via lens L_1 and mirror M_2. After passing through FP1, the beam undergoes its first pass (beam 1) until it is reflected from M_3 (beam 2) and passes through FP2. Then the beam is reflected from PR_1 and traces back its path via FP2 (beam 3) and FP1 (beam 4) and reaches M_4. The beam is once again reflected at M_4, and thus it gets redirected, passes through FP1 and FP2 for the third time (beam 5 and beam 6 respectively) to finally arrive at the single-photon counter (D). The reason for the multi-pass arrangement is to increase the contrast of the inelastically scattered light. Finally, the beam enters into the detector which is single photon counter and the data is stored in the computer for further analysis.

3.4.3. Instrumentation

Here, we will present some details of the important components that constitute the conventional BLS system.

3.4.3.1. Solid State Laser

A laser with single mode having narrow bandwidth is desirable for the increased precision and accuracy of the frequencies measured. To meet this expectation, we have worked with a 300 mW Excelsior solid state continuous wave (CW) laser source (power $\approx$ 235 mW). The laser system consists of the laser head, separate controller unit, which routes the electrical power and monitors the signal between the laser head and the master system. Here a diode laser is used to pump the Nd^{3+} ions doped in the crystal of yttrium vanadate (Nd: YVO_4), which emits photons at 1064 nm wavelength. This infrared output is further converted to visible light by sending it through a nonlinear crystal of lithium triborate (LBO) for frequency doubling (wavelength 532 nm). The emitted laser beam has a diameter of about 670 µm with a beam divergence of about 1.03 mrad. Overall, the laser system is steady and reliable at room temperature in terms of output power and beam pointing.

3.4.3.2. Tandem Fabry-Pérot Interferometer

Both the frequency of SW as compared to the typical excitation frequency of laser and the cross section of the inelastic scattering of photons are quite low. Therefore, the demand for higher spectral resolution and contrast is very much required for the proper functioning of the BLS. In that context, 3+3 pass TFPI is proved to be an ideal choice to overcome these challenges in the BLS set up. The TFPI consists of two single FPI connected in series and the light passes each FPI three times, as can be seen in Fig. 3.16. Before going into the details of TFPI, first we address briefly the transmission characteristics of a single FPI and subsequently the realization and the operations of the tandem mode will be illustrated.
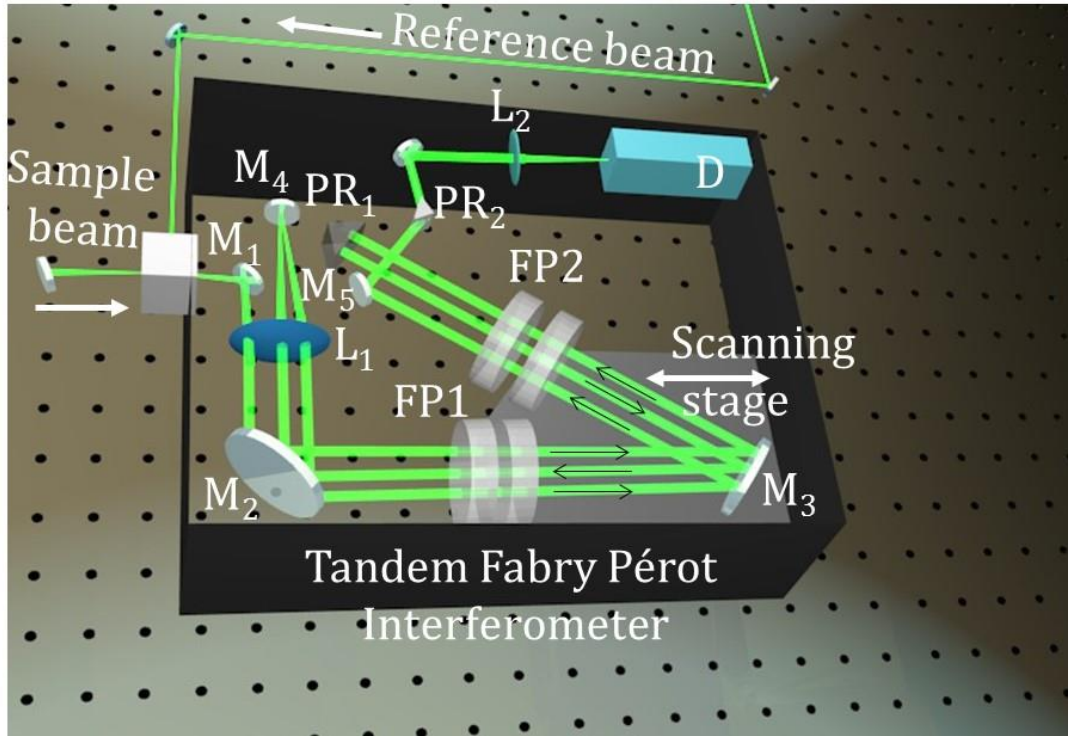
Figure 3.16: Schematic of the tandem Fabry-Pérot interferometer (TFPI).

3.4.3.3. FPI

An FPI consists of a pair of planar and partially reflecting mirrors which are mounted parallel to each other at a distance (L) [27]. The light entering the FPI, undergoes multiple back and forth reflections and transmissions. The transmitted beams interfere with each other and results in the condition for constructive interference under normal incidence given by:

$$L = \frac{n\lambda_0}{2}$$

(3.13)

where n = 1, 2, 3, 4, … refers to the transmission order and λ is the wavelength of the light. The free spectral range (FSR) (difference between the frequencies of the consecutive orders) can be written as:

$$\varDelta f = \frac{c}{2L} = \frac{150}{L} \text{ GHz/mm}$$

(3.14)

Here c denotes the velocity of light. The Finesse of the cavity is related to FSR, as given by:

$$F = \frac{\varDelta f_{FSR}}{\varDelta f_{FWHM}}$$

(3.15)

where Δf_{FWHM} is the full width half maximum of the transmission curve. The Finesse F affects the transmitted intensity I_t off the FPI via:

$$I_t = \frac{I_0}{1 + \left(\frac{4F^2}{\pi^2}\right)sin^2\left(\frac{2\pi L}{\lambda_0}\right)}$$

(3.16)

where I_0 represents the intensity of the incident light. The above intensity expression is known as the Airy function, which relates the periodicity of transmitted intensity with mirror spacing and frequency. The finesse (F) is a quantitative parameter which measures the instrument quality. The relationship between F and reflectivity R of the Fabry-Pérot etalons is given by:

$$F = \frac{\pi\sqrt{R}}{(1-R)}$$

(3.17)

Therefore, a higher reflectivity enhances the finesse and as obtained from Eq. (3.15), increases the frequency resolution as f_{FWHM} decreases. On the other hand, for fixed R, an increase in L reduces the FSR, which improves the frequency resolution as the Finesse remains constant. The contrast of an FPI is given as

$$C = 1 + \frac{4R}{(1-R)^2}$$

(3.18)

The contrast for an n-pass interferometer is the nth power of that of a single-pass one.

3.4.3.4. Tandem Operation

As we can see that the transmitted intensity as a function of the mirror spacing is periodic in nature which can become a major concern for FPI. For instance, if we consider a fixed mirror spacing L and the presence of two wavelengths say λ_1 and λ_2 then

$$2L = m_1\lambda_1 = m_2\lambda_2$$

(3.19)

Thus, the transmission condition is being satisfied for both λ_1 and λ_2 but with different orders. As the reference beam determines the order of transmission spectrum, the order of the second wavelength (which does not match with that of the reference beam) and consequently, the wavelength itself remains inaccessible. Further, it is quite challenging to identify unambiguously whether a peak signal belongs to the Stokes side of a specific transmission order or it belongs to the anti-Stokes side of the previous order. To overcome these hurdles, tandem operation of FPI has been suggested where the light passes consecutively through two interferometers (FP1 and FP2) which are mounted at an angle (α) to each other as shown in Fig. 3.16. The right mirror of each FPI is placed on the common translation stage and the other one on a separate angular orientation device. The scanning stage can move the right mirror of each pair along the optical axis of FP1. A

displacement (d) of the translation stage introduces a change of the mirror distance in FP1 by $\Delta L_1 = d$, while the change for FP2 is given as:

$$\Delta L_2 = \Delta L_1 \cos(\alpha) \tag{3.20}$$

and the synchronization condition is given by:

$$\frac{\delta L_1}{\delta L_2} = \frac{\Delta L_1}{\Delta L_2} \tag{3.21}$$
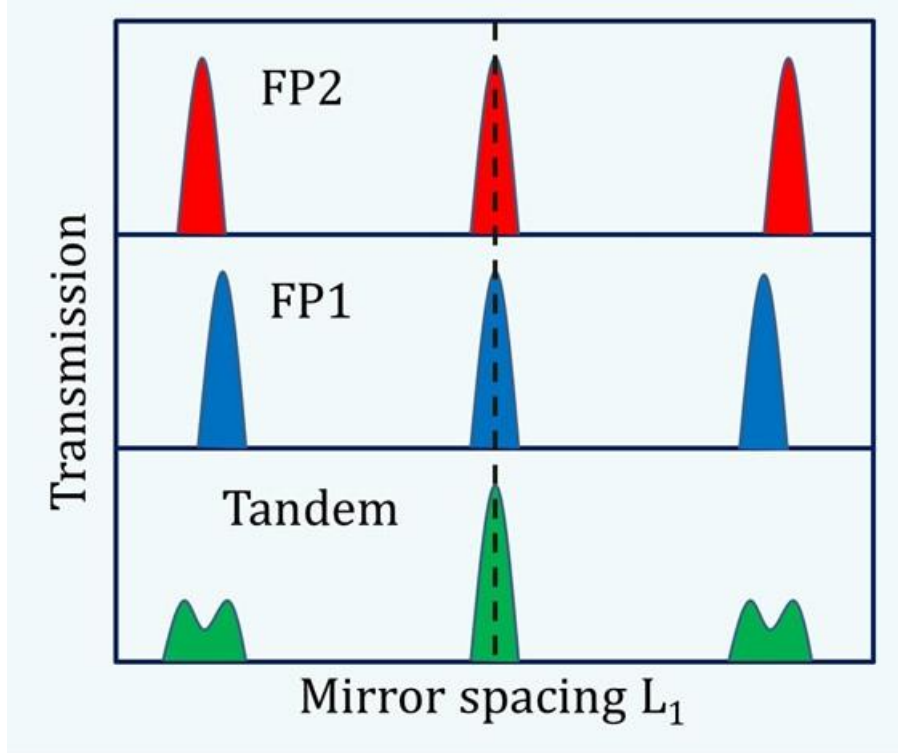
Figure 3.17: Transmission characteristics of FP1 and FP2 and in tandem operation.

Now, the intermixing of different orders can be suppressed. To achieve this, each FPI is adjusted to transmission separately before the scanning of linear stage. Although their transmission orders are different, but they together provide a central transmission order, which can be adjusted by changing the mirror spacing of FP2 (See Fig. 3.17). At the same time, the other orders are suppressed because of the different FSR for both FPIs. This arrangement also increases the FSR of the final spectrum, without affecting the resolution. Now, the change in the mirror spacing after the movement of stage for both FP1 and FP2 can be written as:

$$l_1 = L_{10} + d \tag{3.22}$$
$$l_2 = (L_{10} + d) \cos \alpha \tag{3.23}$$

where L_{10} is the initial mirror spacing of FP1 (at $d = 0$). This removes the previously mentioned ambiguities since the transmission order is now fixed. As mentioned earlier,

the light additionally passes through each FPI three times to enhance the contrast. Finally, after the six passes (3+3) through the FPIs, the light is directed to a photomultiplier, which counts the number of transmitted photons as a function of the mirror-spacing, which is relatable to the frequency shift. The sweeping of the distance through scanning stage relates to the desired frequency window. In order to get adequate statistics, the data is generally recorded for longer duration. As a result, the acquired BLS intensity is directly proportional to the SW intensity at a given frequency. The steps for rigorous alignment inside the TFP have been elaborated in its manual [28].

3.4.4. BLS Microscopy

3.4.4.1. Micro-focused Brillouin Light Scattering

In this section, a full description of the micro-BLS setup will be presented. As we know, the conventional BLS is limited by its spot size (≈50 µm) and functions properly for continuous thin films as well as array of patterned microstructures. However, for the single magnetic elements, micro-BLS has to be used because of its high spatial resolution. Micro-BLS, developed significantly in the past decades, can be thought of as an extension of conventional BLS [29-30]. In our micro-BLS set up, the laser is focused down to a small spot size of about 250 nm on the sample, which allows for a spatial sensitivity, however at the cost of wave vector resolution because of the Heisenberg's uncertainty principle, which states that simultaneous access to position and wave vector with arbitrary high precision is not possible. The required components which are needed to transform the conventional BLS to a micro-BLS include a microscope objective (MO), a complementary -metal-oxide semiconductor (CMOS) camera, a set of high precision three-dimensional translation stages and a number of steering optics. The schematic of the micro-BLS set up is shown in Fig. 3.18.
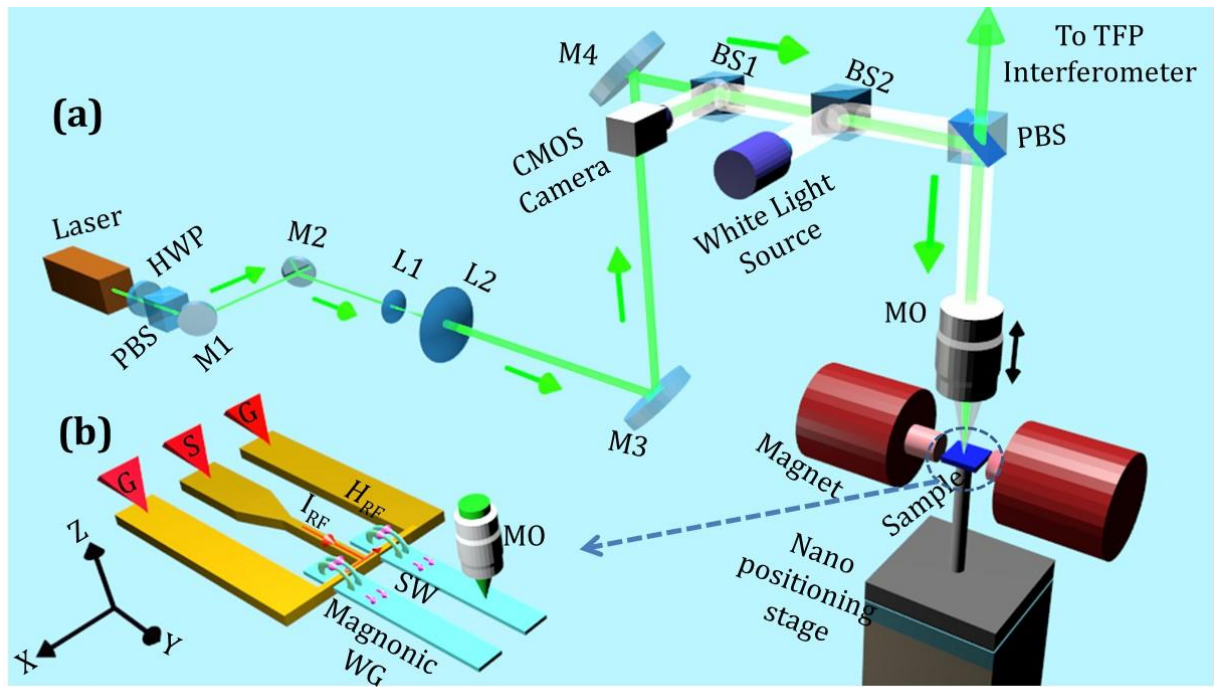
Figure 3.18: (a) Schematic of the microfocused Brillouin light scattering setup. (b) Schematic illustration of the RF excitation through ground-signal-ground (GSG) type antenna.

The MO used in the experiment is from Leica ((model number: HC PL FLUOTAR L) and has a specification such as Magnification: ×100; Numerical Aperture (NA): 0.75; and long working distance: 3.7 mm. It is important to mention here that in micro-BLS, back scattering geometry is used with no provision of changing the angle of incidence. The maximum angle of incidence is decided by the numerical aperture $NA = n\,sin\theta$, where n is the refractive index of the medium (1 for air) and θ is the angle of incidence. In case of NA = 0.75, the value of maximum angle of incidence comes out to 48.6°. Hence, the collected scattered light will correspond to a range of transferred k-vectors to 0 to 17.7 rad/μm. The scattered beam is collected using the same objective lens by which it was focused onto the sample and sent to the TFPI guided by the mirrors for frequency analysis. The CMOS camera from Thorlabs ((Point Grey: Flea3 FL3-U3-13Y3M)) serves the following purpose: (i) it locates the laser spot on to the sample and (ii) it allows for the stabilization of the sample position with respect to the thermal drift. During the measurement, the laser spot needs to be filtered out with a notch filter to avoid the saturation of entire image.

72

To perform a well-defined spatial scan, and for thermal stabilization, a very high precision translation stages (x-y-z) is used. The two-dimensional lateral stages (model number XMS50) and vertical focusing stage (model number: GTS30V) from Newport were used. The spatial resolution of lateral and vertical stages are 50 nm and 1 nm, respectively. These high spatial resolution for stages enables to correct the thermal drift as well as to conduct fine spatial scans. In order to excite SW externally using microwave frequency, a nonmagnetic customized picoprobe (Model No. 40A- GSG-200-GR) from GGB industries is used. The sample is mounted on a holder attached with the stage. By moving the sample position thereby changing the position of the laser onto the sample, the spatially dependent amplitude of the scattered light is measured for a particular excited frequency. To enhance the signal to noise ratio, the density of measured magnons is increased by electrical excitation with an RF frequency sent through a coplanar waveguide (CPW) as schematically shown in Fig. 3.18 (b). The launching of the picoprobe, the stabilization scheme and data acquisition is presented in Figs. 3.19, 3.20 and 3.21, respectively.
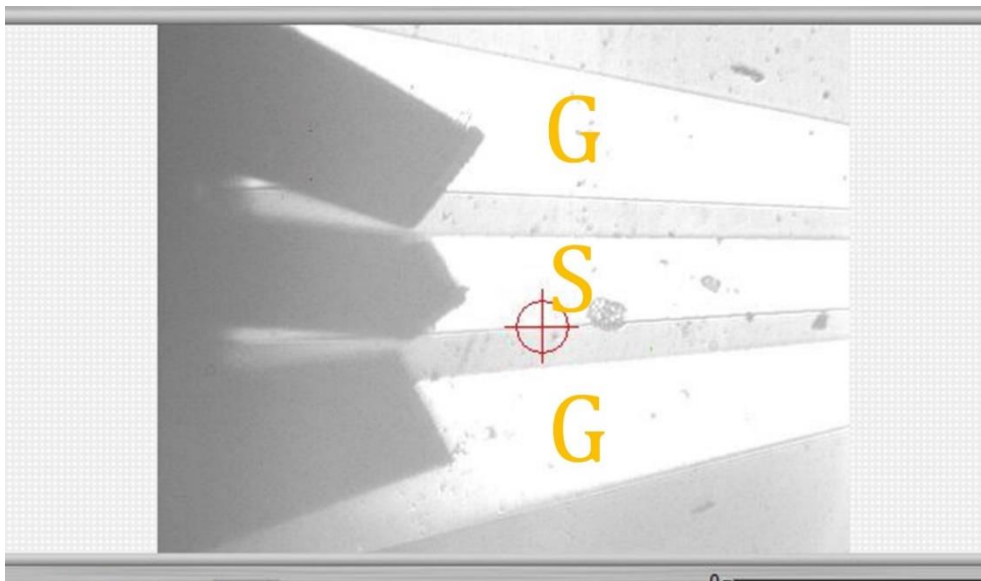
Figure 3.19: Image of the GSG picoprobe during launching on the Au antenna.
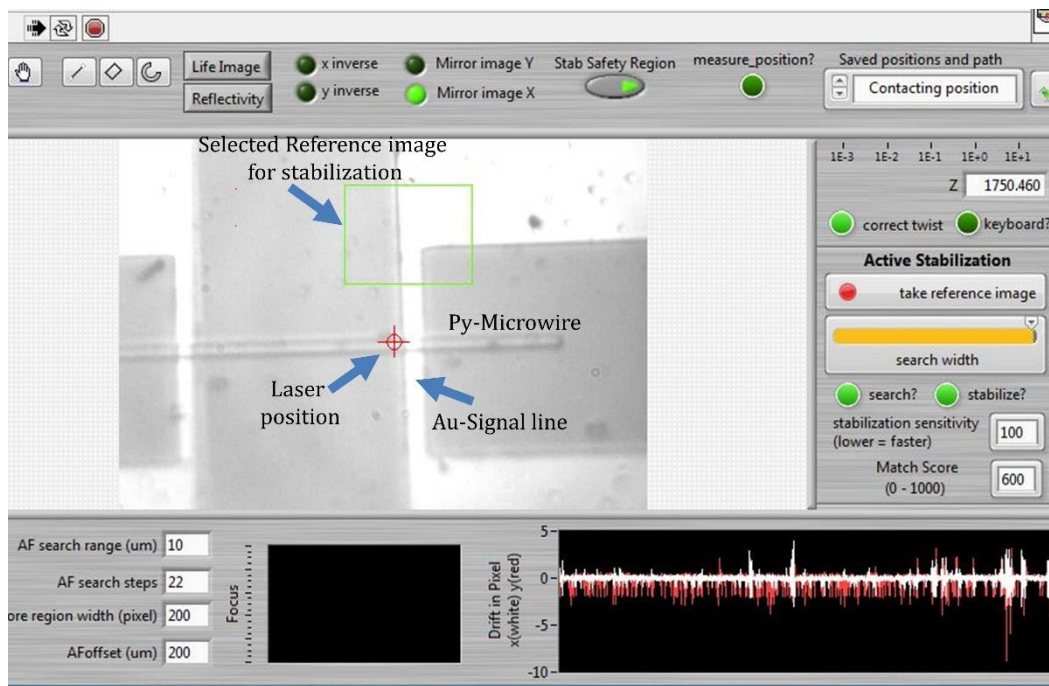
Figure 3.20: Screenshot of the micro-BLS software (TFPDAS4.2) after setting up the stabilization protocol.
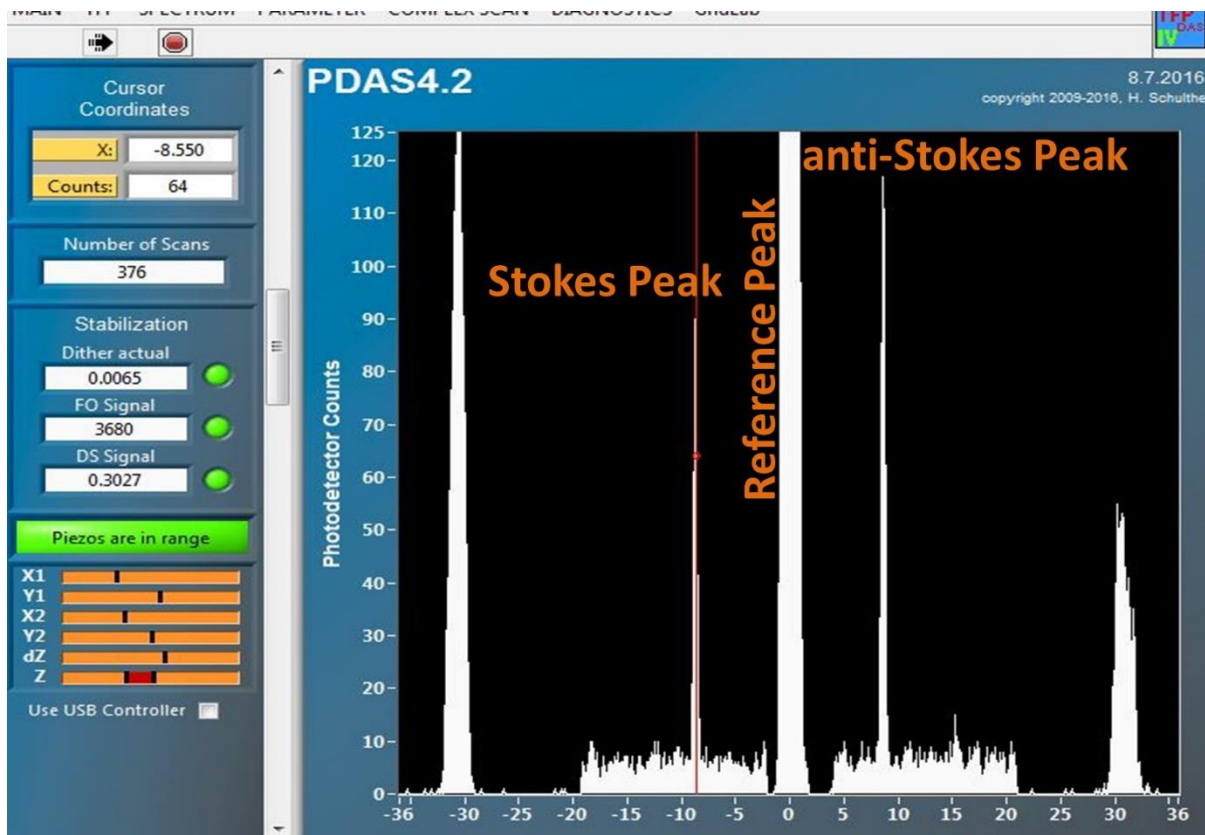
Figure 3.21: The screenshot of TFPDAS4.2 software window during the data acquisition.

3.4.4.1.1. Procedures to Perform Complex Scan

To perform the BLS microscopy, complex scan protocol helps to define the proper imaging of the propagating SWs. There are few standard steps that need to be followed as listed below:

Step I. Call Complex Scan Initialization Window

Under the 'Complex Scan' in the TFPDAS4.2 software, three separate tabs for defining three different dimensions (i.e. x, y, magnetic field) are present. It is important to mention here that if one wants to perform a measurement in which only one dimension is scanned, then only the parameters for dimension 1 needs to be defined. Dimension 1 has to be defined first for every complex scan. The same is applied if one wants to scan two dimensions: all the parameters need to be set for dimensions 1 and 2, and dimension 3 remains empty.

Step II. Configure Transmission Control (TCP) Interface.vi

After calling TCP interface.vi (labview program), dimension 1 can be illustrated by giving its name (say position x) and path of the corresponding labview program. Similar thing should be specified for other dimensions also. When all of the names and paths are entered, hit the start TCP protocol button. This will pop up a new window, the Initialize TCP Connection window.

Step III. To Initialize TCP

This procedure is done to set up the communication between server and client. In order to use local area network (LAN), the IP address of the computer in which TFPDAS4.2 software is installed should be known. Since scanning is done for more than 1 dimension, several TCP connections can be made by assigning different port numbers on the same LAN. The server will listen at a distinct single port number for incoming connection requests. Therefore, it allows for the initialization of a TCP connection these port numbers specified at the server and the client should be the same for a particular dimension. Consequently, 'Initialization of TCP Connection' window on the client as well as the 'Complex Scan window' of TFPDAS4.2 on the server should be done. One has to be careful that the port numbers must be different for each dimension. Since all three transmission control protocols connect to the same server, the communication has to run on three different ports to avoid crosstalk between them.

IV. Define Region of Interest (ROI)

Here, the scan points for each dimension are defined. It is good to have the full information of the scanned dimension such as its name, units and number of points etc. for future data evaluation. Then comes to a region of interest which defines a scan range for a specific scan dimension, i.e., the range over which the parameter associated with some external laboratory equipment (position, field etc.) is changed. Setting the 'Region of Interest' is quite straightforward: type in the first and last value of the scan array and define the number of steps that should be used to cover this region. After this, scan array is created which can be seen on the configuration window.

Step V: Define Post Point Actions

The 'Post-Point Actions' are required for sending the instruction that what should be done after each single scan point for the corresponding dimension. This action depends on whether the program controlling your additional equipment, e.g., the positioning stage and the magnet, can give feedback on the current status of the device. This feedback must be given in the form of a Boolean output. If the Boolean output is false, i.e., the device is still busy setting the next scan point, the TCP interface on the client will stop the automated scan and send a break command back to TFPDAS4.2. If the output is true, i.e., the next scan point has been reached, a continue command is sent and the automated measurement will continue.

Step-6: Define Post Loop Action

In this last step, one can specify how many times the entire dimension should be scanned. Depending upon the measurement protocol, one needs to just increase the number of repetitions of the complex scan configuration window and the corresponding dimension will be scanned as often as you want.

Step VII. Confirm Settings

When all the steps as mentioned above are completed. One can then hit the APPLY SETTING button in the *Initialize TCP Connection* window on the client. A small *TCP Listen* window will pop up showing the status of the TCP connection. During a running complex scan, the received data values will tell which double values are sent from the server, i.e., TFPDAS4.2, to the client, i.e., the programs controlling the corresponding scan dimensions. From the point of view of the client, the TCP is now ready to start an automated measurement.

Step VIII. Start Measurement

While starting a complex measurement, a small dialogue window will pop up. We need to use the 'Select Folder' button in order to choose a folder in which this complex scan shall be stored under the name that has been typed in. We confirm this directory with the 'OK' button. If a running complex scan is needed to abort, one needs to select the 'TFPDAS4.2 Main Window' and press 'ESC'. This will pop up a window asking to confirm that we really want to kill the current Complex Scan. The 'Kill Scan' button will abort the actual 'Complex Scan' and bring the interferometer back to the transmission mode. Then we can exit the 'Complex Scan Execute' window under 'MAIN > Exit'. After these, one can proceed for the automated scanning measurement.

3.4.4.2. Phase-resolved BLS

Analysis of SW phase leads to the accurate assignment of the wave vectors which was hindered in the space-resolved micro-BLS experiment because of the Heisenberg uncertainty principle [31-33]. In fact, investigation of the propagating SW phase has basically equivalent to the wavelength (wave vector) measurement of SWs. The information about the SW phase is realized via the interference of the scattered beam with a temporally coherent reference beam that is generated using an electro-optical modulator (EOM). Change in the probing spatial location across the sample leads to the recording of the propagating SW phases. The intensity of the corresponding interference signal can be expressed as

$$I_{inter} = E_s^2 + 2E_s E_R cos(\Delta\phi_0 + k.r) + E_R^2 \tag{3.24}$$

Here, E_R and E_S represents the electric fields corresponding to the reference beam and the sample respectively, $\Delta\phi_0$ is the initial phase difference between the reference and sample beam. The argument of the cosine function refers to the corresponding phase difference.

3.4.4.3. Time-resolved BLS

The propagation and relaxation characteristics of SW modes in time domain can also be studied using BLS technique. [34-36]. The methodology is to excite the SW externally at a time t_0 and then measure the temporal evolution of the SW intensity as it propagates through the sample. The excitation of SW is done using a train of microwave pulses. The leading edge of the pulse defines the starting time t_0 and the data is recorded at different

time t_i *w.r.t.* t_0. The counts for subsequent pulses are summed up thereby rendering a matrix formed by the intensity of total gathered photons and the corresponding time t_i. Moreover, the two-dimensional intensity map of a SW pulse excited at a fixed frequency for different delays, which manifests the spatial and temporal advancement of the corresponding SW packet, can be obtained.

References

[1] *Sputtering by Particle Bombardment*, Springer, (2007).

[2] *Electron Beam Evaporation, Vacuum Deposition onto Webs, Films and Foils* (Second Edition), Elsevier (2011).

[3] G. R. Sune, *Electron beam lithography for nanofabrication*, PhD thesis, Universitat Autònoma de Barcelona (2008).

[4] K. Kim, Y. Zhao, H. Jang, *et al.* Nature **457**, 706 (2009).

[5] https://www.graphenea.com/

[6] D. Mcmullan, *Scanning Electron Microscopy* 1928–1965, Scanning. **17**, 175 (1995).

[7] R. Van Grieken, A. Markowicz, *Handbook of X-Ray Spectrometry, Second Edition (Taylor & Francis*, 2001).

[8] H. P. Klug and L. E. Alexander, *X-Ray Diffraction Procedures: For Polycrystalline and Amorphous Materials* (Wiley, 1974).

[9] E. Meyer, Prog. Surf. Sci. **41**, 3 (1992).

[10] J. A. Sidles, J. L. Garbini, K. J. Bruland, *et al.*, Rev. Mod. Phys. **67**, 249 (1995).

[11] S. Foner, Rev. Sci. Instrum. **30**, 548 (1959).

[12] P. Masina, T. Moyo, and H. M. I. Abdallah, J. Magn. Magn. Mater. **381**, 41 (2015).

[13] A. Barman and A. Haldar, *Time-domain study of magnetization dynamics in magnetic thin films and micro-and nanostructures,* Solid State Phys, vol **65**. (Elsevier Inc., Burlington, 2014).

[14]. A. Barman and J. Sinha, *Spin Dynamics and Damping in Ferromagnetic Thin Films and Nanostructures* (Springer Publishing AG, Switzerland, 2017).

[15] D. A. Long, *Raman Spectroscopy* (McGraw-Hill, 1977).

[16] P. H. Gammon, H. Kiefte, and M. J. Clouter, J. Phys. Chem. **87**, 4025 (1983).

[17] F. Li, Q. Cui, Z. He*, et al.*, J. Chem. Phys. **123**, 17 (2005).

[18] E. Courtens, J. Pelous, J. Phalippou*, et al.*, Phys. Rev. Lett. **58**, 128 (1987).

[19] S. Reiss, G. Burau, O. Stachs, *et al.*, Bio. Opt. Exp. **2**, 2144 (2011).

[20] L. Brillouin, Ann. Phys. **17**, 88 (1922).

[21] L. I. Mandelstam, Zh. Russ. Fiz-Khim. Ova. **58**, 381 (1926).

[22] E. Gross, Nature **126**, 201 (1930).

[23] J. R. Sandercock, Flammarion, Paris, (1971).

[24] R. Mock, B. Hillebrands, and J. R. Sandercock, J. Phys. E. **20**, 656 (1987).

[25] W. Wettling, R. S. Smith, W. Jantz, *et al.*, J. Magn. Magn. Mater. **28**, 299 (1982).

[26] J. R. Sandercock and W. Wettling, IEEE Trans. Magn. **14**, 442 (1978).

[27] J. R. Sandercock, *Operator Manual for the Tandem Fabry-Pérot Interferometer*, (1999).

[28] J. R. Sandercook, Operator manual of Tandem Fabry-Pérot Interferometer TFP-1, (2010).

[29] V. E. Demidov, S. O. Demokritov, B. Hillebrands*, et al.*, Appl. Phys. Lett. **85**, 2866 (2004).

[30] G. Gubbiotti, G. Carlotti, M. Madami*, et al.*, J. Appl. Phys. **105**, 07D521 (2009).

[31] A. A. Serga, T. Schneider, B. Hillebrands*, et al.*, Appl. Phys. Lett. **89**, 063506 (2006).

[32] F. Fohr, A. A. Serga, T. Schneider*, et al.*, Rev. Sci. Instrum. **80**, 043903 (2009).

[33] K. Vogt, H. Schultheiss, S. J. Hermsdoerfer*, et al.*, Appl. Phys. Lett. **95**, 182508 (2009).

[34] M. Bauer, O. Büttner, S. O. Demokritov*, et al.*, Phys. Rev. Lett. **81**, 3769 (1998).

[35] H. Schultheiss, C. W. Sandweg, B. Obry, *et al.*, J. Phys. D: Appl. Phys. **41**, 164017 (2008).

[36] A. Serga, S. Demokritov, B. Hillebrands, *et al.*, Phys. Rev. Lett. **92**, 117203 (2004).

Chapter 4

4. Numerical Methods

4.1. Introduction

For continuous magnetic medium, there are theories based on macroscopic modelling which consider the magnetization to be uniform throughout the medium. The magnetization dynamics is studied by solving nonlinear ordinary differential equation of Landau Lifshitz Gilbert (LLG) equation by linearizing it under the small precession angle approximation. The study of magnetization dynamics for confined structures is a bit nontrivial because of the demagnetizing field arising from the unsaturated magnetic dipoles at the finite boundaries. The geometry dependent complexity often hinders the reproduction of ideal characteristic features of the studied system. It becomes more evident in case of samples having nonellipsoidal geometries leading towards nontrivial analytical solutions. On the other hand, experiments generally suffer from various limitations because of the facilities available related to the fabrication and characterization tools. Consequently, theory faces stern challenges to reproduce (or predict) the real situation due to the lack of appropriate approximations and boundary conditions used for nanoscale magnetic systems having both short- and long-range interactions. Hence, to explain the experimental findings and for future proposals for novel research avenue, the development of numerical and analytical micromagnetic modelling is undoubtedly necessary.

4.2. Micromagnetic Simulation

The basic philosophy of micromagnetic simulation [1] is to discretize the sample into a number of cells, each of which consists of a macrospin that experiences short-range exchange and long-range dipolar interactions as well as the effect of other existing fields depending upon the system. In the following, some of the tools related to the micromagnetic simulation (i.e. OOMMF [2], LLG Simulator [3], mumax^3 [4] etc.) used in the present thesis will be briefly described.

4.2.1. Various LLG Solvers and Evolvers

When the analytical methods seem to fail in solving the differential equations related to the complex geometries and problems, then the numerical methods with the help of discretization formalism by approximating differential equation are used. There are mainly two widely used approaches to solve LLG equation numerically: finite difference method (FDM) and finite element method (FEM) [5,6]. These techniques utilize the continuum theory to estimate the magnetic features of several nanometers length scale in terms of the local ordering of magnetic moments.

In case of FDM, the whole system space is discretized into a number of regular cuboidal cells (N). Thus, the continuous solution domain is replaced by a discrete set of lattice points and the domain boundaries are replaced by their discrete counterparts. Subsequently, each cell is designated with a magnetization vector and their relative interactions are taken into account by means of the minimization of total energy. Although, FDM features a faster computation as compared to FEM, it is not applicable for complicated geometry like curved boundary or irregular microstructures. A few examples of FDM simulators are Object Oriented Micromagnetic Frameworks (OOMMF), LLG Micromagnetic Simulator, MicroMagus, mumax[3] etc.

4.2.1.1. OOMMF

OOMMF is a public domain micromagnetic simulation program developed at the National Institute of Standards and Technology (NIST) by M. J. Donahue and D. G. Porter [2]. The code is written in C++ and Tcl/Tk language. It is compatible with a wide range of platform namely Unix and Windows. Here, an ODE solver is implemented to relax 3D spins on a 2D mesh of square cells and uses fast Fourier transform (FFT) to compute the self-magnetostatic field. The LLG equation is solved in space and time at temperature $T = 0$ K. The input parameters (such as bulk saturation magnetization (M_s), exchange stiffness constant (A), magneto-crystalline anisotropy (K), Zeeman field (H), sample structure, dimensions and the magnetic field geometry) and the initial conditions of any problem are given using an external script file. There is a provision to insert the sample structure as an image file to the software enabling to incorporate any structural artifacts to be taken into consideration. The sample space is divided into identical cuboidal cells with dimensions equal to or less than the exchange length. Each cell is then assigned with a single spin. Subsequently, the LLG equation is solved assuming the magnetization to be a

continuous function of position and deriving relevant expressions for different energy terms. Then, the stable equilibrium state is achieved by minimizing the total Gibbs free energy with respect to the magnetization.

The simulation methodology is adopted in such a way that the system is brought to equilibrium under the effect of a static bias magnetic field. For that, large enough bias field is initially applied to fully magnetize the sample and allow the magnetization to relax for a long time. The applied field is then reduced to the desired bias field value where the dynamics will be simulated. Subsequently, magnetization is again allowed to relax for a long enough time so that the magnetic torque on the system becomes much smaller than a critical value. During each step, the magnetization configuration is updated by two types of evolvers: first one is a time evolver which captures the LLG dynamics and the second one is an energy minimization evolver which calculates the local minima in energy by using energy minimization techniques. A fourth order Runge Kutta evolver is used as a time evolver which solves LLG equation considering an ordinary differential equation in time. The evolvers are connected to corresponding drivers, namely, time driver and energy minimization driver, which control the time and minimization evolver, respectively. The driver controls the completion of a simulation stage depending upon the stopping criteria described in the input script file. The stopping criterion is determined by the convergence of the maximum torque $\boldsymbol{m} \times \boldsymbol{H}$, where $\boldsymbol{m} = \boldsymbol{M}/M_S$. In the script file, users provide either the stopping time or the stopping value of $d\boldsymbol{m}/dt$, which is set in such a way that the value of the maximum torque ($\boldsymbol{m} \times \boldsymbol{H}$) should be less than 10^{-6} A/m. The simulation will terminate as soon as the stopping criteria matches. After the system acquires a stable, static equilibrium state under the bias magnetic field, the magnetization dynamics is triggered under a uniform excitation (spatially and temporally varying 'sinc' function) applied perpendicular to the sample plane in order to simulate the experimental (BLS) results. The time evolution of the different components of dynamic magnetization averaged over the entire sample volume are then recorded for a total timescale of several ns at intervals of few ps. A small value for damping parameter (say 0.008 for $Ni_{80}Fe_{20}$) was assumed during the dynamic simulation. The time dependent components of magnetization, magnetic field and energies can be extracted in the output file with '.omf', '.ohf' or '.ovf' formats respectively. Also, OOMMF offers the user to set a periodic boundary condition (PBC) in different dimensions for simulating the real signature of systems with finite and smaller sample geometry.

4.2.1.2. LLG Simulator

Designed and licensed by M. R. Scheinfein, LLG Micromagnetic Simulator [3] is also an important tool for the simulation of magnetization dynamics which is again based on FDM method-based evolver such as Euler, Rotation Matrices, Predictor-Corrector, Gauss-Seidel stable method. Some of the key points regarding this simulator are the following:

- The space and time evolution of magnetization can be investigated as a function of temperature as opposed to OOMMF where simulation is performed at T = 0 K.

- As mentioned earlier, LLG supports four integrators to solve ODE. The most primitive one is a Euler Cartesian method which is the fastest but least accurate. The Rotation Matrices method is the integrator of choice for solutions where damping is greater than 0.5. This is employed to study the magnetic ground state configurations in our systems. The Cartesian Predictor-Corrector integrator is the most accurate and also faster when damping is about 0.01. The Gauss-Seidel Stable method is a semi-implicit first-order integration scheme. The integration time steps can be much larger on fine grids using this method.

- The graphical visualization of the magnetic domains and magnetostatic field profiles in simulated FM systems is well represented in both 2D and 3D.

- Calculation of the magnetization parameters in magnetic multilayers is performed easily by manipulating the parameters for each layer.

- This simulator offers to calculate as well as visualize the domain wall dynamics in patterned or unpatterned magnetic heterostructures, while the spin-polarized current can also be injected in order to simulate the working condition of the magnetic spin valve or MTJ like nanostructures. It is also possible to calculate and visualize the effective magnetic field strength inside or outside of the sample considered in the simulation. Hence, it is possible to calculate the internal field and demagnetization field distributions in order to interpret the nature of the inter-element interaction or the magnetic profile inside the element itself.

In this thesis, the results are obtained using the 2.50 version of LLG simulator which works with a single processor.

4.2.1.3. mumax³

The mumax³ [4] is also an FDM-based tool for the micromagnetic simulation. It is an open source, GPU accelerated micromagnetic simulation program which requires high performance graphics card such as GTX series. The GPU-based micromagnetic simulation is generally faster as compared to the CPU-based simulation. The program is compatible with Linux, windows, mac etc. with the NVIDIA GPU. The design and verification of mumax³ code was first published in 2014 by A. Vansteenkiste *et al.* The scripting language Go and CUDA are used for writing this code. The simulation is performed in web-based user interface and the output is obtained in the form of 'ovf' data format similar to OOMMF.

In this simulator, sample can be described within a script in the form of its dimensions and geometry or can be supplied directly by image. Following the FDM method, it discretizes the objects into 2D or 3D grids of orthorhombic cells of equal size. Volumetric quantities like M, K etc. are defined at the middle of the cells, whereas coupling quantities are specified at the faces of the cells. Some of the material parameters and the external stimuli can be set as space and time dependent. Their magnitudes can be varied with an extra term of f(t)×g(x,y,z), *i.e.* time dependent function multiplied by continuously varying spatial profile. With the help of Boolean operation like AND, OR, XOR, etc, even complex geometries can be rotated and translated. The mumax³ provides several types of Runge-Kutta methods to solve the LLG equation with different convergence criteria and error estimation. Out of these, RK45, RK23 and RK12 give freedom to choose automatic time steps to keep error per step close to preset value. Importantly, mumax³ provides a 'relax' function that can find the energy minimum of the system. This function prevents the precession term in LLG equation to act upon the system and the effective field points only towards decreasing energy. However, the system may often reach a saddle point of the energy landscape. The evolver RK23 is more efficient to set a ground state while using the relaxation condition. The mumax³ can determine the evolution of the reduced magnetization m(r,t) which has unit of length. A lot of research problems based on magnetic anisotropy, complex interactions (such as, Heisenberg exchange interaction, DM interaction etc.), temperature dependent variations and many more can be dealt with. To make the numerical experiments more realistic, a system with finite geometry can be repeated with the help of a PBC and simulation can be performed using macro-geometry approach. This is different from what is generally being used in OOMMF.

Also, for simulating hysteresis loops for confined structures, mumax[3] takes less much computation time as compared to OOMMF. In this thesis, the magnetic hysteresis loops have been simulated using mumax[3].

4.2.1.4. DotMag

In order to investigate the nature and origin of various SW modes numerically, spatial mapping of the power and phase profiles is needed. The spatial mapping provides a direct understanding of the relative spin precession amplitudes and phases of different SW modes and helps to visualize their spatial variation throughout the medium. The aforementioned tools do not calculate the SW mode profiles. Hence, our research group indigenously developed a code named DotMag [7] to investigate the SW mode profiles in a variety of confined structures. The output files of the simulations actually consist of a number of '.omf' files containing the information about the magnetization distribution (M (r, t)) over the entire simulation volume at a particular instance of simulation time. These files can be used to inspect the time as well as spatial distribution of the SW amplitude, phase and propagation. For that, former, the $M(r, t)$ is rearranged into three four-dimensional (4D) matrices, *viz.*, $m_i(x, y, z, t)$, $m_j(x, y, z, t)$ and $m_k(x, y, z, t)$, where each matrix corresponds to each component of magnetization. Subsequently, one spatial co-ordinate (say z) of one of the 4D matrices (say m_k) is fixed, which reduces the matrix dimension to three ($m_k(x, y, z_m, t)$). Then a discrete Fourier transform with respect to the time dimension t is performed for each elemental cell. Next, the power value of the FFT spectrum corresponding to the desired frequency is extracted and plotted for each cell. This gives the in-plane space dependent power profiles at a particular resonance frequency. Similarly, the phase profile can be plotted by extracting the phase of complex dynamic magnetization. The frequency resolution depends on the simulation time window and the spatial resolution depends on the discretization used during the micromagnetic simulations. The expressions for the power and phase profiles for a particular resonant mode at $f = f_r$ can then be written as:

$$P^{z_m, f_n}(x, y) = 20 log_{10} FFT[\widetilde{M}^{z_m}(f_n, x, y)]$$

$$\phi^{z_m, f_n}(x, y) = tan^{-1}\left(\frac{Im(\widetilde{M}^{z_m}(f_n, x, y))}{Re(\widetilde{M}^{z_m}(f_n, x, y))}\right)$$

where f_n is the frequency of a resonant mode. The power is presented usually in terms of decibel (dB) and the phase in radian. MATLAB is used to run and control this code, and

the output is obtained with the plot of space dependent power and phase at discrete frequencies. The frequency resolution necessarily depends upon the total simulation time and the spatial resolution of calculated power and phase maps depends upon the discretization of sample (or number of cells) during micromagnetic simulation.

References

[1] S.-K. Kim, J. Phys. D: Appl. Phys. **43**, 264004 (2010).

[2] M. Donahue and D. G. Porter, "*OOMMF User's guide, Version 1.0*, URL: http://math.nist.gov/oommf, (1999).

[3] LLG Micromagnetics Simulator, URL: http://llgmicro.home.mindspring.com (2018).

[4] A. Vansteenkiste, J. Leliaert, M. Dvornik*, et al.*, AIP Advances. **4**, 107133 (2014).

[5] B. Dieny, R. B. Goldfarb, and K.-J. Lee, *Introduction to Magnetic Random-Access Memory* (Wiley-IEEE Press, New York, 2016).

[6] T. Schrefl, J. Magn. Magn. Mater. **207**, 45 (1999).

[7] D. Kumar, O. Dmytriiev, S. Ponraj, *et al.,* J. Phys. D: Appl. Phys. **45**, 015001 (2012).

Chapter 5

5. Direct Observation of Interfacial Dzyaloshinskii-Moriya Interaction from Asymmetric Spin-wave Propagation in W/CoFeB/SiO₂ Heterostructures Down to Sub-nanometer CoFeB Thickness

5.1 Introduction

The Dzyaloshinskii-Moriya interaction (DMI) [1-2] has drawn significant interest due to its fundamental nature and application potential in next generation memory devices. The DMI can be classified into two classes, namely, bulk and interfacial, depending on the type of inversion symmetry breaking [3-4]. Bulk DMI is determined by the detailed symmetry of the lattice structure and it has been studied mostly for B20 structures such as MnSi, etc. [3,5]. Due to the complexity of the nature of symmetry at the interface, it is quite non-trivial to get insight into interfacial DMI.

In last few years remarkable progress on fundamental and technological front in the field of spintronics has been made by utilizing ferromagnetic thin film with structure inversion asymmetry. For applications in magnetic memory devices, emerging device concepts based on domain wall motion [6-8] and skyrmionic lattice [4] have been proposed, which aim to use heavy metal (HM)/ultrathin ferromagnet (FM)/oxide heterostructures. In such heterostructures, due to the strong spin-orbit interaction in HM layer, perpendicular magnetic anisotropy [9-10], Rashba effect [11-12], spin Hall effect [13-14], and interfacial Dzyaloshinskii-Moriya interaction (iDMI) [15] are manifested. Strong iDMI is the key to stabilize the skyrmionic lattice which has significant technological application potential in ultra-dense information storage. Furthermore, iDMI may lead to soliton like domain wall (DW) motion, which can extend Walker breakdown field, stabilizes chiral magnetic order and increases DW velocities even in the precessional regime [16].

The direct precise quantitative estimation of iDMI constant and its scaling behavior with ferromagnetic layer thickness variation are crucial for understanding the origin of iDMI

in HM/FM/oxide heterostructures. Recent studies have applied Brillouin light scattering (BLS) [17-18] technique for such investigations [19-21]. In this technique the wave-vector (k) of the spin-wave is uniquely defined by the wavelength and incident/scattering angle of the laser beam. The advantage of using BLS is that it can detect propagating spin-wave excitation simultaneously at $+k$ and $-k$ wave-vectors (Stokes and anti-Stokes process) [18,22]. The imprint of iDMI in BLS technique is manifested as an asymmetry in the SW dispersion relation for nonreciprocal propagation of DE spin-waves [19,23]. In FM thin films with broken inversion symmetry, different surface anisotropy on both sides of film results in slight change in spin-wave frequency upon reversal of propagation direction [24]. Recent theoretical calculations have shown that the difference in frequency due to asymmetric surface pinning is an order of magnitude smaller than that resulting due to iDMI [25]. Furthermore, the symmetric conventional exchange interaction (known as Heisenberg exchange interaction) produces quadratic dispersion, an even function of the wave number, while the antisymmetric DM exchange is characterized by an odd linear functional dependence [26-28]. The experiments manifesting these effects have been mostly confined to the thin film stacks that essentially contain Pt next to the FM layer [20,23,29-30]. As the Pt/FM layer interface usually gives rise to significant interface anisotropy as well as interfacial DMI, isolation of both the contributions to the asymmetric SW dispersion in such system is nontrivial. Furthermore, a recent study investigated the FM layer thickness dependence of iDMI in Pt/CoFeB/AlO$_x$ and found a decrease in iDMI constant below CoFeB thickness of 1.6 nm mainly due to degradation of interface [23]. For application of effects originating from interface, it is essential to reduce the thickness of the CoFeB layer: thinner magnetic layer will likely have more pronounced interface effects. Apart from the FM layer, underlayer plays a key role in improved interfacial properties in HM/FM/oxide stack. Hence, search for alternative thin film structures with different HM adjacent layer with FM layer with large iDMI originating primarily from interface is the need of the moment in spintronics research. An important thin film heterostructure CoFeB/SiO$_2$ with W underlayer, due to large spin Hall angle (SHA) of W [31], has significant application potential in recently discovered three terminal devices [13]. The advantage of the use of W instead of Pt in magnetic recording industry will be its cost effectiveness. Moreover, the choice of W helps to avoid the complication of induced magnetic moment in Pt which makes it difficult to identify the origin of iDMI. It is also known that W shows a thickness

dependent structural phase transition from high resistive β-W to low resistive α-W. The variation in SHA with various phases of W motivates us to investigate iDMI in these heterostructure [32,33].

Here we report the presence of pure iDMI in W/CoFeB/SiO$_2$ heterostructure using BLS spectroscopy for varying thickness values of the CoFeB layer down to 0.85 nm. We study the influence of the iDMI on spin-wave properties, in particular, by investigating the asymmetry in the spin-wave dispersion relation for DE mode with respect to counter propagating directions. Using analytical expressions for asymmetric dispersion of spin-wave, the experimental data are modeled to extract the iDMI constant. Detailed analysis of linewidth reveals that the lifetime of the magnons is also asymmetric with respect to propagation along $+k$ and $-k$ directions. Most significantly, we find that the iDMI constant varies inversely with the CoFeB thickness down to CoFeB thickness of 0.85 nm, indicating the presence of an almost pure iDMI and absence of other spurious effects contributing to the asymmetric propagation of spin-waves. The dependence of iDMI on W thickness suggests that the strength of iDMI is strongly dependent on the structural phases of W.

5.2. Experimental Details

The thin film heterostructure Sub/d W/1 Co$_{20}$Fe$_{60}$B$_{20}$/2 SiO$_2$ with d = 1, 2, 3, 4, 5, 6 and 7 nm and Sub/2 W/t Co$_{20}$Fe$_{60}$B$_{20}$/2 SiO$_2$ with t = 0.85, 1.0, 1.5, 2.0 and 3.0 nm (digits indicate thickness in nm) were deposited by dc/rf magnetron sputtering in Si (100) wafers coated with 100 nm SiO$_2$. Purpose of varying W underlayer thickness was to select optimum W thickness, which results in significantly reduced magnetic inhomogeneity [34,35] in the film stack. The base pressure of the deposition chamber was better than 2 × 10^{-7} Torr. CoFeB and W were grown using dc power of 28 Watt whereas the SiO$_2$ was grown using rf power of 60 Watt at 13.56 MHz. All thin films were grown in Ar gas atmosphere of 1 mTorr pressure. Sputtering deposition condition (in particular the Ar deposition pressure and power) was optimized carefully to obtain the thin films in few nanometer and sub nanometer regime. A film stack Sub/1 Co$_{20}$Fe$_{60}$B$_{20}$/2 SiO$_2$ without W layer adjacent to CoFeB was used for reference measurement.

BLS study is performed using a Sandercock-type six pass tandem Fabry-Pérot interferometer [36]. Conventional back scattered geometry is used along with the provision of wave-vector selectivity to investigate the SW dispersion relation. To obtain the wave vector selectivity, the sample is rotated in vertical plane thus allowing access to

various angles of incidence of laser on the sample. Details of the BLS set up can be found elsewhere [35,37]. For the larger incidence angles, the spectra were obtained after counting photons for several hours. It ensured that well defined spectra are obtained where the peak position can be estimated with accuracy of ~0.1 GHz. We use free spectral range of (FSR) 50 GHz and a 2^9 multi-channel analyser. The frequency resolution is determined by estimating FSR/2^9 (≈0.1 GHz) for the Stokes and anti-Stokes peaks of the BLS spectra [21, 23]. The instrumental linewidth of our setup is ~ 0.3 GHz as obtained from the analysis of the elastic peak [38] obtained in our experiment.

5.3. Results and Discussions

The BLS experiment was performed in DE [18,38] geometry under the application of an in-plane (IP) magnetic field up to ±0.22 T/μ_0. For the IP applied field, the magnetization is saturated in the plane of the film. The schematic of the general film stack and BLS experimental geometry is shown in Figure 5.1 (a).
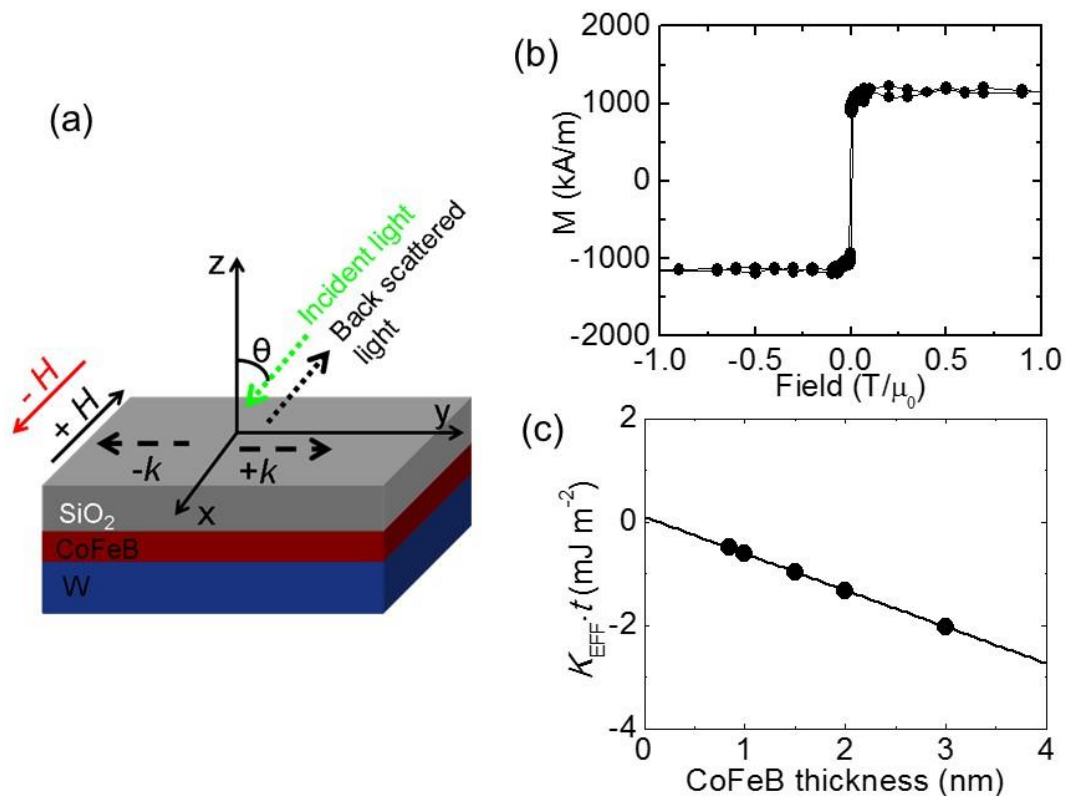
Figure 5.1: (a) Schematic of the film stack along with the BLS measurement geometry. (b) Magnetization hysteresis loop for film stack 2 W/1 CoFeB/2 SiO$_2$ with magnetic field applied within the film plane. (c) The plot of $K_{EFF}.t$ as a function of CoFeB thickness along with the linear fit to estimate the interface anisotropy.

The coordinate convention, the incident light, spin-wave propagation, and applied field directions are indicated. Using Lorentzian function, we fit the Stokes and anti-Stokes peaks in the BLS spectra to extract the peak frequency and linewidth i.e., full width at half maximum. Figure 5.1(b) shows the magnetization hysteresis loop measured by VSM at room temperature for the film stack Sub/2 W/1 CoFeB/2 SiO_2 for magnetic field applied within the sample plane thus indicating in-plane easy-axis. The estimated saturation magnetization from the hysteresis loop is 1100 kA/m. All the films have in-plane magnetization as indicated by VSM measurement. We estimate the effective anisotropy (K_{EFF}) of the film by calculating the areal difference between the OOP and IP magnetization hysteresis loop. In Fig. 5.1(c) we show the plot of $K_{EFF}.t$ vs t and use a linear fit to obtain the interface anisotropy (as determined by the intercept on the y-axis). A nearly zero intercept on the y-axis indicates that interface anisotropy is almost negligible in these film stacks.

Shown in Figure 5.2(a) are the typical BLS spectra measured for zero wave vector ($k = 0$, corresponding to uniform precession mode) at various IP applied magnetic fields. The field values are mentioned above each spectrum. We use Kittel equation (Eq. (5.1)) to fit the increase in frequency with the increase in field for different thicknesses of CoFeB (c.f., Figure 5.2(b), CoFeB thickness value is mentioned in each plot).

$$f = \frac{\mu_0 \gamma}{2\pi} \sqrt{\left(H(H + M_{eff})\right)} \qquad (5.1)$$

Here, $\gamma = g\mu_B/h$, g is the Lande g factor, H is the applied bias magnetic field and M_{eff} is the effective magnetization. We use $\mu_0 = 4\pi \times 10^{-7}$ N/m^2 the vacuum permeability and determine g and M_{eff} as fitting parameter. The best fit to the data yields $g = 2.00\pm0.05$ for all the thicknesses of CoFeB measured here. Similar measurements of frequency vs. bias magnetic field at $k = 0$ were performed for all other samples and the modeling yields the M_{eff} parameters as shown in Figure 5.2(c) for various thickness of CoFeB. As expected, we find that the M_{eff} shows small variation as the CoFeB thickness is varied thus indicating negligible OOP anisotropy.

It is important to mention here that observation of asymmetry in the magnon linewidth of the spin-wave spectra is quite non-trivial. In order to observe such asymmetry a major pre-requisite is to select a sample which has reasonably small linewidth. Thus, before measuring the detailed dispersion, the magnetic homogeneity of Sub/d W/1 $Co_{20}Fe_{60}B_{20}$/2 SiO_2 is investigated as a function of d by analyzing the linewidth of

corresponding BLS spectra at $k = 0$ wave-vector. From this investigation we find that $d =$ 2 nm is the optimum W thickness where the linewidth (magnetic inhomogeneity) is reasonably small as well as the frequency asymmetry is large. Thus, for further investigation of asymmetry in frequency vs wave-vector dispersion and asymmetry in the magnon linewidth we vary CoFeB thickness from 0.85 nm to 3.0 nm by fixing the W underlayer thickness to 2 nm.
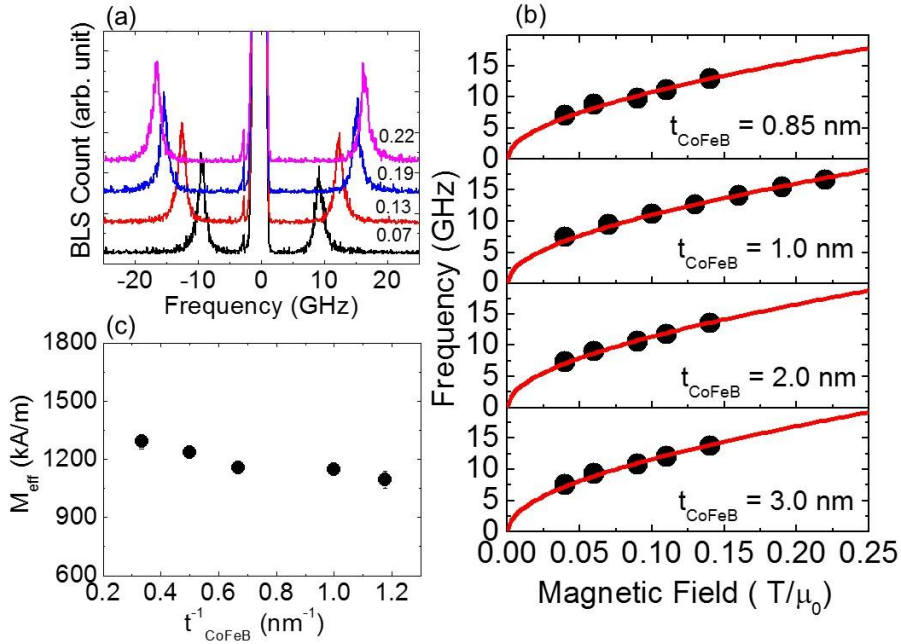
Figure 5.2: (a) Representative BLS spectra measured for the 2W/1 CoFeB/2 SiO$_2$ film stack for various in-plane applied magnetic fields at $k = 0$. Digits mentioned above each spectrum correspond to the magnetic field values in T/µ$_0$. (b) Plot of frequency versus magnetic field for 2W/t CoFeB/2 SiO$_2$ film stack at various t. The value of t is mentioned in each panel. Symbols represent the experimentally measured data point whereas solid curve is the fit using standard Kittel equation. (c) Variation of M_{eff} as a function of inverse of CoFeB thickness.

5.3.1. Asymmetry in Frequency versus Wave-vector due to iDMI

In order to investigate the presence of iDMI in these film stacks, we measured the frequency (f) vs. wave-vector (k) dispersion by switching the direction of the bias field at a fixed field strength of 0.1 T/µ$_0$. The wave-vector (k) is varied by changing the angle of incidence of light *w.r.t.* the film plane. Figures 5.3(a)–(d) show the typical BLS spectra at a fixed wave-vector $k = 2.04 \times 10^7$ rad/m for various thicknesses of CoFeB in 2 W/t

CoFeB/2 SiO$_2$ stack. From these figures it can be seen that for t_{CoFeB} = 3.0 nm, the peak frequencies for Stokes and anti-Stokes components are nearly the same when the applied field direction is interchanged from +x (black line) to –x (red line). The difference between the frequencies due to field reversal (Δf) for both the Stokes and anti-Stokes lines increases continuously with the reduction in CoFeB thickness as can be noticed in Figure 5.3. The value of Δf reaches a maximum of 0.5 GHz for t = 0.85 nm. Such a large difference in Δf is unlikely to arise from the asymmetric surface pinning of the CoFeB layer in these heterostructures. Moreover, no frequency asymmetry is found in the test sample (1 CoFeB/2 SiO$_2$ stack) which does not have a W underlayer. Note that asymmetry in the peak intensity is consistently present at higher k values for each film stack with asymmetry more pronounced for films with W underlayer in comparison to that without W.

The full f vs. k dispersion for two different thickness values of CoFeB (t = 0.85 nm and 1.0 nm) are shown in Figures 5.4(a) and 5.4(b). The experimentally obtained f values are shown using symbols in the Figure. From the plots it is evident that at finite k, the spin-wave frequencies propagating along two opposite directions differ significantly and this asymmetry increases with increase in the value of k. The results shown in Figures 5.4(a) and (b) are modeled by using a modified dispersion relation for DE mode given by Eq. 5.2 [19-21], which takes into account of the shift in the frequency arising due to iDMI.

$$\omega = \omega_0 + \omega_{DM} = \mu_0\gamma\sqrt{([H + Jk^2 + \xi(kL)M_S][H - H_U + Jk^2 + M_S - \xi(kL)M_S])} - \frac{2\gamma}{M_S}Dk$$

(5.2)
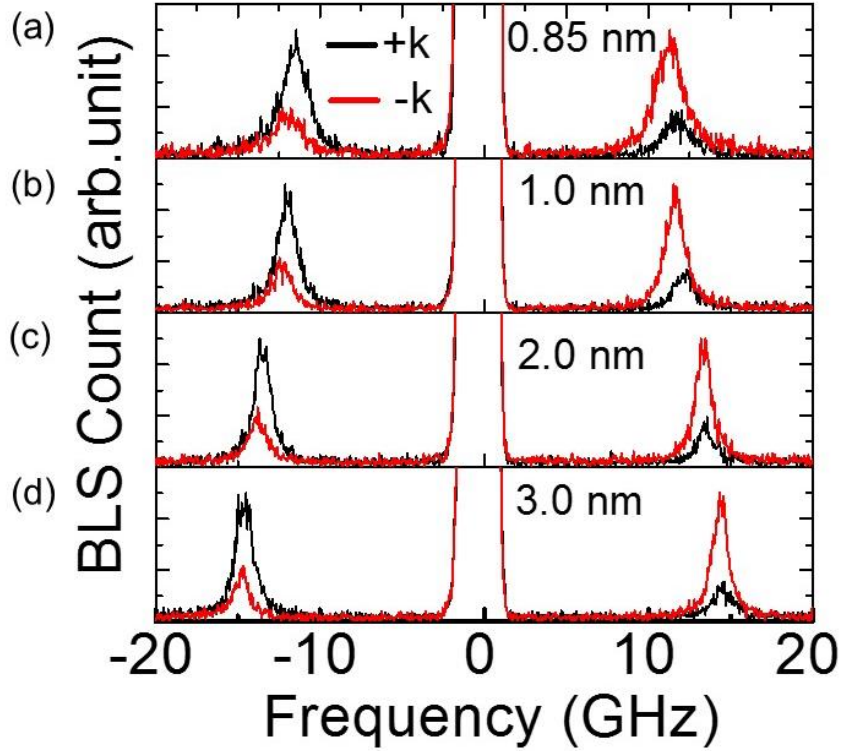
Figure 5.3(a)–(d). BLS spectra measured at wave-vector k = 2.04 × 10^7 rad/m for the 2 W/t CoFeB/2SiO$_2$ film for two counter propagating directions. The spectrum corresponding to particular thickness of CoFeB is indicated by mentioning thickness value in each panel.

Here, g, H, μ_0 and M_s carries the same meaning as used before in Eq. 5.1, $J = 2A/\mu_0 M_s$ the SW stiffness, A the exchange constant, D the iDMI constant, $H_U = 2K_U/\mu_0 M_s$ the uniaxial anisotropy field (K_U the uniaxial anisotropy) and ξ (kL)= 1 − (1−exp |-kL|)/|kL|, where L is the thickness of FM film. The theoretical fit using Eq. 2 is shown by solid curves in Figures 5.4(a) and 5.4(b). For t = 0.85 nm (Fig. 5.4(a)), using g = 2.0 from Kittel fit (as shown in Fig. 5.2) and M_s = 1030 kA/m from VSM (Kittel fit in Fig. 5.2 also yield similar value), the fitted experimental data yields A = 20±2 pJ/m, K_u = (1.02±0.05)×10^5 J/m^3 and D = 0.25 ± 0.02 mJ/m^2. The fitted value of A nearly agrees with the literature value. Following similar modelling, for t = 1.0 nm (Fig. 5.4(b)), these parameters are g = 2.0, M_s = 1100 kA/m, K_u = 1.45×10^5 J/m^3 and D = 0.21 ± 0.02 mJ/m^2. As a matter of comparison, we have added the symmetric dispersion as dashed curves in Figures 5.4 (a) and 5.4(b). These were generated using the standard dispersion relation for DE mode without considering iDMI i.e., by setting ω_{DM} = 0 in Eq. (5.2).
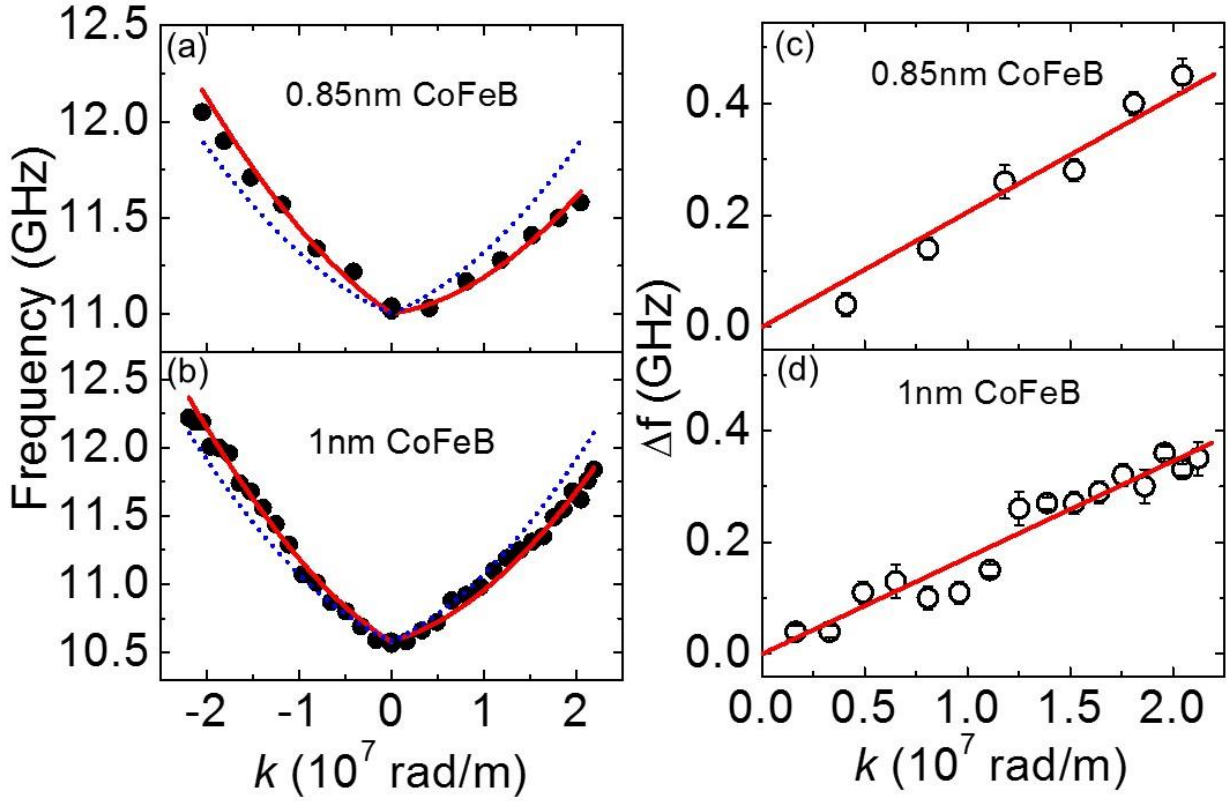
Figure 5.4: Frequency vs. wave-vector dispersion curve for (a) 2 W/0.85 CoFeB/2 SiO$_2$ and (b) 2 W/1 CoFeB/2 SiO$_2$ films. Symbols represent the experimental data points; red solid curves show the fit to the data points using Eq. 5.2. The blue dashed curve shows the dispersion curve in the absence of IDMI. Plot of Δf vs. k for (c) 2 W/0.85 CoFeB/2 SiO$_2$ and (d) 2 W/1 CoFeB/2 SiO$_2$ films. Here, solid line represents the linear fit to the experimental data using Eq. 3 to estimate the DMI constant. The error bar in Δf is shown by considering the error from the fitting of the spin-wave spectra.

The interfacial DMI energy density can also be determined from the frequency difference (Δf) between spin-waves with opposite ($+k$ and $-k$) wave-vectors as given by Eq. 5.3 [19-21]

$$\Delta f = [\omega(-k) - \omega(k)]/2\pi = \frac{2\gamma}{\pi M_s} Dk \qquad (5.3)$$

In this case the estimation of D is primarily determined by the experimentally measured quantities Δf, k and M_s. Figures 5.4(c) and 5.4(d) show the variation of Δf with k, as obtained from measurements from samples with $t = 0.85$ nm and 1.0 nm, respectively. The slope of the linear fit to the data points for the sample with $t = 0.85$ nm gives $D = 0.25$ mJ/m^2, whereas for the sample with $t = 1.0$ nm we obtain $D = 0.21$ mJ/m^2 from the fit.

Thus, the value of D is found to be consistent from two types of modeling of the experimental data. The observed increase in the D with the decrease in CoFeB thickness indicates the signature of an interfacial DMI at the W/CoFeB interface.

5.3.2. Ferromagnetic Layer Thickness Dependence of DMI Constant

In order to confirm that the observed asymmetry in the SW dispersion is induced purely by an iDMI at the W/CoFeB interface and not due to interface anisotropy at the asymmetric interface, we investigate the SW dispersion of samples with higher thicknesses of CoFeB. For this purpose, we discuss below the dependence of Δf and D on the thickness of the CoFeB layer. Displayed in Figures 5.5(a) and 5.5(b) are the variation of Δf and D with the inverse of CoFeB thickness. It is important to note from these plots that both Δf and D increases almost linearly with the decrease in the thickness of CoFeB and the nature of increase for both Δf and D are more or less the same. Linear fit is used to fit both CoFeB thickness dependence of Δf and D [30].

The apparent linear scaling of D with inverse of CoFeB thickness indicates that the asymmetry in the spin-wave dispersion originates primarily from the iDMI. The asymmetry in Δf engendered due to interface anisotropy is known to scale as inverse square of FM layer thickness [38].
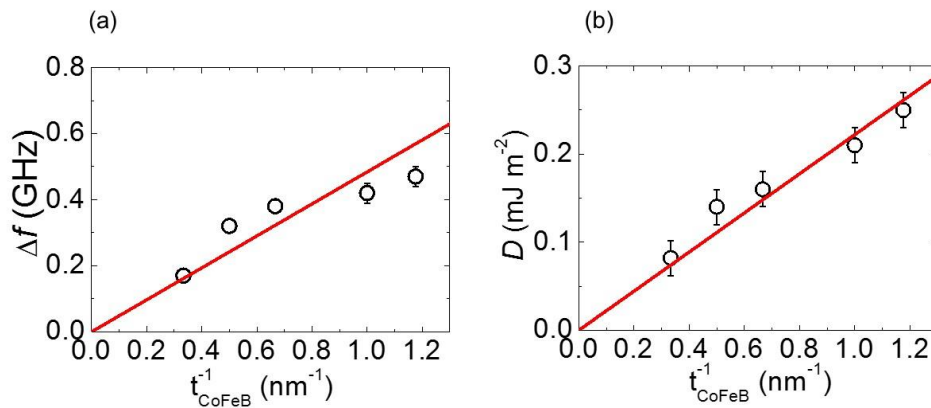
Figure 5.5: (a) Variation of asymmetry in the frequency and (b) Variation of DMI constant with the inverse of CoFeB thickness. The error bar in Δf is shown by considering the error from the fitting of spectra as well as the instrumental resolution to determine the peak frequency and for D it is shown by taking into account the error in estimation of M_s as well as Δf. The linear fit to the data in both the cases is shown using red solid line.

We thus exclude the possibility of any contribution from interface anisotropy on the observed Δf. A remarkable feature to notice here is that neither Δf nor D start to deviate

from the linear behavior with $1/t$ down to $t = 0.85$ nm, thus ensuring that the W/CoFeB interface does not degrade down to such small thickness values. In earlier studies, a sudden decrease was observed in Δf and D below ~ 1.6 nm of CoFeB thickness in Pt/CoFeB and this was explained by considering its origin in degradation of interface [23]. Non-degradation of W/CoFeB interface down to such small thickness is potentially very useful for the applications that aim to use DMI arising purely from interfacial origin such as fast domain wall velocity based spintronics devices.

5.3.3. Asymmetry in Magnon Linewidth due to iDMI.

Another manifestation of the presence of the iDMI in the HM/FM/oxide heterostructures is an asymmetry in the dispersion of magnon lifetime with wave-vector k [39]. In order to get an insight into this asymmetry, we studied the variation in the linewidth of the SW spectra with k. For that purpose, we performed a deconvolution of the linewdith for removing the contribution of the instrumental linewidth [40].

Figure 5.6 displays the variation of linewidth i.e., in magnon lifetime with k at an applied magnetic field 0.1 T/μ_0 for Sub/2 W/1 CoFeB/2 SiO$_2$. Linewidth for SW propagating in $+k$ direction is smaller than the same for spin-wave propagating in $-k$ direction, which indicates longer lifetime of magnon propagating in $+k$ direction (c.f. Figure 5.1(a)). The best fit to experimental variation of linewidth with wave-vector (as shown by continuous line in Fig. 5.6 is obtained using Eq. (4) [19].

$$\frac{\Gamma}{2} = \alpha \gamma \mu_0 (H + Jk^2 - H_U/2 + M_s/2) \left[1 + \frac{\omega_{DM}(k)}{\omega_0(k)} \right] \qquad (5.4)$$

where Γ is the linewidth of the spin-wave spectra and other symbols denote same quantities as described earlier. We use $g = 2.0$, $M_s = 1100$ kA/m, $K_u = 1.45 \times 10^5$ J/m^3 and $D = 0.21$ mJ/m^2 and keep the damping coefficient α as fitting parameter. The best fit to the experimental data is obtained for $\alpha = 0.033 \pm 0.002$. Thus Eq. 5.4 describes qualitatively the asymmetry in the linewidth due to the presence of DMI at the W/CoFeB interface. Figure 5.6 signifies that by using the same parameters as for fitting the dispersion curves in Figure 5.4 we obtain a reasonably good fit for the linewidth of the SW spectra (magnon lifetime). Despite of the presence of significant error bar as accounted from the fit (due to relatively small iDMI value in comparison to the Pt based heterostructures), the observed asymmetry in the dispersion of magnon lifetime with wave-vector (c.f. Fig. 5.6) reconfirms the presence of iDMI primarily originating from W/CoFeB interface in the W/CoFeB/SiO$_2$ film stacks.
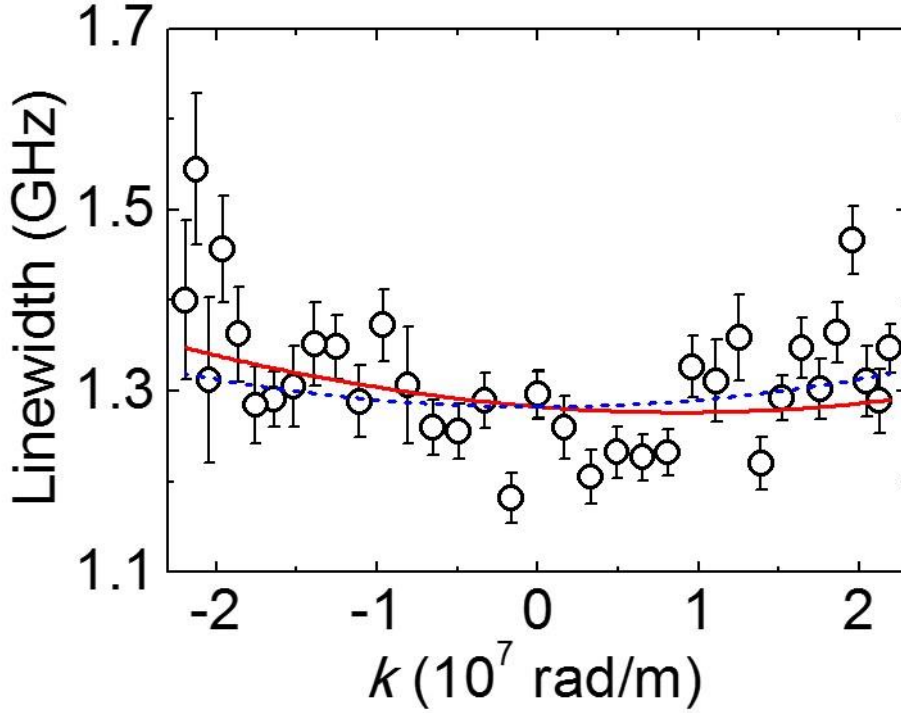
Figure 5.6: Linewidth of the spinwave spectra as a function of wave-vector for 2 W/1 CoFeB/ 2 SiO$_2$ at a bias field of 0.1 T/μ_0. Experimental linewidth data are denoted by symbols. Error bars show standard deviation of the spectral linewidth obtained using Lorentzian function. The solid red line represents the fitted curve using equation (4). Blue dashed line is the same without considering the DMI in the film stack.

5.3.4. Heavy Metal Layer Thickness Dependence of iDMI

We next investigate the underlayer thickness dependence of the strength of iDMI. The detailed characterization of the thickness dependent structural phase transition of W from A15 (distorted tetragonal commonly known as β) to bcc (α-phase) can be found in the existing literature [33]. Figure 5.7(a) shows the representative BLS spectra measured for various thicknesses of W underlayer at $k = 2.04 \times 10^7$ rad/m and IP applied magnetic field of $H = 1$ kOe. It is evident that frequency asymmetry (Δf) first increases slightly with W thickness followed by a maximum of 0.75 GHz at $d = 5$ nm. As we further increase the W thickness, it drops drastically as shown in Fig. 5.7(b). The quantification of the strength of iDMI is done using Eq. 5.3. Fig. 5.7(c) shows that there is a presence of two regimes where iDMI constant varies depending upon the structural phases of W. The highest value of D is found to be 0.38 ± 0.02 mJ/m^2 in case of $d = 5$ nm.
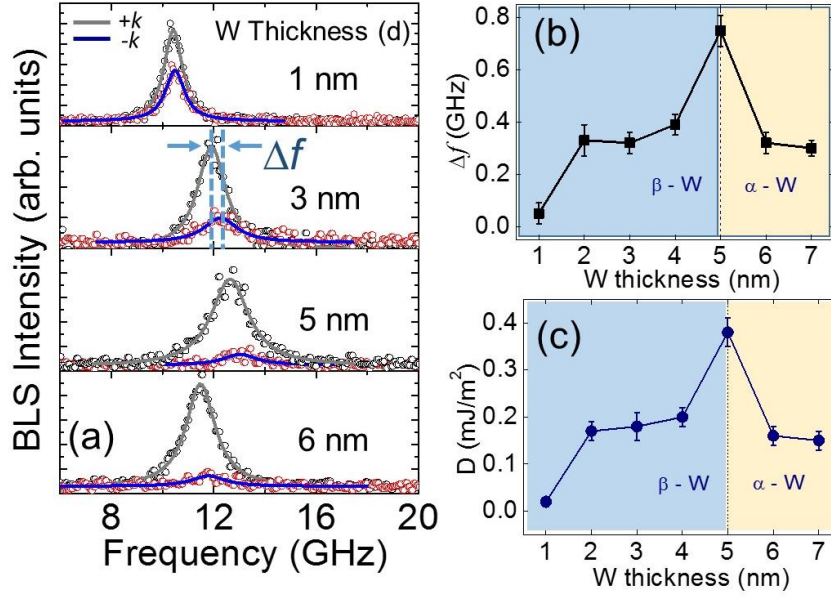
Figure 5.7: (a) Representative BLS spectra measured at wave vector $k = 2.04 \times 10^7$ rad/m for the dW/1 CoFeB/2 SiO$_2$ sample for two counter propagating directions. The spectrum corresponding to specific thickness of W is indicated by mentioning thickness value in each panel. Solid curve is the fit using Lorentzian function. (b) Variation of Δf with W thickness. (c) Variation of D with W thickness. Symbols represent the experimental data points and solid lines are guide to eyes.

5.4. Conclusions

In summary, we have investigated both qualitatively and quantitatively the pure iDMI in W/CoFeB/SiO$_2$ using BLS technique. The detailed study of magnetostatic surface spin-wave properties shows that the interfacial DMI leads to nonreciprocal spin-wave propagation, i.e., different properties for spin-waves propagating in opposite directions. In Damon-Eshbach geometry, by interchanging the magnetic field direction we observe asymmetry in the peak frequency, peak intensity and magnon lifetime. Furthermore, we showed that the iDMI constant scales as the inverse of CoFeB thickness down to 0.85 nm, indicating its origin as purely interfacial. The W/CoFeB interface shows almost negligible degradation down to sub-nanometer CoFeB thickness, which is highly desirable for technological applications those aim to use interface effect, in particular iDMI. Further, iDMI strength increases with the underlayer thickness in the β-W region whereas a sudden decrease is observed in α phase of W. Our investigation will be important for understanding the spin-wave dynamics as well as stabilizing DMI assisted skyrmion,

soliton like domain wall motion, in CoFeB with W underlayer, which is known to have a large spin Hall angle.

References

[1] I. E. Dzyaloshinskii, Sov. Phys. JETP **5**, 1259 (1957).

[2] T. Moriya, Phys. Rev. **120**, 91 (1960).

[3] S. Muehlbauer, B. Binz, F. Jonietz, *et al.,* Science **323**, 915 (2009).

[4] A. Fert, V. Cros, and J. Sampaio, Nature Nanotech. **8**, 152 (2013).

[5] V. E. Dmitrienko, E. Ovchinnikova, S. Collins, *et al.,* Nat. Phys. **10**, 202 (2014).

[6] S. Emori, U. Bauer, S. Ahn, *et al.,* Nat. Mater. **12**, 611 (2013).

[7] K.-S. Ryu, L. Thomas, S.-H. Yang, and S. Parkin, Nat. Nanotech. **8**, 527 (2013).

[8] A. Thiaville, S. Rohart, J. Émilie, and V. Cross, E. Phys. Lett **100**, 57002 (2012).

[9] S. Ikeda, K. Miura, H. Yamamoto, *et al.,* Nat. Mater. **9**, 721 (2010).

[10] J. Sinha, M. Hayashi, A. J. Kellock, *et al.,* Appl. Phys. Lett. **102**, 242405 (2013).

[11] M. I. Miron, G. Gaudin, S. Auffret, *et al.*, Nat. Mater. **9**, 230 (2010).

[12] M. I. Miron, T. Moore, H. Szambolics, *et al.,* Nat. Mater. **10**, 419 (2011).

[13] L. Liu, C. F. Pai, Y. Li, *et al.,* Science **336**, 555 (2012).

[14] J. Kim, J. Sinha, M. Hayashi, *et al.,* Nat. Mater. **12**, 240 (2013).

[15] J. Torrejon, J. Kim, J. Sinha, *et al.*, Nat. Comm. **5**, 4655 (2014).

[16] Y. Yoshimura, K. Kim, T. Taniguchi, *et al.,* Nat. Phys. **12**, 157 (2016).

[17] P. Grunberg, Topics in Appl. Phys. **66**, 303 (1989).

[18] B. Hillebrands in *Modern Techniques for Characterizing Magnetic Materials*, edited by Y. Zhu (Kluwer Academic, Boston, 2005).

[19] K. Di, V. L. Zhang, H. S. Lim, *et al.,* Phys. Rev. Lett. **114**, 047201 (2015).

[20] K. Di, V. L. Zhang, H. S. Lim, *et al.,* Appl. Phys. Lett. **106**, 052403 (2015).

[21] M. Belmeguenai, J.-P. Adam, Y. Roussigné, *et al.,* Phys. Rev. B **91**, 180405 (2015).

[22] J. Barnas and P. Grunberg, J. Magn. Magn. Mater. **82**, 186 (1989).

[23] J. Cho, N. Kim, S. Lee, *et al.*, Nat. Commun. **6**, 7635 (2015).

[24] B. Hillebrands, Phys. Rev. B **41**, 530 (1990).

[25] H. T. Nembach, J. Shaw, M. Weiler, *et al.,* Nat. Phys. **11**, 825 (2015).

[26] A. A. Stashkevich, M. Belmeguenai, Y. Roussigné, *et al.*, Phys. Rev. B **91**, 214409 (2015).

[27] J.-H. Moon, S.-M. Seo, K.-J. Lee, *et al.,* Phys. Rev. B **88**, 184404 (2013).

[28] M. Kostylev, J. Appl. Phys. **115**, 233902 (2014).

[29] H. S. Korner, J. Stigloher, H. G. Bauer, *et al.,* Phy. Rev. B **92**, 220413 (2015).

[30] N-H Kim, D. S. Han, J. Jung, *et al.*, Appl. Phys. Lett. **107**, 142408 (2015).

[31] C.-F. Pai, L. Liu, Y. Li, *et al.*, Appl. Phys. Lett. **101**, 122404 (2012).

[32] K. U. Demasius, T. Phung, W. Zhang, *et al.*, Nat. Commun. **7**, 10644 (2016).

[33] S. Mondal, S. Choudhury, N. Jha, A. Ganguly, J. Sinha, A. Barman, Phys. Rev. B **96**, 054414 (2017).

[34] A. Murayama, K. Hyomi, J. Eickmann, and C. M. Falco, Phys. Rev. B **61**, 8984 (2000).

[35] J. Sinha, C. Banerjee, A. K. Chaurasiya, *et al.*, RSC Advances **5**, 57815 (2015).

[36] R. Mock, B. Hillebrands, and J. R. Sandercock, J. Phys. E-Sci. Inst. **20**, 656 (1987).

[37] A. Haldar, C. Banerjee, P. Laha, and A. Barman, J. Appl. Phys. **115**, 133901 (2014).

[38] B. Hillebrands, P. Baumgart, and G. Guntherodt, Phys. Rev. B **36**, 2450 (1987).

[39] K. Zakeri, Y. Zhang, Y. Chuang, *et al.*, Phys. Rev. Lett. **108**, 197205 (2012).

[40] W. F. Oliver, C. A. Herbst, S. M. Lindsay, and G. H. Wolf, Rev. Sci. Inst. **63**, 1884 (1992).

Chapter 6

6. Dependence of Interfacial Dzyaloshinskii-Moriya Interaction on Layer Thicknesses in Ta/CoFeB/TaO$_x$ Heterostructures from Brillouin Light Scattering

6.1. Introduction

Due to the ever-increasing demand of data storage and processing, much attention is being paid by the scientific community to search for new materials and physics for future storage, memory, logic and communication devices. In such context, broken inversion symmetry systems have emerged as potential candidates which shows striking features like Dzyaloshinskii-Moriya interaction (DMI), which originates due to the breaking of structural inversion symmetry at the interface of heavy metal (HM) possessing strong spin-orbit coupling and ferromagnet (FM) [1-4]. Basically, DMI is an antisymmetric component of interatomic magnetic exchange which favours chiral structure, whereas the symmetric component is commonly known as the Heisenberg exchange interaction that stabilizes spatially uniform magnetization. More recently, for application in magnetic memory devices new concepts based on spin Hall effect [5, 6] perpendicular magnetic anisotropy [7, 8], Rashba effect [9], and interfacial DMI (iDMI) [10] have been proposed. A firm understanding and tunability of iDMI may facilitate the design of the next generation magnetic memory and logic devices based on the chiral magnetic domain walls and skyrmions [10-13]. Achieving large velocity of domain wall by means of current control is envisioned to be useful in high density race-track memory [14]. Although, the phenomena of DMI was predicted two decades ago, its experimental realization has only been possible in ultrathin film heterostructures during the last few years. It has been reported that iDMI leads to spin spiral in Mn monolayers on W(110) [15], nanoscale skyrmion lattices in Fe monolayers on Ir (111) [16] and isolated skyrmion on Pd/Fe bilayers on Ir (111) [17]. Moreover, fast current induced magnetic domain-wall motion has recently been explored via the combination of chiral domain-wall structure and spin-

orbit torque where the chirality and speed of the domain-wall motion depend on the sign, the magnitude of the iDMI and the spin-orbit torque [11]. It is expected that the iDMI at HM/FM would show large sensitivity to the choice of both the HM and FM layers. An interesting theoretical study has recently proposed that DMI affects predominantly the interfacial spins in the FM layer and extends weakly in the FM and HM layers [18]. It is understood that intermixing at the HM/FM interface is detrimental for achieving large iDMI. Furthermore, the strength and the sign of iDMI in multilayered structures is greatly affected by the material composition, stack order, interface quality etc [19]. The tunability in these parameters may provide an efficient way to control the iDMI.

Previous measurements of the quantification of DMI were reported using spin polarized scanning tunnelling microscopy [15], highly resolved spin polarized electron energy loss spectroscopy [20], scanning nitrogen vacancy magnetometry [21], synchrotron based X-ray scattering, current induced magnetic domain-wall dynamics [22], and asymmetric magnetic nucleation measurements [23]. Moreover, numerical and analytical micromagnetics have also been implemented to study DMI [24, 25]. More recently, the direct observation of iDMI using Brillouin light scattering (BLS) technique have been demonstrated [26-30]. An important thin film heterostructure Ta/CoFeB/TaO$_x$ has been studied by Yu *et al.* [31] in the context of switching of perpendicular magnetization by SOT in absence of magnetic field. Furthermore, it has been shown that the chiral magnetic bubbles can be nucleated in Ta/CoFeB/TaO$_x$ heterostructures suggesting the presence of the iDMI [32]. Recent experimental investigations show the FM layer thickness dependence of the strength of iDMI demonstrating $1/t$ behavior. (where t is the FM thickness) [29]. In Pt/CoFeB based system, the iDMI constant has been reported to show interesting non-linear dependence on Pt thickness. Specifically, the iDMI constant has been found to increase with Pt thickness below its spin-diffusion length, whereas above the spin-diffusion length it saturates [33]. In order to gain deep understanding regarding iDMI in Ta/CoFeB/TaO$_x$ thin film heterostructures, a systematic study is needed. However, a systematic study of the influence of FM and HM layer thicknesses on the strength of iDMI in these heterostructures is still missing in the literature.

In this article, we have presented a systematic study of FM and HM layer thickness dependence of iDMI in technologically important Ta/Co$_{20}$Fe$_{60}$B$_{20}$/TaO$_x$ heterostructures from asymmetric spin-wave dispersion probed by Brillouin light scattering technique. We observed a reasonably large iDMI value originated primarily from the interface in

these heterostructures. Further confirmation of the iDMI constant was evidenced by performing the in-plane angular dependence of the frequency non-reciprocity of Ta/Co$_{20}$Fe$_{60}$B$_{20}$/TaO$_x$ thin film heterostructures, which is in good agreement with the analytical theory formulated by the Cortes-Ortuno and Landeros [34] for the dispersion relations of the spin waves in FM thin films with DMI.

6.2. Experimental Details

A series of samples consisting of Substrate/d Ta/1 Co$_{20}$Fe$_{60}$B$_{20}$/0.5 TaO$_x$, with d = 0, 0.5, 0.8, 1, 2, 3, 4, 5, 6 nm and Substrate/2 Ta /t Co$_{20}$Fe$_{60}$B$_{20}$/0.5 TaO$_x$, with t = 0.85, 1, 1.5, 2, 3 nm were deposited by dc/rf magnetron sputtering on Si (100) wafer coated with 100-nm-thick SiO$_2$ at room temperature. The base pressure of the chamber was better than 2 × 10^{-7} Torr and the uniformity in the thickness of the layer was ensured by rotating the substrate at 10 rpm during deposition. Ta was grown using rf power of 40 Watt, whereas for CoFeB, dc power of 38 Watt was used. All these films were grown in Ar gas atmosphere of 1 mTorr pressure. The vibrating sample magnetometer (VSM) measurement was performed to estimate the values of saturation magnetization (M_s). Importantly, all these films are in-plane magnetized as revealed by VSM measurement.

In order to investigate the asymmetric spin-wave dispersion caused by iDMI, BLS measurements were performed in DE geometry using a Sandercock-type six-pass tandem Fabry-Pérot interferometer. Conventional 180° back scattered geometry was used along with the provision of wave-vector selectivity to investigate the spin-wave dispersion relation. In the light scattering process, total momentum is conserved in the plane of the thin film. As a result, the Stokes (anti-Stokes) peaks in BLS spectra correspond to creation (annihilation) of magnons with momentum $k = \frac{4\pi}{\lambda}\sin\theta$, where λ is the wavelength of the incident laser beam (532 nm in our case) and θ refers to the angle of incidence of laser. To get well defined BLS spectra for the larger incidence angles, the spectra were obtained after counting photons for several hours. Free spectral range (FSR) of 50 GHz and a 2^9 multi-channel analyser were used during the BLS measurement. The frequency resolution is determined by estimating FSR/2^9 ($\approx$0.1 GHz) for the Stokes and anti-Stokes peaks of the BLS spectra. In the second part of the BLS experiment, the sample and the magnet were mounted on a two-axis translation stage thereby allowing the variation in the in-plane angle between the applied magnetic field H and the spin-wave wave vector k. The translation stage was attached to a vertically mounted rotation stage making their

axes orthogonal, allowing θ to be set at 45° (in our case). Using this arrangement, we measured the asymmetry in the spin-wave frequency as a function of the angle (ϕ) between the applied bias field and the wave vector k.

6.3. Results and Discussions

Figure 6.1(a) represents the grazing incidence X-ray diffraction (GIXRD) patterns for the sample: Substrate/Ta (6 nm)/CoFeB (1 nm)/TaO$_x$ (0.5 nm). From the analysis of the XRD data, it is revealed that the peak (002) at 35.4° corresponds to the β-Ta phase.
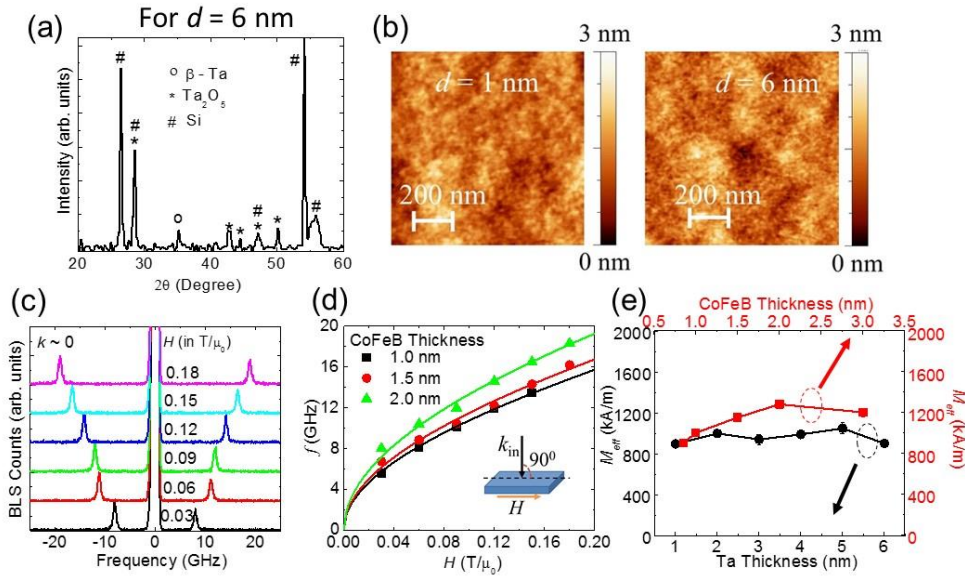
Figure 6.1: (a)Grazing incidence X-ray diffraction (GIXRD) pattern for the sample 6 Ta /1 CoFeB/0.5 TaO$_x$ grown on Si (100) substrate. (b) AFM image of d Ta/1 CoFeB/0.5 TaO$_x$ (0.5) (where d = 1 and 6 nm). (c) Representative BLS spectra measured for 2 Ta/2 CoFeB /0.5 TaO$_x$ for various in-plane applied field at $k \approx 0$. Digits mentioned above each spectrum refer to the magnetic field in T/μ_0. (d) Plot of frequency (f) vs magnetic field (H) for the film stack 2 Ta/t CoFeB/0.5 TaO$_x$ with t = 1, 1.5 and 2 nm. Symbols represent the experimentally measured data points, whereas solid curve is the fit using Eq. 6.1. Inset: Schematic of the measurement geometry. (e) Plot of M_{eff} vs Ta thickness for film stack d Ta/1 CoFeB/0.5 TaO$_x$ (left and bottom axes) and CoFeB thickness 2 Ta/t CoFeB/0.5 TaO$_x$ (right and top axes).

Furthermore, TaO$_x$ peaks with lower intensity and Si substrate peaks were also identified and marked in the figure. These findings are consistent with the existing literature reports [35, 36]. Figure 6.1(b) shows the atomic force microscope (AFM) images for the sample d Ta/1 CoFeB/0.5 TaO$_x$ with d = 1 and 6 nm. The average topographical roughness for all films is in the range of 0.20 to 0.25 nm. To extract the magnetic parameters, we

performed the magnetic field dependence of the spin-wave frequency. Figure 6.1(c) represents the typical BLS spectra measured at normal incidence ($k \approx 0$, corresponding to the uniform precessional mode) at various in-plane applied magnetic field (H) for sample: 2 Ta/2 CoFeB/0.5 TaO$_x$. The value of H is mentioned on each spectrum. The BLS spectra were well fitted with the Lorentzian function to get the frequency value (f) which increases with increasing H. In Fig. 6.1(d), f as a function of H is shown for the samples with t = 1, 1.5 and 2 nm. Standard Kittel formula (c. f. Eq. (6.1)) was used to fit these experimental data.

$$f = \frac{\mu_0 \gamma}{2\pi} \sqrt{\left(H\left(H + M_{eff}\right)\right)} \tag{6.1}$$

Here, $\gamma = g\mu_B/h$, g is the Landé g-factor, and M_{eff} is the effective magnetization. We used $\mu_0 = 4\pi \times 10^{-7}$ N/m^2 the vacuum permeability and determined g and M_{eff} as fitting parameters. The best fit to the data yields g = 2.00 ± 0.05 for all the samples. The plot of M_{eff} versus Ta underlayer thickness (d Ta/1 CoFeB/0.5 TaO$_x$, bottom and left axes) and CoFeB layer thickness (2 Ta/t CoFeB/0.5 TaO$_x$, top and right axes) is shown in Fig. 6.1 (e). Extracted values of M_{eff} are close to the values of saturation magnetization (M_s) measured using VSM for almost all film stacks thus indicating negligibly small interface anisotropy. It is worth to mention here that since all these films are unannealed, the presence of interface anisotropy is ruled out in these stacks.

To investigate the iDMI in these thin film heterostructures, we measured the spin-wave dispersion (f vs k) relation at applied in-plane field of 0.1 T/μ_0. Here, k was varied by changing the angle of incidence of the laser beam. Since the thickness of the CoFeB is much smaller than the optical skin depth of the metal, the spin waves propagating in the opposite directions were simultaneously detected as Stokes and anti-Stokes peaks in the BLS spectra. In order to model our experimental data, we use the equation for the difference in the frequencies of counter-propagating spin waves given below [26, 29],

$$\Delta f = [\omega(-k) - \omega(k)]/2\pi = \frac{2\gamma}{\pi M_s} Dk \tag{6.2}$$

which is linear in D and k. Here D is the iDMI constant. Therefore, Eq. (6.2) provides an elegant way to quantify the strength of iDMI by experimentally measured quantities Δf, M_s and k. Typical BLS spectra recorded at higher wave vector (k = 2.04 × 10^7 rad/m) for different thicknesses of CoFeB are presented in Fig. 6.2(a). Note that the BLS measurement was performed in Damon-Eshbach (DE) geometry as shown schematically.

In all cases, in-plane applied field was 0.1 T/μ_0. By looking at these BLS spectra, it is evident that the frequency difference between Stokes and anti-Stokes peaks (Δf), which is the measure of the strength of iDMI, increases with decreasing CoFeB thickness. In the case of $t = 0.85$ nm, $\Delta f \approx 0.50$ GHz which is reasonably large for Ta/CoFeB/TaO$_x$ system.
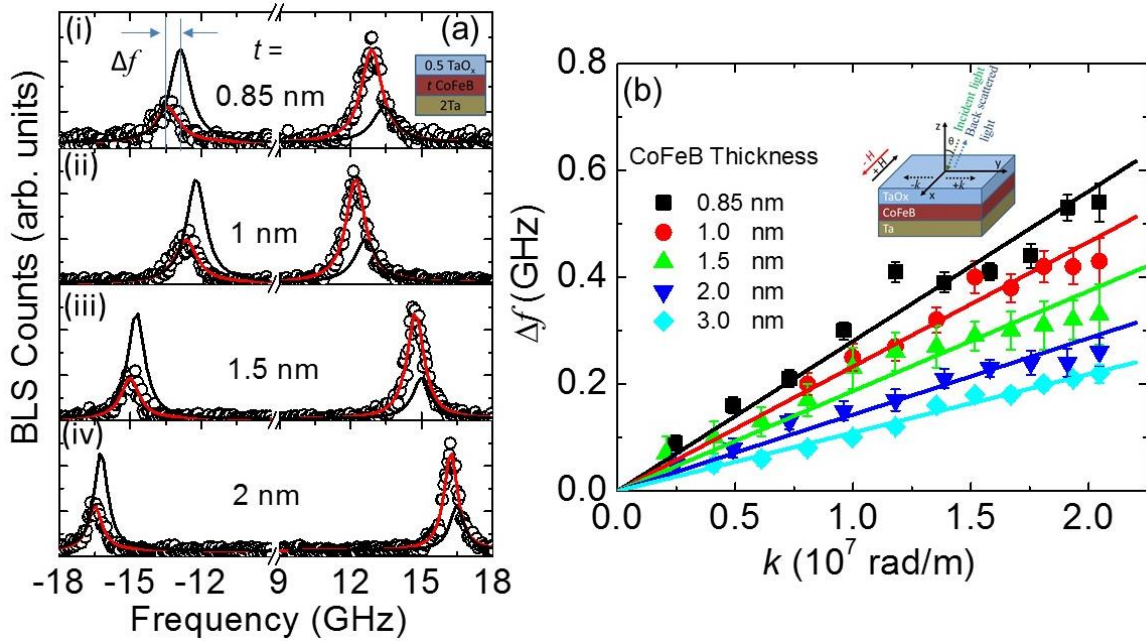
Figure 6.2: (a) Representative BLS spectra measured at wave vector $k = 2.04 \times 10^7$ rad/m for the Ta (2 nm)/ CoFeB (t)/TaO$_x$ (0.5 nm) sample for two counter propagating directions. The spectrum corresponding to particular thickness of CoFeB is indicated by mentioning thickness value in each panel. Solid curve is the fit using Lorentzian function. (b) Plot of Δf vs k for Ta (2 nm)/CoFeB (t)/TaO$_x$ (0.5 nm) samples with various values of t. Symbols represent the experimental data points and solid lines are the fit using Eq. (6.2). Inset: Schematic of the film stack along with BLS geometry.

To get a quantitative estimation of the iDMI, the variation of Δf as a function of k is displayed in Fig. 6.2(b) for all CoFeB thicknesses studied here. Considering $g = 2$ and taking $M_s = 900$ kA/m obtained from VSM measurement, D is obtained as 0.22 ± 0.03 mJ/m^2 from the slope of the linear correlation using Eq. (6.2) for the sample with $t = 0.85$ nm. Similar fitting procedure were applied for other thicknesses of CoFeB and D values were estimated from the slope of the linear fit. We observe that the value of D in these systems are modest in comparison to Pt/FM system [26]. Nevertheless, the pronounced DMI in our system (Ta/CoFeB) is almost three times higher than earlier reported values [37]. Earlier experimental studies of structural characterization in as-deposited and

annealed Ta/CoFeB/MgO have demonstrated that the boron predominantly resides in CoFeB for as-deposited stacks however it diffuses out to adjacent layers once the stacks are annealed [37, 38]. It has been shown that diffusion of B atoms from CoFeB during annealing process leads to the decrement in the strength of DMI [37, 39], primarily due to the segregation of B atoms at the Ta/CoFeB interface. As the film stacks investigated in the present study are as-deposited, hence we propose that such possibility of B diffusion is likely avoided. Further detailed micro-structural study to investigate the presence of boron in as deposited Ta/CoFeB/TaO$_x$ in future is needed to verify such proposition. In general, to achieve large perpendicular magnetic anisotropy and tunnel magneto-resistance Ta/CoFeB/TaO$_x$ stacks are annealed.
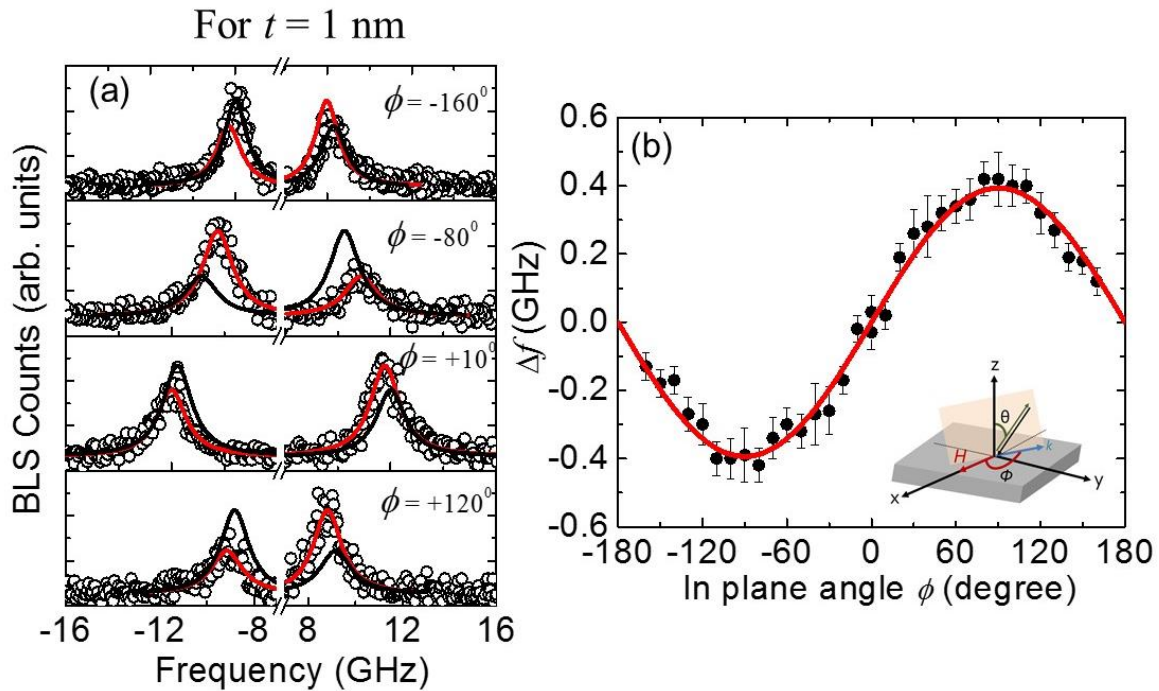
Figure 6.3: (a) BLS spectra of Ta (2 nm)/CoFeB (1 nm)/TaO$_x$ (0.5 nm) sample measured under H = 0.1 T/μ_0, k = 1.67 × 10^7 rad/m for various in plane angles ϕ. (b) The variation of frequency difference (Δf) between Stokes and anti-Stokes peak of Ta (2 nm)/CoFeB (1 nm)/TaO$_x$ (0.5 nm) sample with in-plane angle ϕ. Symbols represent the experimental data points and solid curve is the fit using Eq. (6.3). Inset: Schematic of the 180° backscattering geometry.

Apart from boron diffusion, annealing also causes intermixing which may reduce the iDMI. To cross check the wave-vector (k) dependent Δf measurements, we also performed

asymmetry in the spin-wave frequency as a function of the angle (ϕ) between the bias field and the wave vector k. The relationship between Δf and ϕ is given by Eq. (6.3) [40],

$$\Delta f(k) = \frac{2\gamma D k}{\pi M_S} sin\ \phi \tag{6.3}$$

BLS spectra were taken for values of ϕ in the range -180° ≤ ϕ ≤180° at an interval of 10° and at fixed wave vector $k = 1.67 \times 10^7$ rad/m. In Fig. 6.3(a), typical BLS spectra at various ϕ values are presented for the sample with $t = 1$ nm. It can be noted that Stokes and anti-Stokes peaks are clearly appeared in the BLS spectrum due to the thinness of the ferromagnetic film. According to the Eq. (6.3), the frequency difference between Stokes and anti-Stokes (Δf) peaks is maximal in the vicinity of ϕ = -90° and 90°, whereas it is almost negligible in the vicinity of -180°, 0° and 180°. Figure 6.3(b) shows the variation of Δf as a function of in-plane angle ϕ. To fit the experimental data, we use Eq. (6.3) with the same fitting parameters (like g and M_s) which was used to fit the experimental data of k-dependent BLS measurements. From the sinusoidal fitting, we extract the value of D as 0.19 ± 0.03 mJ/m² which matches reasonably well with the previously obtained value from k-dependent BLS measurements. It is worth to mention here that the error in D is estimated by considering the experimental uncertainties of Δf, M_s, g and k. The implementation of this method provides additional confirmation of reasonably high value of D in these samples.
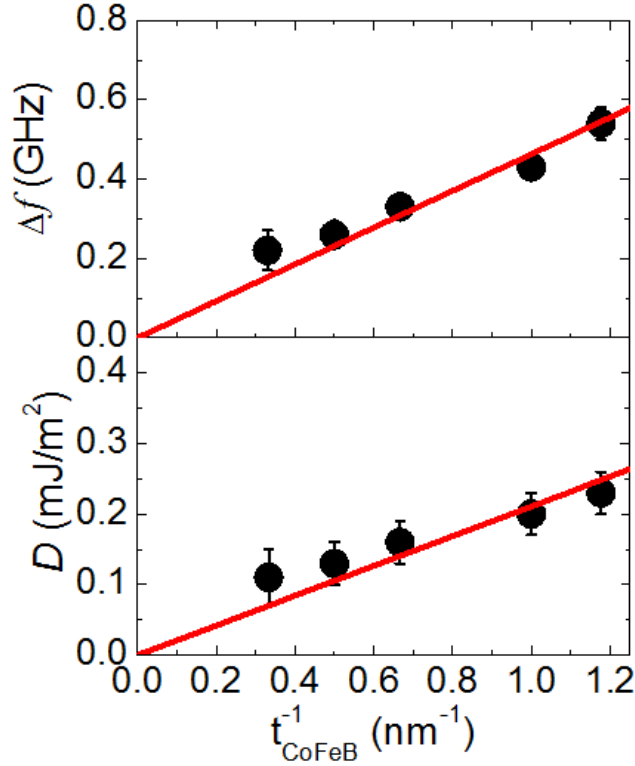
Figure 6.4: Variation of Δf (top panel) and D (bottom panel) with the inverse of CoFeB thickness. The error bar in Δf is shown by considering the error from the fitting of spectra as well as the instrumental resolution to determine the peak frequency and for D, errors in M_s as well as Δf have been taken into account. The red solid lines in both the cases are the linear fits.

We next investigate the dependence of the strength of iDMI on FM layer thickness t. Figure 6.4 shows the variation of Δf measured at $k = 2.04 \times 10^7$ rad/m (top panel) and deduced iDMI energy density D (bottom panel) with the inverse of CoFeB thickness. It is clear from these plots that both Δf and D increases almost linearly with decrease in the CoFeB thickness. The best linear fit to the inverse of CoFeB thickness dependence of Δf and D elucidate that both Δf and D approach zero as t tends to infinity confirming the interfacial origin of DMI in our samples. Importantly, this linear scaling behaviour does not deviate even for sub-nanometer thickness of CoFeB, which makes it potentially suitable candidate for spintronic devices utilizing interfacial effects.

To understand the effects of underlayer thickness on the strength of iDMI, we performed Ta underlayer thickness dependence of iDMI in samples described by Sub/dTa /1 $Co_{20}Fe_{60}B_{20}$/0.5 TaO_x, with d = 0, 0.5, 0.8, 1, 2, 3, 4, 5, 6 nm. To date, not much attention has been paid to explore the influence of underlayer thickness in the context of iDMI.
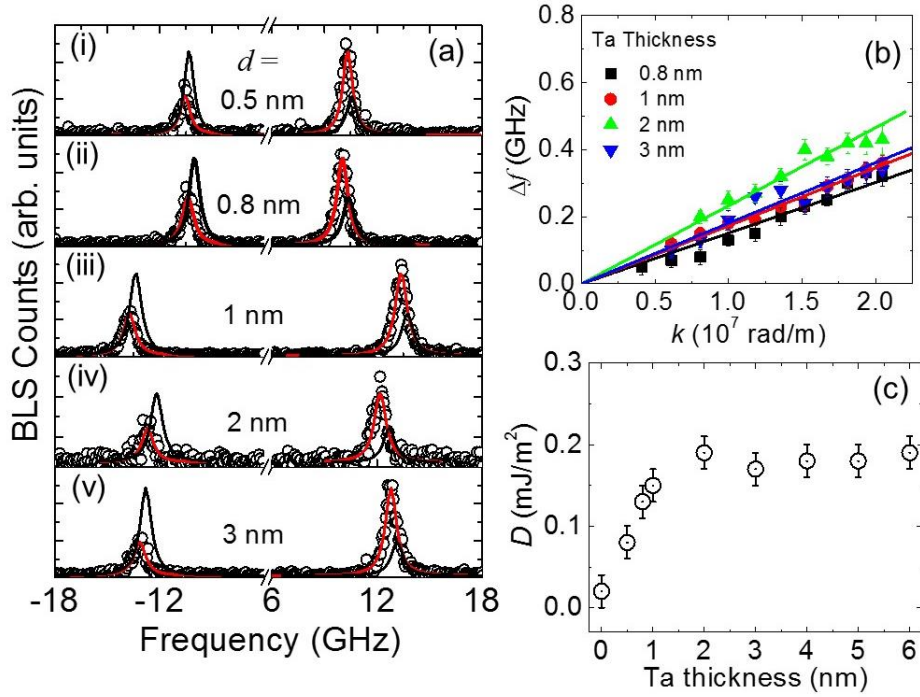
Figure 6.5: (a) Representative BLS spectra (i - v) measured at wave vector $k = 2.04 \times 10^7$ rad/m for the dTa/1 CoFeB/0.5 TaO$_x$ sample for two counter propagating directions. The spectrum corresponding to specific thickness of Ta is indicated by mentioning thickness value in each panel. Solid curve is the fit using Lorentzian function. (b) Variation of Δf with k for d Ta/1 CoFeB/0.5 TaO$_x$ samples with various d values. Symbols represent the experimental data points and solid lines are the fit using Eq. (6.2). (c) Variation of D with the Ta thickness.

Recently, Tacchi *et al.* studied the role of Pt thickness on the strength of iDMI in Pt/CoFeB revealing that D first increases and then saturates with Pt thickness [33]. Figure 6.5(a) shows the typical BLS spectra recorded for various d values at $k = 2.04 \times 10^7$ rad/m. It can be seen that Δf increases slightly as d increases from 0 to 2 nm and then saturates for $d \geq 2$ nm. To obtain the quantitative estimation of D, variation of Δf as a function of k has been presented in Fig. 6.5(b) for several d values, and extraction of D parameter is performed from the linear fit (using Eq. (6.2). In Fig. 6.5(c) the variation of D with Ta thickness is shown whose trend resembles well with the recent findings by Tacchi *et al.* [33] in their study of Pt/CoFeB films.

6.4. Conclusions

In summary, we have systematically studied the FM layer and HM underlayer thickness dependence of iDMI in technologically important Ta/CoFeB/TaO$_x$ heterostructure using

BLS spectroscopy. By measuring the spin-wave frequency non-reciprocity, we observe significantly large iDMI in these stacks likely due to the absence of B diffusion at the Ta/CoFeB interface as these films are unannealed. Furthermore, presence of large iDMI was also cross verified by the sinusoidal angular dependence of spin-wave non-reciprocity, Δf. In the case of FM thickness variation, we observe that D varies linearly with the inverse of CoFeB thickness demonstrating its purely interfacial origin, whereas in the case of Ta thickness dependence, D shows a sharp variation in the sub-nanometer thickness range and attains a nearly constant value above Ta thickness of 1 nm. Our detailed FM and HM thickness dependent studies will enrich the understanding regarding the tunability of iDMI in these heterostructures for controlling chiral spin structure and magnetic domain-wall based magnetic storage and memory devices.

References

[1] I.E. Dzyaloshinskii, Sov. Phys. JETP **5**, 1259 (1957).

[2] T. Moriya, Phys. Rev. **120**, 91 (1960).

[3] A. Fert, V. Cros, and J. Sampaio, Nat. Nanotechnol. **8**, 152 (2013).

[4] S. Mühlbauer, B. Binz, F. Jonietz, *et al.,,* Science **323**, 915 (2009).

[5] L. Liu, C.-F. Pai, Y. Li, *et al.,* Science **336**, 555 (2012).

[6] J. Kim, J. Sinha, M. Hayashi, *et al.,* Nat. Mater. **12**, 240 (2013).

[7] J. Sinha, M. Hayashi, A. J. Kellock, *et al.,* Appl. Phys. Lett. **102**, 242405 (2013).

[8] S. Ikeda, K. Miura, H. Yamamoto, *et al.,* Nat. Mater. **9**, 721 (2010).

[9] I. M. Miron, G. Gaudin, S. Auffret, *et al.,* Nat. Mater. **9**, 230 (2010).

[10] J. Torrejon, J. Kim, J. Sinha, *et al.,* Nat. Commun. **5**, 4655 (2014).

[11] K. S. Ryu, L. Thomas, S. H. Yang, and S. Parkin, Nat. Nanotechnol., **8**, 527 (2013).

[12] S. Emori, U. Bauer, S. M. Ahn, E. Martinez, and G. S. D. Beach, Nat. Mater. **12**, 611 (2013).

[13] G. Chen, T. Ma, A. T. N'Diaye, *et al.,* Nat. Commun. **4**, 2671 (2013).

[14] S. S. P. Parkin, M. Hayashi, and L. Thomas, Science, **320**, 190 (2008).

[15] M. Bode, M. Heide, K. von Bergmann, *et al.,* Nature **447**, 190 (2007).

[16] S. Heinze, K. von Bergmann, M. Menzel, *et al.,* Nat. Phys. **7**, 713 (2011).

[17] N. Romming, C. Hanneken, M. Menzel, *et al.,* Science **341**, 636 (2013).

[18] H. Yang, A. Thiaville, S. Rohart, A. Fert, and M. Chshiev, Phys. Rev. Lett. **115**, 267210 (2015).

[19] X. Ma, G. Yu, X. Li, *et al.*, Phys. Rev. B **94**, 180408 (2016).

[20] K. Zakeri, Y. Zhang, J. Prokop, *et al.*, Phys. Rev. Lett. **104**, 137203 (2010).

[21] I. Gross, L. J. Martínez, J. P. Tetienne, *et al.*, Phys. Rev. B **94**, 064413 (2016).

[22] V. E. Dmitrienko, E. N. Ovchinnikova, S. P. Collins, *et al.*, Nat. Phys. **10**, 202 (2014).

[23] S. Pizzini, J. Vogel, S. Rohart, *et al.*, Phys Rev. Lett. **113**, 047203 (2014).

[24] A. Thiaville, S. Rohart, É. Jué, V. Cros, and A. Fert, Europhys. Lett. **100**, 57002 (2012).

[25] M. Cubukcu, J. Sampaio, K. Bouzehouane, *et al.*, Phys. Rev. B **93**, 020401 (2016).

[26] K. Di, V. L. Zhang, H. S. Lim, *et al.*, Phys. Rev. Lett. **114**, 047201 (2015).

[27] K. Di, V. L. Zhang, H. S. Lim, *et al.*, Appl. Phys. Lett. **106**, 052403 (2015).

[28] J. Cho, N.-H. Kim, S. Lee, Nat. Commun. **6**, 7635 (2015).

[29] A. K. Chaurasiya, C. Banerjee, S. Pan, *et al.*, Sci. Rep. **6**, 32592 (2016).

[30] R. Soucaille, M. Belmeguenai, J. Torrejon, *et al.*, Phys. Rev. B **94**, 104431 (2016).

[31] G. Yu, L.-T. Chang, M. Akyol, *et al.*, Appl. Phys. Lett. **105**, 102411 (2014).

[32] G. Yu, P. Upadhyaya, K.L. Wong, *et al.*, Phys. Rev. B **89**, 104421 (2014).

[33] S. Tacchi, R. E. Troncoso, M. Ahlberg, *et al.*, Phys. Rev. Lett. **118**, 147201 (2017).

[34] D. Cortés-Ortuño and P. Landeros, J. Phys.: Condens. Matter **25**, 156001 (2013).

[35] H. Yu, S. Zhu, X. Yang, *et al.*, PLOS ONE **8**, e66447 (2013).

[36] J. J. Colin, G. Abadias, A. Michel, and C. Jaouen, Acta Mater. **126**, 481 (2017).

[37] R. Lo Conte, E. Martinez, A. Hrabec, *et al.*, Phys. Rev. B **91**, 014433 (2015).

[38] J. Sinha, M. Gruber, M. Kodzuka, *et al.*, J. Appl. Phys. **117**, 043913 (2015).

[39] R. A. Khan, P. M. Shepley, A. Hrabec, *et al.*, Appl. Phys. Lett. **109**, 132404 (2016).

[40] V. L. Zhang, K. Di, H. S. Lim, *et al.*, Appl. Phys. Lett. **107**, 022402 (2015).

Chapter 7

7. Direct Observation of Unusual Interfacial Dzyaloshinskii-Moriya Interaction in Graphene/NiFe/Ta Heterostructure

7.1. Introduction

One of the key motivations of modern spintronics research is to achieve low power consumption, faster information processing and higher storage density in thin-film based magnetic memory devices. Ferromagnetic (FM) thin films adjacent to nonmagnetic thin layers give rise to a range of important phenomena, relevant for the emergent field of spin-orbitronics. These include perpendicular magnetic anisotropy (PMA) [1], spin pumping [2], spin torque [3], spin Hall effect [4], Rashba effect [5, 6], interfacial Dzyaloshinskii-Moriya interaction (iDMI) [7] and chiral damping [8]. While most of these phenomena are associated with high spin-orbit interaction, and heavy metal (HM) layers are natural choices for the nonmagnetic layer, emerging materials like two-dimensional materials and topological insulators may also play important roles in engineering the interface magnetism. The iDMI, is an anti-symmetric exchange interaction which originates due to the broken inversion symmetry at the HM/FM interface, where HM possess high spin-orbit coupling [7]. It favors canted spin configurations which gives rise to various magnetization structures at the nanoscale such as skyrmions [9-11] and chiral helices [12]. In addition, it can improve domain wall velocities by suppressing Walker breakdown in magnetic racetrack memory devices and lead to non-reciprocal spin-wave propagation leading towards applications in the high-speed spin-wave logic device [13]. Recently, the direct observation of iDMI has been evidenced mainly in HM/FM/oxide heterostructures [14-25].

Graphene and other 2-D materials such as MoS_2 have shown promises in spintronics [26]. The fascinating properties of graphene such as massless Dirac Fermions in the linear dispersion of its electronic structure, well-defined monolayer formation, and long spin-diffusion length have created burgeoning interest in the scientific community for its applications in spintronics research [26-28]. The use of graphene in magnetic sandwich

structures which aims to search for new materials have been described theoretically as well as experimentally in the context of magnetic tunnel junctions [29-34]. In recent years, it has been shown that graphene plays a key role in Rashba effect [5, 6], enhancement of spin injection efficiency [35, 36] and quantum spin Hall effect [37]. Moreover, there is sufficient experimental evidence that the formation of graphene-metal contacts significantly modifies the electronic and/or magnetic properties of the interface and investigations related to charge transfer from metal to graphene have also been reported [38-40]. In addition, the weak spin-orbit coupling (SOC) in sp^2 carbon also suggested that electron spin should be carried nearly unaffected over unprecedented distances, making feasible, practical applications of lateral spintronics [41,42]. The in-plane sp^2 bonding is mainly responsible for the structural stability and mechanical strength of graphene, whereas out-of-plane $p\pi$ states control its transport and interfacial properties. Pioneering works initially resounded such high expectations [43], while more recent experimental results have confirmed the potential of graphene for transporting spin signal at room temperature over tens of micrometers, which makes it a better candidate for technological realization [36, 44, 45].

There is a recent report on the giant enhancement of PMA in Co-graphene heterostructures despite graphene having a small spin-orbit interaction, indicating the unusual nature of the graphene-FM interface [46]. A low-damage high-throughput grazing-angle sputter deposition on graphene has been successfully demonstrated [47]. However, the promotion of graphene-FM heterostructures for applications of spin-orbitronics has not been intensely started yet. Recently, Yang *et al.* have reported the observation of significant DMI at the graphene-FM interface by employing both first principle calculation and magnetic imaging experiments [48]. Most recently, Ajejas *et al.* have reported the existence of sizeable DMI at gr/Co interface from the Kerr experiments [49]. The physical origin of the observed DMI in both Ref. 48 and 49 was attributed to the conduction electron mediated Rashba effect originated at the graphene-FM interface. Yang *et al.* used Co films grown by molecular beam epitaxy (MBE) on chemical vapor deposited graphene on Ru (0001) substrate to demonstrate the DMI in their system. However, for applications, it is desirable to have DMI in systems that are easily compatible with standard Si based technology. Moreover, MBE is not an industry compatible growth method due to the lower growth rate. Hence, it is desirable to have

DMI in FM layer grown by sputtering, which is a simple, yet versatile deposition method used in industry.

In this paper, we demonstrate direct observation of iDMI in graphene/$Ni_{80}Fe_{20}$/Ta heterostructures grown on Si substrates by magnetron sputtering. We use asymmetric spin-wave dispersion probed by Brillouin light scattering (BLS), a technique which has already been established as a direct and reliable method of measuring the iDMI [14,15, 19,20]. We present a systematic study of iDMI as a function of the thickness of $Ni_{80}Fe_{20}$ and show that the iDMI in this system originate from the interface between $Ni_{80}Fe_{20}$ and graphene. Furthermore, by controlling the defects at the interface by Ar deposition pressure during growth of $Ni_{80}Fe_{20}$, we establish that the DMI in this system arises from the defect induced spin-orbit coupling. This is further supported by a correlation between the DMI and spin-mixing conductance, both of which are related to spin-orbit coupling.

7.2. Experimental Details

We have used high-quality commercial CVD graphene (from Graphenea) on a Si/SiO_2 substrate. A series of samples consisting of substrate/graphene/$Ni_{80}Fe_{20}$ (t)/Ta (2), with t = 3, 4, 6, 8, 10, 15 nm (digits indicate thickness in nm) were deposited at room temperature. NiFe/Ta bilayers were deposited with a varying thickness of NiFe using DC magnetron sputtering at varying Ar working pressure at 3 μTorr base pressure. The Ar working pressure for deposition of NiFe thin films on graphene is varied from 2 mTorr to 10 mTorr for intentionally tailoring the defects in the graphene layer. A set of reference samples of $Ni_{80}Fe_{20}$ (t)/Ta (2) were also simultaneously prepared on Si/SiO_2 substrates. The growth rate of NiFe is kept low at <1.4 Å/sec. The thickness of NiFe film was determined using x-ray reflectivity (XRR) technique for different Ar working pressure. The sputtering target was placed at an angle of 45° *w.r.t.* the surface of the substrate to minimize the possible bombardment of ions or neutral atoms on the graphene layer. The distance between the substrate and the sputtering target was approximately 8 cm.

In order to investigate the asymmetric SW dispersion caused by iDMI, BLS measurements were performed in DE geometry, *i.e.* by applying the magnetic field perpendicular to the plane of incidence of the laser beam. This allows for probing the spin waves propagating along the in-plane direction perpendicular to the applied field, *i.e.* in the DE geometry where the iDMI effect on the non-reciprocity in SW frequency is maximal at the room temperature. The details of the BLS measurement can be found elsewhere [14,19,20,50].

To get well defined BLS spectra for the larger incidence angles, the spectra were obtained after counting photons for several hours. We have also performed FMR measurements for calculating effective damping parameter (α_{eff}) and spin-mixing conductance ($g_{\uparrow\downarrow}$) using a co-planer waveguide (CPW) based broadband FMR set-up for excitation frequencies of 2–12 GHz. More details of the FMR setup can be found in Refs. [51] and [52].

7.3. Results and Discussions

The magnetization hysteresis loop measured by VSM at room temperature for the film stacks NiFe (10 nm)/Ta (2nm) and Gr/NiFe (10 nm)/Ta (2nm) are shown in Figure 7.1(a) and 7.1(b), respectively. It is observed that the value of saturation magnetization (M_s) in sample with graphene is little lower while the coercivity is a bit higher than the reference sample (without graphene underlayer).
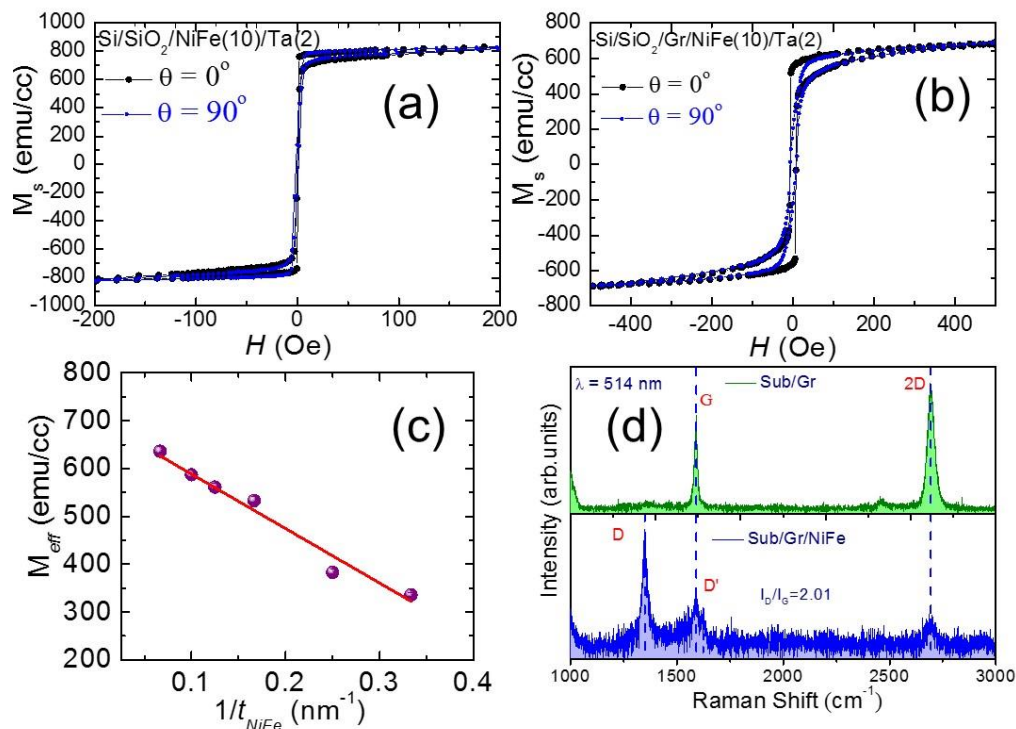
Figure 7.1: Magnetization hysteresis loop for sample stack (a) NiFe (10 nm)/Ta (2 nm) and (b) Gr/NiFe (10 nm)/Ta (2 nm) (deposited at 2-mTorr Ar working pressure) with magnetic field applied within the film plane. Here θ refers to the angle between two mutually perpendicular directions within the sample plane. (c) Variation of Meff (extracted from magnetic-field dependence using BLS) as a function of inverse of NiFe thickness in Gr/NiFe/Ta system. Red solid line is the best linear fit. (d) Raman spectra of CVD-grown graphene on Si/SiO2 before (top panel) and after (bottom panel) the deposition of NiFe (10 nm)/Ta (2 nm) bilayer thin films.

Fig. 7.1(c) shows the variation of effective magnetization (M_{eff}) (extracted from field dependent BLS measurement with the inverse of the NiFe thickness. A linear variation of M_{eff} with inverse of NiFe thickness with negative slope is observed. The *y*-inercept refers to the value of saturation magnetization (M_s). The M_s values obtained from field dependent BLS measurement agree well with that of VSM as well as FMR measurement. The Raman spectra of CVD grown graphene on a Si/SiO$_2$ before and after the deposition of NiFe (10 nm)/Ta (2 nm) bilayer thin films are shown in Figure 7.1(d). G and 2D peaks related to graphene are observed at 1590 cm^{-1} and 2695 cm^{-1}, respectively. The D peak observed in Fig. 7.1(d) (top panel) at 1349 cm^{-1} corresponds to the defects induced due to sputter deposition of NiFe/Ta bilayer, which is well known and appears due to intervalley scattering [47]. The D' peak observed in Fig. 7.1(d) (bottom panel) centered at 1620 cm^{-1} is also a disorder induced Raman peak, which comes from intravalley scattering. Spectral weights of graphene modes were obtained by fitting to Lorentzian function. We use the spectral weight ratio (I_D/I_G ratio) as a quantitative measure of sputtering damage. The I_D/I_G ratio for graphene after deposition of FM/capping layer is 2.01 ± 0.02, which indicates that some defects are introduced in the graphene layer after deposition. We calculate the average crystallite size (L_a) using the relation: $L_a = (2.4 \times 10^{-10})\lambda_{laser}^4 (nm) \left(\frac{I_D}{I_G}\right)^{-1}$, where λ_{laser} = 514 nm is excitation wavelength of laser used for Raman measurement [47], average nanocrystallite size (L_a) of 8.33 nm is obtained in our case. The vibrating sample magnetometer (VSM) measurement was performed to estimate the values of the saturation magnetization (M_s) of the samples. All the films are in-plane magnetized as revealed by VSM measurement.

To quantify the strength of iDMI in these graphene-based heterostructures, we measured the SW dispersion (*f* vs. *k*) relation at the applied in-plane field of *H* = 1 kOe. Here, transferred wave vector *k* was selected by changing the angle of incidence of the laser beam. The spin waves propagating in the opposite directions were simultaneously detected as Stokes and anti-Stokes peaks in the BLS spectra. In order to model our experimental data, we use the equation for the difference in the frequencies of counter-propagating spin waves given below [18]

$$\Delta f = \left\{ \frac{[f(-k,M_z)-(f(k,M_z))]-[f(-k,-M_z)-(f(k,-M_z))]}{2} \right\}; \tag{7.1}$$

$$\Delta f = \frac{2\gamma}{\pi M_s} Dk + \Delta\epsilon, \tag{7.2}$$

where M_z denotes the magnetization along applied magnetic field. $\Delta\epsilon(k) = \epsilon(K_\perp, k) - \epsilon(K_\perp, -k)$, where $K_\perp$ is the interfacial magnetic anisotropy, describes a correction in frequency due to interface anisotropy and any other offset.
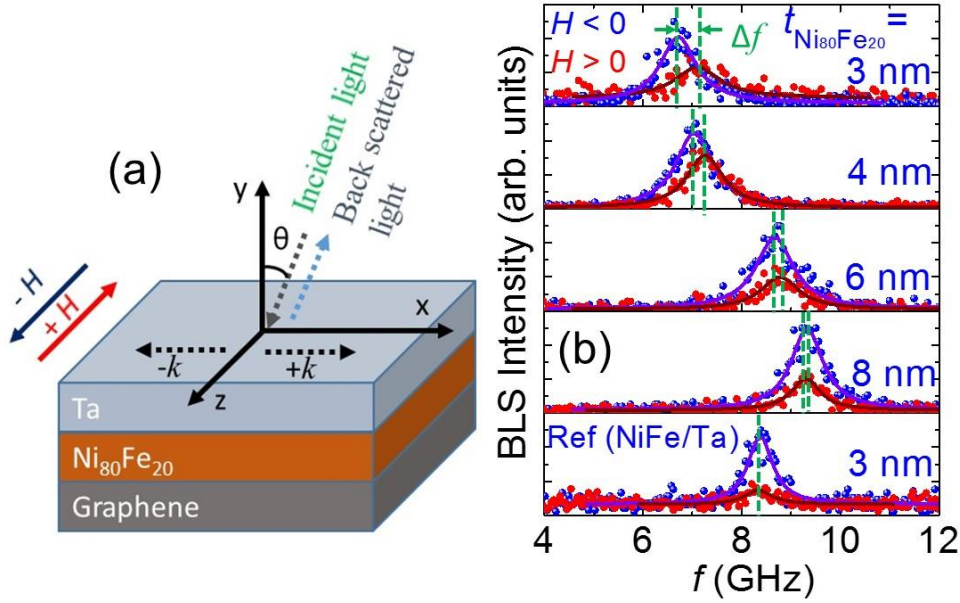
Figure 7.2: (a) Schematic of the film stack along with BLS geometry. (b) Representative BLS spectra for DE spin waves acquired at a fixed wave vector k = 18.1 rad/µm under oppositely oriented external applied fields H = 1 kOe in graphene/Ni$_{80}$Fe$_{20}$ (t)/Ta (2 nm) sample (deposited at 10 mTorr Ar pressure) (top four panels) and reference sample NiFe (3 nm)/Ta (2 nm) (at the bottom most panel) for two counter propagating directions of spin waves. The spectrum corresponding to particular thickness of Ni$_{80}$Fe$_{20}$ is indicated by mentioning thickness value in each panel. Solid curve is the fit using Lorentzian function.

The second term $\Delta\epsilon$ is very small compared to the first (DMI) term on the right-hand side. The first term is linear in D and k, where D is the iDMI constant. Here γ is the gyromagnetic ratio whereas M_s is the saturation magnetization. Therefore, Eq. (7.2) provides a direct way to quantify the strength of iDMI by experimentally measured quantities Δf, M_s and k. Figure 7.2(a) shows the schematic of the BLS measurement. As Eq. (7.2) suggests that the amount of frequency asymmetry is linear in k, typical BLS spectra for DE spin waves recorded at higher wave vector (k = 18.1 rad/µm) under oppositely oriented external magnetic fields in graphene/ Ni$_{80}$Fe$_{20}$ (t)/Ta (2), where t = 3, 4, 6, 8 nm, are presented in

Fig. 7.2(b). For clarity, anti-Stokes side of BLS spectra for oppositely oriented magnetic fields are shown with the corresponding Lorentzian fits. By looking at these BLS spectra, it is evident that the frequency difference between counter propagating spin waves (Δf), which is the measure of the strength of iDMI, decreases with increasing t (NiFe thickness). In the case of t = 3 nm, $\Delta f \approx 0.24$ GHz which is reasonably large for graphene/NiFe/Ta system. In addition, typical BLS spectra for reference sample (NiFe (3 nm)/Ta (2 nm)) is also presented in the lower panel of Fig. 7.2(b). Interestingly, almost negligible Δf is observed for the reference sample which ruled out the possibility of DMI contribution from the interface of NiFe and Ta capping layer. It should be noted here that such a large non-reciprocity in spin-wave frequency is indicative of the presence of iDMI in these systems. Earlier, Hehn *et al.* have shown that frequency non-reciprocity in Pt/NiFe, originated due to normal uniaxial interface anisotropy (NUIA), is weaker by an order of magnitude, which is almost negligible [16].

To quantify the magnitude of iDMI for various thicknesses of NiFe in graphene based heterostructures, full k-dependent BLS measurements have been performed by varying the angle of incidence of the laser beam under oppositely oriented magnetic fields. Figure 7.3(a) represents the variation of Δf as a function of the SW wave vector (k) for samples with different t. The best linear fit to the data using Eq. (7.2) provides the quantitative estimation of iDMI. The linear correlation of Δf with k thus yields a direct way of measuring the magnitude of iDMI. A maximum D of 67 ± 10 µJ/m^2 was observed for t = 3 nm from the slope of the linear correlation. This observation of significant and sizeable D in these graphene-based heterostructures, which can be attributed to the extrinsic spin-orbit coupling arising due to the presence of defects in graphene after FM/Ta deposition. In our case, conduction electron mediated Rashba-DMI mechanism may play a minor role as described recently by Yang *et al.* for graphene/FM systems as the thickness of the NiFe layers used in our experiment is much above the monolayer of NiFe [48].
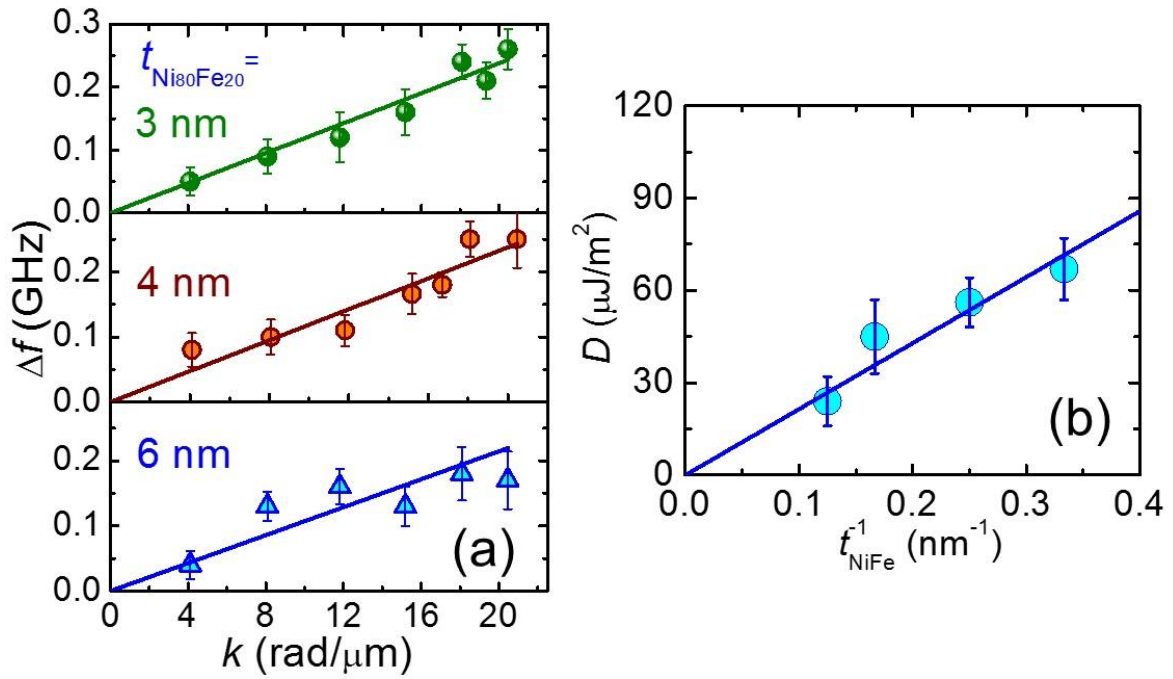
Figure 7.3: (a) Plot of Δf vs k for graphene/Ni$_{80}$Fe$_{20}$ (t_{NiFe})/Ta (2 nm) samples with various values of t_{NiFe}. Symbols represent the experimental data points and solid lines are the fit using Eq. (7.2). (b) Variation of D with the inverse of Ni$_{80}$Fe$_{20}$ thickness. The error bar in Δf is shown by considering the error from the fitting of spectra as well as the instrumental resolution to determine the peak frequency and for D, errors in M_s as well as Δf have been taken into account. The blue solid line is the linear fit.

Figure 7.3(b) shows the variation of D, extracted from the procedure mentioned above as a function of the inverse of Ni$_{80}$Fe$_{20}$ thickness. Interestingly, an almost linear scaling behaviour of D with the inverse of FM thickness is observed, which indicates its origin primarily from the graphene/FM interface. To further confirm the presence of iDMI in these heterostructures, reference samples (without graphene underlayer) were also measured. Importantly, almost negligible frequency asymmetry is observed in the reference sample.
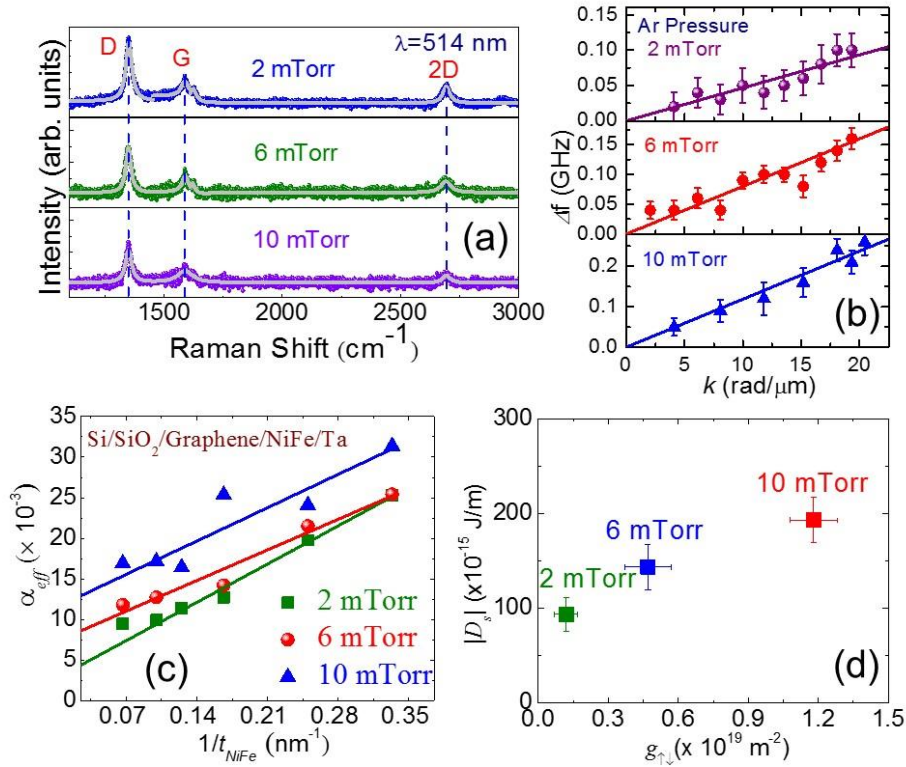
Figure 7.4: (a) Raman spectra of CVD grown graphene on a Si/SiO_2 after the deposition of NiFe (10 nm)/Ta(2 nm) bilayer thin films at different Ar pressure. (b) Plot of Δf vs k for graphene/NiFe (3 nm)/Ta (2 nm) samples deposited at various Ar pressure. Symbols represent the experimental data points and solid lines are the fit using Eq. (7.2). (c) Variation of effective damping constant with the inverse of NiFe thickness for various Ar pressure investigated from FMR measurement. (d) Plot of surface DMI constant with spin mixing conductance. Ar pressure value is mentioned on each data point.

Next, we investigate the effect of defects induced in graphene layer achieved by varying Ar pressure during NiFe layer deposition. Shown in Figure 7.4(a) are the Raman spectra taken after 10 nm of NiFe deposition at various Ar pressure. There is a substantial change in the Raman I_D/I_G ratio with Ar pressure as evident by analyzing the Raman data. We notice that the I_D/I_G ratio increases from 201% to 227% when Ar pressure increases from 2 mTorr to 10 mTorr. The I_D/I_G ratio and L_a for graphene/NiFe bilayer thin films with varying Ar pressure are summarized in Table 7.I. This observed behaviour can be explained by taking into account of the impact of Ar neutral atoms similar to Chen *et al.*, where a similar increase of I_D/I_G ratio was found with Ar pressure [47].

TABLE 7.I. Various parameters as a function of Ar working pressure during deposition of NiFe on graphene. I_D/I_G ratio is obtained from Raman spectra. Average crystallite size (L_a) is estimated from Raman spectra. Saturation magnetization (M_s) estimated from field dependent BLS measurement. Spin-mixing conductance ($g_{\uparrow\downarrow}$) is obtained from FMR measurement. The strength of surface DMI (D_s) is determined from BLS technique.

Ar working pressure (mTorr)	I_D/I_G	L_a (nm)	Saturation Magnetization (emu/cc)	Spin-mixing conductance (m^{-2}) × 10^{19}	Surface DMI constant (J/m) × 10^{-15}
2	(2.01 ± 0.02)	8.33 ± 0.08	708	0.12 ± 0.05	93 ± 10
6	(2.04 ± 0.02)	8.21 ± 0.07	670	0.47 ± 0.10	143 ± 10
10	(2.27 ± 0.02)	7.38 ± 0.06	606	1.18 ± 0.10	193 ± 10

The increase of defects with Ar pressure is also expected to give rise to a defect induced extrinsic spin-orbit coupling. In fact, theoretical calculations showed that sp^3 distortion induced by an impurity can lead to a large increase in the spin-orbit coupling in graphene [51]. There are also several experimental reports that show the presence of spin-orbit coupling in graphene by hydrogenation, fluorination or the presence of adatoms [52-54]. To investigate the effect of the defects on iDMI for graphene/NiFe based heterostructures, the variation of Δf as a function of spin-wave wave vector (k) for samples with t = 3 nm deposited at different Ar pressure is shown in Fig. 7.4(b). The data is well fitted with Eq. (7.2). The M_s values used in the fitting are shown in Table 1. These values are determined using BLS and FMR measurements and cross checked using vibrating sample magnetometer. The differennce in slopes of the linear fittings to the data points results from the variation of D in these samples. This variation of iDMI is likely due to the defect induced extrinsic spin-orbit coupling of graphene.

To further understand this behavior, we determined spin pumping from NiFe layer to graphene by FMR measurements. Similar to iDMI, spin pumping is also an interfacial effect, and hence a correlation between the two is expected, which is recently established

in ferromagnet/heavy metal systems [18]. According to the theory of spin pumping, the effective damping parameter, α_{eff} of the FM is given by:

$$\alpha_{eff} = \alpha_0 + \alpha_{SP} \qquad (7.3)$$

here α_0 is the intrinsic Gilbert damping, whereas α_{SP} is the damping due to spin-pumping effect, which is given by [2]:

$$\alpha_{SP} = \frac{\gamma h g_{\uparrow\downarrow}}{4\pi M_s t_{NiFe}} \qquad (7.4)$$

where, $g_{\uparrow\downarrow}$ is the spin-mixing conductance, and h is the Planck's constant. Other parameters carry the same meaning as discussed earlier in this paper.

From the FMR data we determine, the spin-mixing conductance ($g_{\uparrow\downarrow}$) by performing NiFe thickness dependent study. In comparison to our reference samples, an enhancement of damping parameter was observed in the sample with graphene consistent with Eq. (7.3). This enhancement can be attributed to spin pumping as previously reported for this system [55]. Figure 7.4(c) shows the variation of α_{eff} with the inverse of NiFe thickness ($1/t_{NiFe}$) for the samples deposited at various Ar pressure. From the linear fitting of the effective damping parameter versus the inverse of NiFe thickness with Eq. (7.3), we determine $g_{\uparrow\downarrow}$. The obtained values of $g_{\uparrow\downarrow}$ with different Ar pressure for the graphene/NiFe samples are displayed in the Table I. We see a clear increase of $g_{\uparrow\downarrow}$ with Ar pressure indicating an enhanced spin pumping with Ar pressure. This enhanced spin pumping with Ar pressure can be attributed to defect induced spin-orbit coupling at the interface. It is observed that surface DMI constant D_s ($D*t_{NiFe}$) and $g_{\uparrow\downarrow}$ both increase with the increase in Ar pressure, thus indicating a direct correlation between these two quantities. Figure 7.4(d), shows a plot of D_s with spin-mixing conductance $g_{\uparrow\downarrow}$, which clearly shows this correlation. This correlation, which is already established in the FM/HM system [18] and antiferromagnet (AFM)/FM system [25] further supports our claim that defect induced extrinsic spin-orbit coupling at the interface is the primary origin of iDMI in our system.
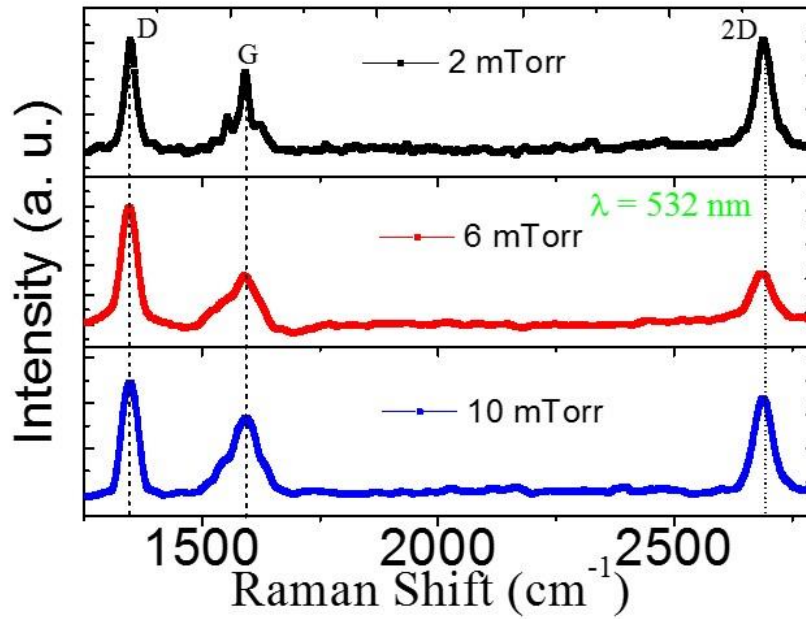
Figure7.5: Raman measurements for Gr/NiFe(3)/Ta(2) samples grown at different Ar working pressure.

Shown in Figure 7.5 represents the Raman spectra taken for Gr/NiFe (3)/Ta (2) for different Ar partial pressure. Since the Raman spectra in case of Gr/NiFe/Ta heterostructure degrades due to high thickness of metal above Gr, in the manuscript, we have shown Raman measurements with thick metal films to prove that, we are able to detect Graphene even after the 10 nm NiFe layer.
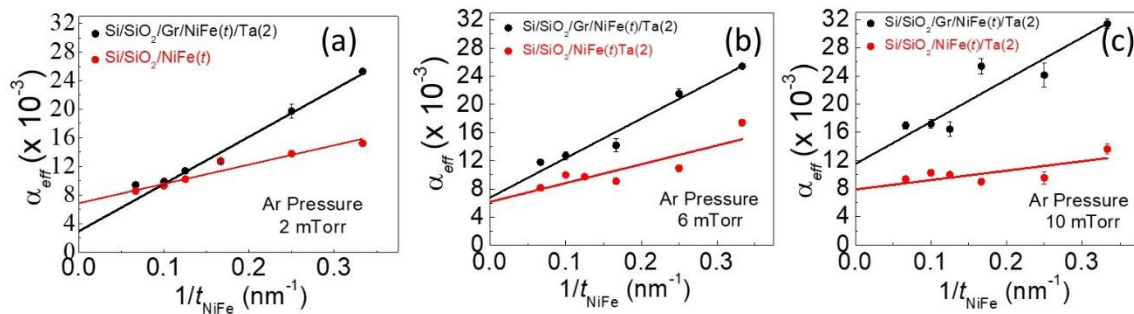
Figure 7.6: Variation of effective damping constant with the inverse of NiFe thickness for the samples with graphene and without graphene for various Ar pressure (a) 2 mTorr (b) 6 mTorr (c) 10 mTorr investigated from FMR measurement.

In order to determine the spin mixing conductance from FMR, measurement, a comparison of the behaviour of damping constant vs. inverse of FM thickness in Gr/NiFe and reference NiFe samples have been shown in Fig. 7.6. The slope of these curves for

125

Gr/NiFe samples are higher than the reference NiFe samples indicating an enhanced spin pumping.

7.4. Conclusions

In summary, we have systematically studied the FM layer thickness dependence of iDMI in technologically important graphene/Ni$_{80}$Fe$_{20}$/Ta heterostructures using BLS spectroscopy. By measuring the spin-wave frequency non-reciprocity, we observe a sizeable iDMI in these stacks. FM thickness variation reveals that D varies linearly with the inverse of NiFe thickness demonstrating its purely interfacial origin. Furthermore, we observe a tunability of surface DMI constant and spin-mixing conductance with defect density in the graphene layer obtained by varying Ar pressure during DC sputtering of NiFe. Remarkably, there is a direct correlation between surface DMI constant and spin-mixing conductance, while both are found to be correlated with the increase in defect density. Hence, we conclude that defect induced extrinsic spin-orbit coupling may play a major role in the observed iDMI in these samples. Our detailed FM layer thickness and Ar pressure dependent study of iDMI will enrich the understanding on the observation and tunability of iDMI in these 2D heterostructures for controlling chiral spin structure and magnetic domain-wall based magnetic storage, memory and logic devices.

References

[1] P. F. Carcia, A. D. Meinhaldt, and A. Suna, Appl. Phys. Lett. **47**, 178 (1985).

[2] Y. Tserkovnyak, A. Brataas, and G.E.W. Bauer, Phys. Rev. B **66**, 224403 (2002).

[3] J. C. Slonczewski, J. Magn. Magn. Mater. **159** L1 (1996).

[4] M. I. Dyakonov and V. I. Perel, Sov. Phys. JETP Lett. **13**, 467 (1971).

[5] X. Wang and A. Manchon, Phys. Rev. Lett. **108,** 117201 (2012).

[6] I. E. Dzyaloshinskii, Sov. Phys. JETP **5**, 1259 (1957).

[7] T. Moriya, Phys. Rev. **120**, 91 (1960).

[8] E. Jué, C.K. Safeer, M. Drouard, *et al.*, Nat. Mater. **15**, 272 (2015).

[9] S. Heinze, K. von Bergmann, M. Menzel, *et al.,* Nat. Phys. **7**, 713 (2011).

[10] H. Du, D. Liang, C. Jin, *et al.,* Nat. Commun. **6**, 7637 (2015).

[11] N. Nagaosa and Y. Tokura, Nat. Nanotechnol. **8**, 899 (2013).

[12] Y. Togawa, Y. Kousaka, K. Inoue, and J.-I. Kishine, J. Phys. Soc. Japan **85**, 112001 (2016).

[13] Y. Yoshimura, K.-J. Kim, T. Taniguchi, *et al.*, Nat. Phys. **12**, 157 (2015).

[14] H. T. Nembach, J. M. Shaw, M. Weiler, E. Jué, and T. J. Silva, Nat. Phys. **11**, 825 (2015).

[15] K. Di, V. L. Zhang, H. S. Lim, *et al.*, Phys. Rev. Lett. **114**, 047201 (2015).

[16] A. A. Stashkevich, M. Belmeguenai, Y. Roussigné, *et al.*, Phys. Rev. B **91**, 214409 (2015).

[17] J. Cho, N.-H. Kim, S. Lee, *et al.*, Nat. Commun. **6**, 7635 (2015).

[18] X. Ma, G. Yu, C. Tang, *et al.*, Phys. Rev. Lett. **120**, 157204 (2018).

[19] A.K. Chaurasiya, C. Banerjee, S. Pan, *et al.*, Sci. Rep. **6**, 32592 (2016).

[20] A.K. Chaurasiya, S. Choudhury, J. Sinha, and A. Barman, Phys. Rev. Appl. **9**, 014008 (2018).

[21] X. Ma, G. Yu, X. Li, *et al.*, Phys. Rev. B **94**, 180408(R) (2016).

[22] S. Tacchi, R. E. Troncoso, M. Ahlberg, *et al.*, Phys. Rev. Lett. **118**, 147201 (2017).

[23] G. W. Kim, A. S. Samardak, Y. J. Kim, *et al.*, Phys. Rev Appl. **9**, 064005 (2018).

[24] Y. Chen, Q. Zhang, J. Jia, *et al.*, Appl. Phys. Lett. **112**, 232402 (2018).

[25] X. Ma, G. Yu, S. A. Razavi, *et al.*, Phys. Rev. B **98**, 104428 (2018).

[26] A. H. Castro Neto, F. Guinea, N. M. R. Peres, K.S. Novoselov, and A.K. Geim, Rev. of Mod. Phys. **81**, 109 (2009).

[27] W. Han, R. K. Kawakami, M. Gmitra, and J. Fabian, Nat. Nanotechnol. **9**, 794 (2014).

[28] S. Roche, J. Åkerman, B. Beschoten, *et al.*, 2D Mater. **2**, 030202 (2015).

[29] E. Cobas, A. L. Friedman, O.M.J. van't Erve, J.T. Robinson, and B.T. Jonker, Nano Lett. **12,** 3000 (2012).

[30] T. M. G. Mohiuddin, E. Hill, *et al.*, IEEE Trans. Mag. **44**, 2624 (2008).

[31] S. Y. Dedkov, A. Generalov, E. N. Voloshina, and M. Fonin, Rap. Res. Lett. **5**, 226 (2011).

[32] R. Sato, T. Hiraiwa, J. Inoue, S. Honda, and H. Itoh, Phys. Rev. B **85**, 094420 (2012).

[33] V. M. Karpan, G. Giovannetti, P. A. Khomyakov, *et al.*, Phys. Rev. Lett. **99**, 176602 (2007).

[34] V. Lee, C. Park, C. Jaye, *et al.*, J. Phys. Chem. Lett. **1**, 1247 (2010).

[35] W. Han, K. Pi, K. M. McCreary, *et al.*, Phys. Rev. Lett. **105**, 167202 (2010).

[36] B. Dlubak, M.-B. Martin, C. Deranlot, *et al.*, Nat. Phys. **8,** 557 (2012).

[37] C. L. Kane and E. J. Mele, Phys. Rev. Lett. **95**, 226801 (2005).

[38] T. Aizawa, R. Souda, Y. Ishizawa, *et al.*, Surf. Sci. **237**, 194 (1990).

[39] K. Yamamoto, M. Fukushima, T. Osaka, and C. Oshima, Phys. Rev. B **45**, 11358 (1992).

[40] G. Giovannetti, P. A. Khomyakov, G. Brocks, V. M. Karpan, J. van den Brink, and P. J. Kelly, Phys. Rev. Lett. **101**, 026803 (2008).

[41] S. Roche and O. V. Sergio, J. Phys. D: Appl. Phys. **47**, 094011 (2014).

[42] S. Pierre, B.-M. Anne, and P. Frédéric, J. Phys.: Condens. Mat. **19**, 165222 (2007).

[43] N. Tombros, C. Jozsa, M. Popinciuc, H. T. Jonkman, and B. J. van Wees, Nature **448**, 571 (2007).

[44] M. H. D. Guimarães, P. J. Zomer, J. Ingla-Aynés, *et al.*, Phys. Rev. Lett. **113,** 086602 (2014).

[45] M. Drögeler, F. Volmer, M. Wolter, *et al*., Nano Lett. **14**, 6050 (2014).

[46] H. Yang, A. D. Vu, A. Hallal, *et al*., Nano Lett. **16**, 145 (2016).

[47] C. T. Chen, E. A. Casu, M. Gajek, and S. Raoux, Appl. Phys. Lett. **103**, 033109 (2013).

[48] H. Yang, G. Chen, A. A. C. Cotta, *et al*., Nat. Mater. **17**, 605 (2018).

[49] F. Ajejas, A. Gudín, R. Guerrero, *et al*., Nano Lett. **18**, 5364 (2018).

[50] R. Mock, B. Hillebrands, and R. Sandercock, J. Phys. E-Sci. Instru. **20**, 656 (1987).

[51] A.H. Castro Neto and F. Guinea, Phys. Rev. Lett. **103**, 026804 (2009).

[52] J. Balakrishnan, G. K. W. Koon, M. Jaiswal, A. H. C. Neto, and B. Özyilmaz, Nat. Phys. **9,** 284 (2013).

[53] D. Marchenko, A. Varykhalov, M.R. Scholz, *et al*., Nat. Commun. **3,** 1232 (2012).

[54] S. Irmer, T. Frank, S. Putz, *et al*., Phys. Rev. B **91**, 115141 (2015).

[55] A. K. Patra, S. Singh, B. Barin, *et al*., Appl. Phys. Lett. **101**, 162407 (2012).

Chapter 8

8. Improved Magnetic Damping and Interfacial Dzyaloshinskii Moriya Interaction in CoFeB|MgO with N-doped Ta Underlayer Investigated using Brillouin Light Scattering Technique

8.1 Introduction

With growing need to achieve perpendicular magnetic anisotropy (PMA) [1] in ultrathin films for spintronics based devices, it is important to develop solid understanding of magnetic inhomogeneity [2,3] and damping [4,5] in them. A high degree of magnetic uniformity over large length scale in ultrathin film is beneficial for device applications where interface magnetic properties play key role. Perpendicularly magnetized Ta|CoFeB|MgO heterostructure [6] is attracting much attention recently as it constitutes the heart of magnetic tunnel junction and the recently discovered three terminal devices [7]. It is known that in Ta|CoFeB|MgO heterostructure the PMA arises owing to electronic effect at CoFeB|MgO interface [6]. The choice of underlayer is also known to control the strength of magnetic anisotropy in these heterostructure [8]. It has been found recently that the PMA of Ta|CoFeB|MgO film can be tuned by changing the N-flow rate during Ta underlayer deposition [9]. Specifically, CoFeB|MgO films grown on optimally N-doped Ta underlayer has larger interface anisotropy than the film deposited on Ta underlayer. Due to complicated sample preparation for the direct structural characterization when the CoFeB thickness is ~ 1 nm (required in achieving PMA) [10] it is quite difficult to investigate the structural inhomogeneity which in turn leads to magnetic inhomogeneity [3, 11-15]. One of the main contributors of magnetic damping in the thin film is magnetic inhomogeneity whose precise control and understanding is worth to address. A reliable and non-destructive method to investigate magnetic inhomogeneity is the investigation of spin wave. Brillouin light scattering (BLS) is a powerful technique to study spin wave frequencies in magnetic thin films and multilayers [16-20]. Earlier in Giant Magneto resistive (GMR) structures spin wave spectra studies using BLS allowed deep

understanding of interlayer exchange coupling [21]. In a typical BLS measurements the laser is focused onto a sample, and the photons are inelastically back-scattered by the spin waves [18]. Due to momentum and energy conservation the events comprising of annihilation of magnons propagating towards the incoming laser beam (the anti-Stokes process), and creation of magnons propagating in the opposite direction (the Stokes process) take place. The linewidth of the BLS spectra contains the information of magnetic inhomogeneity [11,14-15] and in turn the magnon lifetime [2,3]. Earlier, the linewidth of the spin wave spectra in perpendicularly magnetized ultrathin films has been used to explain magnetic inhomogeneity both qualitatively and quantitatively [11, 15,22]. On the other hand, HM/FM/oxide heterostructure is also known to possess interfacial Dzyaloshinskii Moriya interaction (iDMI) which originates due to the breaking of structural inversion symmetry at the interface of heavy metal (HM) possessing strong spin-orbit coupling and ferromagnet [23-24]. The direct observation of IDMI has been possible from the asymmetric SW dispersion by employing BLS spectroscopy [25-31].

Using BLS technique here we investigate thermal spin waves in Ta(N)|CoFeB|MgO films. Peak frequency corresponding to uniform precession mode for zero wave vector is detected. The peak frequency varies with external applied field consistent with earlier reported results of perpendicularly magnetized and in-plane magnetized thin films. The magnetic inhomogeneity in these films is investigated by analyzing the linewidth of the BLS spectra. Furthermore, it is shown that the use of N-doped Ta underlayer in CoFeB|MgO heterostructure results in improved magnetic uniformity. Also, the asymmetric SW dispersion reveals the presence of increased iDMI in N-doped Ta underlayer in /CoFeB/MgO heterostructure [30].

8.2. Experimental Details

Thin films were grown by dc/rf magnetron sputtering in ultra-high vacuum (base pressure $\sim 2 \times 10^{-7}$ Pa) onto thermally oxidized Si [100] substrates (SiO$_2$ thickness is 100 nm). Ta and Co$_{20}$Fe$_{60}$B$_{20}$ layers were grown using dc power while MgO was deposited using rf power in Ar atmosphere. Nitrogen doping in the Ta underlayer was performed by mixing N$_2$ with Ar during Ta deposition. Based on the flow rate of N$_2$ and Ar during sputter deposition of Ta, we define a quantity $Q = S_{N2}/S_{Ar}+S_{N2}$. Q was varied up to 9% with $Q = 0$ corresponding to pure Ta underlayer. The film stacks investigated in the present study are Sub|1 Ta|1 CoFeB|2 MgO|1 Ta, Sub|4 TaN($Q\sim$1%)|1 CoFeB|2 MgO|1 Ta and

Sub|4 TaN($Q\sim9\%$)|1 CoFeB|2 MgO|1 Ta (digits represent thickness in nm). The films were subsequently annealed at 300 °C for one hour with no magnetic field applied during the process. The static magnetic properties of these films were measured using Vibrating Sample Magnetometer (VSM). The detailed film characteristics (magnetic dead layer thickness and interface anisotropy) have been described elsewhere [9]. As the aim of this work is to understand the magnetic inhomogeneity of ferromagnetic layer originating mainly due to underlayer/CoFeB interface, so we fix the CoFeB layer thickness to 1 nm. The magnetic dead layer thickness, if any, present in the stack will not be important for investigating magnetic inhomogeneity. Backscattered geometry was selected for performing BLS study of thermal spin waves. The main constituent of the set-up is a Sandercock-type six-pass tandem Fabry-Pérot interferometer [32]. Conventional 180° back scattered geometry was used along with the provision of wave-vector selectivity to investigate the spin-wave dispersion relation. In the light scattering process, total momentum is conserved in the plane of the thin film. As a result, the Stokes (anti-Stokes) peaks in BLS spectra correspond to creation (annihilation) of magnons with momentum $k = \frac{4\pi}{\lambda}\sin\theta$, where λ is the wavelength of the incident laser beam and θ refers to the angle of incidence of laser. A laser beam of wavelength 532 nm (from solid state laser) is focused on to the sample and the inelastically scattered light from the sample due to interaction between incident photons and magnons is analyzed to determine SW frequency. Here the frequency shift of the scattered beam from the incident laser frequency corresponds to thermally excited magnon frequency. An in-plane magnetic field H up to 3.1 kOe is applied parallel to the sample surface and perpendicular to the plane of incidence of light DE geometry. For the investigation of magnetic inhomogeneity in all these samples the BLS spectra is measured for $k = 0$ wave vector whereas for the investigation of the asymmetric SW dispersion caused by iDMI, k-dependent BLS measurement in DE geometry was performed for two different values of the applied magnetic field. Further details of BLS set up may be found in Ref [33].

8.3. Results and Discussions

Figures 8.1(a-c) show the hysteresis loops measured using VSM for in-plane and out-of-plane directions for three different Q values. The nominal CoFeB film thickness was fixed to 1 nm for all the measurement shown here. The saturation magnetization was calculated by dividing the measured moment value by volume of the ferromagnetic film

considering its nominal thickness. Effective anisotropy for the film was estimated by taking the areal difference between the IP and OOP hysteresis loops.
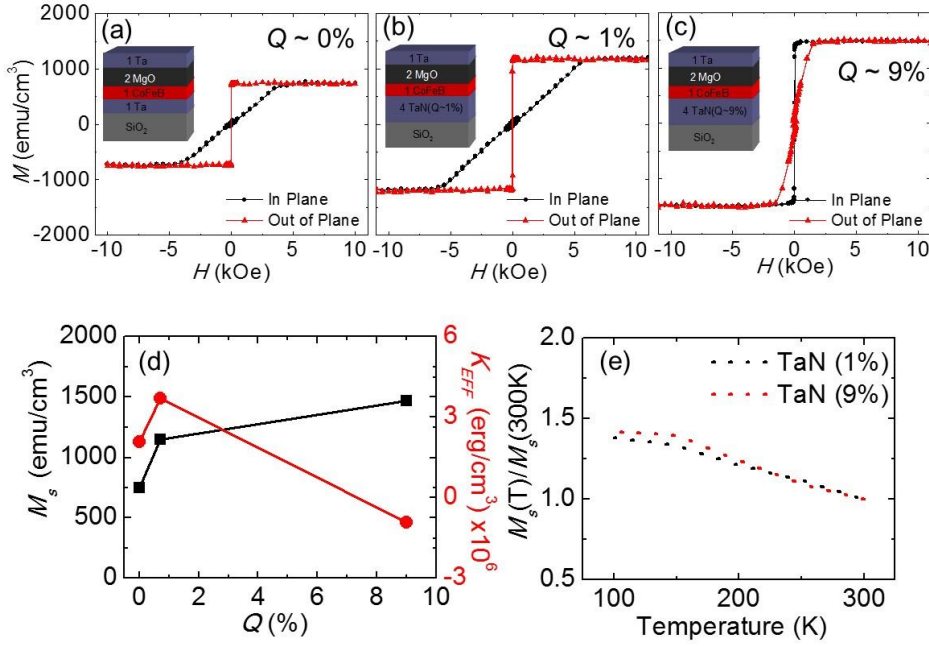
Figure 8.1: (a-c) In-plane and out-of-plane magnetic hysteresis loops plotted in same panel for $Q \sim 0$, 1 and 9%. Inset in each panel shows the schematic diagram of the stack. Digits in the schematic correspond to thickness in nm. (d) Saturation magnetization (left axis, square) and effective anisotropy (right axis, circle) plotted as a function of N-doping in the underlayer. (e) Relative change in the saturation magnetization plotted as a function of temperature for $Q \sim 1\%$ and $Q \sim 9\%$.

The positive K_{eff} corresponds to OOP easy axis for M whereas the negative K_{eff} corresponds to in-plane easy axis. In Fig. 1(d) we plot the saturation magnetization (left axis) and K_{eff} (right axis) as a function of Q. With increase in Q the M_s increases monotonically. The K_{eff} increases for $Q \sim 1\%$, however it reduces to negative value corresponding to in-plane easy axis for $Q \sim 9\%$. In Fig. 8.1(e) we show the relative change in M_s when the temperature is lowered to 100 K for $Q \sim 1\%$ and $Q \sim 9\%$ films. We observe 42% and 38% increase in M_s for $Q \sim 1\%$ and $Q \sim 9\%$ films at 100K respectively. Earlier for $Q \sim 0\%$ 32% increase in M_s has been reported [34]. From these studies we understand that these films are thermally robust within the temperature cycling between 300K to 100K.
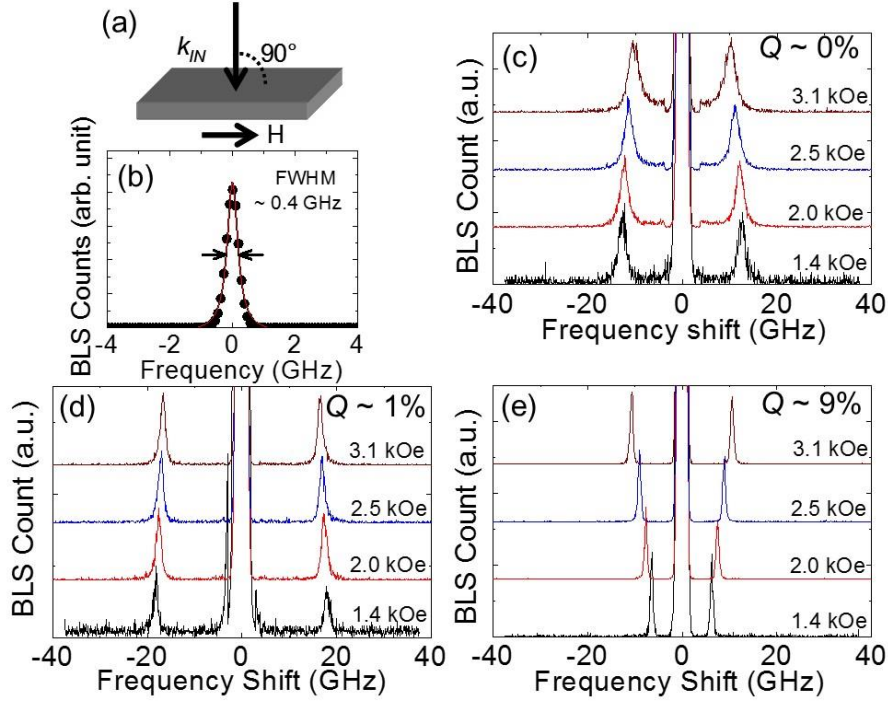
Figure 8.2: (a) Schematic for BLS measurement geometry. (b) Lorentzian fit to a typical elastic peak in the BLS spectra. (c)-(e) BLS spectra of the Ta(N)|CoFeB|MgO films at different applied fields for $Q \sim 0$, 1% and 9% underlayer. Field values are mentioned for corresponding spectra.

In Fig. 8.2(a) we show the measurement schematic for BLS experiment. The laser light impinges at 90° on the sample (parallel to sample normal) thus enabling the measurement for $k = 0$ wave vector. An IP magnetic field H up to 3.1 kOe was applied parallel to the sample surface and orthogonal to incident laser beam. In Fig. 8.2(b) we show the Lorentzian fit to a typical elastic peak of the BLS spectra to get an estimate of instrumental linewidth broadening [35]. From the fit we obtain the value of linewidth broadening ~ 0.4 GHz which gives the measure of lower limit of the linewidth in our BLS spectra. The typical BLS spectra obtained for the film stack are shown in Fig. 8.2(c-e). Note that we see the peaks corresponding to the uniform precession mode in all cases due to magnon creation (Stokes) and magnon annihilation (anti-Stokes) resulting from SW excitation. Negligibly small difference is found in the intensity, peak frequency and linewidth between Stokes and anti-Stokes peaks at any applied field. The magnitude of the observed frequency is related to the effective magnetization (M_{eff}) [36]. For OOP magnetized films the $4\pi M_{eff}$ is estimated using Eq. (8.1) [36]

$$4\pi M_{eff} = 4\pi M_S - \frac{2K_{eff}}{M_S} \tag{8.1}$$

We use the M_s and K_{eff} values extracted from the VSM measurement. For Ta and TaN (1%) underlayer films we obtain $4\pi M_{eff}$ of -5.5 kOe and -6.5 kOe, respectively from Eq. (8.1). The larger peak frequency observed in the case of TaN (1%) is due to larger effective anisotropy and M_{eff} of this film. The BLS peaks as shown in Fig. 8.2(c-e) are fitted using Lorentzian function and the peak frequency and the linewidth (full width at half maximum, FWHM) are obtained.
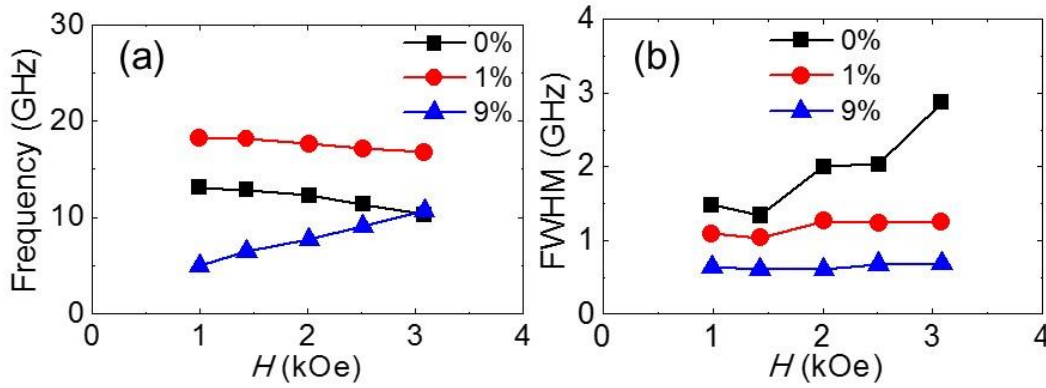
Figure 8.3: Variation of peak frequency (a) and linewidth (b) with applied magnetic field for all three film stacks.

In Fig. 8.3(a) and 8.3(b) the peak frequency and the linewidth obtained from the anti-Stokes peaks as a function of the applied IP magnetic field are shown for all three films. From Fig. 8.3(a) we notice that the films with Ta and TaN (1%) underlayers show a decrease in frequency with the increase in applied magnetic field. For the PMA film, it is known that on increasing the strength of applied IP magnetic field the peak frequency first decreases and reaches a minimum at critical field followed by a subsequent increase. The angle between the magnetization and the film plane is determined by the competition between the PMA and the applied IP field. The critical field corresponds to the field at which the magnetization is oriented along the film plane at particular applied field. In contrary, the film with TaN (9%) underlayer shows an increase in the frequency with the increase in applied field, a signature of in-plane magnetized ferromagnetic thin film.

To further understand the dependence of the peak frequency on applied in-plane magnetic field in perpendicularly magnetized films (Ta and TaN (1%)) the data is fitted using Eq. 8.2. [37]

$$\left(\frac{\omega}{\gamma}\right)^2 = (H_C^2 - H^2) + \frac{4\pi M_S N_{//}}{H_C}(H_C^2 + H^2) \tag{8.2}$$

where $N_{//}$ is the demagnetization factor, $\gamma = \gamma_e g/2$ is the gyro magnetic ratio, $\gamma_e = 1.759 \times 10^7$ Hz/Oe is the value for free electron, g is the spectroscopic splitting factor and H_c is the critical field [37]. Considering the film to be isotropic within the film plane we can assume $N_{//} \equiv N_{xx} \approx N_{yy}$. As the demagnetization factors satisfy $N_{xx} + N_{yy} + N_{zz} = 1$ and the films have thickness ~1 nm, we may assume $N_{zz} = 1$ and $N_{//} \approx 0$. The fits using Eq. 8.2 for Ta and TaN (1%) underlayer cases are shown using red solid curves in Fig. 8.4(a) and 8.4(b). The intercept on x-axis made by the red curve represents the critical field at which the peak frequency takes minima. The critical field obtained using the fit nearly matches to the saturation field for the hard axis loop estimated using VSM. From the fit we obtain $H_c \approx 4.8$ kOe for Ta and $H_c \approx 6.6$ kOe for TaN(1%) underlayer films.

In Fig. 8.4(c) we show the dependence of frequency on applied field for the in-plane magnetized TaN(9%) underlayer film. The increase in frequency with the increase in bias field is fitted using standard Kittel Eq. (8.3) [37] as shown by the red solid curve in Fig. 8.4(c).

$$f = \frac{\gamma}{2\pi}\sqrt{\left(H + \frac{2K}{M_S}\right)\left(H + \frac{2K}{M_S} + 4\pi M_{eff}\right)} \tag{8.3}$$

Here K is the in-plane anisotropy. Here, we use $g = 1.9$ and $K = 0$ and determine $4\pi M_{eff}$ as fitting parameter. The obtained value of $4\pi M_{eff}$ from the fit is 2.2 kOe. From the fits in Figs. 4(a)-(c) we infer that peak frequency dependence on applied magnetic field for Ta, TaN(1%) is consistent with OOP case [36] and TaN(9%) is consistent with in-plane case of previously reported literatures [37]. For PMA films in our experiment to precisely estimate the minimum frequency in the vicinity of critical field similar to Ref [36] is quite challenging. It is primarily due to the fact that the maximum magnetic field achievable in our set-up is well below the critical field. We hope to address this issue in future.

We now discuss below the linewidth of the BLS spectra and its dependence on the Q as well as the applied magnetic-field (peak frequency). The linewidth shows a drastic reduction with the increase in Q over the whole range of the applied magnetic field (Fig. 8.3(b)), indicating a significant reduction in the damping parameter with Q. In addition, within the investigated field range (upto 3.1 kOe), the linewidth of the film with Ta underlayer increases by nearly by a factor of two with applied magnetic field whereas the

linewidth of films with TaN(1%) and TaN(9%) underlayer show negligibly small increase with applied field (Fig. 8.3(b)).
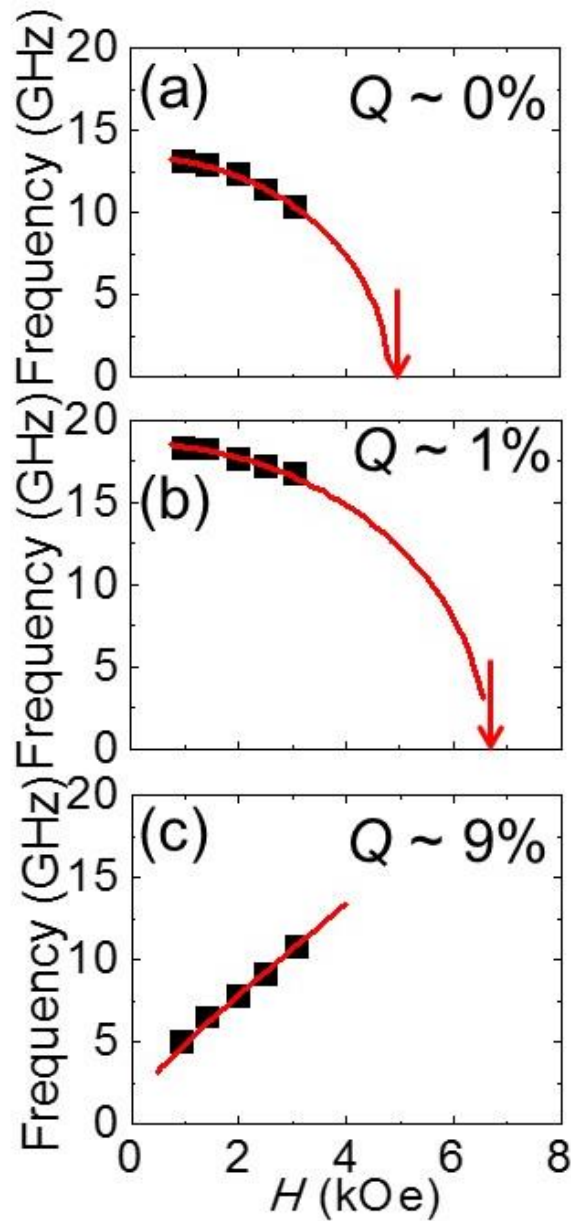
Figure 8.4: (a) and (b) Peak frequency dependence on field fitted using standard expression for Ta and TaN (1%) underlayer samples with PMA. The red curve shows the fit using Eq. 8.2. (c) Plot of frequency dependence on field for TaN(9%) underlayer film. The red curve shows the fit using standard Kittel Eq. 8.3.

The behavior of linewidth in a PMA film across the critical field has been earlier investigated for Co/Au film and extremely large linewidth at critical field has been

reported [15]. Due to diverging nature of the linewidth when the critical field (4.8 kOe) is approached we observe the significant increase of linewidth for Ta underlayer. For the case of TaN (1%), since the applied in-plane field is well below the critical field (6.6 kOe), we do not observe remarkable increase in the linewidth. In order to get more insight into these results, the linewidth of the BLS spectra for all three films are plotted as a function of the peak frequency in Figs. 8.5 (a-c). The sharp decrease in linewidth with increasing frequency for film with Ta underlayer indicates extrinsic contribution (interfacial roughness [14] or structural inhomogeneity [12, 13]) to the magnetic inhomogeneity in this film. In contrary, a nearly constant linewidth for TaN (1%) and TaN (9%) underlayers indicate that the extrinsic factors contributing to magnetic inhomogeneity are suppressed by doping N into the underlayer.

It is worth mentioning here that the linewidth data shown in Fig. 8.3 and Fig. 8.5 are not deconvoluted to remove the contribution for instrumental broadening [35]. Note that in the linewidth data contribution due to the spectrometer broadening will be uniformly present in the BLS signal for all three films and thus it will not change our interpretation.
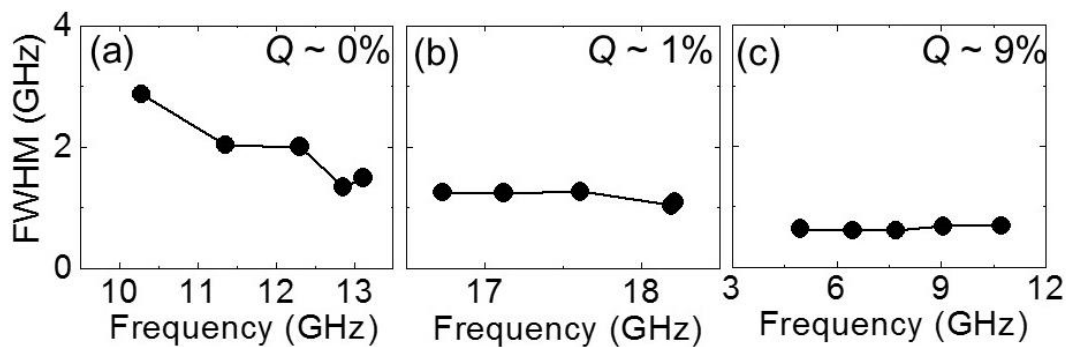
Figure 8.5: Variation of the linewidth (FWHM) of the BLS spectra with peak frequency for the samples with (a) $Q = 0\%$, (b) $Q = 1\%$ and (c) $Q = 9\%$.

Despite of presence of instrumental linewidth broadening in the BLS spectra, we are able to extract crucial information of reduction of interfacial roughness in these ultra-thin films. An important point to note here, using other characterization techniques e.g., transmission electron microscopy or grazing angle X-ray diffraction to study the interfacial roughness is quite challenging. It may also be possible that the improved structure related magnetic uniformity in TaN(1%) film assist to some extent in achieving larger PMA in this film as observed earlier [9]. A detailed study of linewidth for large field

range for both in-plane and out-of-plane direction and for different k vectors will be useful for the detailed quantitative understanding of magnetic inhomogeneity in these films.
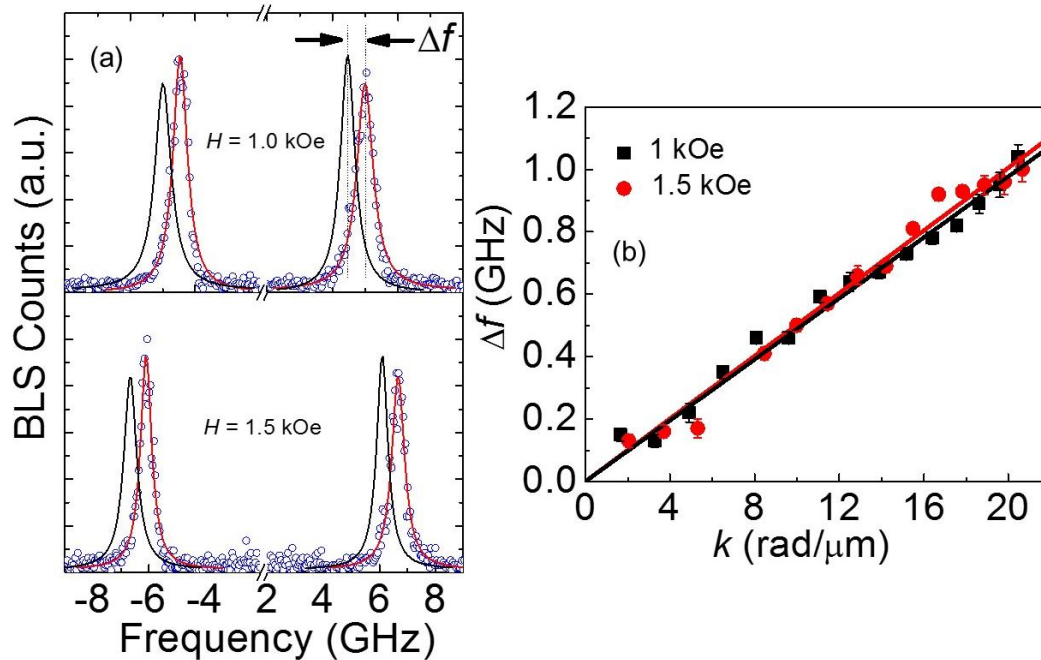
Figure 8.6: (a) Representative BLS spectra measured at wave vector k = 16.7 rad/μm for the Sub|4 TaN(9%)|1 CoFeB|2 MgO|1 Ta sample for two counter propagating directions. The spectrum corresponding to particular applied magnetic field is indicated by mentioning its value in each panel. Solid curve is the fit using Lorentzian function. (b) Plot of Δf vs k for both values of H. Symbols represent the experimental data points and solid lines are the fit using Eq. (8.4).

Nevertheless, the observation of large enough perpendicular magnetic anisotropy (~ 6.5 kOe) and reduced spin wave linewidth (damping [38]) by a factor of 2, that is nearly independent of applied field (spin wave frequency) for the film with Q~1% (N-doped Ta underlayer) is important for application in spin transfer torque magneto-resistive random access memory (STT-MRAM) devices due to the larger thermal stability and smaller write current. In addition, the in-plane magnetized sample (Q = 9%) showed the smallest linewidth (estimated damping of ~0.006 using Ref. [38]), which would be useful for magnonic devices where a long propagation length of the SWs is required.

Next, we investigate the presence of iDMI in the sample Sub|4 TaN(9%)|1 CoFeB|2 MgO|1 Ta. For that, k – dependent BLS measurement is performed in DE geometry. Shown in Figure 8.6(a) is the representative BLS spectra taken at k = 16.7 rad/um for applied

magnetic field H = 1 kOe (top panel) and 1.5 kOe (lower panel). The spectra consisting of Stokes and anti-Stokes peak are well fitted with the Lorentzian function in order to extract SW frequency. It can be seen that there is a significant amount of frequency non-reciprocity (frequency difference between Stokes and anti-Stokes peak (Δf)) present in the system. To get a quantitative estimation of the iDMI, the variation of Δf as a function of k is displayed in Fig. 8.6 (b) for two values of applied magnetic field. We use the equation for the difference in the frequencies of counter-propagating spin waves given below:

$$\Delta f = [\omega(-k) - \omega(k)]/2\pi = \frac{2\gamma}{\pi M_s}Dk \tag{8.4}$$

Considering g = 1.9 (used previously) and taking M_s = 1480 kA/m obtained from VSM measurement, D is obtained as 0.72 ± 0.03 mJ/m^2 from the slope of the linear correlation using Eq. (8.4). It is important to mention here that the TaN/FM system resulted into a dramatic increase of iDMI strength as opposed to Ta/FM system [33].

8.4. Conclusions

In summary, we have investigated SW spectra in Ta(N)|CoFeB|MgO films using BLS technique. Frequency corresponding to uniform precession mode in the BLS spectra of perpendicularly magnetized as well as in-plane film is found. For out-of-plane magnetized sample the spin wave frequency takes minima at a critical field which corresponds to the anisotropy field. The linewidth decreases by nearly a factor of 2, which suggests that the magnetic inhomogeneity reduces with enhanced N-doping in the Ta underlayer. The reduced inhomogeneity in these films by modifying underlayer|CoFeB interface indicates in a large reduction in the value of magnetic damping, which is important for applications in both spintronic and magnonic devices. Moreover, the DMI investigation reveals stronger DMI of 0.72 mJ/m^2 present in TaN(9%)/CoFeB/MgO heterostructure. Our study will be important for understanding the spin wave dynamics as well as stabilizing DMI assisted Skyrmion structure in CoFeB with N-doped Ta underlayer.

References

[1] M. T. Johnson, P. J. H. Bloemen, F. J. A. denBroeder, and J. J. deVries, Rep. Prog. Phys., **59**, 1409 (1996).

[2] B Hillebrands, in *Modern Techniques for Characterizing Magnetic Materials* edited by Y. Zhu (Kluwer Academic, Boston, 2005).

[3] R. L. Stamps, R. E. Camley, B. Hillebrands, and G. Guntherodt, Phys. Rev. B, **47**, 5072 (1993).

[4] J. M. Shaw, H. T. Nembach, and T. J. Silva, Appl. Phys. Lett., **105**, 062406 (2014).

[5] R. D. McMichael, D. J. Twisselmann, and A. Kunz, Phys. Rev. Lett. **90**, 227601 (2003).

[6] S. Ikeda, K. Miura, H. Yamamoto, *et al.*, Nat. Mater. **9**, 721 (2010).

[7] L. Liu, C.-F. Pai, Y. Li, *et al.*, Science, **336**, 555 (2012).

[8] D. C. Worledge, G. Hu, D. W. Abraham, *et al.*, Appl. Phys. Lett. **98**, 022501 (2011).

[9] J. Sinha, M. Hayashi, A. J. Kellock, *et al.*, Appl. Phys. Lett. **102**, 242405 (2013).

[10] J. Sinha, M. Gruber, M. Kodzuka, *et al.*, J. Appl. Phys. **117**, 043913 (2015).

[11] K. Hyomi, A. Murayama, J. Eickmann, and C. M. Falco, J. Magn. Magn. Mater. **528**, 198 (1999).

[12] J. M. Shaw, H. T. Nembach, and T. J. Silva, J. Appl. Phys. **108**, 093922 (2010).

[13] M. L. Schneider, T. Gerrits, A. B. Kos, and T. J. Silva, J. Appl. Phys. **102**, 053910 (2007).

[14] A. Murayama, K. Hyomi, J. Eickmann, and C. M. Falco, J. Appl. Phys. **82**, 6186 (1997)

[15] A. Murayama, K. Hyomi, J. Eickmann, and C. M. Falco, Phys. Rev. B, **58**, 8596 (1998).

[16] B. Hillebrands, Phys. Rev. B, **41**, 530 (1990).

[17] B. Hillebrands, P. Baumgart, and G. Guntherodt, Phys. Rev. B **36**, 2450 (1987).

[18] P. Grunberg, Topics in Appl. Phys. **66**, 303 (1989).

[19] M. Vohl, J. Barnas, and P. Grunberg, Phys. Rev. B **39**, 12003 (1989).

[20] J. Barnas, and P. Grunberg, J. Magn. Magn. Mater. **82**, 186 (1989).

[21] F. Saurenbach, J. Barnas, G. Binasch, *et al.*, Thin Solid Films, **175**, 317 (1989).

[22] A. Murayama, K. Hyomi, J. Eickmann, and C. M. Falco, Phys. Rev. B, **61**, 8984 (2000).

[23] I. E. Dzyaloshinskii, Sov. Phys. JETP **5**, 1259 (1957).

[24] T. Moriya, Phys. Rev. **120**, 91 (1960).

[25] K. Di, V. L. Zhang, H. S. Lim, *et al.*, Phys. Rev. Lett. **114**, 047201 (2015).

[26] A.K. Chaurasiya, C. Banerjee, S. Pan, *et al.*, Sci. Rep. **6**, 32592 (2016).

[27] A. A. Stashkevich, M. Belmeguenai, Y. Roussigné, *et al.*, Phys. Rev. B **91**, 214409 (2015).

[28] J. Cho, N.-H. Kim, S. Lee, *et al.*, Nat. Commun. **6**, 7635 (2015).

[29] X. Ma, G. Yu, C. Tang, *et al.*, Phys. Rev. Lett. **120**, 157204 (2018).

[30] A.K. Chaurasiya, S. Choudhury, J. Sinha, and A. Barman, Phys. Rev. Appl. **9**, 014008 (2018).

[31] X. Ma, G. Yu, X. Li, T. Wang, D. Wu, K. S. Olsson, Z. Chu, K. An, J. Q. Xiao, K. L. Wang, and Xiaoqin Li, Phys. Rev. B **94**, 180408(R) (2016).

[32] R. Mock, B. Hillebrands, and R. Sandercock, J. Phys. E-Sci. Inst. **20**, 656 (1987).

[33] A. Haldar, C. Banerjee, P. Laha, and A. Barman, J. Appl. Phys., **115**, 133901 (2014).

[34] J. Kim, J. Sinha, S. Mitani, *et al.*, Phys. Rev. B **89**, 174424 (2014).

[35] W. F. Oliver, C. A. Herbst, S. M. Lindsay, and G. H. Wolf, Rev. of Sci. Instr. **63**, 1884 (1992).

[36] J. R. Dutcher, J. F. Cochran, I. Jacob, and W. F. Egelhoff, Phys. Rev. B, **39**, 10430 (1989).

[37] G. Gubbiotti, G. Carlotti, S. Tacchi, *et al.*, Phy. Rev. B, , **86**, 014401 (2012).

[38] V. E. Demidov, S. Urazhdin, E. R. J. Edwards, and S. O. Demokritov, Appl. Phys. Lett. **99**, 172501 (2011).

Chapter 9

9. Reconfigurable Spin-Wave Nonreciprocity Induced by Dipolar Interaction in a Coupled Ferromagnetic Bilayer

9.1. Introduction

The engineering of spin waves (SWs)—the elementary excitations in magnetic systems with coupled electron spins—in magnetic structures is attracting a lot of attention in the scientific community, motivated by applications based on the field of magnon spintronics [1], which also provides a rich playground to study the fundamental principles of magnetic wave phenomena [2–9]. Since SW frequencies can vary from GHz to THz and can be externally controlled by applying magnetic fields or by designing the system architecture to create desired magnonic properties, devices for high-frequency applications and data processing are envisioned [10–17]. In the context of data processing, the nonreciprocity of spin waves, which can appear in the phase, amplitude, or frequency, has been presented as a powerful tool for possible applications in communication and logic devices [18–20]. Nonreciprocal phenomena have been the focus of studies on photonic and electronic structures as well, in which they have been found to enable fundamental operation modes in devices such as isolators, circulators, or gyrators [21,22]. Similarly, nonreciprocal magnon transport yields these key functionalities as well [18]. Consequently, achieving nonreciprocity in the spin-wave dispersion up to a significant, ideally tunable, degree is of high relevance for magnon-based applications. Spin-wave nonreciprocity has been known since the pioneering work of Damon and Eshbach [23], where it was predicted that the magnetization precession amplitude of the surface mode should be asymmetric with respect to the propagation direction. Such behaviour is well known and has been experimentally measured by several groups [24–26]. However, the amplitude nonreciprocity itself does not imply nonreciprocity in frequency. In our current bilayer case, symmetry breaking along the thickness will induce a frequency shift of the two counterpropagating waves. Spin-wave frequency nonreciprocity has already been discussed for ferromagnetic (FM) films with

different magnetic anisotropies at the surfaces [27–32] and for films with interband magnonic transitions [33]. It has, moreover, been theoretically and experimentally demonstrated that the interfacial Dzyaloshinskii-Moriya interaction (iDMI) [34–37] induced in ultrathin FM layers capped with heavy-metal films noticeably influences the SW spectra, generating nonreciprocity in the dispersion [38–54]. Additionally, nonreciprocal properties can be introduced into FM materials by the intrinsic dipolar interactions. It has been reported that arrays of magnetic nanopillars coupled by dipolar interaction [55], ferromagnetic nanotubes [56], systems composed of a FM film exchange-coupled to a one-dimensional periodic structure [57,58], and antiferromagnetic trilayers [59,60] show SW nonreciprocity. Although the physical properties of magnetic multilayers have been extensively studied in past decades, the focus was put on the celebrated giant change of magnetoresistance with the relative magnetic orientation of adjacent FM layers [61–63]. Interestingly, early studies of double layers and multilayers by Brillouin light scattering (BLS) had already evidenced frequency nonreciprocity for antiparallel alignment of the magnetic layers [64–68], in agreement with theoretical work [18,69–73]. However, a theory with the potential of making specific predictions is so far still missing, which hinders establishing the advantages and/or disadvantages of specific systems in comparison with others.

Here, the spin-wave dynamics of a FM bilayer system is investigated using a theoretical model, micromagnetic simulations, and BLS experiments. By analyzing both the magnetic properties of each layer and their equilibrium configurations, optimal conditions for increasing the frequency nonreciprocity of counterpropagating SWs in the Damon-Eshbach (DE) configuration are predicted and then confirmed with micromagnetic simulations and BLS for a prototype permalloy/Ir/CoFeB sample. An explicit expression is provided for the frequency shift f of two counterpropagating SWs. In the long wavelength limit (small wave vector k), we find that the SW nonreciprocity scales linearly with k, so that an effective DMI constant of dipolar origin can be defined. At intermediate values of k, there is a maximum in f that depends only on the thicknesses of the FM layers and the nonmagnetic spacer, while for larger k, f decreases exponentially. Thus, we demonstrate that the proposed bilayer systems exhibit remarkable properties as compared with the widely discussed heavy-metal–ferromagnetic ultrathin systems. In particular, in bilayer systems with antiparallel coupling, and in fundamental contrast to DMI-driven systems, the nonreciprocity can be notably larger for thicker FM layers also.

This opens up the possibility to create reconfigurable nonreciprocal devices [18,74,75] by controlling the relative magnetic orientation between the coupled FM layers. In the proposed bilayer system, frequency nonreciprocity can be turned on and off simply by switching from antiparallel to parallel magnetization, without any rotation of the applied magnetic field. Such switching can even be controlled and conveniently achieved by applying, for example, spin-transfer or spin-orbit torques via a local critical current. Moreover, both states, parallel and antiparallel, are well known from applications of giant magnetoresistance (GMR) and tunnel magnetoresistance (TMR) and can be tuned to have excellent stability at remanence. Therefore, the bilayer has a remarkable advantage over other systems, such as DMI-driven systems, where reconfigurability can be achieved by rotating the magnetization either in-plane, from the DE to the backward-volume (BV) configuration, or by tipping the magnetization out of the plane [41,45,46,52]. Also, in interfacial DMI systems there is a noticeable increment in magnetic damping due to the heavy metal, which is avoided when a coupled magnetic bilayer is used instead. Another advantage is that the bilayer system is compatible with standard deposition processes in the same manner as that in which GMR stacks are fabricated, and can be integrated into CMOS architectures.
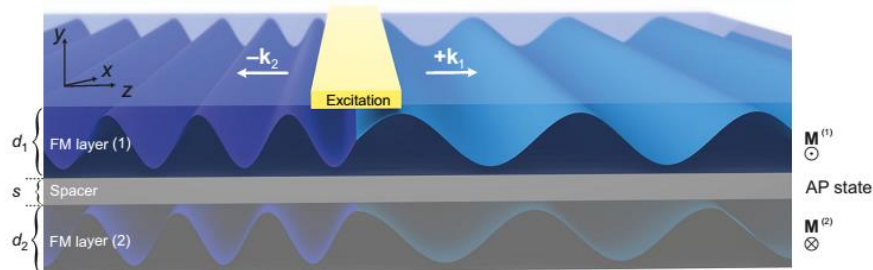
Figure 9.1: Overview of the magnetic bilayer system. The static magnetization configuration is in the antiparallel (AP) state. A spin wave is excited below the yellow region, traveling along positive and negative wave vectors with different wavelengths as indicated by the different color of the waves.

9.2. Theory and Simulations

9.2.1. Theory

A schematic illustration of the bilayer system considered, composed of two interacting FM layers (1) and (2) with in-plane magnetization, is shown in Fig. 9.1. The two layers are allowed to exhibit different magnetic parameters and thicknesses $d1$ and $d2$, and s denotes the separation between them. The equilibrium magnetization of layer $v = 1, 2$ makes an angle ϕ_v with the z axis, which is chosen as the propagation direction of the SWs, with wave vector $\boldsymbol{k} = k\hat{z}$. As we shall see, the nonreciprocity is enhanced in the DE configuration, particularly in the antiparallel state. Nonetheless, the theoretical approach accounts for the general case where the wave vector and magnetization may be oriented along arbitrary directions within the film plane, and moreover accounts for the highly relevant magnetostatic fields created by the dynamic magnetizations. The Landau–Lifshitz–Gilbert (LLG) equation is linearized and solved with the effective field contribution. For the symmetric case of two identical FM layers with the same thickness $d1 = d2 = d$, aligned along x but antiparallel to each other, an analytic formula for the SW dispersion relation for small external fields is derived and reads

$$f_{m_1}(k) = \frac{\gamma}{2\pi}\left\{g(k) + \sqrt{[p(k) - g(|k|)][q(k) - g(|k|) - 2C_J]}\right\} \tag{9.1}$$

$$f_{m_2}(k) = \frac{\gamma}{2\pi}\left\{-g(k) + \sqrt{[q(k) + g(|k|)][p(k) + g(|k|) - 2C_J]}\right\} \tag{9.2}$$

where $f_{m_1}(k)$ and $f_{m_2}(k)$ correspond to the two modes, namely the low and high frequency modes, of the bilayer system. In what follows, the mode analyzed will be the low-frequency one that corresponds to $fm1\ (k)$. The individual terms are defined by

$$g(k) = \mu_0 M_S \zeta(k)^2 e^{-|k|s} kd/2 \tag{9.3}$$

$$p(k) = \mu_0 H_u + \mu_0 M_S k^2 \lambda_{ex}^2 + \mu_0 M_S[1 - \zeta(k)] \tag{9.4}$$

$$q(k) = \mu_0 H_u - \mu_0 H_s + \mu_0 M_S k^2 \lambda_{ex}^2 + \mu_0 M_S \zeta(k) \tag{9.5}$$

where,

$$\zeta(k) = \frac{\sinh{(kd/2)}}{kd/2} e^{-|k|d/2} \tag{9.6}$$

$$C_J = \frac{J_{bl} - 2J_{bq}}{M_S d} \tag{9.7}$$

Here $J_{bl}/M_S d$ ($J_{bq}/M_S d$) is the bilinear (biquadratic) interlayer exchange field, $\mu_0 H_u$ is a possible uniaxial in plane anisotropy field, M_s is the saturation magnetization, λ_{ex} is the exchange length, and γ is the gyromagnetic ratio. Also, $\mu_0 H_s$ represents a surface uniaxial anisotropy field, which competes with the static dipolar field, allowing one to define an effective magnetization $\mu_0 M_{eff} = \mu_0 M_s - \mu_0 H_s$. The general case, assuming two different FM layers with different magnetic parameters, which is more complex, can be solved with the help of the eigenproblem. From Eqs. (9.1)–(9.3), it is clearly visible that it is the term $g\,(k)$ that introduces the nonreciprocity. Only this term changes sign as a function of the wave number k. All other terms, $p\,(k)$, $q\,(k)$, and $\zeta\,(k)$, are positive for both wave-vector directions, and $\zeta\,(k)$ is bounded by 1. Then, considering the limit of small wave numbers yields

$$f_{m_1}(k \to 0) = f_{m_1}(0) - \frac{\gamma \mu_0}{4\pi} M_S d \left(k + \frac{\gamma \mu_0}{2\pi} \frac{H_u}{f_{m_1}(0)} |k| \right) \tag{9.8}$$

for the low-frequency mode, while the high-frequency mode, $f_{m_2}(k)$, follows a similar behavior (not shown). Upon inspection, one may realize that the magnon dispersion relation for a bilayer with an antiparallel orientation of the two ferromagnetic layers in the limit of small k resembles the well-known asymmetric dispersion of ultrathin magnetic films with a DMI [41,42,52]. Indeed, the frequency shift becomes $f_{AP} \approx \mu_0 \gamma (M_s d/2\pi) k$, which allows one to introduce an effective Dzyaloshinskii Moriya constant, since the frequency shift in HM/FM interfaces follows the same linear behavior with k. Thus, this effective constant induced in the system is given by $D^{dip} = \mu_0 M_s^2 d/4$). Due to the dipolar nature of the nonreciprocity induced in the system, the effective constant increases linearly with thickness and quadratically with the saturation magnetization. Despite the simplicity of D^{dip}, this expression is very practical and useful, as it provides the relevant magnetic parameters for optimizing the nonreciprocal system in order to reach the desired properties for application purposes, where the nonreciprocity turns out to be relevant for operations in communication and logic devices [1,13]. Also, it allows one to identify if a bilayer is able to emulate a heavy-metal–ferromagnet system with respect to its nonreciprocal SW propagation. For instance, in bilayers of the heavy-metal–ferromagnet type, it has been found that the Dzyaloshinskii-Moriya constant D^{DM} is around 0.7 mJ/m² for a ferromagnet of thickness 1.6 nm [46]. Here, we can show that similar properties (i.e., $D^{DM} = D^{dip}$) can be reached for the same thickness of the ferromagnet (1.6 nm) if a saturation magnetization of M_s = 1190 kA/m is

used. To further increase D^{DM}, it is possible to decrease the film thickness to less than 1 nm [48], which is analogous to increasing D^{dip} by increasing the thicknesses of both FM layers. This, added to the wide versatility of our system, allows us to establish that a ferromagnetic bilayer is an excellent candidate for nonreciprocal magnonic devices, which, due to its simplicity and scalability, outperforms other systems proposed for corresponding applications in magnon-based data processing, where, for instance, the control of nonreciprocity allows the creation of unidirectional caustic spin waves [76] that are relevant for the suppression of cross-interference between devices within a magnonic circuit [57]. In the extended-k regime, we obtain further from Eqs. (1) and (2) the following analytical expression for f_{AP} for two counterpropagating spin waves:

$$\Delta f_{AP} = \frac{2\gamma}{\pi}\mu_0 M_S sinh^2\left(\frac{kd}{2}\right)\frac{e^{-|k|(d+s)}}{kd} \tag{9.9}$$

Note that Eq. (9.9) is valid for the modes $f_{m_1}(k)$ and $f_{m_2}(k)$ such a way that we predict that both modes show asymmetric dispersion with the same magnitude of frequency shift. Equation (9.9) shows that interlayer exchange fields are not required for generating nonreciprocity, neither for small nor for large wave vectors. This demonstrates that the effect results solely from the dynamic dipolar interaction. Interlayer exchange coupling may, however, be used to (i) stabilize the AP alignment and (ii) influence the accessible frequency range.

9.2.2. Micromagnetic Simulations

To validate the results of the theory, micromagnetic simulations are performed using the GPU-accelerated code mumax[3] [77]. For this, a long magnetic bilayer stripe with length l = 20 μm and width w = 80 nm is considered. To mimic the thin magnetic film, periodic boundary conditions are applied along the x and z directions. The material parameters are chosen in accordance with those mentioned above for the two systems, S_I and S_{II}. Using

$$\boldsymbol{h} = \tilde{h}\frac{sin\,(k_0 z)}{k_0 z}\frac{sin\,(2\pi f_0 t)}{2\pi f_0 t}\hat{y} \tag{9.10}$$

as an external rf-field source, the spin waves are excited with a sinc pulse in space with a cutoff wavelength $\lambda_0 = 2\pi/k_0$ = 9.77 nm, and in time with a cutoff frequency f_0 = 50 GHz. The coordinate system is based on the global coordinate system given in Fig. 9.1. To reconstruct the SW dispersion relation, the magnetization configuration is stored every

10 ps for 12.5 ns and subsequently Fourier transformed in 2D. Additionally, simulations of the hysteresis loops for in-plane and out-of-plane applied fields are performed. In this context, the total energy and the torque are subsequently minimized stepwise at varying applied-field values.

9.3. Experimental Details

9.3.1. Sample Preparation

A Ta(5 nm)/Co$_{40}$Fe$_{40}$B$_{20}$(5.7 nm)/Ir(0.6 nm)/Ni$_{81}$Fe$_{19}$(6.7 nm)/Ta cap layer stack is prepared on thermally oxidized Si substrates by magnetron sputtering in an Ar partial pressure of 0.35 Pa (2.62 mTorr) at room temperature. The deposition rates of each individual material are precalibrated by x-ray reflectivity (XRR). An underlayer of Ta (4 nm) is used to improve the adhesion. Ferromagnetic CoFeB and NiFe layers are deposited from alloy targets with compositions of Co$_{40}$Fe$_{40}$B$_{20}$ and Ni$_{81}$Fe$_{19}$ (in at.%), respectively (at a deposition rate of 0.3 Å/s). The ferromagnets are separated by a (nonmagnetic) Ir spacer layer to achieve antiferromagnetic alignment at zero field (via Ruderman–Kittel–Kasuya–Yoshida (RKKY) coupling). A Ta cap layer is used to provide an oxidation barrier.

9.3.2. BLS Measurements

To investigate the spin-wave nonreciprocity, BLS measurements are performed in the DE geometry, i.e., by applying a bias magnetic field in the sample plane but perpendicular to the plane of incidence of the laser beam. This allows for probing the spin waves propagating along the in-plane direction perpendicular to the applied field, i.e., in the DE geometry, where the nonreciprocity in the spin-wave frequency is maximal at room temperature. BLS relies on an inelastic light-scattering process due to the interaction of the incident photons with magnons. The conventional 180° backscattered geometry is used alongwith the provision of wave-vector selectivity to investigate the spin-wave dispersion relation [78,79]. Monochromatic light (wavelength λ = 532 nm and power P = 65 mW) from a solid-state laser is focused on the sample surface. In the light scattering process, the total momentum is conserved in the plane of the thin film. As a result, the Stokes (anti-Stokes) peaks in the BLS spectra correspond to the creation (annihilation) of magnons with momentum $k = 4\pi/\lambda \sin \theta$, where λ is the wavelength of the incident laser beam and θ refers to the angle of incidence of the laser. Cross-polarizations between the incident and scattered beams are adopted in order to eliminate any phonon contribution to the scattered light, and only the magnon contribution is measured.

Subsequently, the frequencies of the scattered light are analyzed using a Sandercock-type six-pass tandem Fabry-Pérot interferometer from JRS Scientific Instruments [80]. To get well-defined BLS spectra for the larger incidence angles, the spectra are obtained after counting photons for several hours. Because of the low frequency in the AP-coupled region, a free spectral range (FSR) of 30 GHz (20 GHz) for higher (lower) wavevectors and a 2^{10} channel multichannel analyzer are used during the BLS measurement. The frequency resolution is determined by estimating FSR/2^{10} ≈ 0.05 GHz (0.02 GHz) for higher (lower) wave vectors for the Stokes and anti-Stokes peaks of the BLS spectra. The sample magnetization is first saturated by applying a high enough magnetic field of −140 mT followed by reducing the field slowly to the bias magnetic field $\mu_0 H$, and BLS spectra are measured at that field for different values of the wave vector. The maximum value of the wave vector in our experiment is 20.4 rad/μm and the resolution is 2.06 rad/μm. For the first few wave vectors, the Stokes and anti-Stokes peaks merge with the tail of the elastic peaks and cannot be resolved; hence, we present the BLS spectra from k = 6.1 rad/μm. The nonreciprocity in the spin-wave frequency (f) is calculated by taking the difference between the anti-Stokes and Stokes peaks observed in the BLS spectra. Note that the BLS measurements are performed in the conventional way, i.e., by investigating thermally excited spin waves. The effect on the frequency nonreciprocity, however, relies solely on the dispersion of the system and is thus not influenced by the exact method of spin-wave excitation.

9.4. Results and Discussions

To obtain the information about the magnetic ground state and the material parameters, magnetometry measurements were performed. Conventional vibrating sample magnetometry (VSM) measurements have been performed using a MicroSense VSM EZ7. The sample magnetization, $M(H)$ was determined using superconducting quantum interference device vibrating sample magnetometry (SQUID-VSM), using a Quantum Design Magnetic Properties Measurement System (MPMS). Only the ascending hysteresis loop for the SQUID-VSM measurement is shown. The effective anisotropy constant (K_{eff}) was determined by acquiring in-plane and out-of-plane hysteresis loops. Moreover, the in-plane hysteresis loops provided an independent access to the bilinear and biquadratic coupling constants to be compared with the ones resulting from the FMR fittings. Subsequently, the BLS measurements has been performed with an external field of $\mu_0 H$ =

−5 mT, where the small plateau indicating the field region of AFM alignment is clearly visible in the in-plane hysteresis curve. However, extraction of the material parameters indicates a strong biquadratic coupling constant present in the system, as evidenced by the strong curvature of the $M(H)$ loop in Fig. 9.2(a). The out of plane hysteresis loop is shown in Fig. 9.2(b). The observed behavior was modelled using the simulation code mumax[3]. The open symbols in Fig. 9.2 corresponds to the averaged magnetization extracted at the applied field for both, the ascending and descending hysteresis loop branches. The high-resolution transmission electron microscopy (HR-TEM) image of the studied sample is presented in Fig. 9.2(c).
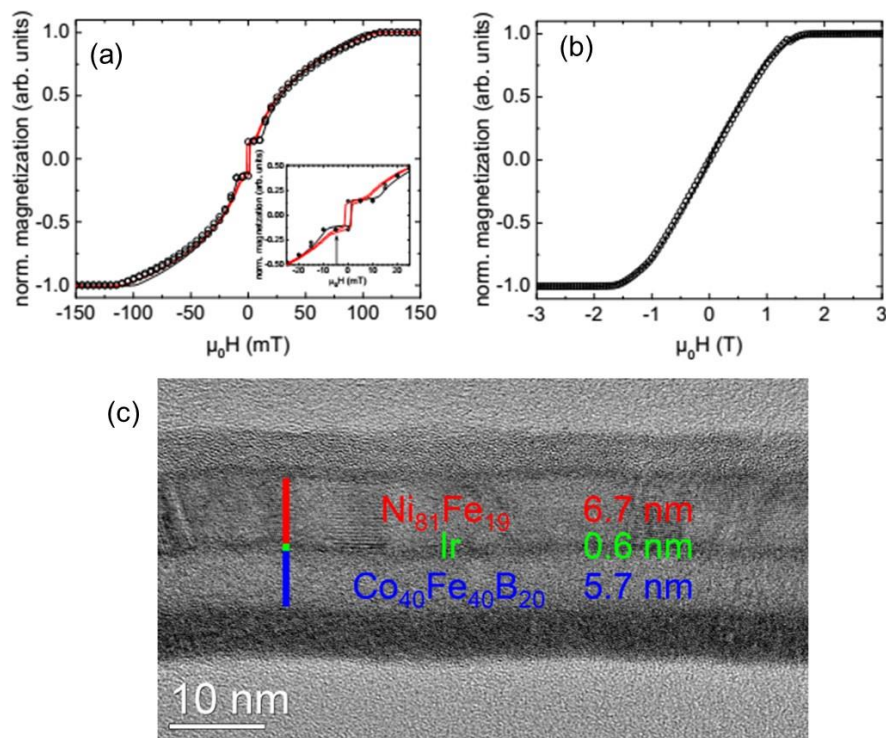
Figure 9.2: Hysteresis loops for (a) $\theta_H = 90\,°$ (in-plane external field) and (b) $\theta_H = 0\,°$ (out-of-plane external field). The solid lines correspond to the SQUID-VSM (black) and conventional VSM (red) measurements. The open symbols denote the micromagnetic simulations from mumax[3] for the ascending and descending hysteresis loop branch. The inset shows the AF state for small external fields. The black arrow marks the external field applied for the BLS measurements. (c) Representative HR-TEM micrograph of the Ta(5.0 nm)/Co$_{40}$Fe$_{40}$B$_{20}$(5.7 nm)/Ir(0.6 nm)/Ni$_{81}$Fe$_{19}$(6.7 nm)/Ta(0.9 nm)/Ta oxide(3.7 nm) layer stack deposited onto thermally oxidized silicon.

To illustrate the main findings of the paper, permalloy (Py) and cobalt (Co) layers are first considered. For Py [assumed as layer (1)], a saturation magnetization $M_S^{(1)} = 658$ kA/m

and an exchange length $\lambda_{ex}^{(1)}$ = 5.47 nm are used, while for Co [layer (2)] the saturation magnetization is $M_s^{(2)}$ = 1150 kA/m and $\lambda_{ex}^{(2)}$ = 5.88 nm. Also, the gyromagnetic ratio is γ = 1.7587 × 10^{11} rad/T s, for simplicity assumed to be the same for both layers. Two kinds of bilayer configurations are addressed, a Py/Py bilayer referred to as S_I, and a Co/Py bilayer denoted by S_{II}, for which a uniaxial anisotropy field of $\mu_0 H_u^{(2)}$ = 69.6 mT is assumed because of the hexagonal Co layer. In order to induce an AP alignment between the two FM layers, we introduce an s = 1 nm thick spacer, leading to an interlayer exchange coupling constant of J = −1.5 mJ/m². The spin-wave dispersion relations calculated for different thicknesses of the FM layers for systems S_I and S_{II} are shown in Figs. 9.2(a) and 9.2(c). Here, the frequency of the counterpropagating SWs is calculated as a function of the wave vector k for AP magnetization. Micromagnetic simulations are performed and are shown by the open symbols.

The main deviation between theory and simulation occurs for large wave vectors, which corresponds to wavelengths of the same order of magnitude as the film thickness, so that the nonhomogeneous profile of the dynamic magnetization through the thickness will start to have a significant influence on the mode frequencies. In effect, the profile will tend to lower the nonreciprocity, so that the frequencies of the micromagnetic simulation are lower than those predicted by theory. In case of the nonsymmetric system S_{II}, the deviation for large thicknesses occurs already at k = 0, because of the strong breaking of symmetry of the effective field due to the two layers having different magnetic parameters. Our calculations and simulations for SI in the case of parallel orientation of the two magnetizations yield a fully reciprocal dispersion.
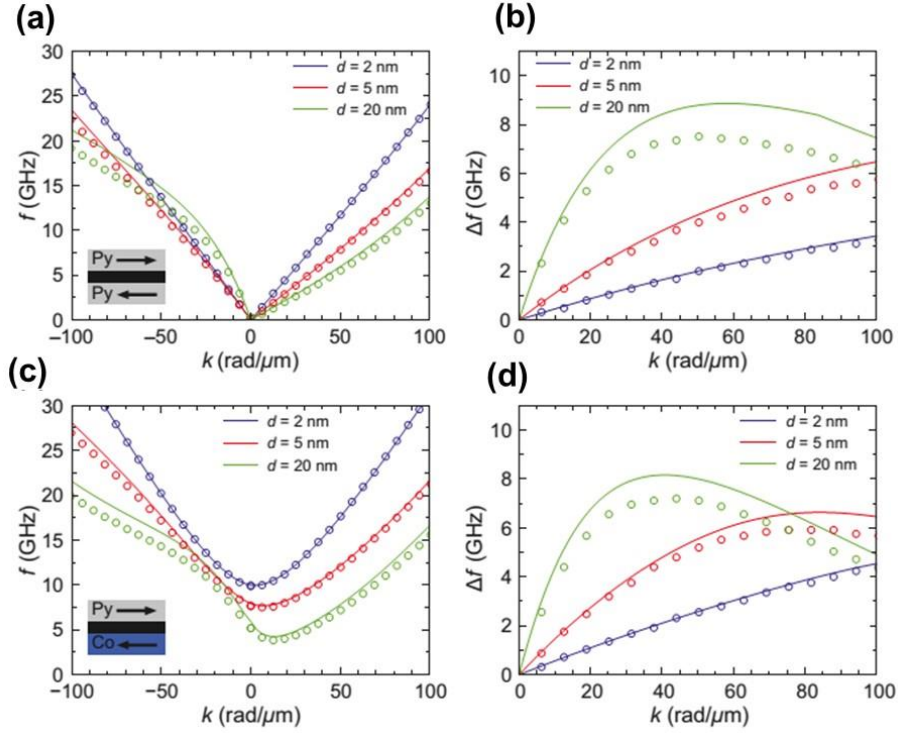
Figure 9.3: Nonreciprocal magnon spectrum for coupled ferromagnetic bilayers. (a) Nonreciprocal spin-wave dispersion relation for the Py/Py system S_I and (c) for the Py/Co system S_{II}. (b), (d) Corresponding frequency shift f of two counterpropagating spin waves as a function of the wave number, for the case of antiparallel equilibrium states of the bilayers. In all plots, the open symbols show the results of the micromagnetic simulation and the solid lines depict the theory. The material parameters are given in the main text.

We note, however, that this is not the case for the asymmetric system S_{II}, for which a small nonreciprocity of about 0.6 GHz (at k = 20 rad/μm) remains even in the P case. Nonetheless, in both cases the nonreciprocity for antiparallel alignment by far exceeds that for parallel alignment, so that via switching between these two configurations the nonreciprocal behaviour of spin waves can be turned on and off. This, in turn, allows for fabricating a nonreciprocal magnonic device that relies solely on the dynamic coupling of the spin waves in the FM bilayer. In order to understand the physical mechanisms behind the large enhancement of the spin-wave nonreciprocity, the dynamic dipolar stray fields outside and inside the FM films are carefully analyzed. Figures 9.3(a) and 9.3(b) depict these fields created by the magnetic charges in the bilayer system for the AP state, where the large arrows represent the orientation of the dynamic magnetization.
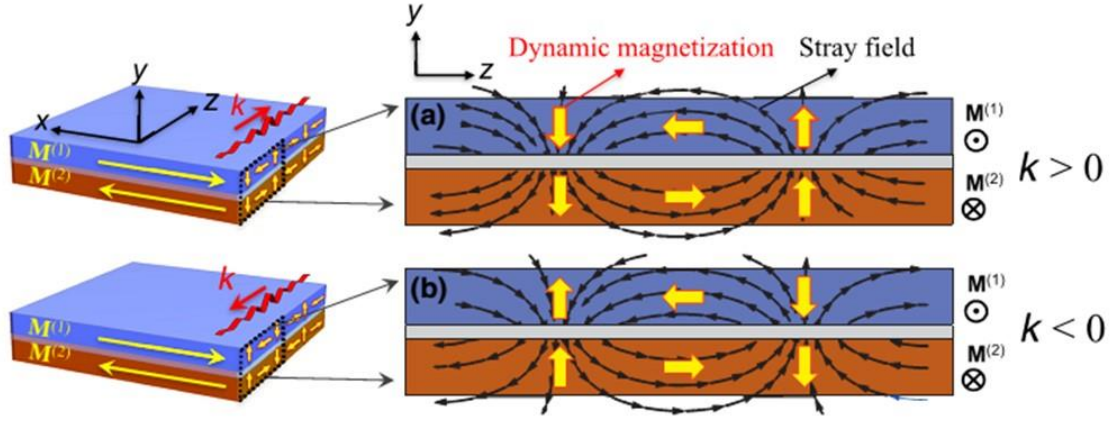
Figure 9.4: Dynamic stray fields induced by the surface and volumetric magnetic charges in a ferromagnetic bilayer. The large arrows depict the orientation of the dynamic magnetization, while the static magnetizations point along the $\pm x$ directions. The distributions of dynamic magnetizations and stray fields are shown in (a) for $k > 0$ and (b) for $k < 0$, for an antiparallel equilibrium state. In agreement with Fig. 9.3, the lower-energy state is obtained for $k > 0$, shown in (a), where the dynamic magnetization and stray field are almost parallel.

The main feature of these configurations is that the relative orientations of the dynamic stray field and the dynamic magnetization depend on the static magnetization alignment and the wave number k. Therefore, the dynamic dipolar interaction energy density $d = -(\mu_0/2)\mathbf{m}\cdot\mathbf{h}^{\mathrm{stray}}$ differs between the cases presented. Here, the distribution of the stray field $\mathbf{h}^{\mathrm{stray}}$ and the dynamic magnetizations for $k > 0$ and $k < 0$ are depicted in Fig. 9.4. In the AP state with $k > 0$ [Fig. 9.4(a)], the stray fields and the dynamic magnetizations are always parallel, in such a way that d becomes small. Thus, this frequency represents a state of low energy that appears only in the AP configuration. In the configuration shown in Fig. 9.4(b) ($k < 0$), the stray fields are always opposite to the out-of-plane dynamic magnetization, inducing a higher d as compared with the case presented in Fig. 9.3(a), notably increasing the SW frequencies, and therefore introducing nonreciprocity into the system. In strong contrast to the DMI previously used, the nonreciprocity effects presented here are strongly tunable by the FM-layer thickness d, which also affects the maximum frequency difference. Furthermore, in the case of system S_I, it is easy to see that in the limits $d \to 0$ and $d \to \infty$ this frequency asymmetry becomes zero and, thus, there is a particular wave vector for which f_{AP} is maximum, which can be determined from the relation $\tanh(k_*d/2) = k_*d/[1+k_*(d+s)]$.
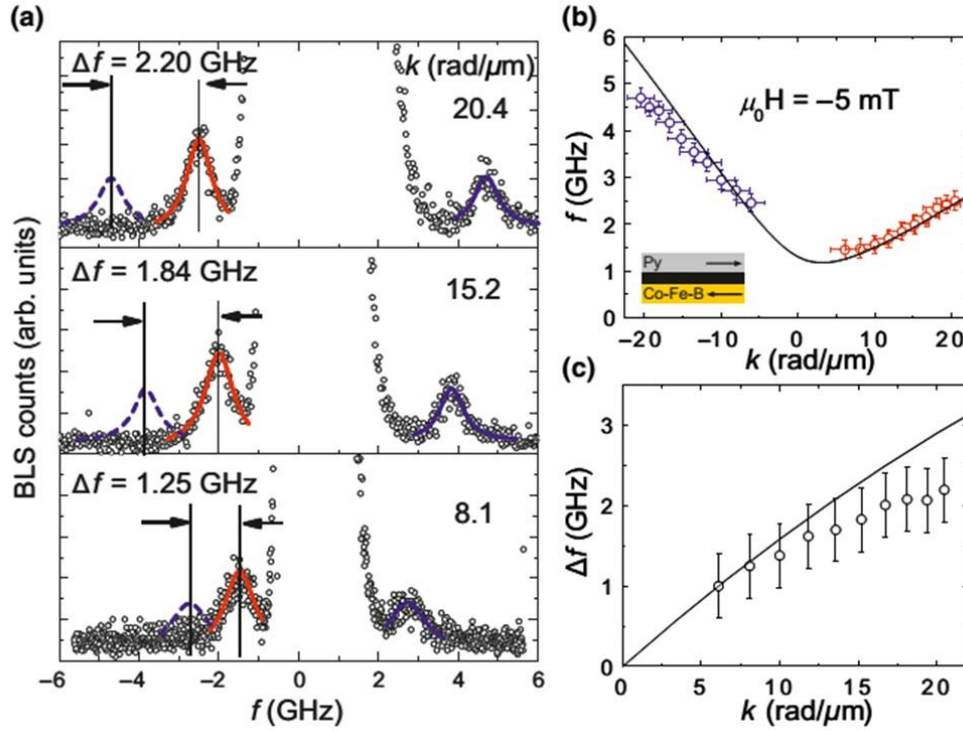
Figure 9.5: Representative Brillouin light-scattering spectra for Damon-Eshbach spin waves recorded at an external applied field $\mu_0 H = -5$ mT in a $Co_{40}Fe_{40}B_{20}$(5.7 nm)/Ir(0.6 nm)/$Ni_{81}Fe_{19}$(6.7 nm) bilayer sample for two counterpropagating directions. The spectra correspond to a specific wave vector k as given in each panel. The open symbols are the experimental data points, whereas the solid curves (red and blue) are fits using a Lorentzian function. To show the frequency asymmetry (Δf), the mirror curve of the antiStokes peak (blue dotted curve) is superimposed. (b) Asymmetric spin-wave dispersion relation measured at $\mu_0 H = -5$ mT (in the antiferromagnetically coupled region). (c) Variation of f as a function of k. The solid lines in (b) and (c) correspond to analytical calculations.

Consequently, only the geometrical parameters d and s determine the wave number k_*, for which the largest nonreciprocity is expected. Moreover, it is noted that the maximum frequency shift $f_{AP}(k_*)$ decays exponentially with the separation of the layers s and increases with the layer thickness d, due to the dipolar nature of the induced nonreciprocity.

To further validate the theory presented, BLS experiments are performed [6,28]. Three representative Brillouin light-scattering spectra for DE spin waves recorded at selected wave numbers under an in-plane bias magnetic field ($\mu_0 H = -5$ mT) are shown in Fig. 9.5(a). According to vibrating-sample magnetometry (with a conventional VSM) and

SQUID-VSM loops, this corresponds to the antiferromagnetically coupled region for the $Co_{40}Fe_{40}B_{20}(5.7nm)/Ir(0.6nm)/Ni_{81}Fe_{19}(6.7nm)$ sample investigated, where the thicknesses are estimated from transmission electron microscopy (TEM) measurements. In order to estimate the frequency difference Δf between the counterpropagating spin waves (anti-Stokes and Stokes peaks), the mirror curve of the anti-Stokes peak is shown by a blue dotted curve for each spectrum. It is evident that f increases with increasing wave number. The value of f attains a maximum of 2.20 GHz at $k = 20.4$ rad/μm. Figure 9.5(b) shows the spin-wave dispersion relation measured at $\mu_0 H = -5$ mT. The dispersion relation is asymmetric with respect to the two oppositely propagating spin waves. Shown in Fig. 9.5(c) is the variation of f as a function of k for the AP state. In order to fit the theoretical model to the experimental data, all the material parameters, besides the exchange constant, are determined experimentally. Ferromagnetic resonance (FMR) experiments are carried out to measure all magnetic properties of the bilayer, such as the effective magnetization $\mu_0 M_{eff}$, the bilinear (biquadratic) interlayer exchange coupling constant J_{bl} (J_{bq}), and the anisotropy field $\mu_0 H_u$. As already discussed above, both the spacer thickness s and the FM-layer thicknesses d are crucial parameters for describing the nonreciprocity. These geometric parameters are determined by TEM. The experimentally determined material parameters are listed in Table 9.1. The agreement between the theory and the BLS experiments is good. In Fig. 9.5(b), it is visible that the positive wave numbers fit almost perfectly. However, for negative wave numbers the agreement is somewhat less perfect. To exclude the possibility that the material parameters cause this effect, the spin-wave dispersion for the parallel alignment was also measured. For the parallel case, the agreement is almost perfect. The deviation in the branch at negative k with higher group velocity may be related to the fact that in our system the in-plane anisotropy is rather weak (about a millitesla), so that some small tilting of the two ferromagnetic layers away from the AP alignment is not unlikely, due to a nonvanishing biquadratic coupling contribution. This scenario is confirmed by magnetometry data. In any case, such a small misalignment would lead to a reduction in the nonreciprocity, in particular for higher wave-vector values. A tilt angle of $25°$ would lead to a reduction in the nonreciprocity of approximately 50%.

Table 9.1: Experimentally determined material parameters. The magnetic properties are determined by FMR, SQUID, and conventional VSM. The layer thicknesses and the spacer thickness are determined by cross-section TEM

	d (nm)	$\mu_0 M_{eff}$ (mT)	$\mu_0 H_u$ (mT)	J_{bl} (mJ/m²)	J_{bq} (mJ/m²)	s (nm)
$Ni_{81}Fe_{19}$	6.7	942.5	4.0	-0.195	-0.044	0.6
$Co_{40}Fe_{40}B_{20}$	5.7	1442.9	0.0			

To achieve a parallel alignment of both layers, a strong magnetic field $\mu_0 H = -140$ mT was applied. Figure 9.6(a-c) are the representative BLS spectra recorded at various k values. The solid lines in Fig. 9.6(d) correspond to the presented theory. Since most of the parameters were already set by fitting the FMR, SQUID, VSM and TEM measurements, the only parameter left and needed to fit the BLS data was the intralayer exchange constant.
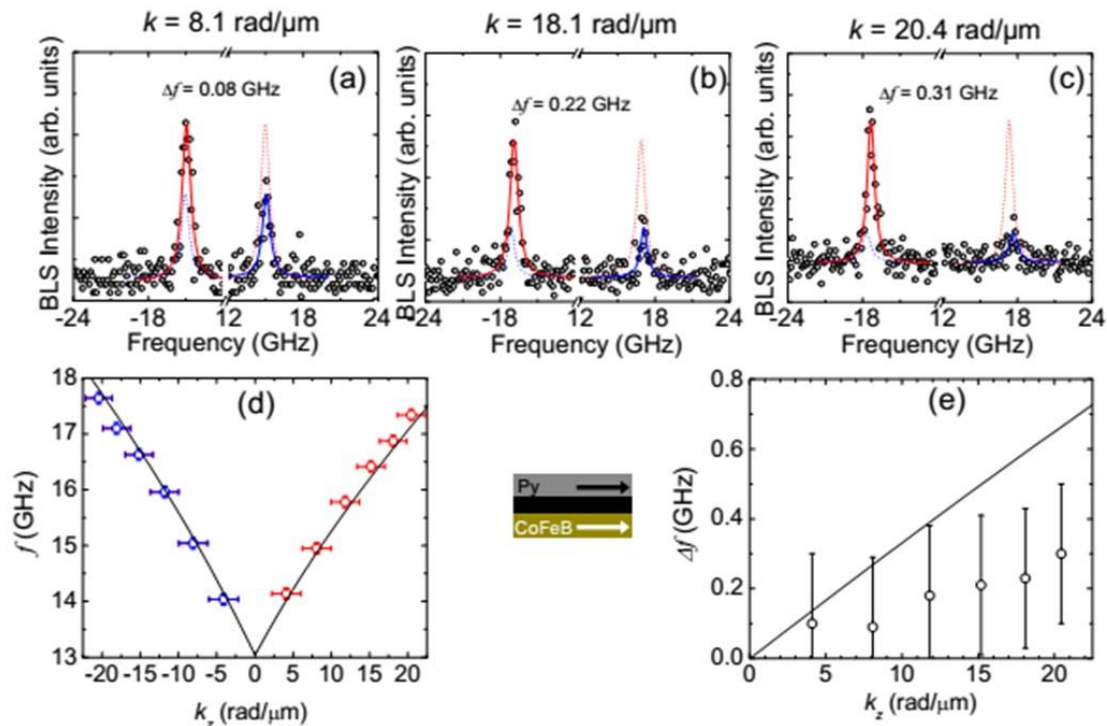
Figure 9.6: (a-c) Representative BLS spectra recorded at various SW wave vectors as mentioned in each panel for the sample measured in parallel alignment. (d) the measured dispersion relation for the sample $Co_{40}Fe_{40}B_{20}(5.7$ nm$)/Ir(0.6$ nm$)/Ni_{81}Fe_{19}(6.7$ nm$)$. The open symbols represent the frequencies obtained from fitted BLS spectra. The solid black lines are calculated using the theory presented in the chapter.

The small discrepancy between experiment and theory may result from the known fact that Ta yields an interface region of magnetically dead atomic layers which hardly can be avoided [81]. This indeed would lead to a difference between the geometric thicknesses obtained by TEM and the magnetic ones being relevant for the magnetic measurements. Another source of discrepancy may be canted antiferromagnetic state, which can arise from nonvanishing biquadratic exchange coupling contribution. Fig. 9.6(e) depicts the frequency shift for the parallel case, where at k = 20 rad/µm a maximum discrepancy close to 0.4 GHz is observed between theory and experiment. This discrepancy is much lower than the antiparallel case (about 0.8 GHz in the antiparallel case), nevertheless it looks larger due to the different frequency scales used in each plot.

9.5. Conclusions

The dynamic magnetic properties of a coupled ferromagnetic bilayer system are studied. By means of a spin-wave theory, micromagnetic simulations, and Brillouin light-scattering measurements, it is demonstrated that the dipolar interaction between the FM layers produced by the dynamic magnetizations is a notable source of nonreciprocity in the spin-wave frequency, with a remarkable property of reconfigurability that relies on control of the relative magnetic orientation of the interacting FM layers. In such bilayer structures, we can have in-plane remanent stable states with a parallel as well as an antiparallel configuration, as is well known from GMR and TMR applications. Therefore, one can reconfigure the bilayer system reliably into a reciprocal and a nonreciprocal device just by the magnetic-field history or, alternatively, by applying a local torque to one of the layers via a critical current density. The change from nonreciprocal to reciprocal spin waves is more difficult to obtain by switching the magnetization by 90◦ in the plane or 90◦ out of the plane, as required in other nonreciprocal systems. Also, in the small-wave-vector limit, we show that the bilayer system can emulate the nonreciprocity produced by the Dzyaloshinskii-Moriya interaction in FM–heavy-metal stacks, even for ultrathin ferromagnetic films. Thus, the bilayer system exhibits the ability to mimic the extensively studied dynamic properties of FM–heavy-metal layers and, at the same time, presents an easy way to control the magnitude of the nonreciprocity by means of the geometry and the equilibrium configuration. These findings open up alternative routes for the creation of nanoscale nonreciprocal magnonic devices and motivate a deeper

study of this type of system, in order to optimize its design according to the desired application requirements.

References

[1] A. V. Chumak, V. I. Vasyuchka, A. A. Serga, and B. Hillebrands, Nat. Phys. **11**, 453 (2015).

[2] G. Gubbiotti, S. Tacchi, G. Carlotti, *et al.*, Appl. Phys. Lett. **90**, 092503 (2007).

[3] K.-S. Lee, D.-S. Han, and S.-K. Kim, Phys. Rev. Lett. **102**, 127202 (2009).

[4] S. Neusser and D. Grundler, Adv. Mat. **21**, 2927 (2009).

[5] A. A. Serga, A. V. Chumak, and B. Hillebrands, J. Phys. D: Appl. Phys. **43**, 264002 (2010).

[6] G. Gubbiotti, S. Tacchi, M. Madami, *et al.*, J. Phys. D: Appl. Phys. **43**, 264003 (2010).

[7] Z. K. Wang, V. L. Zhang, H. S. Lim, *et al.*, ACS Nano **4**, 643 (2010).

[8] J. Ding, M. Kostylev, and A. O. Adeyeye, Phys. Rev. B **84**, 054425 (2011).

[9] S. Tacchi, G. Duerr, J. W. Klos, *et al.*, Phys. Rev. Lett. **109**, 137202 (2012).

[10] S.-K. Kim, K.-S. Lee, and D.-S. Han, Appl. Phys. Lett. **95**, 082507 (2009).

[11] A. V. Chumak, V. I. Vasyuchka, A. A. Serga, *et al.*, Phys. Rev. Lett. **108**, 257207 (2012).

[12] H. Yu, G. Duerr, R. Huber, *et al.*, Nat. Commun. **4**, 2702 (2013).

[13] M. Jamali, J. H. Kwon, S.-M. Seo, K.-J. Lee, and H. Yang, Sci. Rep. **3**, 3160 (2013).

[14] A. V. Chumak, A. A. Serga, and B. Hillebrands, Nat. Commun. **5**, 4700 (2014).

[15] T. Brächer, F. Heussner, P. Pirro, *et al.*, Sci. Rep. **6**, 38235 (2016).

[16] B. Rana and Y. C. Otani, Phys. Rev. Appl. **9**, 014033 (2018).

[17] A. V. Sadovnikov, V. A. Gubanov, S. E. Sheshukova, Yu P. Sharaevskii, and S. A. Nikitov, Phys. Rev. Appl. **9**, 051002 (2018).

[18] R. E. Camley, Surf. Sci. Rep. **7**, 103 (1987).

[19] J. Lan, W. Yu, R. Wu, and J. Xiao, Phys. Rev. X **5**, 041049 (2015).

[20] X. S. Wang, H. W. Zhang, and X. R. Wang, Phys. Rev. Appl. **9**, 024029 (2018).

[21] N. Reiskarimian and H. Krishnaswamy, Nat. Commun. **7**, 11217 (2016).

[22] D. L. Sounas and A. Alù, Nat. Photonics **11**, 774 (2017).

[23] R. W. Damon and J. R. Eshbach, J. Phys. Chem. Solids **19**, 308 (1961).

[24] L. K. Brundle and N. J. Freedman, Electron. Lett. **4**, 132 (1968).

[25] T. Wolfram and R. E. DeWames, Prog. Surf. Sci. **2**, 233 (1972).

[26] V. E. Demidov, M. P. Kostylev, K. Rott, *et al.*, Appl. Phys. Lett. **95**, 112509 (2009).

[27] B. Hillebrands, Phys. Rev. B **41**, 530 (1990).

[28] B. Hillebrands, *Light Scattering in Solids VII: Crystal-field and Magnetic Excitations* (Springer, Berlin, Heidelberg, 2000), p. 174.

[29] P. K. Amiri, B. Rejaei, M. Vroubel, and Y. Zhuang, Appl. Phys. Lett. **91**, 062502 (2007).

[30] M. Mruczkiewicz, M. Krawczyk, G. Gubbiotti, *et al.*, New J. Phys. **15**, 113023 (2013).

[31] M. Mruczkiewicz, E. S. Pavlov, S. L. Vysotsky, *et al.*, Phys. Rev. B **90**, 174416 (2014).

[32] O. Gladii, M. Haidar, Y. Henry, M. Kostylev, and M. Bailleul, Phys. Rev. B **93**, 054430 (2016).

[33] K. Di, H. S. Lim, V. L. Zhang, S. C. Ng, and M. H. Kuok, Appl. Phys. Lett. **103**, 132401 (2013).

[34] I. Dzyaloshinsky, J. Phys. Chem. Solids **4**, 241 (1958).

[35] T. Moriya, Phys. Rev. Lett. **4**, 228 (1960).

[36] A. Fert and P. M. Levy, Phys. Rev. Lett. **44**, 1538 (1980).

[37] N. Nagaosa and Y. Tokura, Nat. Nanotech. **8**, 899 (2013).

[38] L. Udvardi and L. Szunyogh, Phys. Rev. Lett. **102**, 207204 (2009).

[39] K. Zakeri, Y. Zhang, J. Prokop, *et al.*, Phys. Rev. Lett. **104**, 137203 (2010).

[40] A. T. Costa, R. B. Muniz, S. Lounis, A. B. Klautau, and D. L. Mills, Phys. Rev. B **82**, 014428 (2010).

[41] D. Cortés-Ortuño and P. Landeros, J. Phys: Condens. Matter **25**, 156001 (2013).

[42] J.-H. Moon, S.-M. Seo, K.-J. Lee, *et al.*, Phys. Rev. B **88**, 184404 (2013).

[43] K. Di, V. L. Zhang, H. S. Lim, *et al.*, Appl. Phys. Lett. **106**, 052403 (2015).

[44] K. Di, V. L. Zhang, H. S. Lim, *et al.*, Phys. Rev. Lett. **114**, 047201 (2015).

[45] V. L. Zhang, K. Di, H. S. Lim, *et al.*, Appl. Phys. Lett. **107**, 022402 (2015).

[46] J. Cho, N.-H. Kim, S. Lee, *et al.*, Nat. Commun. **6**, 7635 (2015).

[47] H. T. Nembach, J. M. Shaw, M. Weiler, E. Jue, and T. J. Silva, Nat. Phys. **11**, 825 (2015).

[48] M. Belmeguenai, J.-P. Adam, Y. Roussigné, *et al.*, Phys. Rev. B **91**, 180405(R) (2015).

[49] A. A. Stashkevich, M. Belmeguenai, Y. Roussigné, *et al.*, Phys. Rev. B **91**, 214409 (2015).

[50] N.-H. Kim, J. Jung, J. Cho, *et al.*, Appl. Phys. Lett. **108**, 142406 (2016).

[51] J. M. Lee, C. Jang, B.-C. Min, *et al.*, Nano Lett. **16**, 62 (2016).

[52] S. Tacchi, R. E. Troncoso, M. Ahlberg, *et al.*, Phys. Rev. Lett. **118**, 147201 (2017).

[53] R. A. Gallardo, D. Cortés-Ortuño, T. Schneider, *et al.*, Phys. Rev. Lett. **122**, 067204 (2019).

[54] R. A. Gallardo, D. Cortés-Ortuño, R. E. Troncoso, and P. Landeros, *Three-dimensional Magnonics* (Jenny Stanford Publishing, Berlin, Heidelberg, 2019), p. 121.

[55] R. Verba, V. Tiberkevich, E. Bankowski, *et al.*, Appl. Phys. Lett. **103**, 082407 (2013).

[56] J. A. Otálora, M. Yan, H. Schultheiss, R. Hertel, and A. Kákay, Phys. Rev. Lett. **117**, 227203 (2016).

[57] K. Di, S. X. Feng, S. N. Piramanayagam, *et al.*, Sci. Rep. **5**, 10153 (2015).

[58] M. Mruczkiewicz, P. Graczyk, P. Lupo, *et al.*, Phys. Rev. B **96**, 104411 (2017).

[59] S. Wintz, V. Tiberkevich, M. Weigand, *et al.*, Nat. Nanotechnol. **11**, 948 (2016).

[60] V. Sluka, T. Schneider, R. A. Gallardo, *et al.*, Nat. Nanotech. **14**, 328 (2019).

[61] M. N. Baibich, J. M. Broto, A. Fert, *et al.*, Phys. Rev. Lett. **61**, 2472 (1988).

[62] A. Fert, Rev. Mod. Phys. **80**, 1517 (2008).

[63] P. A. Grünberg, Rev. Mod. Phys. **80**, 1531 (2008).

[64] P. Grünberg, J. Appl. Phys. **57**, 3673 (1985).

[65] P. Grünberg, R. Schreiber, Y. Pang, M. B. Brodsky, and H. Sowers, Phys. Rev. Lett. **57**, 2442 (1986).

[66] P. X. Zhang and W. Zinn, Phys. Rev. B **35**, 5219 (1987).

[67] G. Binasch, P. Grünberg, F. Saurenbach, and W. Zinn, Phys. Rev. B **39**, 4828 (1989).

[68] M. Vohl, J. Barnas, and P. Grünberg, Phys. Rev. B **39**, 12003 (1989).

[69] R. E. Camley and A. A. Maradudin, Solid State Commun. **41**, 585 (1982).

[70] K. Mika and P. Grünberg, Phys. Rev. B **31**, 4465 (1985).

[71] P. Grünberg and K. Mika, Phys. Rev. B **27**, 2955 (1983).

[72] R. L. Stamps and R. E. Camley, J. Magn. Magn. Mater. **54**, 803 (1986).

[73] J. Barnas and P. Grünberg, J. Magn. Magn. Mater. **82**, 186 (1989).

[74] N. R. Bernier, L. D. Tóth, A. Koottandavida, *et al.*, Nat. Commun. **8**, 604 (2017).

[75] Z. Shen, Y.-L. Zhang, Y. Chen, *et al.*, Nat. Commun. **9**, 1797 (2018).

[76] J.-V. Kim, R. L. Stamps, and R. E. Camley, Phys. Rev. Lett. **117**, 197204 (2016).

[77] A. Vansteenkiste, J. Leliaert, M. Dvornik, *et al.*, AIP Adv. **4**, 107133 (2014).

[78] A. K. Chaurasiya, C. Banerjee, S. Pan, *et al.*, Sci. Rep. **6**, 32592 (2016).

[79] A. K. Chaurasiya, S. Choudhury, J. Sinha, and A. Barman, Phys. Rev. Appl. **9**, 014008 (2018).

[80] R. Mock, B. Hillebrands, and R. Sandercock, J. Phys. E: Sci. Instrum. **20**, 656 (1987).

[81] H. T. Nembach, T. J. Silva, J. M. Shaw, *et al.*, Phys. Rev. B **84**, 054424 (2011).

Chapter 10

10. Magnetic Field Controlled Transition in Spin-Wave Dynamics in Kagome Artificial Spin Ice Structure

---

10.1. Introduction

Artificial spin ice (ASI) systems are engineered magnetic materials or metamaterials designed by nanopatterning strongly interacting single domain nanoislands in a geometrically frustrated array [1]. Frustration in a physical system emerges from inability of simultaneously minimizing all interactions [2]. In 2006, Wang *et al.* carried out pioneering experiments on lithographically-defined arrays of interacting nanomagnets and explored interesting physics analogous to spin ice materials (Pyrochlores, $Dy_2Ti_2O_7$ etc) [3]. This has triggered flurry of research efforts to investigate ASI because of the fundamental physics involved as well as potential applications such as reconfigurable and reprogrammable memory, logic and more recently reconfigurable magnonics [4-7]. Due to its resemblance with water ice systems, most of the studies on ASIs have revealed the occurrence of classical spin liquid states [8], Coulomb phases [9], monopole-like excitation [10] and spin fragmentation [11]. The quasiparticle monopole – anti monopole pair in these systems are often manifested as topological defects (TDs) and are separated by a Dirac string [12-13]. In addition, a lot of attention has been paid by the scientific community to explore the tunability of the high frequency dynamics due to the TDs in the ASI [14-16]. These high frequency responses are somewhat closely related to the magnetic microstates, which leads to further functional design of these ASIs for the tunability in their magnon response [17-22]. To further enhance the knowledge base regarding the TDs, novel mechanisms are being proposed. Recently, the ground state in the kagome ASI has been realized via topological magnetic writing [23-24]. Apart from the conventional ASI based on square and kagome lattice arrangement, there has been a considerable progress in other possible geometrically frustrated arrays such as shakti lattice [25], tetris lattice [26] and coupled islands [27]. In the context of experimental

probing of the spin dynamics, ferromagnetic resonance (FMR) technique has been mostly employed which is based on the global excitation and probing of a large area ASI subject to an external sweep field [13-14, 28-31]. Because of the large array of nano islands in such studies, it is quite unclear to attribute that the observed changes in FMR frequencies relies upon the number of nanobars that have been reversed or whether the precise spin configuration of the array plays a crucial role. The main motivation behind this work is to understand the spin dynamics in a limited array size which gives the better way of understanding the switching behaviour of the ASI nanostructures as opposed to the widely used FMR technique. In addition, the optical technique such as Brillouin light scattering (BLS), which is a powerful tool for probing spin dynamics, has never been employed for the investigation of spin waves in kagome ASI till date.

In this article, we have performed a comprehensive study of the spin-wave (SW) dynamics in connected and disconnected kagome ASI (c-ASI and d-ASI hereafter) systems made of $Ni_{80}Fe_{20}$ (permalloy, Py hereafter) in magnetically saturated as well as disordered state by employing BLS technique complemented by micromagnetic simulation. The detailed bias magnetic field dependent study has been performed to underpin the field evolution of spin dynamics of these systems.

10.2. Experimental and Simulation Methods

Arrays of kagome ASI structure with total area of 90×90 μm^2 were fabricated using electron-beam lithography (EBL) and lift off process. A computer added design (CAD) file containing ASI pattern is loaded in the EBL unit to write the pattern onto a single layer polymethyl methacrylate (PMMA) resist (950K) coated on Si/SiO$_2$ substrate. After writing and development of the resist pattern using MIBK developer, 25-nm-thick Py film was deposited on it by thermal evaporation at a base pressure of 2.6×10^{-6} Torr. The samples were then capped with 3.7-nm-thick Al$_2$O$_3$ layer to protect it from oxidation. For the sample c-ASI, the length (l) and width (w) of the constituent Py nanobars are 300 nm and 80 nm, respectively. In the case of d-ASI, the values of l and w were kept the same as c-ASI but a 50-nm gap (here gap is defined as the distance between the edges of the common vertex centres) is introduced between the nanobars.

The preliminary characterization of the samples was performed using scanning electron microscopy (SEM) in order to inspect the formation of desired structure of ASI. To investigate the magnetic microstate of these kagome ASI, magnetic force microscopy

(MFM) was performed at the remanent state. Furthermore, the magnetic hysteresis loops of the samples were measured using static magneto-optical Kerr effect (MOKE). The output of a He-Ne laser was focused to a spot size of 10 μm at the center of the ASI nanostructures and the Kerr rotation was probed under the laser spot as a function of applied bias magnetic fields (H). Here, H was applied along the horizontal arm of kagome lattice as shown in Fig. 10.1 (b) and its maximum amplitude was sufficient to saturate the sample magnetization. BLS measurements were performed in Damon-Eshbach (DE) geometry using a Sandercock-type six-pass tandem Fabry-Pérot interferometer [32]. Conventional 180° backscattered geometry was used to investigate the field evolution of spin waves. In the light scattering process, total momentum is conserved in the plane of the thin film. As a result, the Stokes (anti-Stokes) peaks in BLS spectra correspond to creation (annihilation) of magnons with momentum $k = \frac{4\pi}{\lambda}\sin\theta$, where λ is the wavelength of the incident laser beam (532 nm in our case), and θ refers to the angle of incidence of laser. To get well defined BLS spectra for the larger incidence angles, the spectra were obtained after counting photons for several hours. Free spectral range (FSR) of 30 GHz and a 2^{10} multi-channel analyser were used during the BLS measurement. The frequency resolution is determined by estimating FSR/2^{10} ($\approx$0.03 GHz) for the Stokes and anti-Stokes peaks of the BLS spectra. A variable bias magnetic field (H) was applied during the measurements. The other details can be found elsewhere [33].

To interpret the experimental results, we have performed micromagnetic simulations by using Object Oriented Micromagnetic Framework (OOMMF) software [34]. The mimicked arrays from the SEM image have been discretized into rectangular prism-like cells of 5×5×25 nm^3 dimensions. The lateral dimensions of the cells were taken below the exchange length (*lex*) of Py. The material parameters used for the simulations are: gyromagnetic ratio, γ = 2.211 ×10^5 A^{-1} s^{-1}, saturation magnetisation, M_S = 800 kA/m, and the exchange stiffness constant, A = 1.3 × 10^{-11} J/m and Gilbert damping, a = 0.008. To simulate the magnetization dynamics, we first simulated the magnetic microstates at desired bias field values followed by application of an rf excitation field along the y-axis of the array. The simulated time-varying magnetization was collected for 4 ns at 10 ps steps for each sample. We have also used LLG micromagnetic simulator [35] for the simulation of the MFM images using the same parameters as mentioned above.

10.3. Results and Discussion

Figures 10.1(a) and (b) represent the scanning electron micrographs (SEM) images for connected (c-ASI) and disconnected (d-ASI) kagome ASI samples. The variation in the measured dimensions are: ±3% in length, ±2% in width and ± 1.5% in the inter-bar distance for d-ASI, while the heights of the nanobars are found to vary by ±3% as obtained from the atomic force microscope (AFM) images.
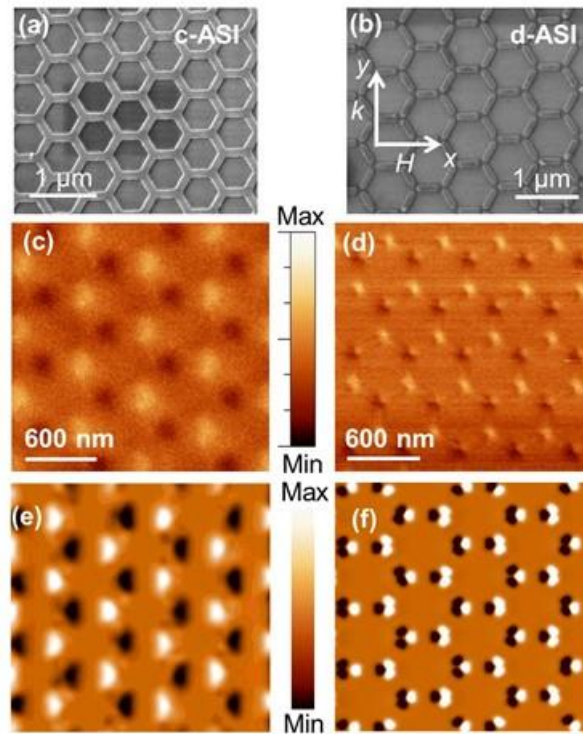
Figure 10.1: The SEM images of the (a) connected (c-ASI) and (b) disconnected (d-ASI) ASI kagome lattice. The measured MFM images taken at remanence for (c) c-ASI and (d) d-ASI. Simulated MFM images for (e) c-ASI and (f) d-ASI at remanence.

The SEM images confirm good quality of the samples. Figures 10.1(c) and 10.1(d) show the remanent state MFM images for the samples c-ASI and d-ASI, respectively. The MFM image in Fig. 10.1(d) reveals that the magnetization orientation in most of the vertices of the d-ASI ASI obey the spin ice rule, *i.e.* "two-in one-out" or "one-in two-out", characteristic of kagome ASI. We have also simulated the MFM images at remanence for both c-ASI and d-ASI (Fig. 10.1(e) and Fig. 10.1(f)) using LLG simulator showing an excellent agreement between the simulated and experimental MFM images.

10.3.1. Magnetization Reversal of Kagome ASI

Figure 10.2 represents the magnetic hysteresis loops measured by longitudinal MOKE for both samples c-ASI and d-ASI. Both the loops are wide with coercive fields of few

hundreds of Oe as opposed to a Py thin film due to the shape anisotropy of the nanobars and their mutual dipole- exchange interactions. The difference in geometric structures of c-ASI and d-ASI causes
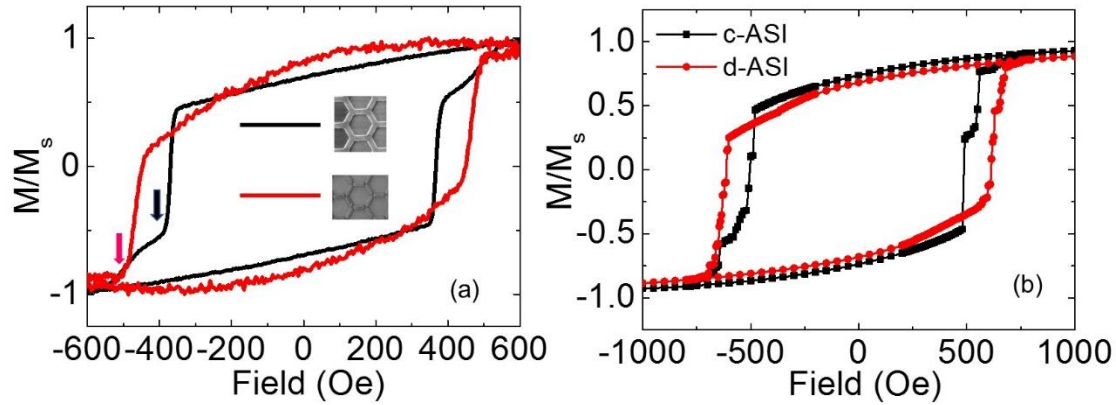
Figure 10.2: (a) MOKE hysteresis loops showing the magnetization reversal for connected (c-ASI) and disconnected (d-ASI) kagome ASI samples. (b) Simulated hysteresis loop for both the samples.

various change in their respective loops including coercive field (370 Oe for c-ASI and 450 Oe for d-ASI), remanence (70% for c-ASI and 82% for d-ASI), curvature, as well as a two-step reversal for c-ASI as opposed to a single step reversal for d-ASI. This two-step feature indicates switching of two different parts of the sample at two different magnetic fields. Figure 10.2 (b) shows the simulated hysteresis loops which are in qualitative agreement with the experimental loops. We will further investigate how the magnetization reversal behaviours affect the high frequency SW dynamics of these samples.

10.3.2. Spin-Wave Dynamics of Kagome ASI

Figures 10.3 (a) and 10.3 (c) show the representative BLS spectra for c-ASI and d-ASI taken at $k \approx 0$ in the DE geometry at different values of H mentioned in each panel. The corresponding simulated SW spectra are also shown in Figs. 10.3 (b) and 10.3(d).
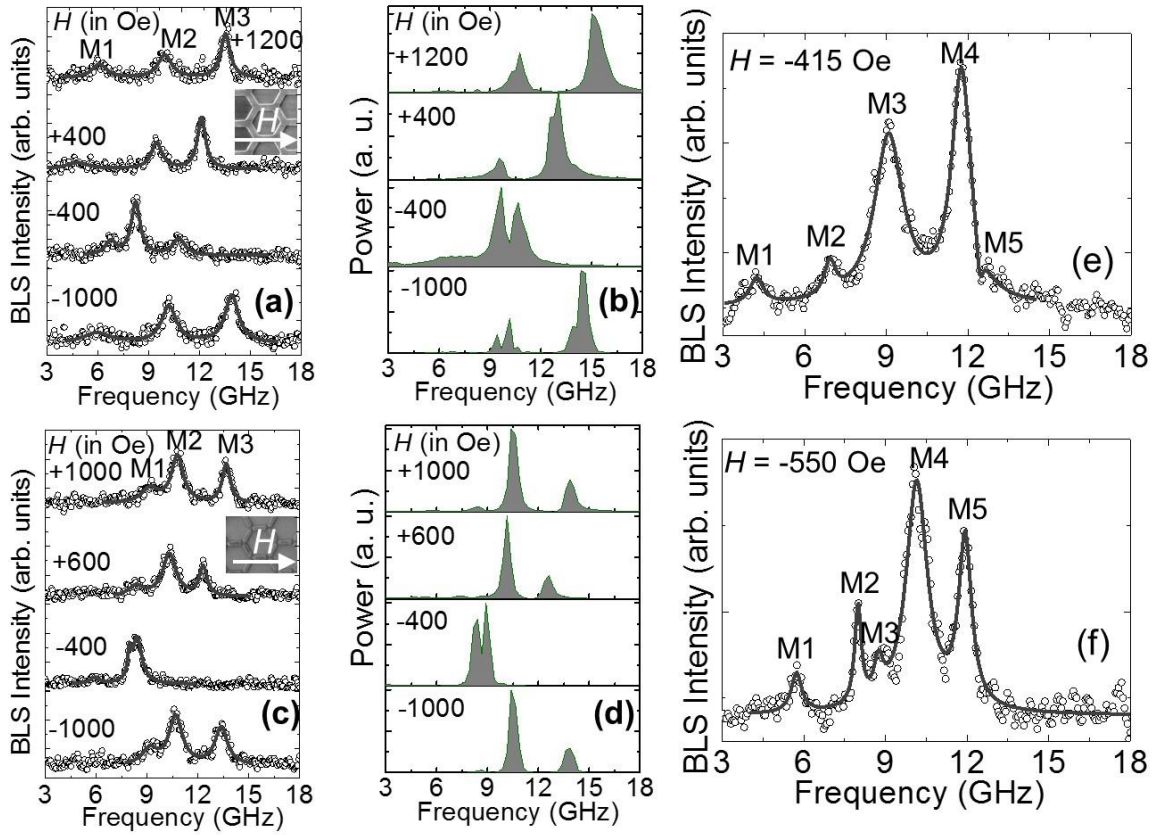
Figure 10.3: Representative BLS spectra measured at wave vector $k \approx 0$ for different bias magnetic fields from (a) c-ASI and (c) d-ASI. Each spectrum corresponds to a specific magnetic field as indicated next to the spectrum. The solid grey curves represent Lorentzian multipeak fits. The SW modes M1, M2, and M3 are marked according to the ascending value of the frequency. The simulated SW spectra for (b) c-ASI and (d) d-ASI. (e) and (f) are the representative BLS spectra taken in the field regime where magnetization reversal occurs for both c-ASI and d-ASI respectively.

In the experiment, H was varied between +1.4 kOe ≤ H ≤ -1.4 kOe by tracing the upper branch of the magnetic hysteresis and the SW frequencies were recorded from BLS spectra. For both c-ASI and d-ASI, we have observed three dominant modes whose frequencies and BLS intensities vary significantly and nonmonotonically with H. In addition, there exist a remarkable frequency difference between c-ASI and d-ASI due to their different inter-nanobar interaction as was also evident from their magnetic hysteresis loops. Figure 10.3 (e) and 10.3(f) are the experimental BLS spectra taken at H = -415 Oe and -550 Oe for c-ASI and d-ASI respectively.

It is clear from this figure that two additional higher frequency SW modes (M4 and M5) appear in both the cases. These modes grow at the expense of the modes M2 and M3 as the magnitude of negative H increases further. These spectra are special in the sense that a dramatic increase of the number of modes are observed. The origin of these additional modes will be elaborated later in this paper.

Next, we have investigated the detailed magnetic field dispersion and the nature of the observed SW modes as discussed in the following. The magnetic field dispersion of SW frequency is plotted in Figs. 10.4(a) and 10.4(b) for c-ASI and d-ASI, respectively. The experimental BLS spectra taken at varying H values are presented as three-dimensional surface plots whereas numerical simulation results using OOMMF are superposed on the experimental plots by filled symbols. The SW modes exhibit distinct and non-monotonic dispersion for +1.4 kOe ≤ H ≤ -1.4 kOe.
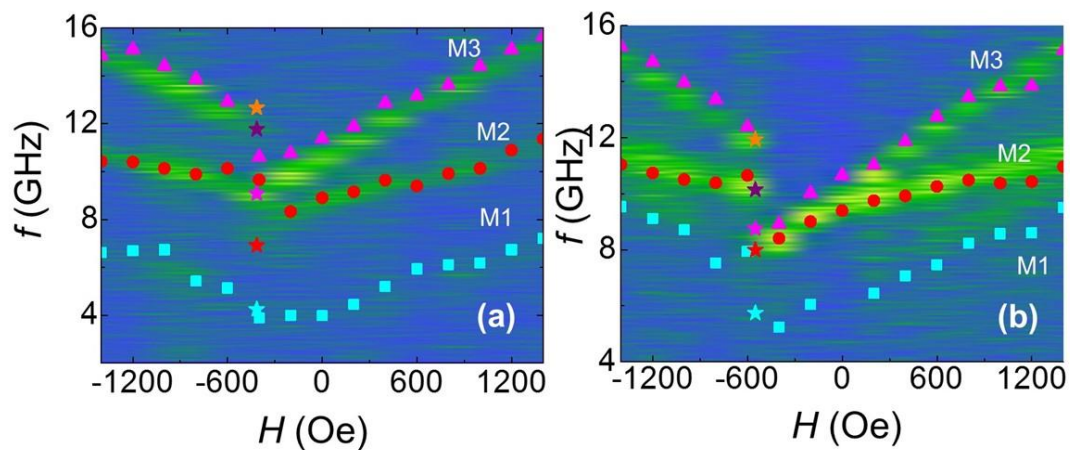
Figure 10.4: Frequencies of the SW modes as a function of applied bias magnetic field along the horizontal bar. The experimental bias field dependent SW frequencies are shown as three-dimensional surface plots, whereas the simulated SW mode frequencies are shown by filled symbols for (a) c-ASI and (b) d-ASI. The different SW branches are denoted by M1, M2 and M3. The experimental data taken in the field regime where magnetization reversal occurs (corresponding to the SW modes observed in Fig. 10.3(e) and 10.3(f)) are shown by star symbols for both c-ASI and d-ASI.

In Fig. 10.4(a), the intensity of the lowest frequency mode M1 is much lower than the other two modes. The frequency splitting between M2 and M3 decreases with the reduction of field from +1.4 kOe to become minimum at H = -200 Oe, beyond which it increases again. The frequencies of all the three modes experience a minimum at H = -400 Oe, which is close to the first switching field for c-ASI as shown by the black arrow in

Fig. 10.2 (a). For $H <$ -400 Oe, the mode frequencies experience a sharp transition showing a jump by up to about 3 GHz in M3. The relative intensities of M2 and M3 are also got exchanged, i.e. M2 becomes more dominant mode as opposed to M2, which was dominant over M3 for $H <$ -400 Oe but after further increase in the magnitude of the negative field the intensities of the modes become nearly equal. Figure 10.4(b) shows the field dependence SW frequencies for d-ASI where again three distinct modes have been observed. Unlike for c-ASI, the BLS intensity of Mode M2 is highest for d-ASI at positive fields. Here, the lowest frequency mode M1 appears very close to M2. Here also, the frequency splitting between M2 and M3 decreases with decreasing field from +1.4 kOe and they merge together for $H =$ -200 Oe, beyond which the modes split again and their splitting slowly increases with the increase in negative field amplitude. The tunability of the field dispersion characteristics of these high frequency modes in connected and disconnected kagome type ASI demonstrate a novel approach to use them for designing future spintronic and magnonic devices for microwave filtering applications where the forbidden and allowed frequency regimes can be manipulated.

10.3.3. Numerical Simulations

To explain the experimental findings, the static spin configurations and x-component of the demagnetizing field have also been simulated using OOMMF. Further, to investigate the nature and the origin of the SW modes, we have calculated their power and phase profiles for both c-ASI and d-ASI by fixing one of the spatial coordinates in the space- and time-dependent magnetization, followed by performing a discrete fast Fourier transform (FFT) with respect to time by using a home-grown code [36]. A substantial variation in the spin configuration observed in the negative field regime.

Figure 10.5 shows the static spin configuration, x component of demagnetizing field, SW mode profiles for c-ASI at three different bias magnetic fields corresponding to just below, at and above the transition in mode frequency values. Figure 10.5(a) shows that the spins in the horizontal nanobars of c-ASI continue to align along the +x direction even at $H =$ -400 Oe, while the spins in the tilted nanobars rotate in the clockwise (anticlockwise) direction in the upper (lower) half of the hexagon forming a forward onion-like state. At $H =$ -550 Oe, the spins in certain nanobars start to reverse their orientation in the direction of H forming vortex-like configuration in some of the hexagons in the lower half of the array (shown by ticks ($\sqrt{}$) Fig. 10.5 (f)). However, in some of the hexagons it forms neither a vortex nor an onion state as shown by asterisks

(*) in Fig. 10.5 (f). When H is further increased to -800 Oe, full reversal of spins in all the nanobars occurs (Fig. 10.5 (m)) forming reverse onion-like states in all hexagons. The corresponding spatial maps of the x-component of demagnetizing field (H_d) are presented in the Fig. 10.5 (b,g,n). As expected, the direction of H_d lies in the direction opposite to the applied field H = -400 Oe. At H = -550 Oe, the direction of H_d points towards H only for the reversed nanobars at that field. As we move further to H = -800 Oe, the direction of H_d lies completely along H.
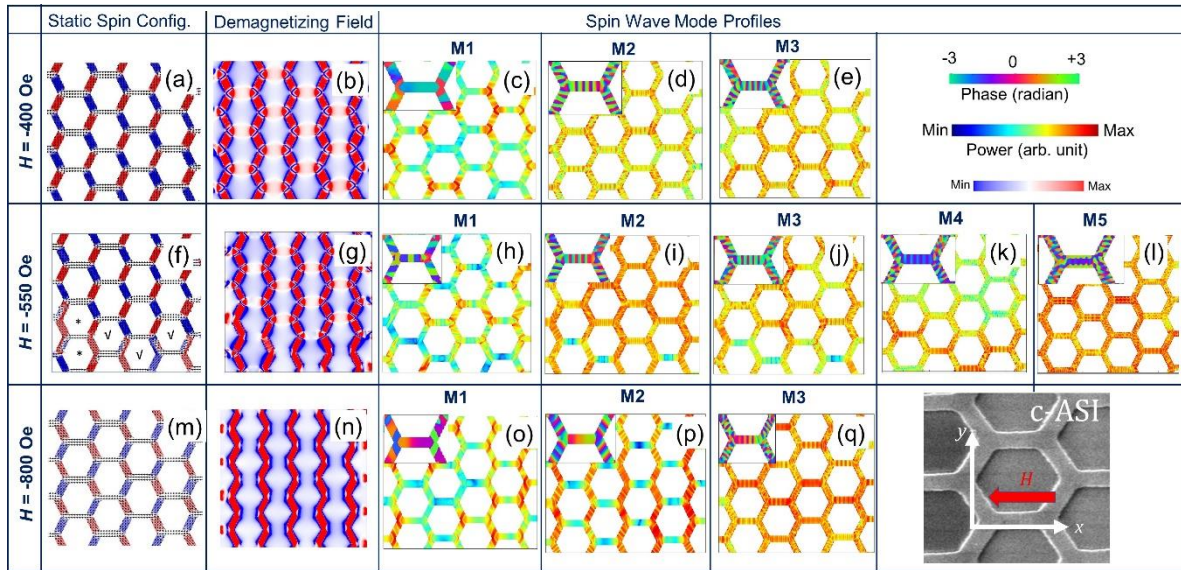
Figure 10.5: Simulated static spin configuration (a,f,m) and x-component of the demagnetizing field (b,g,n) for c-ASI. Simulated SW mode profiles at H = -400 Oe (c-e), -550 Oe (h-l) and -800 Oe (o-q) for c-ASI. The schematic of the measurement and simulation geometry is also shown at right bottom corner. The phase profiles are shown in the inset at the left corner of each power profile. The color maps are given at the right top corner.

Figures 10.5 (c-e) show the power profiles of M1, M2 and M3 for c-ASI at H = -400 Oe. The corresponding phase profiles are shown in the insets at the left corner of each image. The mode M1 (Fig. 10.5 (c)) is the edge mode (EM) at the junction of the three nanobars and maximum power is concentrated at the vicinity of the two junctions, while in the tilted nanobars it shows a Damon-Eshbach (DE, m) like behaviour with m = 3. Mode M2 shows a backward volume (BV, n) character in the horizontal nanobar with n = 9 and DE character in the tilted nanobars with m = 9. M3 also shows similar character with n = 11 and m = 7. At H = -550 Oe, i.e. in the transition regime, the number of SW modes have drastically increased to five. Here M1 becomes a BV-like mode with n = 3 in the horizontal

nanobars, and DE-like mode with $m = 5$. M2 has $n = 9$, $m = 7$ with higher power than for $H = -400$ Oe. M3 has $n = 11$, $m = 7$, similar to M3 for $H = -400$ Oe. M4 has $n = 11$, $m = 9$. M5 has mixed BV-DE character in the individual nanobars and it is difficult to resolve the mode numbers from the phase profile. As we further increase H to -800 Oe where a complete magnetization reversal occurred to a reverse onion mode, the mode characters are very different from those at $H = -400$ Oe. Here, M1 has $n = 2$, $m = 3$, while M2 has $n = 2$, $m = 5$. Although the phase contrast in the horizontal nanobars on both sides of the nodal plane is not high (far less than π) and the power is also small, it can still be considered as a BV-like mode with $n = 2$. M3 has $n = 9$ and $m = 9$, similar to M2 at $H = -400$ Oe. This drastic variation in the mode quantization number with the magnetic field leads to the observed abrupt change in the frequencies of the SW modes.
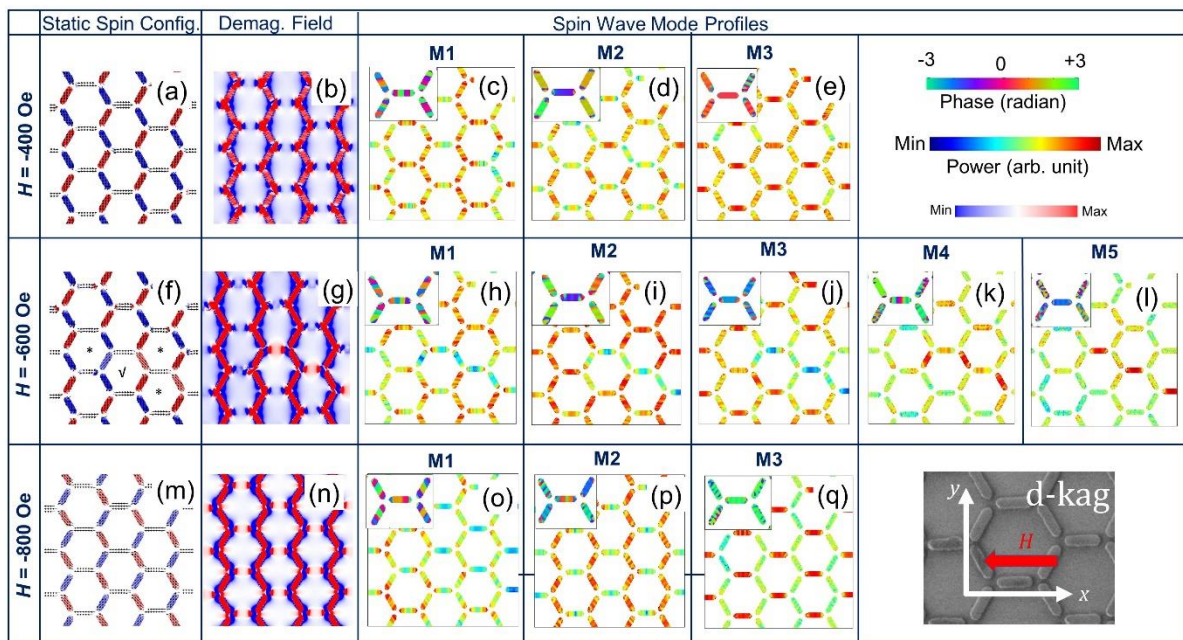
Figure 10.6: Simulated static spin configuration (a,f,m) and x-component of the demagnetizing field (b,g,n) for c-ASI. Simulated power maps for various precessional modes at $H = -400$ Oe (a-c), -600 Oe (d-h) and -800 Oe (i-k) for d-ASI. The schematic of the geometry is also shown at right bottom corner. Phase profiles are shown inside the rectangular box at the left corner of each images. The color maps are given at the right top corner.

Next, we investigate the static spin configuration, x-component of the demagnetizing field and SW mode profiles for d-ASI at three different applied bias fields, $H = -400$, -600 and -800 Oe as shown in Fig. 10.6. In d-ASI, static spin configuration follows a similar trend as c-ASI. However, only one vortex state ($\sqrt{}$) and three asterisk states (*) are formed in this case (Fig. 10.6(f)). In addition, the direction of H_d in the horizontal nanobars is opposite

to that observed in c-ASI. The partial reversal occurred at H = -600 Oe causes local reversal in H_d as shown in Fig. 10.6 (g)). The striking difference in the frequency of the various SW modes between c-ASI and d-ASI are related with this change in the spin configuration and H_d. The simulated power maps are shown together with the corresponding phase profiles in the inset of each image. Here, at H = -400 Oe, M1 corresponds to n = 5, m = 5, M2 has n = 3, m = 7, and M3 shows uniform mode (UM), m = 9. At H = -600 Oe, M1 has n = 5, m = 5, M2 has n = 7, m = 5, M3 has n = 3, m = 7, M4 has n = 6, m = 9, M5 has n = 1, m = 9. Hence, M2 and M4 are two new modes generated at transition, while three other modes retain their character with some modulation of power and phase distribution. This key observation is also evident in the experimental BLS spectra taken in the transition regime where the partial reversal of nanobars occurred for both c-ASI and d-ASI as shown in Fig. 10.3 (e & f). At H = -800 Oe, the mode characters have become drastically different. Here M1 corresponds to n = 4, m = 5, M2 has n = 7, m = 9 and M3 has n = 1, m = 11. Again, this drastic change in mode character has led to the observed transition in frequency. which show a significantly different behaviour from H = -400 Oe for d-ASI, while for c-ASI, only one mode gets modified and the other two retain their identity. The characteristic features of these SW spectra as observed from BLS experiment matches qualitatively well with that obtained using simulation. The additional modes appear most likely due to the local spin configuration during magnetization reversal. Moreover, the local modification of the internal field due the variation of H_d leads to the significant change in the SW frequencies associated with the reversed nanobars between c-ASI and d-ASI.

10.3.4. A Comparison of SW Spectra and Mode Profiles Simulated with/without 2D-Periodic Boundary Condition

To validate the simulation, a comparative study of the simulation with/without 2D-PBC performed on a unit cell and large array of ASI has also been presented. Figure 10.7 shows a comparison of SW spectra simulated for d-ASI at H = +1400 Oe with/without applying 2D-periodic boundary conditions (2D-PBC). It is important to mention that for unit cell, the cell size was chosen to be 2 nm × 2 nm × 25 nm and the dynamic simulation was run for 4 ns at the step of 10 ps with 2D-PBC. In the case of large array (3.4 μm × 2.7 μm), the cell size was chosen to be 2.5 nm × 2.5 nm × 25 nm and the dynamic simulation was run for both 4 ns and 20 ns at the step of 10 ps with and without applying 2D-PBC. The material parameters used for the simulations are: gyromagnetic ratio, γ = 2.211 ×10^5 A^{-1}

s^{-1}, saturation magnetisation, M_S = 800 kA/m, and the exchange stiffness constant, A = 1.3 × 10^{-11} J/m and Gilbert damping, a = 0.008. It is evident that the primarily three SW modes are observed in all the cases and the peak frequency do not vary much which validates the above presented simulation.
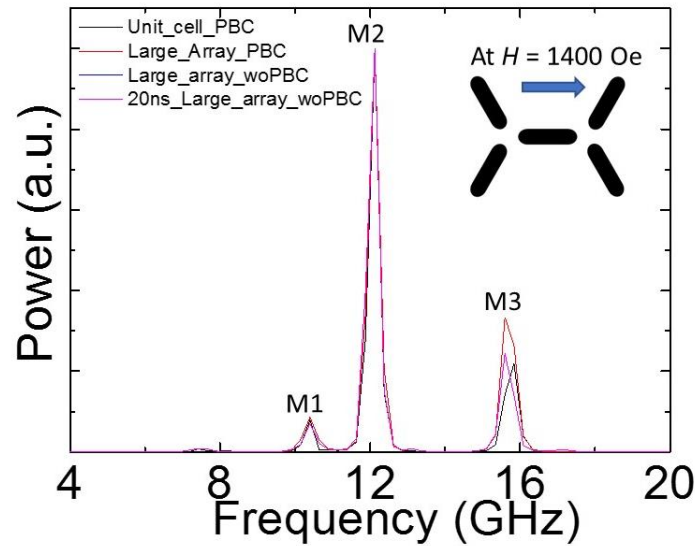
Figure 10.7: Simulated FFT power spectra for d-ASI in various scenarios such as unit cell with 2D-PBC, large array with (without) 2D-PBC, and large array with dynamic simulation run for longer duration (20 ns).

To investigate the nature of SW modes, we have simulated the power and phase maps of various SW modes observed in d-ASI at H = +1400 Oe. Figure 10.8 shows the comparison of the simulation results obtained under various protocol. In Fig. 10.8(a), the power and phase profiles of all three modes simulated for a unit cell with 2D-PBC is shown. The characters of the modes are edge mode (EM), BV-like mode (quantization number, n) in the horizontal nanobars and DE-like modes (quantization number, $m)$ in the tilted nanobars. Here M1 corresponds to n = 3 and m = 5, M2 has n = 5, m = 3 and M3 has n = 1. Subsequently, we have also simulated the mode profiles by considering a large array with 2D-PBC (without 2D-PBC) as shown in Fig. 10.8 (b) and 10.8(c) respectively. Here the dynamic simulation was run for 4 ns duration. Shown in Fig. 10.8(d), we also tested the validity of the presented simulation by running the dynamics for 20 ns for a large array without 2D-PBC. It is evident that the characteristics of SW mode profiles does not vary much whether 2D-PBC is applied or not.
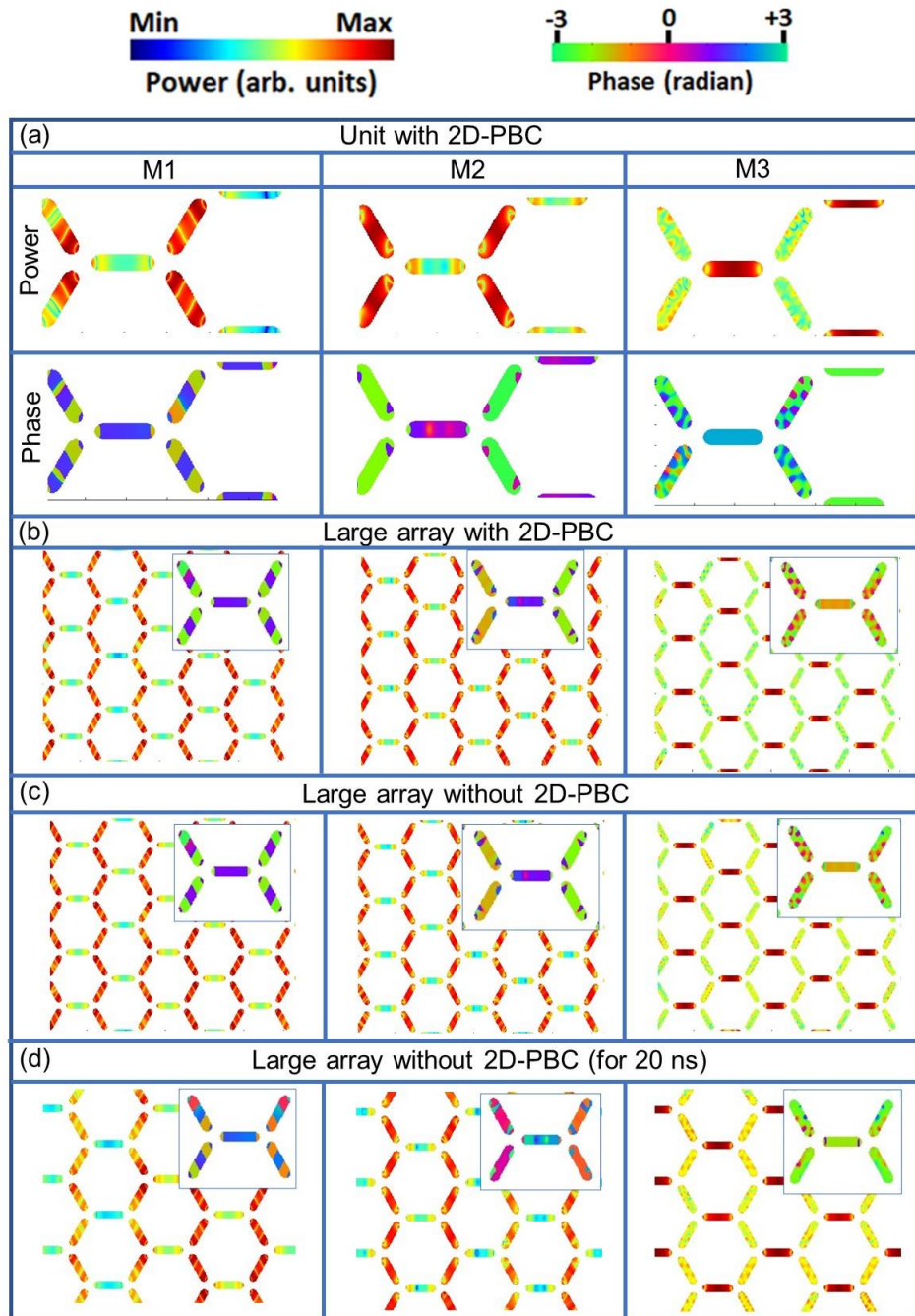
Figure 10.8: Simulated power maps for various precessional modes in d-ASI at H = 1.4 kOe for (a) unit cell with 2D-PBC (b) large array with 2D-PBC (c) large array without 2D-PBC and (d) large array without 2D-PBC for dynamics captured for 20 ns. Phase profiles are shown inside the rectangular box at the left corner of each images.

10.4. Conclusions

In conclusion, we have experimentally and numerically studied the magnetization dynamics of connected (c-ASI) and disconnected (d-ASI) kagome artificial spin ice nanostructures made of Py nanobars using Brillouin light scattering technique

complemented with micromagnetic simulations. The MFM images reveal that the magnetic microstates of kagome ASI obey the spin ice rule and a good agreement is found with the simulated images using micromagnetic simulation. The magnetic hysteresis loop measured by MOKE exhibits two-step reversal process for c-ASI but a single step reversal for d-ASI. Bias field dependent SW spectra measured by BLS reveal distinct features both in SW frequency (f) as well as BLS intensity for c-ASI and d-ASI. Both c-ASI and d-ASI exhibit frequency minimum, occurring at negative bias magnetic fields, when ramped down from a positive saturation field. A sharp jump in the mode frequencies was observed beyond the minima. This jump is somewhat related to the switching field observed from the MOKE loops and the variation in the magnetic microstates. This jump is associated with a remarkable change in the SW mode profiles and mode quantization numbers with H. This demonstrates a rapid control of SW modes by a small variation in magnetic field. Simulated internal field profiles throw further insights into the drastic variation of SW modes in this system system. Investigation and control of SW modes of these kagome artificial spin-ice nanostructures will be important for fundamental understanding and applications in devices requiring frequency selective SW propagation, microwave filter etc.

References

[1] L. J. Heyderman and R. L. Stamps, J. Phys.: Condens. Matter 25, 363201 (2013).

[2] E. Mengotti, L. J. Heyderman, A. F. Rodríguez, *et al.,* Nat. Phys. 7, 68 (2011).

[3] R. Wang, C. Nisoli, R. Freitas, *et al.,* Nature 439, 303 (2006).

[4] Z. Budrikis, P. Politi, and R. L. Stamps, New J. Phys. **14**, 045008 (2012).

[5] C. Nisoli, R. Wang, J. Li, *et al.,* Phys. Rev. Lett. **98**, 217203 (2007).

[6] W. R. Branford, S. Ladak, D. E. Read, K. Zeissler, and L. F. Cohen, Science **335**, 1597 (2012).

[7] S. Ladak, D. Read, T. Tyliszczak, W. R. Branford, and L. F. Cohen, New J. Phys. **13**, 023023 (2011)

[8] Y. Qi, T. Brintlinger, and J. Cumings, Phys. Rev. B **77**, 094418 (2008).

[9] Y. Perrin, B. Canals, and N. Rougemaille, Nature **540**, 410 (2016).

[10] S. Ladak, D. E. Read, G. K. Perkins, L. F. Cohen, and W. R. Branford, Nat. Phys. **6**, 359 (2010)

[11] B. Canals, I. A. Chioar, V.-D. Nguyen, *et al.,* Nat. Commun. **7**, 11446 (2016).

[12] L. D. Jaubert and P. C. Holdsworth, Nat. Phys. **5**, 258 (2009).

[13] S. Gliga, A. Kákay, R. Hertel, and O. G. Heinonen, Phys. Rev. Lett. **110**, 117205 (2013).

[14] V. S. Bhat, F. Heimbach, I. Stasinopoulos, and D. Grundler, Phys. Rev. B **93**, 140401(R) (2016).

[15] X. Zhou, G.-L. Chua, N. Singh, and A. O. Adeyeye, Adv. Funct. Mater. **26**, 1437 (2016).

[16] J. Dubowik, P. Kuswik, M. Matczak, *et al.,* Phys. Rev. B **93**, 224423 (2016).

[17] M. B. Jungfleisch, W. Zhang, E. Iacocca, *et al.,* Phys. Rev. B **93**, 100401(R) (2016).

[18] E. Iacocca, S. Gliga, R. L. Stamps, and O. Heinonen, Phys. Rev. B **93**, 134420 (2016).

[19] M. Krawczyk and D. Grundler, J. Phys. Condens. Matter **26**, 123202 (2014).

[20] J. Topp, D. Heitmann, M. P. Kostylev, and D. Grundler, Phys. Rev. Lett. **104**, 207205 (2010).

[21] Y Li, G Gubbiotti, F Casoli, *et al.,* J. Phys. D: Appl. Phys. **50,** 015003 (2017).

[22] D. M. Arroo, J. C. Gartside, and W. R. Branford, Phys. Rev. B. **100**, 214425 (2019).

[23] J. C. Gartside, D. M. Arroo, D. M. Burn, *et al.,* Nat. Nanotechnol. **13,** 53 (2018).

[24] Y.-L. Wang, Z.-L. Xiao, A. Snezhko, *et al.,* Science **352**, 962 (2015).

[25] Y. Lao, F. Caravelli, M. Sheikh, *et al.,* Nat. Phys. **14**, 723 (2018).

[26] I. Gilbert, Y. Lao, I. Carrasquillo, *et al.,* Nat. Phys. **12**, 162 (2016).

[27] J. Sklenar, Y. Lao, A. Albrecht, *et al.,* Nat. Phys. **15**, 191 (2019).

[28] V. S. Bhat, F. Heimbach, I. Stasinopoulos, and D. Grundler, Phys. Rev. B **96**, 014426 (2017).

[29] M. B. Jungfleisch, J. Sklenar, J. Ding, *et al.,* Phys. Rev. Appl. **8**, 064026 (2017).

[30] A. Talapatra, N. Singh, and A. O. Adeyeye, Phys. Rev. Appl. **13**, 014034 (2020).

[31] W. Bang, J. Sturm, R. Silvani, *et al.,* Phys. Rev. Appl. **14**, 014079 (2020).

[32] R. Mock, B. Hillebrands, & R. Sandercock, J. Phys. E-Sci. Inst. **20,** 656 (1987).

[33] A. K. Chaurasiya, C. Banerjee, S. Pan, *et al.,* Sci. Rep. **6**, 32592 (2016).

[34] M. Donahue and D. G. Porter, *OOMMF User's Guide Version 1.0 Interagency Report NISTIR 6376* (Gaithersburg, MD: National Institute of Standard and Technology) (http://math.nist.gov/oommf) (1999).

[35] M. R. Scheinfein and E A Price *LLG User Manual* v2.50 http://llgmicro.home.mindspring.com (2003).

[36] D. Kumar, O. Dmytriiev, S. Ponraj and A. Barman, J. Phys. D: Appl. Phys. **45**, 015001 (2012).

Chapter 11

11. Propagating Spin Waves in Magnonic Waveguides Studied using Micro-focused Brillouin Light Scattering

11.1. Introduction

An alternate way to carry and process information via spin wave (SW) has gathered much attention recently because of its much lower dissipation as opposed to the Joule-heating prone charge-based information processing [1-4]. A substantial development has been made by the scientific community to realize the magnonic devices in terms of control and manipulation of SW, SW nanochanneling, on-chip integration etc [5-10]. A key component of any magnonic device is a waveguide that transmits SWs from one location to another, the properties of which are dependent upon the structural and material parameters such as size, shape, modulation, Gilbert damping etc [11]. One of the crucial parameters is SW decay length, which ranges from few to tens of micrometers in a variety of materials like NiFe, CoFeB, Heusler alloys and yittrium iron garnet (YIG). It is of utmost importance for the integration of magnonic devices for technological realization [12-14]. Moreover, a different route to control SW decay length is undoubtedly necessary to address possible solution for the efficient CMOS based computing technologies. In this context, magnetostatic surface spin wave (MSSW), which propagates in the direction perpendicular to the applied bias magnetic field holds key promises because of its large group velocity, low attenuation and relative ease for experimental realization [15]. Furthermore, it has been proposed that SWs may be regarded as a link between phase-locked nano-oscillators to carry spin current in the magnetic microstructure subjected to the thermal gradient which makes them useful for building of logic devices [16-21]. In recent years, the local control and manipulation of the amplitude and phases of propagating signals has been proved to be another key aspect for the development of digital functionalization [22-23]. To this end, several ways have already been proposed including the use of magnetic field inhomogeneity [24], non-linear SW properties [25],

dynamic magnonic crystals (MCs) [26], variation of local magnetization orientation [27-28], voltage controlled magnonic nanochannels [29] and SW phase manipulation [30]. On the other hand, the magnetic properties of externally programmable MCs can be modulated periodically and it can be switch "on" and "off" by external stimuli such as electric field [31], strain [32] and magnetic field [33], paving a way for magnon based logic devices. These possibilities give rise to the development of reprogrammable magnonics [34] which can bridge the gap between cross-disciplinary fields such as photo-magnonics [35], magphonics [36] or spin-mechatronics [37]. To avoid the Ohmic losses in current controlled nanoscale magnetic elements, magneto-electric coupling can be a novel alternative method by voltage controlled magnetic anisotropy (VCMA) [38]. Therefore, the search of the magnonic waveguides with improved functionalities besides energy efficient local manipulation is demanding for the technological applications. Thanks to the advances in electron beam lithography and state-of-the-art nanofabrication techniques, the miniaturization of nanoscale magnonic devices with intriguing properties have been possible nowadays. Furthermore, the tunability of the magnonic band gap in magnonic waveguides with external stimuli such as electric field offers a new avenue of research for efficient alternative approach for the development of magnonic devices.

In conventional BLS spectroscopy, the collective SW dynamics is measured from area covering hundreds of μm^2. For an appreciable signal acquired from nanometer sized elements, an ordered arrangement of hundreds of elements in an array is required. Such investigations yield the averaged properties of an ensemble of elements and hence the information about the power and phase of the SW dynamics of the individual elements are lost. In order to overcome this challenge, the conventional BLS spectroscopy has been upgraded to introduce a microscopic spatial resolution. In this chapter, we have experimentally studied the propagating SWs in two types of system, namely a $Ni_{80}Fe_{20}$ (Py) microstripe and VCMA modulated CoFeB/MgO SW waveguides using micro-focused BLS technique. In the former case, the Py microstripe is excited with an RF source using a microwave antenna and the propagating SW has been imaged. In the latter case, VCMA has been used to excite and modulate SWs in the CoFeB/MgO heterostructure.

11.2. Experimental Details

11.2.1. Microfocused Brillouin Light Scattering Microscopy

Microfocused BLS (micro-BLS), developed significantly in the past decades, is an extension of conventional BLS [39-40]. Here, the laser is focused down to a small spot size of about 250 nm on the sample, which allows for a high spatial resolution. However, this is achieved at the cost of wave vector resolution because of the Heisenberg's uncertainty principle, which states that simultaneous access to position and wave vector with arbitrary high precision is not possible. The required components which are needed to transform the conventional BLS to a micro-BLS include a microscope objective (MO), a CMOS camera, a set of high precision three-dimensional translation stages and a range of steering optics. The MO used in our set up is from Leica (model number: HC PL FLUOTAR L; Material number: 11566063) and has specifications as magnification: X100; Numerical aperture (NA): 0.75; and long working distance: 3.7 mm. It is important to mention here that in micro-BLS, backscattering geometry is used which does not allow any provision of changing the angle of incidence. The maximum angle of incidence is decided by the numerical aperture $NA = n\,sin\theta$, where n is the refractive index of the medium (1 for air) and θ is the angle of incidence. For a NA = 0.75, the value of maximum angle of incidence is 48.6°. Hence, the collected scattered light will correspond to a range of transferred k-vectors from 0 to 17.7 rad/μm. The scattered beam is collected using the same objective lens by which it was focused onto the sample and sent to the Tandem Fabry-Pérot interferometer (TFPI) guided by the mirrors for frequency analysis. The CMOS camera from Thorlabs (Point Grey: Flea3 FL3-U3-13Y3M) serves the following purpose: i) to locate the laser spot on to the sample and (ii) to stabilize the sample position with respect to the thermal drift. During the measurement, the laser spot is needed to be filtered out with a notch filter to avoid saturation of the entire image. To perform a well-defined spatial scan, and to maintain high stabilization against thermal drift, a very high precision motorized translation stage (x-y-z) is used. The x-y-z stage is composed of high travel range linear stages (model number XMS50) for horizontal motion control and vertical focusing stage (model number GTS30V) from Newport. The travel range of lateral and vertical stage are 30 mm and 50 mm, while their spatial resolution is 50 nm and 1 nm, respectively. These high spatial resolution for stages enables to correct the thermal drift

as well as to conduct fine spatial scans. In order to excite the SW externally using microwave frequency, a nonmagnetic customized picoprobe (Model No. 40A- GSG-200-GR) from GGB industries is used. The sample is mounted on a holder attached to the stage. By moving the sample position and thereby changing the position of the laser onto the sample, the spatially dependent amplitude of scattered light is measured for a particular excitation frequency. In order to enhance the signal to noise ratio of the BLS spectra, the density of measured magnons is stimulated by electrical excitation with an RF frequency sent through a coplanar waveguide (CPW) antenna. The RF frequency is launched on the sample by a homemade probe station.

11.2.2. Sample Fabrication

The Py microstripe sample was fabricated using a combination of multistep electron-beam lithography and optical lithography techniques on an oxidized Si substrate (Si/SiO$_2$). A single layer of polymethyl methacrylate (PMMA) resist was first spin-coated on the substrate followed by electron-beam lithography to write the rectangular stripe pattern. The resist was then developed in methyl isobutyl ketone (MIBK) and isopropyl alcohol (IPA) solution (MIBK:IPA ratio of 1:3). A 20-nm-thick Py layer was subsequently deposited on the resist pattern using electron-beam evaporation in a chamber with a base pressure of 2×10^{-8} torr. The desired waveguide structures were obtained after metal lift off in acetone assisted by ultrasonic agitation. In the second step, a CPW antenna with minimum width of 3.6 μm and 50 Ω nominal characteristic impedance was patterned using electron-beam lithography and followed by lift off processing as described above. The antenna was composed of 80-nm-thick Au deposited by sputtering on top of a 5-nm-thick Cr adhesive layer deposited by electron-beam evaporation. The larger contact pads of the antenna, with ground–signal–ground (GSGs) configuration was patterned by optical lithography. A thin film stack of Cr (5 nm)/Au (200 nm) was then deposited using the above-mentioned deposition techniques followed by metal lift off.

For the second system, we have chosen the heterostructure: substrate|Ta(10 nm)|Co$_{20}$Fe$_{60}$B$_{20}$(1.8 nm)|MgO(2 nm)|Al$_2$O$_3$(10 nm). It is noteworthy that, the magnetization state in an ultrathin CoFeB film strongly depends upon its thickness. Here the magnetization direction tends to align along the out-of-plane (OOP) axis below a critical value of its thickness ($\sim$ 1.5 nm). On the contrary, the magnetization tends to be aligned along the in-plane (IP) direction above the critical thickness. We have chosen the

$Co_{20}Fe_{60}B_{20}$ (CoFeB) thickness to be 1.6 nm to ensure that its easy axis of magnetization lies in the sample plane, while maintaining significant perpendicular magnetic anisotropy (PMA) at the CoFeB/MgO interface. The details of the sample fabrication are described later in this Chapter.

11.3. Results and Discussions

11.3.1. Investigation of Propagating SW in a Py Microstripe

Figure 11.1(a) shows the scanning electron microscopy (SEM) image of the investigated sample structure. Fig. 11.1(b) is the magnified view of the sample structure which gives the information about the width (w) of the Py nanostripe to be 1.45 μm and the width (d) of the CPW antenna to be 3.6 μm.
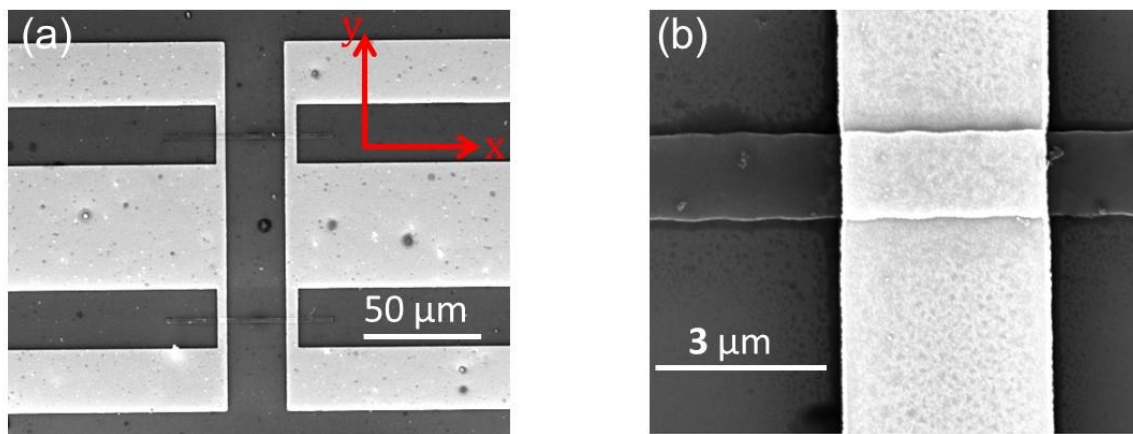
Figure 11.1: (a) SEM image of the Py microstripe with the CPW antenna. The coordinate axes are shown in the inset. (b) Magnified view of the SEM image to estimate the width of the antenna and the Py microstripe.

In order to find out the resonance frequency at an applied magnetic field, an external excitation is provided with the help of GSG probe attached to the microwave signal generator. The RF field generated by the antenna has a maximum wave vector defined by 2π/d = 1.70 rad/μm. The external excitation using this method has been heavily adopted by the magnonics community for the experimental investigation of propagating SW. The excited SWs have been probed locally using the micro-technique with a laser spot diameter of 250 nm. The laser spot diameter was estimated by using a standard knife-edge technique.

Figure 11.2(a) shows an optical image of the sample illustrating the stabilization protocol equipped with the image search algorithm established during the measurement. An in-plane magnetic field (H) of 0.7 kOe is applied along the y direction (along the width of the waveguide). Figure 11.2(b) shows the representative BLS spectra measured at an external applied RF frequency (f) = 8.6 GHz and microwave power (P) = +10 dBm. In order to find the resonance frequency, we scanned the RF frequency at fixed value of H and P. A strong BLS peak was observed at f = 8.6 GHz as shown in the BLS spectrum where the BLS counts is found to be maximum for given H and P at the fixed acquisition time. Single frequency appears on the both sides of the Rayleigh line namely Stokes and anti-Stokes peak. This is the first step to know the resonance frequency. The peaks are well fitted with the Lorentzian function as shown in Fig. 11.2(b).
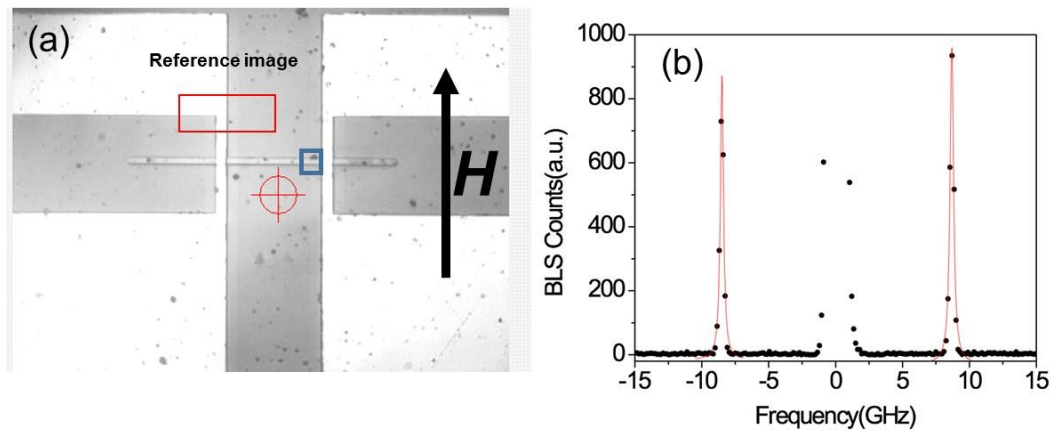
Figure 11.2: (a) Optical image of the Py microstripe sample along with the excitation antenna sample as seen on the computer display during the measurement. Red rectangular part is the reference image chosen to stabilize the image during the scan procedure. (b) Representative BLS spectrum taken at excitation frequency f= 8.6 GHz, microwave power P = +10 dBm and in-plane applied field H = 0.7 kOe.

After determining the resonance frequency precisely, the 2D imaging of the propagating SW has been performed. Figure 11.3(a) shows a two-dimensional spatial profile of the BLS intensity for the FMR peak taken on the left side of the microwave antenna under applied frequency, f = 8.6 GHz and P = +10 dBm at H = 0.7 kOe. The direction of propagation has been shown with the arrow. An area of 5 x 2.7 μm^2 was chosen as marked in the figure and the laser spot was raster scanned with 200 nm step size. Data acquisition time for each scan point was fixed at 2.5 minutes per spectrum. The SW intensity is systematically detected up to distances of several micrometres on both left and right side

of the antenna. Figure 11.3(b) represents the spatial decay of the BLS intensity along the length of the microstripe (x-direction) integrated over the central part of the map. From an exponential fit to the experimental data points, the decay constant (defined as the distance over which the SW intensity drops by a factor of e) is found to be 4.2 μm for the investigated Py microstripe.
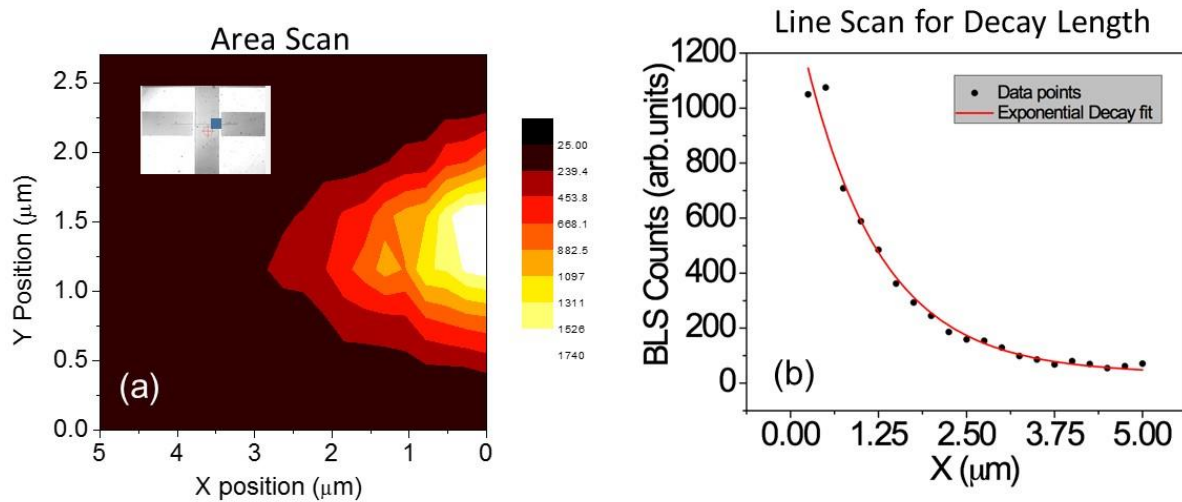
Figure 11.3: (a) Two-dimensional spatial map of the BLS intensity for the propagating SW mode with frequency 8.6 GHz at the left side of the antenna. For this map, the BLS intensity, proportional to the SW intensity, was recorded over a 5 × 2.7 μm^2 area on the left side of the antenna by raster scanning the laser spot at 200 nm steps. The blue shaded rectangle is the scanned area as marked in the inset. (b) Dependence of BLS intensity on the propagation distance from the left edge of the antenna. The red solid line represents an exponential fit to the measured data as described in the text.

The numerical simulation of SW propagation was performed using the OOMMF software [41]. To investigate the nature and the origin of the SW modes, we have calculated their power and phase profile by fixing one of the spatial coordinates in the space- and time-dependent magnetization, followed by performing a discrete fast Fourier transform (FFT) with respect to time by using a home-grown code [42]. For the simulation, a Py stripe of dimension 10 × 2.7 μm^2 was subjected to an in-plane magnetic field of H = 0.7 kOe applied along the width of the Py stripe. The whole Py stripe was discretized into rectangular prism-like cells of 5×5×20 nm^3 dimensions.
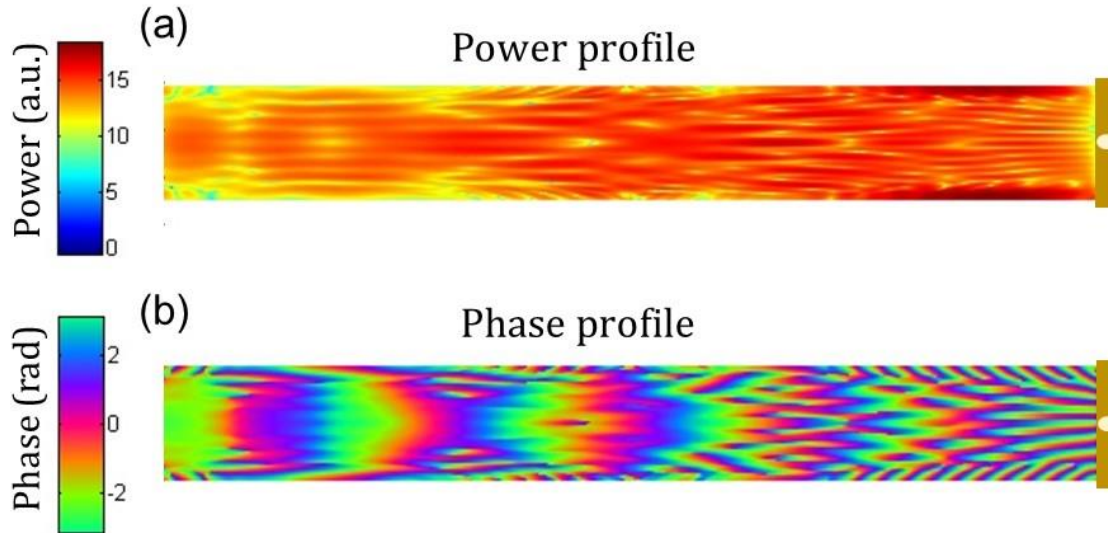
Figure 11.4: (a) Simulated power spectra showing the propagating nature of SW in Py waveguide. The SWs are excited at the end of the waveguide with sinusoidal excitation field. (b) Corresponding phase profiles of SW mode. The color maps for power and phase profiles are shown on the left side.

The lateral dimensions of the cells were taken below the exchange length (~5.6 nm) of Py. The material parameters used for the simulations are: gyromagnetic ratio, $\gamma = 2.211 \times 10^5$ $A^{-1}s^{-1}$, saturation magnetisation, $M_S = 860$ kA/m, and the exchange stiffness constant, $A = 1.3 \times 10^{-11}$ J/m and Gilbert damping, $\alpha = 0.008$. In the simulation, SWs are excited by a sinusoidal point excitation of desired frequency at the end of the Py waveguide. The sinusoidal magnetic field is given by $h_x = A_0\sin(2\pi f(t-t_0))$, where $A_0 = 5$ mT and $f = 8.6$ GHz. The excited SW in the DE geometry propagates along the length of the waveguide. The corresponding power and phase profiles are presented in Fig. 11.4 (a) and (b), respectively.

11.3.2. Direct Observation of Voltage Controlled Magnonic Band Gap in Ta/CoFeB/MgO Heterostructure by Utilizing VCMA Effect

The Physics behind the Electric Field Modulation of Interfacial Perpendicular Magnetic Anisotropy in FM/oxide Heterostructure

Generally, strong interfacial perpendicular magnetic anisotropy (iPMA) can be observed at the interfaces between $3d$ transition metal (or their alloys) FMs and heavy nonmagnetic (NM) metals. However, iPMA cannot be modulated by an electric field in

such systems because of the absence of insulating or dielectric layer at the interface. However, PMA can also be obtained at the FM/oxide interface. Among them, the CoFeB/MgO heterostructures [43] have drawn immense attention because of their application in magnetic tunnel junction [44]. The origin of iPMA and VCMA at the CoFeB/MgO interface can be interpreted as follows. At CoFeB/MgO interface, the oiu-of-plane (OOP) $3d_{z^2}$-orbitals of Fe strongly bond with OOP $2p_z$-orbitals of oxygen leading towards a substantial charge transfer from $3d_{z^2}$-orbitals to $2p_z$-orbitals. Therefore, the number of electrons in OOP orbitals is reduced as opposed to the number of electrons in in-pane (IP) orbitals, which, in turn, introduces a considerable PMA through the spin-orbit coupling (SOC) of FM [45]. When an electric field is applied across the FM/oxide interface, the number of electrons in the OOP $3d$-orbitals of Fe are modified with respect to the IP orbitals, which was explained from first principles calculations [46]. This affects the bonding strength between $3d$- and $2p$-orbitals resulting in a substantial change of iPMA. Although electric field control of electronic occupation state is believed to be the main mechanism behind VCMA, several alternative theories are also found in the literature. One of those theories claims the control of iPMA due to the coupling between magnetic dipoles and electric quadrupole of electronic orbital in FM which is generated due to the inhomogeneous electric field at the FM/oxide interface [46]. Another theory claims that the applied electric field at FM/oxide interface modifies the Rashba SOC, which, in turn, modulates the iPMA [47]. Recently, the piezoelectric property of oxide (MgO) layer through magneto-elastic coupling is appeared to be responsible for the modulation of iPMA via development of tensile and compressive strain in the oxide layer [48]. In practice, all the above-mentioned mechanisms can be present and contribute simultaneously to the modulation of iPMA. Nevertheless, it is believed that the presence of an oxide layer is essential for modulation of iPMA where the relative change in the electronic occupation state in the $3d$-orbitals of FM plays a crucial role in achieving VCMA. Furthermore, since the penetration depth of electric field in metal is only a few ångström (Å), hence the VCMA effect is limited primarily in ultrathin FM films. This justifies the choice of the ultrathin CoFeB film in our case.

Theoretical calculations show that the change in the number of electrons in $3d$-orbitals of FM linearly scales with the applied electric field (E_G) at the FM/oxide interface [46, 49]. As a result, the change in the magnetic moment and iPMA must also be linearly related to the electric field [50], i.e.

$$\Delta K_{\mathrm{s}} = \beta E_{\mathrm{G}} \qquad\qquad (11.1)$$

Here, ΔK_{s} is the change in iPMA, whereas β is defined as the magneto-electric or VCMA coefficient. The strength and sign of β depends upon several factors such as the composition of FM [51] or adjacent dielectric layer [52], underlayer material (i.e. the layer beneath the FM/oxide heterostructure) [53], substrate [54] as well as temperature [55].

Figure 11.5(a) shows the schematic of the sample. The samples were prepared by multistep nanofabrication method. First, $Ta(10)|Co_{20}Fe_{60}B_{20}(1.6)|MgO(2)|Al_2O_3(10)$ multilayered heterostructure was deposited on $Si(001)|SiO_2(700\ nm)$ substrate by radio frequency (RF) sputtering at room temperature and at a base pressure of about 1×10^{-8} Torr. Here the numbers in the parentheses represent the nominal thicknesses (in nm) of the corresponding layers. This was followed by annealing of the film stack at 280°C in vacuum under a perpendicular magnetic field of 600 mT for 1 hr. Remarkably, since PMA present in the heterostructure is interfacial (i.e. at CoFeB/MgO interface) in nature, the thickness of CoFeB is selected as 1.6 nm in order to enhance the magneto-electric effect while keeping the easy axis of magnetization in the plane of the sample at the same time. In the subsequent step, rectangular blanket area of lateral dimensions 70 μm × 10 μm was patterned from the annealed multilayer stacks by using mask-less UV photolithography followed by Ar^+ ion milling down to the SiO_2 layer. In the third step, electron-beam lithography alignment markers and bottom metal gate electrodes were patterned by mask-less UV photolithography followed by deposition of $Ti(5)|Au(100)$ layer by electron-beam evaporation. In the fourth step, 100-nm-thick Al_2O_3 layer was deposited everywhere barring the top of the square area and the metal electrodes. In the fifth step, electron-beam lithography was used to pattern the 1D grid-like stripes on the top of the sample which was followed by deposition of a 120-nm-thick indium tin oxide (ITO) top gate electrode layer by DC sputtering technique. Here, each stripe-like top gate electrode is 220 nm wide having an edge-to-edge separation of 220 nm (i.e. pitch = 440 nm). It is worth mentioning that, ITO is chosen as the top electrode as it is optically transparent which is essential for the BLS) measurement through the electrodes to acquire thermally excited magnons from the CoFeB/MgO heterostructure. In the final step, all the contacts for application of DC gate voltage were made by mask-less photolithography and deposition of $Ti(5)|Au(200)$ layer by electron-beam evaporation.

Figure 11.5 shows a schematic representation of the sample under investigation. Here, a patterned ITO layer of thickness 120 nm has been deposited on top of the substrate|Ta(10nm)|Co$_{20}$Fe$_{60}$B$_{20}$(1.8 nm)|MgO(2 nm)|Al$_2$O$_3$(10 nm) heterostructure. This ITO layer serves as the top gate electrode to apply the electric field (E_G) or voltage (V_G) across the CoFeB/MgO interface. There is an Au antenna fabricated on the top of the sample to excite the spin wave externally.
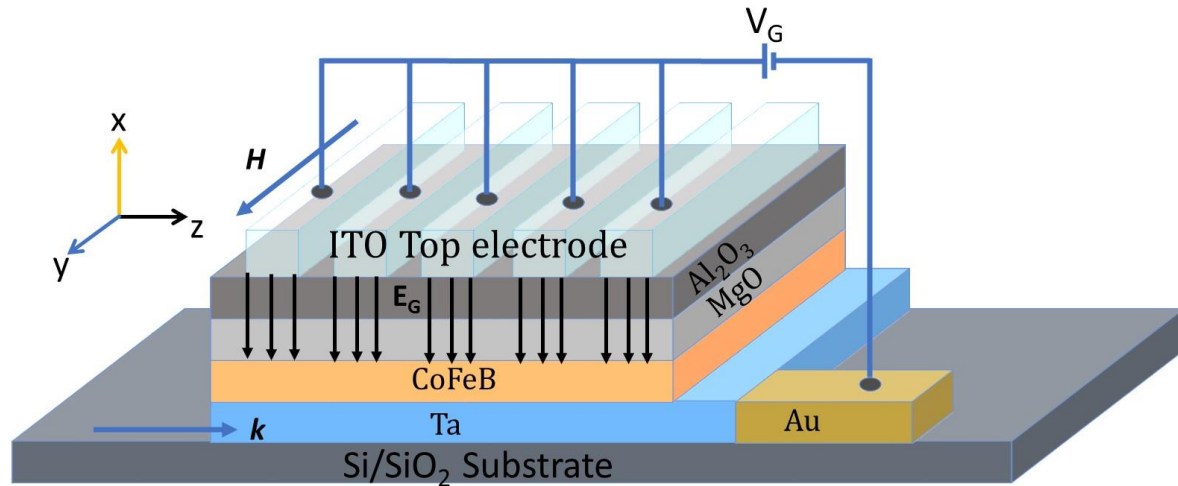
Figure 11.5: Schematic of the sample structure.

Therefore, this sample is special in the sense that on can excite the spin waves externally by both RF source as well as an electric field controlled VCMA. Importantly, a positive gate voltage denotes that the top gate electrode has a positive potential with respect to the CoFeB film. This sample can be considered as a one-dimensional electric field controlled magnonic waveguide (1D-EFCMWG). All the measurements presented in this thesis have been carried out in the Damon-Eshbach (DE) geometry, i.e. the (in-plane) SW wave vector (k) lies perpendicular to the magnetic field (H) applied in the plane of the sample.

Figure 11.6 shows the representative BLS spectra from the 1D-EFCMWG taken at an applied in-plane magnetic field, H = 1 kOe, excitation frequency (f) = 5.8 GHz and microwave power (P) = +10 dBm. It is important to mention here that the excitation frequency f of 5.8 GHz was selected from the BLS spectrum measured thermally without any external excitation. Here, the direction of SW propagation (k) is perpendicular to the 1D Stripe like electrode made of ITO. The magnetic anisotropy becomes different in the regions with or without the electrodes under the application of a moderate voltage

(electric field). Hence, the propagating SW experiences a periodic potential along its propagation direction. In this way, this system behaves as 1D dynamic MC integrated to the magnonic waveguide.

Figure 11.6 reveals a single peak in the BLS spectrum for $V_G = 0$ V. This is because without any gate voltage the magnonic waveguide is a continuous thin film without any modulation of magnetic properties. As soon as we turn on the gate voltage, the SW mode splits into two clear peaks.
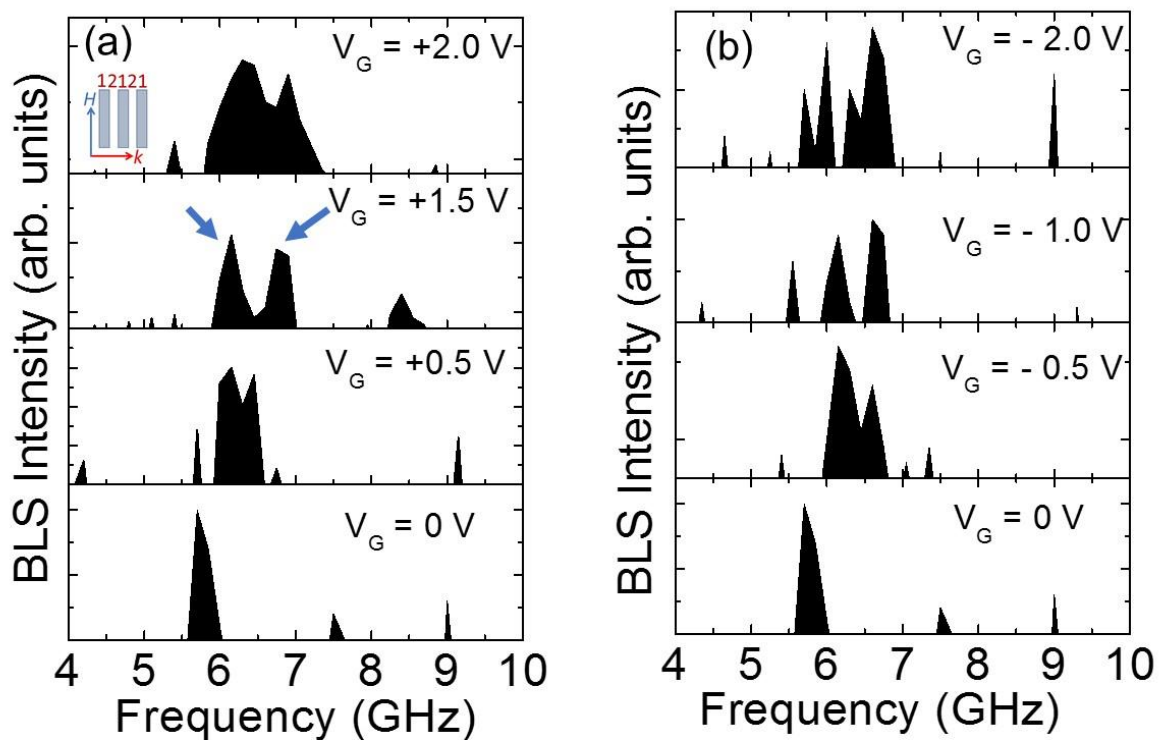
Figure 11.6: (a) Representative BLS spectra taken at $H = 1$ kOe for (a) positive gate voltage (+V_G) (b) negative gate voltage (-V_G). Inset: Schematic of the two stripe-like regions, namely region 1 (without ITO electrode) and region 2 (with ITO electrode).

The mode frequency also shifts towards a slightly higher frequency. With further increase in the gate voltage the frequency does not increase significantly, but the frequency gap between the two peaks increases further and appearance of mode modes are observed. The overall increase in the SW mode frequency may be attributed to the increase in the average magnetic anisotropy of the system, which causes the increase in the effective

magnetic field and SW frequency. On the other hand, the increase in the contrast between the magnetic anisotropy in the two stripe-like regions, namely region 1 (without ITO electrode) and region 2 (with ITO electrode) with the increase in gate voltage causes the widening of the MBG in this system.

The variation of MBG as a function V_G is shown in Fig. 11.7. The gate voltage V_G is applied upto ± 3 V. For positive V_G, we observe a monotonic increase in MBG up to +2.5V beyond which it drops suddenly. On the contrary, for negative V_G the MBG shows a maximum at $V_G = -1.5$V beyond which it drops. The increase in MBG for negative V_G is steeper than that for positive V_G resulting in an asymmetry in the variation in MBG with V_G. The drop in the MBG beyond certain voltage is most likely due to the degradation and in the CoFeB/MgO interface as a result of dielectric breakdown. A maximum value of MBG of 0.82 GHz is observed at V_G = +2.5V. This kind of artificially engineered 1D- EFCMWG with continuously tunable MBG by application of moderate voltage (electric field) will be important for the development of energy efficient magnonic devices for information processing.
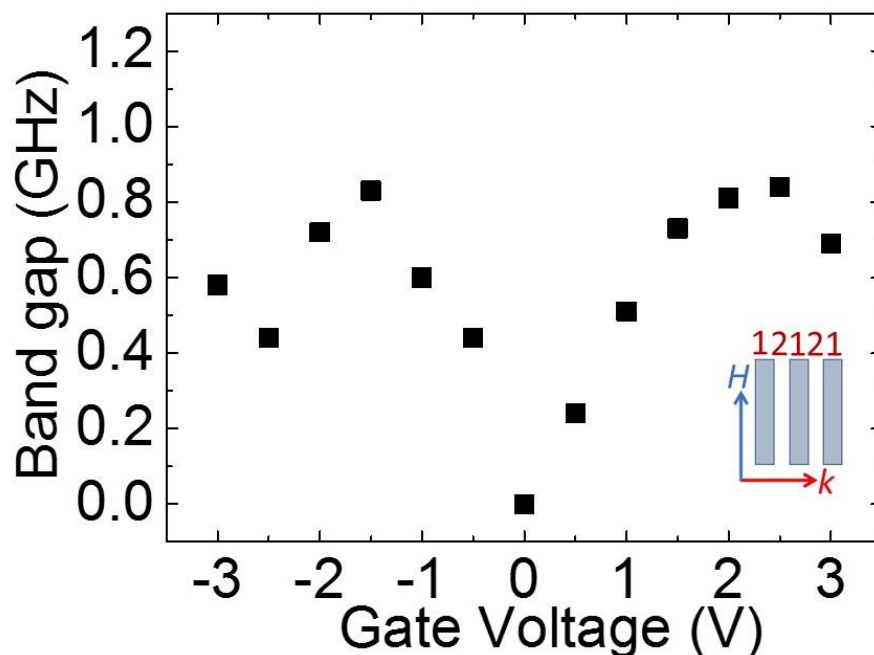

Figure 11.7: Variation of magnonic band gap as a function of gate voltage V_G.

11.4. Conclusion

We have experimentally investigated the propagation of spin waves in a magnonic waveguide made of Py using microfocused BLS technique. Using an appropriate design of

the rf antenna combined with the choice of excitation frequency and microwave power, a prominent propagating spin wave mode was observed. By performing a spatial 2D-scan of the BLS intensity, the propagation characteristics of the excited SW mode has been extracted. We have also performed numerical micromagnetic simulation to understand the spin wave power and phase profiles of the excited mode. Furthermore, we have explored a voltage controlled dynamic MC by utilized voltage controlled magnetic anisotropy effect in CoFeB/MgO heterostructure. Under the application of electric field to an array of patterned top electrodes on the CoFeB/MgO heterostructure, the single frequency mode splits into two modes, the spacing between which gives an estimate of the magnonic band gap in this artificial one-dimensional electric field controlled magonic waveguide (1D-EFCMWG). The observed MBG is found to be continuously tunable with both the polarity and magnitude of the applied gate voltage across CoFeB/MgO interface. This opens up a new avenue for energy-efficient stimulus, i.e., electric field, which may play a vital role in designing spin-based magnonic nanocircuits with minimal-power consumption.

References

[1] D. Grundler, Nat. Phys. **11**, 438 (2015).

[2] R. L. Stamps, S. Breitkreutz, J. Åkerman, *et al.*, J. Phys. D **47**, 333001 (2014).

[3] B. Lenk, H. Ulrichs, F. Garbs, and M. Münzenberg, Phys. Rep. **507**, 107 (2011).

[4] A. V. Chumak, V. I. Vasyuchka, A. A. Serga, and B. Hillebrands, Nat. Phys. **11**, 453 (2015).

[5] S. Urazhdin, V. E. Demidov, H. Ulrichs, *et al.*, Nat. Nanotechnol. **9**, 509 (2014).

[6] V. E. Demidov, S. Urazhdin, and S. O. Demokritov, Nat. Mater. **9**, 984 (2010).

[7] K. Wagner, A. Kakay, K Schultheiss, *et al.*, Nat. Nanotechnol. **11**, 432 (2018).

[8] Q. Wang, P. Pirro, R. Verba, *et al.*, Sci. Adv. **4**, e1701517 (2018).

[9] M. Madami, S. Bonetti, G. Consolo, *et al.*, Nat. Nanotechnol. **6**, 635 (2011).

[10] L. J. Cornelissen, J. Liu, R. A. Duine, J. B. Youssef, and B. J. van Wees, Nat. Phys. **11**, 1022 (2015).

[11] P. Pirro, P. Bracher, A. V. Chumak, *et al.*, Appl. Phys. Lett. **104**, 012402 (2014).

[12] V. E. Demidov, S. O. Demokritov, K. Rott, P. Krzysteczko, and G. Reiss, Phys. Rev. B **77**, 064406 (2008).

[13] T. Sebastian Y. Ohdaira, T. Kubota, *et al.*, Appl. Phys. Lett. **100**, 112402 (2012).

[14] H. Yu, R. Huber, T. Schwarze, *et al.*, Appl. Phys. Lett. **100**, 262412 (2012).

[15] R. W. Damon and J. R. Eshbach, J. Phys. Chem. Solids **19**, 308 (1961).

[16] A. Slavin and V. Tiberkevich, Phys. Rev. Lett. **95,** 237201 (2005).

[17] M. A. Hoefer, M. J. Ablowitz, B. Ilan, M. R. Pufall, and T. J. Silva, Phys. Rev. Lett. **95,** 267206 (2005).

[18] G. Consolo, B. Azzerboni, L. Lopez-Diaz, *et al.*, Phys. Rev. B **78**, 014420 (2008).

[19] M. A, Hoefer, T. J. Silva, and M. D. Stiles, Phys. Rev. B **77,** 144401 (2008).

[20] X. Chen and R. H. Victora, Phys. Rev. B **79,** 180402(R) (2009).

[21] M. Zahedinejad, A. A. Awad, S. Muralidhar, *et al.*, Nat. Nanotechnol. **15**, 47 (2020).

[22] A. Khitun, M. Bao, and K. L. Wang, J. Phys. D **43**, 264005 (2010).

[23] S.-K. Kim, J. Phys. D **43**, 264004 (2010).

[24] S. O. Demokritov, A. A. Serga, A. André, *et al.*, Phys. Rev. Lett. **93**, 047201 (2004).

[25] A. V. Chumak, A. A. Serga, and B. Hillebrands, Nat. Commun. **5**, 4700 (2014).

[26] M. Vogel, A. V. Chumak, E. H. Waller, *et al.,* Nat. Phys. **11**, 487 (2015).

[27] S. Barman, A. Barman, and Y. Otani, J. Phys. D **43**, 335001 (2010).

[28] A. Haldar, D. Kumar, and A. O. Adeyeye, Nat. Nanotechnol. **11**, 437 (2016).

[29] S. Choudhury, A. K. Chaurasiya, A. K. Mondal, *et al.*, Sci. Adv. **6**, eaba5457 (2020).

[30] T. Schneider, A. A. Serga, B. Leven, and B. Hillebrands, Appl. Phys. Lett. **92**, 022505 (2008).

[31] Q. Wang, A. V. Chumak, L. Jin, *et al.*, Phys. Rev. B **95**, 134433 (2017).

[32] N. S Gusev, A. V. Sadovnikov, S. A. Nikitov, M. V. Sapozhnikov, and O. G. Udalov, Phys. Rev. Lett. **124**, 157202 (2020).

[33]C. Banerjee, S. Choudhury, J. Sinha, and A. Barman, Phys. Rev. Appl. **8**, 014036 (2017).

[34] M. Krawczyk and D. Grundler, J. Phys. Condens. Matter **26**, 123202 (2014).

[35] J. W. Kłos, M. Krawczyk, Y. S. Dadoenkova, *et al.*, J. Appl. Phys. **115**, 174311 (2014).

[36] P. Graczyk and M. Krawczyk, Phys. Rev. B **96**, 024407 (2017).

[37] M. Matsuo, E. Saitoh, and S. Maekawa, J. Phys. Soc. Jpn. **86**, 011011 (2016).

[38] B. Rana and Y. Otani, Commun. Phys. **2**, 90 (2019).

[39] G. Gubbiotti, G. Carlotti, M. Madami, *et al.*, J. Appl. Phys. **105**, 07D521 (2009).

[40] A. A. Serga, T. Schneider, B. Hillebrands, *et al.*, Appl. Phys. Lett. **89**, 063506 (2006).

[41] M. Donahue and D. G. Porter, *OOMMF User's Guide Version 1.0 Interagency Report NISTIR 6376* (Gaithersburg, MD: National Institute of Standard and Technology) (http://math.nist.gov/oommf) (1999).

[42] D. Kumar, O. Dmytriiev, S. Ponraj and A. Barman, J. Phys. D: Appl. Phys. **45,** 015001 (2012).

[43] S. Ikeda, K. Miura, H. Yamamoto, *et al.*, Nat. Mater. **9**, 721 (2010).

[44]. H. Ohno, Science **291**, 840 (2001).

[45] H. X. Yang, M. Chshiev, B. Dieny, *et al.*, Phys. Rev. B **84**, 054401 (2011).

[46] M. Tsujikawa and T. Oda, Phys. Rev. Lett. **102**, 247203 (2009).

[47] S. Miwa, M. Suzuki, M. Tsujikawa, *et al.*, Nat. Commun. **8**, 15848 (2017).

[48] S. E. Barnes, J. Ieda, and S. Maekawa, Sci. Rep. **4**, 4105 (2014).

[49] V. B. Naik, H. Meng, J. X. Xiao, *et al.*, Appl. Phys. Lett. **105**, 052403 (2014).

[50] C.-G. Duan, J. P. Velev, R. F. Sabirianov, *et al.*, Phys. Rev. Lett. **101**, 137201 (2008).

[51] A. Okada, S. Kanai, M. Yamanouchi, *et al.*, Appl. Phys. Lett. **105**, 052415 (2014).

[52] D. D. Lam, F. Bonell, S. Miwa, *et al.*, J. Korean Phys. Soc. **62**, 1461 (2013).

[53] Y. Shiota, F. Bonell, S. Miwa, *et al.*, Appl. Phys. Lett. **103**, 082410 (2013).

[54] Y. Hayashi, Y. Hibino, F. Matsukura, *et al.*, Appl. Phys. Exp. **11**, 013003 (2017).

[55].Y. Hibino, T. Koyama, A. Obinata, *et al.*, Appl. Phys. Lett. **109**, 082403 (2016).

Chapter 12

12. Summary and Future Perspectives

12.1. Summary

In summary, the results contained in this dissertation are based on the investigation of spin orbit coupling induced phenomena such as interfacial Dzyaloshinskii-Moriya interaction (iDMI), spin pumping effect, spin waves (SW) nonreciprocity induced by dipolar interaction etc. in a variety of material combinations comprised of heavymetal/ferromagnet, 2D material/ferromagnet, synthetic antiferromagnets etc. This dissertation also explores the spin waves in artificial spin ice (ASI) nanostructures, and 1D magnonic waveguides fabricated using state-of-the-art nanofabrication. The preliminary characterizations of the samples are performed by the X-ray diffraction (XRD), scanning electron microscopy (SEM), transmission electron microscopy (TEM), atomic force microscopy (AFM) and the static magnetic properties were studied using magnetic force microscopy (MFM), magneto-optical Kerr effect magnetometry (MOKE) and vibrating sample magnetometry (VSM). We have investigated the spin dynamics using conventional as well as microfocused Brillouin Light Scattering (BLS) technique. The experimental results are modelled and analysed by solving the Landau-Lifshitz-Gilbert (LLG) equation for the respective system using macrospin formalism, micromagnetic simulations.

Firstly, we have investigated both qualitatively and quantitatively the pure iDMI in W/CoFeB/SiO$_2$ using BLS technique. The detailed study of magnetostatic surface spin-wave properties shows that the iDMI leads to nonreciprocal spin-wave propagation, i.e., different properties for spin-waves propagating in opposite directions. In Damon-Eshbach geometry, by interchanging the magnetic field direction we observe asymmetry in the peak frequency, peak intensity and magnon lifetime. Furthermore, we showed that the iDMI constant scales as the inverse of CoFeB thickness down to 0.85 nm, indicating its origin as purely interfacial. The W/CoFeB interface shows almost negligible degradation down to sub-nanometer CoFeB thickness, which is highly desirable for technological applications those aim to use interface effect, in particular iDMI. Further, iDMI strength increases with the underlayer thickness in the β-W region whereas a

sudden decrease is observed in α phase of W. This study will be important for understanding the spin-wave dynamics as well as stabilizing DMI assisted skyrmion, soliton like domain wall motion, in CoFeB with W underlayer, which is known to have a large spin Hall angle.

After exploring a reasonable amount of iDMI at W/CoFeB interface, we have extended our study to other thin film heterostructures. Here, we have systematically studied the FM layer and HM underlayer thickness dependence of iDMI in technologically important Ta/CoFeB/TaO$_x$ heterostructure using BLS spectroscopy. By measuring the spin-wave frequency non-reciprocity, we observe significantly large iDMI in these stacks likely due to the absence of B diffusion at the Ta/CoFeB interface as these films are unannealed. Furthermore, presence of large iDMI was also cross verified by the sinusoidal angular dependence of spin-wave non-reciprocity, Δf. In the case of FM thickness variation, we observe that D varies linearly with the inverse of CoFeB thickness demonstrating its purely interfacial origin, whereas in the case of Ta thickness dependence, D shows a sharp variation in the sub-nanometer thickness range and attains a nearly constant value above Ta thickness of 1 nm. This detailed FM and HM thickness dependent studies are very important to understand the tunability of iDMI in these heterostructures for controlling chiral spin structure and magnetic domain-wall based magnetic storage and memory devices.

Next, we have extended our study to explore iDMI at 2D/FM interface. We investigate iDMI in graphene/NiFe/Ta heterostructures where we perform the FM layer thickness dependence of iDMI. By measuring the spin-wave frequency non-reciprocity, we observe a sizeable iDMI in these stacks. FM thickness variation reveals that D varies linearly with the inverse of NiFe thickness demonstrating its purely interfacial origin. Furthermore, we observe a tunability of surface DMI constant and spin-mixing conductance with defect density in the graphene layer obtained by varying Ar pressure during DC sputtering of NiFe. Remarkably, there is a direct correlation between surface DMI constant and spin-mixing conductance, while both are found to be correlated with the increase in defect density. Hence, we conclude that defect induced extrinsic spin-orbit coupling may play a major role in the observed iDMI in these samples.

Next, we have investigated SWs in Ta(N)|CoFeB|MgO films using BLS technique. Frequency corresponding to uniform precession mode in the BLS spectra of

perpendicularly magnetized as well as in-plane film is found. For out-of-plane magnetized sample the spin wave frequency takes minima at a critical field which corresponds to the anisotropy field. The linewidth decreases by nearly a factor of 2, which suggests that the magnetic inhomogeneity reduces with enhanced N-doping in the Ta underlayer. The reduced inhomogeneity in these films by modifying underlayer|CoFeB interface indicates in a large reduction in the value of magnetic damping, which is important for applications in both spintronic and magnonic devices. Moreover, the DMI investigation reveals stronger DMI of 0.72 mJ/m^2 present in TaN(9%)/CoFeB/MgO heterostructure. This study shows a way to stabilize DMI assisted skyrmion structure in CoFeB with N-doped Ta underlayer.

The results obtained from HM/FM and 2D/FM heterostructures motivated us to explore other multilayer thin films heterostructure exhibiting SW frequency nonreciprocity originated due to different mechanism other than iDMI. In that context, we have studied the dynamic magnetic properties of a coupled ferromagnetic bilayer system. By means of a spin-wave theory, micromagnetic simulations, and Brillouin light-scattering measurements, we demonstrate that the dipolar interaction between the FM layers produced by the dynamic magnetizations is a notable source of nonreciprocity in the spin-wave frequency, with a remarkable property of reconfigurability that relies on control of the relative magnetic orientation of the interacting FM layers. In such bilayer structures, we can have in-plane remanent stable states with a parallel as well as an antiparallel configuration, as is well known from GMR and TMR applications. Therefore, one can reconfigure the bilayer system reliably into a reciprocal and a nonreciprocal device just by the magnetic-field history or, alternatively, by applying a local torque to one of the layers via a critical current density. Also, in the small-wave-vector limit, we show that the bilayer system can emulate the nonreciprocity produced by the Dzyaloshinskii-Moriya interaction in FM–heavy-metal stacks, even for ultrathin ferromagnetic films. Thus, the bilayer system exhibits the ability to mimic the extensively studied dynamic properties of FM–heavy-metal layers and, at the same time, presents an easy way to control the magnitude of the nonreciprocity by means of the geometry and the equilibrium configuration. These findings open up alternative routes for the creation of nanoscale nonreciprocal magnonic devices and motivate a deeper study of this type of system, in order to optimize its design according to the desired application requirements.

Next, we have experimentally and numerically studied the magnetization dynamics of connected (c-ASI) and disconnected (d-ASI) kagome artificial spin ice nanostructures made of Py nanobars using BLS technique complemented with micromagnetic simulations. The MFM images reveal that the magnetic microstates of kagome ASI obey the spin ice rule and a good agreement is found with the simulated images using micromagnetic simulation. The magnetic hysteresis loop measured by MOKE exhibits two-step reversal process for c-ASI but a single step reversal for d-ASI. Bias field dependent SW spectra measured by BLS reveal distinct features both in SW frequency (f) as well as BLS intensity for c-ASI and d-ASI. Both c-ASI and d-ASI exhibit frequency minimum, occurring at negative bias magnetic fields, when ramped down from a positive saturation field. A sharp jump in the mode frequencies was observed beyond the minima. This jump is somewhat related to the switching field observed from the MOKE loops and the variation in the magnetic microstates. This jump is associated with a remarkable change in the SW mode profiles and mode quantization numbers with H. This demonstrates a rapid control of SW modes by a small variation in magnetic field. Simulated internal field profiles throw further insights into the drastic variation of SW modes in this system system. The investigation and control of SW modes of these kagome ASI nanostructures will be important for fundamental understanding and applications in devices requiring frequency selective SW propagation, microwave filter etc.

Finally, we have experimentally demonstrated the propagation of spin waves in a magnonic waveguide made of Py using micro-BLS technique. An appropriate design of the antenna and the choosing the excitation frequency and microwave power, a prominent spin wave mode can be observed. By performing the spatial 2D-scan of the SW intensity, we find the propagation characteristics of the excited SW mode. The spin wave power and phase profiles of the excited mode has been revealed by micromagnetic simulation. Furthermore, our study of a 1D magnonic waveguide (1D-MWG) by utilizing voltage controlled magnetic anisotropy (VCMA) effect in CoFeB/MgO heterostructure shows that the single frequency mode splits into two modes and the difference of which gives rise to magnonic band gap in these artificial 1D-EFCMWG under the influence of electric field. The observed magnonic band gap (MBG) is tunable with the both polarity of applied gate voltage across CoFeB/MgO interface through 1D array of strip like ITO electrodes. This observation opens up a new avenue for energy-efficient stimulus, i.e.,

electric field, which may play a vital role in designing spin-based magnonic nanocircuits with minimal-power consumption.

12.2. Future Perspectives

The results presented in this thesis unlocks many other aspects to be investigated in the studied systems. Nowadays, a significant attention is being paid to study thin film heterostructures with repetition of the layers to enhance the DMI constant which is essentially required for the stabilization of chiral spin textures such as skyrmions. So far, we have explored Ta and W based heterostructures, a FM sandwiched between two different heavy metal with opposite sign of the DMI holds promise for the overall increment in the iDMI. In recent years, a new strategy has come up in order to tune the tune the iDMI by utilizing voltage controlled magnetic anisotropy (VCMA) effect. Hence, the properties studied in various HM/FM/oxide heterostructures presented in the thesis can be extended for exploring their tunability under the application of electric field. Further, the direct investigation of iDMI in graphene/FM based system using BLS can also be carried out with other FM (Co, CoFeB, CoFe etc.). In case of synthetic antiferromagnets based on CoFeB/Ir/NiFe, the key ingredients of the study rely on the tuning of stray fields to manipulate stability and sensitivity together with the additional degrees of freedom provided by the layers and coupling between them. These systems may also be relevant for the development of spin-torque oscillators based on synthetic antiferromagnets with increased frequency range and reduced linewidth. The dynamics of synthetic antiferromagnets is also relevant for switching by spin–orbit torques in devices containing synthetic antiferromagnetic layers. The other interesting research problem that can be pursued is the dynamics of skyrmions in these materials. The work in this direction has not been intensely started yet which offers a nice opportunity to explore the intriguing properties in these multilayers.

In case of kagome ASI system, we observed the magnetic field-controlled transition in the SW dynamics of the respective connected and disconnected ASI. However, these systems possess a definite lattice arrangement and form a type of magnonic crystals. It would be interesting to investigate the spin wave dispersion characteristics of ASIs by employing BLS spectroscopy. However, despite the successful implementation of optical techniques such as BLS to investigate the spin dynamics in ASI, a clear one-to-one mapping of defect strings and spin dynamics in 2D is missing. In that context, space resolved micro focused

BLS can play a vital role to bridge this gap. Another key direction for the ASI research is the utilization of ASI for logic and neuromorphic computing concepts. From this end, the integration of spin-torque oscillators and magnetoresistance devices in artificial spin ice might provide desirable functionalities and lead to concepts that are important for next-generation computing and memory devices.

In the case of propagating spin waves in a Py microwire, this study can be extended further by making antidots of various shape, size and lattice constant on this microwire. The SW propagation characteristics through these MCs can be investigated to unravel its intriguing properties. On the other hand, choosing a different FM layer having a very small magnetic damping such as YIG will help to achieve the longer SW propagation length. In case of voltage controlled 1D-MWG by utilizing VCMA effect in CoFeB/MgO heterostructure, we have shown that under the application of electric field, the single frequency mode splits into two modes and the difference of which gives rise to magnonic band gap in these artificial 1D-EFCMWG. This study unlocks the possibility for the investigation of MBG in 2D- EFCMWG. Also, imaging of the propagating spin wave and the possibility to enhance the group velocity of SWs by utilizing VCMA may open a new pathway to propose spin-based magnonic nanocircuits with ultralow-power consumption.